Title
Tropical convective transition diagnostics and the dynamics of convective deep inflow

Author
Kuo, Yi-Hung

Publication Date
2021

Peer reviewed|Thesis/dissertation

UNIVERSITY OF CALIFORNIA

Los Angeles

Tropical convective transition diagnostics and the dynamics of convective deep inflow

A dissertation submitted in partial satisfaction

of the requirements for the degree

Doctor of Philosophy in Atmospheric and Oceanic Sciences

by

Yi-Hung Kuo

2021

ABSTRACT OF THE DISSERTATION

Tropical convective transition diagnostics and the dynamics of convective deep inflow

by

Yi-Hung Kuo
Doctor of Philosophy in Atmospheric and Oceanic Sciences
University of California, Los Angeles, 2021
Professor J. David Neelin, Chair

Moist convection drives much of the circulation and precipitation in Earth's atmosphere, especially in the tropics, and thus has far-reaching consequences for human activities. The parameterization of moist convection in general circulation models (GCMs) remains a major source of error in these models, highlighting the importance of understanding the physical processes by which deep convection interacts with larger scales. A physical pathway contributing to the uncertainty of parameterizations concerns how environment air enters convective updrafts, i.e., *entrainment*. This dissertation addresses several aspects of the physics of convection, including causal pathways by which the environmental water vapor impacts convection and the implications of this for model parameterizations, related process-oriented diagnostics for comparing convective processes in GCMs to observations, and theoretical foundations for a different view of the entrainment process.

First, it has been noted that as the atmospheric column water vapor (CWV) exceeds a critical threshold, precipitation sharply picks up. This "pickup" has been demonstrated to be consistent with the lower-free-tropospheric humidity impacting updraft buoyancy—thus convection—through entrainment. By performing a set of parameter perturbation exper-

iments in the NCAR Community Earth System Model (CESM), we establish the causal relationship of the observed transition to deep convection—only when the convective scheme includes substantial entrainment can the model reproduce the pickup. The change in the precipitation–CWV relation also leads to a moist troposphere compared with when there is no entrainment. The reevaporation of convective precipitation is found to have only minor effects on the pickup.

Second, from observations and reanalyses, we compile and expand the set of statistics characterizing the transition to deep convection at fast timescales—termed "convective transition statistics." Given that the spatial autocorrelation scales of tropospheric temperature and humidity are greater than that of precipitation, the precipitation–CWV relationship is robust to spatial resolution up to $\sim 1^\circ$ and time-averaging up to $\sim$6 hours. The critical CWV at which precipitation starts to pick up increases with bulk tropospheric temperature, while the corresponding critical column relative humidity (CRH) decreases. This is consistent with prior entraining plume calculations. The CWV value relative to critical appears to be an effective predictor of conditional instability (hence precipitation) with only minor geographic variations in the tropics. The distribution of precipitation intensity drops rapidly for low CWV, and develops into a robust long-tail distribution for CWV around and above critical. The robustness of convective transition statistics—especially to the spatial-temporal resolution—suggests that these are suitable for model diagnostic purposes.

Third, we compared the convective transition statistics calculated using high-frequency (1-6 hourly) output from a set of GCMs to the observed. Comparing statistics among models that primarily differ in representations of moist convection suggests that convective transition statistics can substantially distinguish differences in convective representation and its interaction with the large-scale flow, while models that differ only in spatial–temporal resolution, microphysics, or ocean–atmosphere coupling result in similar statistics. Most of the models simulate some version of the observed sharp pickup of precipitation as well as that convective onset occurs at higher CWV but at lower column RH as temperature

increases. However, departures from observations in various aspects of the precipitation–CWV relationship are also noted in many models.

Lastly, a puzzle regarding entrainment profiles in the vertical is addressed. Observations and large-eddy simulations has pointed to a "deep-inflow" updraft mass flux structure, in which mass enters the updraft through a deep layer in the lower troposphere. Looking for a simple explanation for the observed deep inflow, we investigate the nonlocal response of vertical velocity field to buoyancy under the anelastic framework. We find that the vertical structure of response is determined by the horizontal length scales contributing to the buoyancy structure. For a wide range of conditions relevant for isolated cumulonimbus and organized systems, the nonlocal dynamics entailing interaction between the buoyant layer and the surface results in the deep inflow. Furthermore, the largest, most heavily-precipitating contributions to convection are suggested here to be a simplifying factor for their representations in convective parameterizations.

The dissertation of Yi-Hung Kuo is approved.

Gang Chen

Rong Fu

Eric D. Maloney

J. David Neelin, Committee Chair

University of California, Los Angeles

2021

To my mom,

my nanny Mrs. Chiu,

and aunt Mrs. Tseng-Huang.

In memory of Akio Arakawa and Kou-Nan Liou,

who passed away earlier this year.

Also, a special thanks to Wen-Li Yang and Yoshiki Tanaka ...

TABLE OF CONTENTS

LIST OF FIGURES

LIST OF TABLES

ACKNOWLEDGMENTS

Back in the late 2013/early 2014 when I was about to finish my Math PhD and had to make a decision of whether to accept the Postdoc offer in the filed of Petroleum Engineering, my then-advisor Dr. Long Lee encouraged me to apply for PhD programs in Atmospheric Sciences and Oceanography, and Drs. C. Roberto Mechoso and J. David Neelin decided to take me in as a graduate student—there are no words to express my gratitude.

I enjoyed my time as a graduate student at UCLA. Roberto advised me in the first few years, took me to the University of São Paulo, Brazil where we taught a Numerical PDE class designed for a quarter in 4 days as part of the GOAmazon funding requirement. I enjoyed the Brazilian food very much as well as his 201B lectures on Dynamics. Dr. James C. McWilliams has been giving excellent lectures on Ocean (202), GFD (201A) and Turbulence (201C). I lost count how many times I repeatedly sat in Jim's lectures at some point. Dr. Gang Chen agreed to offer a class in dynamics when I suggested. My fellow graduate students, now Drs. Baird G. Langenbrunner and Kathleen A. Schiro, were there when I needed help in Python, English, general discussion, etc. Without Joyce Meyerson's wizardry at plotting, none of my figures would be presentable. And the AOS office staff—especially Denise Lopez—made my life much easier without having to worry about administrative hurdles. Oh, and the weekly 270 seminars, I have found all but literally a handful of the talks enjoyable—kudos to the organizers.

This dissertation presents published and to-be-published work on how environment moisture impacts tropical precipitation with contributions by collaborators at UCLA and other institutions, notably Dr. Eric M. Maloney at Colorado State University, Dani Coleman and Dr. Chih-Chieh Chen at NCAR, Thomas Jackson and Dr. John P. Krasting at GFDL, Drs. Wei-Ting Chen and Chien-Ming Wu at National Taiwan University.

The contents in chapters 2-4 were published in *Journal of the Atmospheric Sciences*, © Copyright 2017, 2018, 2020 American Meteorological Society (AMS).

Chapter 2 is adapted from Kuo et al. (2017), supported by the Office of Biological and Environmental Research of the U.S. Department of Energy Grant DE-SC0011074, National Oceanic and Atmospheric Administration Grants NA14OAR4310274 and NA15OAR4310097, and National Science Foundation Grant AGS-1540518.

Chapter 3 is adapted from Kuo et al. (2018), supported by National Oceanic and Atmospheric Administration Grants NA15OAR4310097 and NA14OAR4310274, the Office of Biological and Environmental Research of the U.S. Department of Energy Grant DE-SC0011074, and National Science Foundation Grant AGS-1540518.

Chapter 4 is adapted from Kuo et al. (2020), supported by National Oceanic and Atmospheric Administration (NOAA) Grants NA15OAR4310097 and NA18OAR4310280, and National Science Foundation (NSF) Grant AGS-1540518, the Office of Biological and Environmental Research of the U.S. Department of Energy Grant DE-SC0011074.

The content of chapter 5 has been prepared for publication, and was supported by National Science Foundation grant AGS-1936810 and National Oceanic and Atmospheric Administration grant NA18OAR4310280.

Finally, my advisor David who has patiently guided me from writing manuscripts to thinking like an atmospheric scientist. I've always wondered whether my enthusiasm in the MDTF package development unwittingly forced him into the PI position rather than focusing on other more interesting subjects.

The people to whom I have to express gratitude are so many, I perhaps should simply say, in the style combining Zhi-Fan Chen and Richard Dawkins, *so I thank the Flying Spaghetti Monster.*

Yi-Hung Kuo

Los Angeles, California

August, 2021

VITA

2017	M.S. (Atmospheric and Oceanic Sciences), UCLA
2014	Ph.D. (Mathematics), University of Wyoming
2011	M.S. (Mathematics), National Taiwan University
2009	B.S. (Mathematics), National Taiwan University

PUBLICATIONS

1. Neelin, J. D., C. Martinez-Villalobos, S. N. Stechmann, F. Ahmed, G. Chen, J. M. Norris, Y.-H. Kuo, G. Lenderink, 2021: Precipitation extremes and water vapor: Relationships in current climate and implications for climate change. *Curr. Clim. Change Rep.*, in press.

2. Schiro, K. A., S. C. Sullivan, Y.-H. Kuo, H. Su, P. Gentine, G. S. Elsaesser, J. H. Jiang, and J. D. Neelin, 2020: Environmental controls on tropical mesoscale convective system precipitation intensity. *J. Atmos. Sci.*, **77**, 4233–4249.

3. Kuo, Y.-H., J. D. Neelin, C.-C. Chen, W.-T. Chen, L. J. Donner, A. Gettelman, X. Jiang, K.-T. Kuo, E. Maloney, C. R. Mechoso, Y. Ming, K. A. Schiro, C. J. Seman, C.-M. Wu, and M. Zhao, 2020: Convective transition statistics over tropical oceans for climate model diagnostics: GCM evaluation. *J. Atmos. Sci.*, **77**, 379–403.

4. Turk, F. J., R. Padullés, C. O. Ao, M. de la Torre Juárez, K.-N. Wang, G. W. Franklin, S. T. Lowe, S. M. Hristova-Veleva, E. J. Fetzer, E. Cardellach, Y.-H. Kuo, and J. D. Neelin, 2019: Benefits of a closely-spaced satellite constellation of atmospheric polarimetric radio occultation measurements. *Remote Sens.*, **11**, 2399.

5. Maloney, E. D., A. Gettelman, Y. Ming, J. D. Neelin, D. Barrie, A. Mariotti, C.-C. Chen, D. R. B. Coleman, Y.-H. Kuo, B. Singh, H. Annamalai, A. Berg, J. F. Booth, S. J. Camargo, A. Dai, A. Gonzalez, J. Hafner, X. Jiang, X. Jing, D. Kim, A. Kumar, Y. Moon, C. M. Naud, A. H. Sobel, K. Suzuki, F. Wang, J. Wang, A. Wing, X. Xu, and M. Zhao, 2019: Process-oriented evaluation of climate and weather forecasting models. *Bull. Amer. Meteor. Soc.*, **100**, 1665–1686.

6. Kuo, Y.-H., K. A. Schiro, and J. D. Neelin, 2018: Convective transition statistics over tropical oceans for climate model diagnostics: Observational baseline. *J. Atmos. Sci.*, **75**, 1553–1570.

7. Kuo, Y.-H., J. D. Neelin, and C. R. Mechoso, 2017: Tropical convective transition statistics and causality in the water vapor-precipitation relation. *J. Atmos. Sci.*, **74**, 915–931.

8. Kamchatnov, A. M., Y.-H. Kuo, T.-C. Lin, T.-L. Horng, S.-C. Gou, R. Clift, G. A. El, and R. H. J. Grimshaw, 2013: Transcritical flow of a stratified fluid over topography: analysis of the forced Gardner equation. *J. Fluid Mech.*, **736**, 495–531.

9. Kamchatnov, A. M., Y.-H. Kuo, T.-C. Lin, T.-L. Horng, S.-C. Gou, R. Clift, G. A. El, and R. H. J. Grimshaw, 2012: Undular bore theory for the Gardner equation. *Phys. Rev. E*, **86**, 036605.

CHAPTER 1

Overview

Despite the importance of moist convection in regulating the energy budget of the Earth system and the impacts on human society—primarily via precipitation or the lack thereof—the parameterization of moist convection in general circulation models (GCMs) has always remained a challenging yet fascinating subject, even with recent advances in cloud-resolving simulations and machine learning techniques. A major physical pathway contributing to the uncertainty of the representation of moist convection is *entrainment*—i.e., the process of environment air mixing into convective updrafts.

Prior studies have demonstrated a clear relationship between precipitation and and lower-free-tropospheric humidity. This relationship is consistent with the environment temperature and humidity impacting the buoyancy of convective updrafts via entrainment. However, a conclusive causal relationship has yet to be established. Adding another piece to the puzzle is the vertical structure of entrainment. The profiles of entrainment rate and convective mass flux are closely related (if not mathematically identical), and are central to the formulation of convective parameterizations. Efforts have been made to quantify entrainment. Recently, primarily via radar wind profiler observations, but consistent with earlier large-eddy simulations and aircraft measurements, it has been noted that convective updrafts tend to draw air mass from a deep layer (0∼4 km) through organized inflow under a wide range of conditions—in contrast with the conventional view of entrainment through localized, small-scale mixing. This dissertation presents published and to-be-published work addressing these aspects of the moist convective physics and the entrainment process, organized as follows.

Chapter 2—through a set of parameter perturbation experiments in the NCAR CESM—addresses the causality of the observed precipitation–humidity relationship, and investigates how the environment reacts to different values of entrainment parameters in the deep-convective parameterization.

Chapter 3 complies and extends the set of statistics characterizing the precipitation–moisture relationship from observations and reanalyses. The sensitivity of these statistics to spatial-temporal resolution and instrumentation is examined.

In chapter 4, the observed statistics in chapter 3 are compared with high-frequency (1-6 hourly) output from a set of GCMs as diagnostic tools targeting deep-convective parameterizations, going beyond the conventional diagnostics based on performance metrics.

Looking for a simple explanation to the observed deep inflow, chapter 5 studies the nonlocal response of vertical velocity field to buoyancy under the anelastic framework.

CHAPTER 2

Tropical convective transition statistics and causality in the water vapor-precipitation relation

Abstract

Previous work by various authors has pointed to the role of lower-free-tropospheric humidity in affecting the onset of deep convection in the tropics. Empirical relationships between column water vapor (CWV) and precipitation have been inferred to result from these effects. Evidence from previous work has included deep convective conditional instability calculations for entraining plumes, in which the lower-free-tropospheric environment affects the onset of deep convection due to the differential impact on buoyancy of turbulent entrainment of dry versus moist air. The relationship between deep convection and water vapor is, however, a two-way interaction because convection also moistens the free troposphere. The present chapter adds an additional line of evidence toward fully establishing the causality of the precipitation-water vapor relationship. Parameter perturbation experiments using the coupled Community Earth System Model (CESM) with high-time-resolution output are analyzed for a set of statistics for the transition to deep convection, coordinated with observational diagnostics for the Green Ocean Amazon (GOAmazon) campaign and tropical western Pacific Atmospheric Radiation Measurement (ARM) sites. For low values of entrainment in the deep convective scheme, these statistics are radically altered and the observed pickup of precipitation with CWV is no longer seen. In addition to helping cement the dominant direction of causality in the fast-time-scale precipitation–CWV relationship, the results point to impacts of entrainment on the climatology. Because at low entrainment

convection can fire before tropospheric moistening, the climatological values of relative humidity are lower than observed. These findings can be consequential to biases in simulated climate and to projections of climate change.

2.1 Introduction

Previous work by various authors has identified relationships between humidity in the lower free troposphere and the onset of deep convection in the tropics, and entrainment processes have been hypothesized to be instrumental in explaining these relationships. Analysis of TOGA COARE data and subsequent modeling studies revealed that intrusions of dry air above the planetary boundary layer into the Western Pacific warm pool region tend to inhibit deep convection locally (Brown and Zhang 1997, Parsons et al. 2000, Redelsperger et al. 2002). The cloud-resolving model (CRM) and single-column model simulations confirmed the sensitivity of moist convection to mid-tropospheric humidity (Derbyshire et al. 2004). In the case of weak vertical wind shears, further CRM studies demonstrated that water vapor in the lower atmosphere is more critical for the onset of deep convection than sea surface temperature (Tompkins 2001). Over daily and monthly timescales, analysis of data provided by the Special Sensor Microwave Imager (SSM/I) on board orbiting satellites together with in situ measurements have revealed connections between column relative humidity (CRH) in the atmosphere and precipitation (Bretherton et al. 2004, Sobel et al. 2004). Satellite observations also showed a positive correlation between column water vapor (CWV) and precipitation anomalies during Madden-Julian oscillation (MJO; Madden and Julian 1971) events (e.g., Waliser et al. 2009). Analysis of general circulation model (GCM) simulations found that the gross moist stability (GMS) of the atmosphere tends to lead MJO precipitation, and the GMS reduction ahead of peak MJO precipitation is due mainly to vertical advection (Benedict et al. 2014). Intercomparisons of GCM simulations have suggested that the models reproducing the most realistic MJO capture a transition from low-level moisten-

ing for light precipitation to upper-level moistening for heavy precipitation (Klingaman et al. 2015a,b). A number of studies have also examined various aspects of impacts of entrainment on model simulations: sensitivity of climatology or MJO metrics to entrainment (e.g., Bechtold et al. 2008, Zhu and Hendon 2015, Del Genio et al. 2012); the impacts of entrainment characteristics on large-scale features like double-ITCZ bias in certain GCMs (Mapes and Neale 2011, Oueslati and Bellon 2013, Hirota et al. 2014); the simulated diurnal cycle (Bechtold et al. 2004, Del Genio and Wu 2010); the coupling with boundary layer processes (Rio et al. 2009, Hourdin et al. 2013); the closure assumptions and entrainment representations in convective parametrizations (Raymond and Blyth 1986, Kuang and Bretherton 2006, Romps and Kuang 2010); and how the uncertainty of entrainment characteristics can contribute to the uncertainty in projected climate changes (Sanderson 2011, Sherwood et al. 2014).

On fast (convective) timescales, satellite observations have also revealed an empirical precipitation-CWV relationship. An outstanding feature of this relationship is the sharp increase in precipitation rate, referred to as precipitation pickup, which occurs when CWV exceeds a certain threshold value (Peters and Neelin 2006, Neelin et al. 2009). Also over the fast timescale, analyses of *in situ* data collected at DOE Atmospheric Radiation Measurements (ARM; Stokes and Schwartz 1994) sites over both tropical ocean (Nauru and Manus Islands in the Tropical Western Pacific; Mather et al. 1998) and tropical land [ARM mobile facility deployed at Manacapuru, Brazil as part of the Green Ocean Amazon (GOAmazon) campaign; referred to as GOAmazon herein], have revealed associations among the onset of deep convection and temporal and vertical humidity variations. These studies concluded that lower free-tropospheric humidity affects the onset of deep convection because turbulent entrainment of dry versus moist air has different impacts on buoyancy of convective plumes (Jensen and Del Genio 2006, Holloway and Neelin 2009, 2010, Lintner et al. 2011, Schiro et al. 2016). Another conclusion was that CWV can be used as a proxy for environmental impacts on conditional instability. Estimates of entraining plume buoyancies using radiosonde measurements in the Tropical Western Pacific (Holloway and Neelin 2009) and Amazon (Schiro

et al. 2016), together with tropical ocean basin satellite retrievals in comparison to climate model diagnostics (Sahany et al. 2012) imply a substantial role for entrainment in explaining the observed precipitation pickup, consistent with large-eddy simulation (LES) results (Khairoutdinov and Randall 2006).

The evidence gathered from both observational and modeling approaches across various temporal and spatial scales, therefore, clearly reveals connections between free-tropospheric moistening and deep convection. Diagnostic studies and offline calculations from GCM output, however, do not alone make a full case for the causality of the observed precipitation-CWV relationship. This is because convection also acts to loft moisture (including condensate which can subsequently reevaporate), and one must distinguish the active role of free tropospheric moisture in affecting the onset of conditional instability from the hypothesis that CWV simply increases passively in association with convection due to the effect of convective moistening of the column.

The present chapter focuses on the dominant direction of causality in the fast-timescale precipitation-CWV relationship, and addresses the impacts of entrainment on the two-way interaction between deep convection and environmental humidity. Our methodology is based on analysis of parameter sensitivity experiments (Bernstein and Neelin 2016) in the Community Earth System Model (CESM), which is able to simulate the sharp precipitation pickup with the default setting (Sahany et al. 2012, 2014). We show that the set of statistics associated with the transition to deep convection (or convective transition statistics) in the CESM can be radically altered if different values of entrainment are prescribed in the deep convective scheme. In particular, the pickup of precipitation with increased CWV is no longer captured at low values of entrainment. The sensitivity of these statistics to reevaporation is also examined to quantify any contribution to the precipitation pickup that might arise from reevaporation of condensate. Furthermore, the results demonstrate that entrainment has first order effects on the simulated climatologies of precipitation, humidity, and temperature. Because at low entrainment convection can fire before the lower troposphere

is moistened, the climatological values of relative humidity remain lower than observed in the tropics. Showing a dramatic change in convective transition statistics in absence of the entrainment pathway in a model with the two-way interaction of convection and moisture contributes an additional line of evidence for the direction of causality in the precipitation-water vapor relationship. These findings can be consequential to a better understanding of both climatological biases and improved simulations of climate change, underscoring the importance of the examined causal pathway.

The rest of this chapter is organized as follows. Section 2.2 gives the setup of the parameter perturbation experiments, together with a brief description of the CESM and the deep convective scheme. Section 2.3 examines composite time series of simulated precipitation, CWV, and other relevant variables for heavily precipitating events. After background on impacts of entrainment on climatology in section 2.4, section 2.5 presents the simulated convective transition statistics corresponding to different values of entrainment, and reevaporation rate in section 2.6. The convective transition statistics are coordinated with observational counterparts in Schiro et al. (2016). Section 2.7 further explores the model composite time series, focusing on the differences due to different entrainment values and ocean-land contrast. Finally, section 2.8 draws conclusions based on the effects of entrainment and reevaporation on the fast-timescale statistics and discusses potential applications of our results for model diagnostics.

2.2 Model and data

The simulations analyzed here are integral parts of a set of parameter perturbation experiments (Bernstein and Neelin 2016) with the fully coupled Community Earth System Model version 1.0.5 (CESM1; Hurrell et al. 2013) using CMIP5 historical greenhouse gas and aerosol forcing. The CESM simulations start from 1 January 1976, using an existing standard parameter simulation with the Community Climate System Model version 4 (CCSM4, a subset

of CESM1; Gent et al. 2011) as the initial condition. In CESM terminology this approach to starting a simulation is referred to as branch runs and aims to reduce the time required for model spin-up. The atmosphere component of CESM is the Community Atmosphere Model (CAM; Neale et al. 2010) with horizontal resolution of about 1.9° × 2.5° (latitude by longitude 144 × 96 grid points) and 26 levels in the vertical. The ocean component is the Parallel Ocean Program (POP; Smith et al. 2010) with horizontal resolution of about 1° (gx1v6; 384 × 320 grid points) and 60 levels in the vertical.

The CAM deep convective scheme (Zhang and McFarlane 1995, ZM hereafter) is based on an entraining plume calculation modified to include turbulent mixing (Neale et al. 2008) and convective momentum transports (Richter and Rasch 2008). The reevaporation of convective precipitation is also taken into account following Sundqvist (1988). Here we concentrate on two sets of experiments in which the only parameter changed are the parcel fractional mean entrainment rate (dmpdz), which controls the entrainment of environmental air in the convective plume, and the convective precipitation evaporation rate (zmconv_ke, or k_e hereafter), which controls the reevaporation of convective precipitation, respectively. Note that dmpdz is only used in the entraining plume calculations for the cloud base mass flux closure in the ZM scheme. In the buoyancy computations for the rising plume at each level, a fraction (determined by dmpdz) of environmental air relative to updraft mass flux is assumed to be mixed into the plume, conserving dry static energy and moisture. Entrainment thus affects convection directly through the entraining plume calculations, though it may have other indirect effects. Also note that dmpdz affects only deep convection (the shallow convection is handled separately). The CESM default values are dmpdz = 1 in units of 10^{-3} m^{-1} and $k_e = 1$ in units of 10^{-5} $(\mathrm{kg\ m^{-2}s^{-1}})^{-1/2}\mathrm{s}^{-1}$. The range of dmpdz explored is from 0 to 2 with default k_e, and the range of k_e explored is from 0.1 to 10 with default dmpdz. For dmpdz $\neq 1$ or $k_e \neq 1$, the initial state is slightly out of equilibrium due to the branch-run approach. The timescale for the simulated climate to effectively equilibrate is about 2 years for hydrological cycle statistics including the precipitation-CWV relationship

(Bernstein and Neelin 2016), although statistics affected by deep ocean circulation may not be fully equilibrated. Therefore, we can interpret that the differences obtained in the simulated convective transition statistics and climatology are due to varying entrainment or reevaporation, and not to initial transients. In addition to convective precipitation given by ZM, the CAM also includes a calculation for large-scale precipitation, which can be produced when the environment is saturated due to e.g., detrainment or moisture convergence.

The CESM simulations we analyze cover the period of 1976-2005 (1976-1998 for auxiliary cases dmpdz $= 0.08, 0.16, 0.25$) to overlap with the data available from the Global Precipitation Climatology Project (GPCP; Adler et al. 2003), which is used as our baseline for comparison. For more details regarding the setup and coordinated parameter perturbation experiments under global warming conditions, see Bernstein and Neelin (2016).

Capturing the fast-timescale convective onset requires special output from the CESM simulations. The output we analyze includes a set of relevant 2D fields at every time step for which they are computed (30 min), which can therefore be interpreted as instantaneous values as opposed to averages when model histories are written at multiple time steps. The variables selected for analysis comprise convective and total (convective + large-scale) precipitation rates (P_c and P, respectively), column-integrated water vapor (CWV), mass-averaged column air temperature ($\widehat{T}$), and column-integrated saturation specific humidity ($\widehat{q_{sat}}$). Here the column is defined as 1000-200 mb. The Kahan summation algorithm (Kahan 1965) is adopted for compiling the convective transition statistics to avoid possible round-off error. For verification we use observational and reanalysis datasets, including the Remote Sensing System (RSS) Version-7 microwave radiometer total columnar water vapor values (Hilburn and Wentz 2008), precipitation from the GPCP (version 2.2), and temperature profile from the NCEP-DOE AMIP-II Reanalysis (Reanalysis-2) dataset (Kanamitsu et al. 2002).

2.3 Temporal correlation between CWV and precipitation — The problem of determining causality

Previous studies analyzing observations in the maritime and continental tropics have examined composite time series centered at locally high (total) precipitation, and found that CWV and precipitation are closely related, pointing to the importance of atmospheric moisture to the onset of deep convection (Holloway and Neelin 2010, Adams et al. 2013). In this section, we briefly review similar time series composites from the model to verify that causal relationships are difficult to infer from the temporal sequence alone.

Specifically, we construct composite time series of CESM output for heavy convective precipitation events at geographical locations corresponding to Manus Island (2.1°S, 146.9°E; Tropical Western Pacific) and the GOAmazon mobile facility near Manaus (3.1°S, 60°W; Amazon), where ARM mobile facility observational data are available (Fig. 2.A.1). Here, heavy convective precipitation events are defined as having convective precipitation rates exceeding the mean convective precipitation rate averaged over all convectively precipitating events with respect to the threshold value of 0.1 mm h^{-1} within a 96-hour window at the single grid point closest to the specified location. Figure 1 shows such composites (together with those of total precipitation), centered at heavy convective precipitation events in the standard entrainment case (dmpdz = 1). The qualitative features indicated by the curves in Fig. 2.1 are robust with respect to the value selected for the threshold defining heavy precipitation, and do not change significantly if the composites are centered at locally high total precipitation (see Fig. 2.C.1). The time series of each individual heavily precipitating event may look very different from the composites shown here (e.g., see Fig. 2 in Holloway and Neelin 2010).

At both the maritime and continental location, the values of CWV increase (decrease) before (after) the P_c maximum, with a broad maximum surrounding the sharp precipitation maximum. This is consistent with short duration precipitation events occurring within a

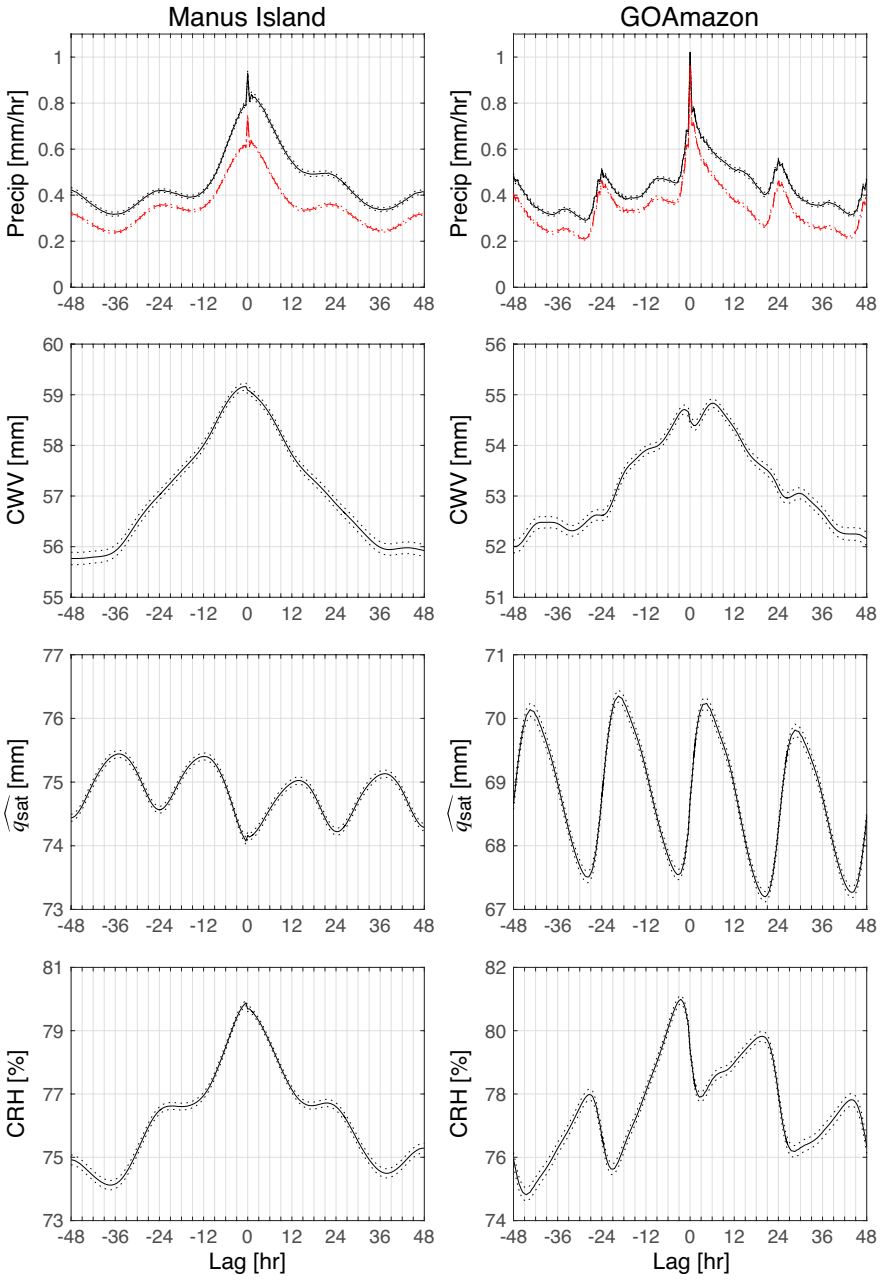

Figure 2.1: Model composite time series centered at locally high convective precipitation (defined as being greater than the mean of all convectively precipitating events with respect to the threshold of 0.1 mm h^{-1}) within a 96-hour window for the standard entrainment case (dmpdz = 1). The top panels show the total (black) and convective (red) precipitation. Dotted curves in all panels represent ± 1 standard error. The qualitative features indicated by these curves are robust with respect to the threshold defining heavy precipitation. See Supplement for composites centered at locally high total precipitation and composites calculated using observational data.

high water vapor environment that tends to have longer temporal autocorrelation. Both locations are influenced by a temperature diurnal cycle, represented by $\widehat{q_{sat}}$, which is used here as a proxy for temperature. The column relative humidity CRH $\equiv$ CWV/$\widehat{q_{sat}}$ provides one measure of the relationship to temperature, i.e., how far the column is from saturation. We note that the main impact of CWV to convection occurs via conditional instability, for which the temperature dependence is subtler than simple column saturation (Sahany et al. 2014). Vertical structure changes can reduce the usefulness of CRH relative to other measures of temperature (Neelin et al. 2009), such as lower tropospheric layer relative humidity. In climatological analysis in section 2.4, we use CRH to account for large-scale temperature changes among experiments with different parameter values; CRH provides a useful measure for such equilibrated situations. At Manus Island (tropical maritime), the temporal relationship of CRH to P_c is similar to that of CWV. At the GOAmazon site (tropical continental), the diurnal cycle is stronger as seen in $\widehat{q_{sat}}$ (which is strongly influenced by boundary layer temperature). Precipitation exhibits modest diurnal cycle in these composites, while that of CWV is small. CRH has a stronger temporal structure that is not closely related with precipitation.

The model composites at Manus Island in the standard entrainment case shown in Fig. 2.1 capture neither the magnitudes of precipitation rate nor the rapid CWV increase due to mesoscale processes found with observations (Fig. 2.A.1; Holloway and Neelin 2010, Fig. 7). This is at least partially due to the model resolution. Nevertheless, the composites from the standard entrainment case capture the relationship between environmental humidity and precipitation that has been seen from observations. The model composites at the GOAmazon site, over land, show a large amplitude of the diurnal cycle in comparison with observations (Fig. 2.A.1; Adams et al. 2013, Fig. 2). The composites from both the model and observations show that CWV increases and decreases rather symmetrically near the precipitation maximum over both tropical maritime and continental locations examined. These features could be consistent with either the hypothesis that lower free tropospheric moisture has the

dominant effect on convection via entrainment or the alternative hypothesis that convection simply tends to moisten the atmosphere (through detrainment or reevaporation). These, however, due to the lack of asymmetry in the lead-lag relationship, are not enough to infer *causality*—that is, to determine *whether entrainment results in the observed precipitation pickup.*

In another line of evidence, radiosonde measurements from tropical ARM sites (Nauru, Manus, and GOAmazon) have shown that the moisture increase prior to deep convection tends to be in the lower free troposphere, while it tends to be in the upper troposphere after precipitation (e.g., Fig. 5 in Holloway and Neelin 2009; Fig. 7 in Schiro et al. 2016), consistent with composites in (Sherwood and Wahrlich 1999, Figs. 5 and 6). Such changes of vertical moisture structure associated with precipitation, are potentially consistent with a causal role for lower free tropospheric water vapor via entrainment, with the upper tropospheric changes due mainly to convective moistening. However, they do not alone establish causality of the observed precipitation-CWV relationship. Here we address this question by examining CESM simulations subject to different values of entrainment and reevaporation rate.

2.4 Climatological sensitivity to entrainment

Before turning to fast-timescale statistics, we provide a sense of changes at the largest tropical scales in the set of parameter sensitivity experiments with different values of entrainment. As noted in the Introduction, entrainment can impact the climatology simulated by GCMs. Figure 2.2 shows the simulated climatological values of CRH, $\widehat{T}$, CWV, total and convective precipitation (P and P_c, respectively), averaged over the tropics (20°S to 20°N) separately for ocean and land points as a function of entrainment parameter dmpdz. For reference, the corresponding values calculated using observational and reanalysis datasets are also plotted at dmpdz = 1.8. As entrainment increases, average CRH over ocean and land increases monotonically and $\widehat{T}$ decreases monotonically, with the sharpest transition for dmpdz less

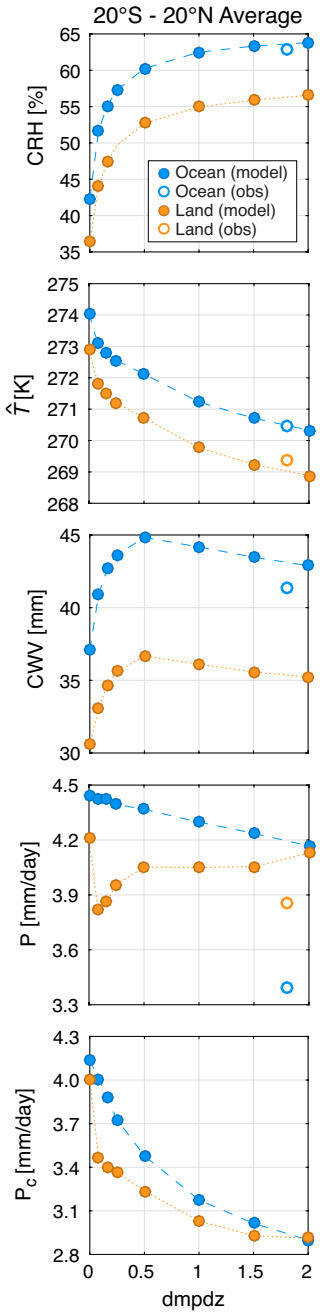

Figure 2.2: Average climatological values of simulated column relative humidity CRH, mass-averaged column air temperature $\widehat{T}$, column-integrated water vapor CWV, total precipitation P, and convective precipitation P_c over the tropics (20°S-20°N) for different entrainment values dmpdz $= 0, 0.08, 0.16, 0.25, 0.5, 1, 1.5$ and 2. The standard errors associated with the 3-year tropical averages are smaller than those represented by the marker size. For comparison, the corresponding values calculated using RSS CWV (over ocean), GPCP precipitation, and Reanalysis-2 temperature, are also plotted at dmpdz $= 1.8$ (only for visual clarity).

than 0.5. Averaged CWV also increases drastically as dmpdz increases over both ocean and land for dmpdz less than 0.5, after which it exhibits a slight decrease with further increase in dmpdz. This decrease at high entrainment is likely associated with decreasing $\widehat{T}$, and CRH reasonably accounts for this temperature effect since the relationship between the boundary layer and free troposphere is fairly constant through this range. Averaged over the tropics, total precipitation is relatively insensitive to entrainment (a slow decrease with increasing entrainment over ocean, and small variations near low entrainment over land). Convective precipitation decreases modestly as dmpdz increases over both ocean and land, with the ratio of convective to total precipitation decreasing from 94% to 71% (ocean-land difference within 2%). This is consistent with the more restrictive conditions on conditional instability resulting in convection firing at higher CRH with increasing dmpdz, and with it being easier to reach saturation in the vicinity of convection associated with these higher CRH values.

The simulated precipitation in comparison with observations indicates that the simulation of the hydrologic cycle has room for improvement. Regardless of other metrics, the values of simulated CRH, $\widehat{T}$, and CWV alone in comparison to observations/reanalysis seem to suggest a dmpdz value larger than the CESM default setting, which may degrade the model performance in other aspects. For instance, Hannah and Maloney (2014) noted in the CAM5 hindcast experiments that higher entrainment values erroneously improve MJO predictive skill because of tradeoffs between vertical MSE advection and cloud-radiative feedbacks. The choice of an optimal set of parameters often involves tradeoffs among different metrics in model performance (e.g., see Kim et al. 2011), and requires a systematic approach for multiobjective optimization (Langenbrunner 2015).

The dependences of simulated CRH and CWV on entrainment shown in Fig. 2.2 are consistent with what one would expect from entraining plume calculations, although explaining the detailed dependence of $\widehat{T}$ may requires further radiation budget analysis. Over fast timescale, atmospheric moisture can be removed efficiently through convection-induced precipitation, provided large-scale moisture divergence is negligible. When entrainment ef-

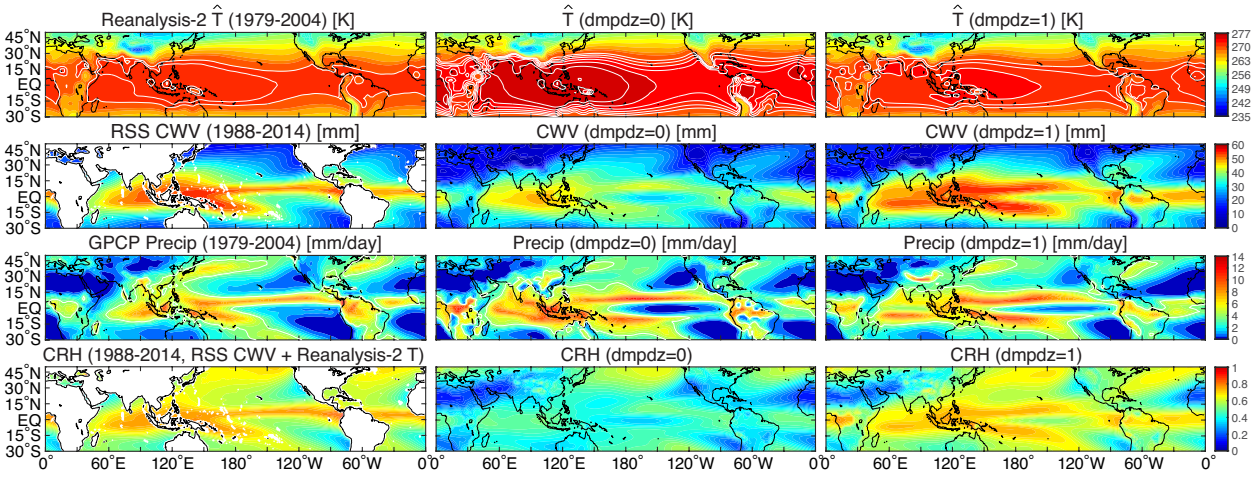

Figure 2.3: Climatology of $\widehat{T}$, CWV, P, and CRH calculated using observational and reanalysis datasets, and CESM simulations for no-entrainment (dmpdz = 0) and standard-entrainment (dmpdz = 1) cases. White contours in the uppermost panels indicate $\widehat{T} \geq 270$ K with 1 K increment, as well as the 4 mm/day contour. The climatological values for CESM simulations are calculated using the 30-min output for the period of 1979-2004, and the values for observations/reanalysis use 6-hourly and monthly data. In particular, the RSS CWV (also used for calculating CRH) is monthly mean. The simulated CRH values calculated using the 30-min output are not very different from those calculated using monthly-mean output, hence justifying the comparison here.

fects are included in the parameterization, convection can fire only when the environmental humidity is high enough. Thus, entrainment effects result in a moister and relatively cool atmosphere than when these effects are neglected. In contrast, without entrainment, convection occurs without preconditioning of environmental humidity, i.e., the lower free troposphere does not have to moisten before conditional instability can occur. The environment thus favors a low humidity state, resulting in a moisture-depleted and relatively warm atmosphere. These CESM cases that take into account convective moistening (including reevaporation) demonstrate how the large-scale environment react to varying entrainment, serving as a background for the convective transition statistics presented in the following section.

Complementary to Fig. 2.2, Fig. 2.3 shows the climatological values of $\widehat{T}$, CWV, total precipitation, and CRH from observational and reanalysis datasets together with those from

CESM simulations for dmpdz = 0 and dmpdz = 1. Regarding the former datasets, we show $\widehat{T}$ calculated using Reanalysis-2 and precipitation from GPCP, both of which are for the 1979-2004 period. CWV is from RSS for the 1998-2014 period. The CRH is calculated using the monthly RSS CWV and Reanalysis-2 temperature field, which is for the 1998-2014 period. Although the observational datasets cover different periods and are subject to different temporal resolutions, it does not affect our discussion. Comments on biases in Reanalysis-2 CWV fields are included in the Supplement.

Overall, Fig. 2.3 shows that the no-entrainment case simulates the warmest and driest atmosphere. In this case, the tropical-mean value of CWV is about 7 mm (or 13% in terms of relative difference) lower than the default case, while the corresponding CRH is lower by about 20% (or 27% in relative difference). Temperature contributes to this quantitative difference. Although not the main focus here, it is worth remarking on certain aspects of the climatological simulation. An overextension of the South Pacific Convergence Zone may be noted in the Tropical Eastern Pacific, and the Atlantic Intertropical Convection Zone has excessive precipitation just south of the equator; these issues are both common in climate models (e.g., Mechoso et al. 1995, Lin 2007, Oueslati and Bellon 2015). Entrainment impacts this quantitatively, but qualitatively these issues persist across all values of entrainment examined (including in the dmpdz = 2 case not shown here). Large differences in precipitation occur at regional scales, but these scales can be affected by multiple parameters (Bernstein and Neelin 2016). Examination of fast-process statistics is more directly relevant to the relationships at the timescale of convection. These statistics can provide independent measures of the convective process that can reveal differences in behavior even when it would be difficult to distinguish between effects of a parameter based on climatological metrics alone.

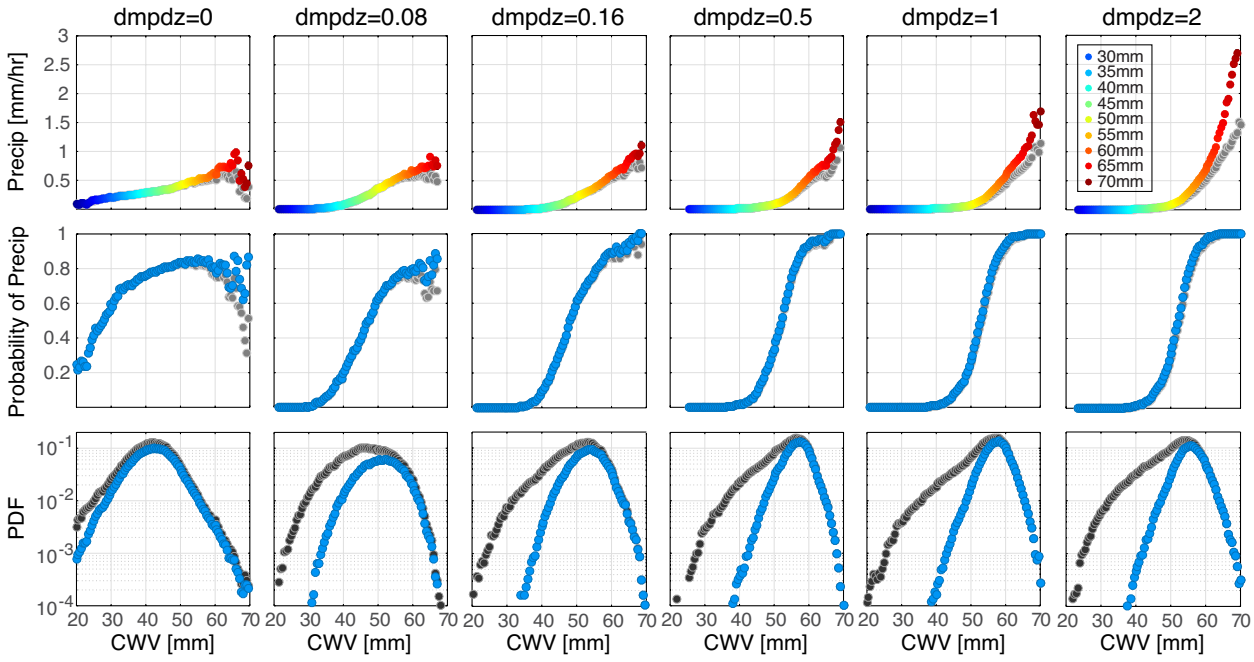

Figure 2.4: The CESM-simulated convective transition statistics at Manus Island in the Tropical Western Pacific for various entrainment (dmpdz) cases. The upper panels show the average total (color) and convective (gray) precipitation rate conditioned on CWV. The middle panels show the corresponding conditional probability of total (blue; $P > 0.1$ mm h^{-1}) and convective (gray; $P_c > 0.1$ mm h^{-1}) precipitation. The PDF of CWV for all (dark gray) and precipitating (blue; $P > 0.1$ mm h^{-1}) events are shown in the lower panels. In the upper panels, the colors indicate the corresponding CWV value, and the standard errors associated with total precipitation rate are smaller than that represented by the marker size. Underpopulated bins (PDF $< 10^{-4}$) are trimmed, and do not affect the discussion here.

2.5 Entrainment impacts on convective transition statistics

We next turn to the simulated convective transition statistics for different values of dmpdz compiled at fast timescales for two ARM sites at Manus Island in the Tropical Western Pacific (Fig. 2.4), and the GOAmazon mobile facility in the central Amazon near Manaus, Brazil (Fig. 2.5). For both locations we use model output sampled at the grid point including site coordinates as well as two adjacent grid points to both the east and west at both sites. The top panels in Figs. 2.4 and 2.5 show conditionally averaged precipitation rates for both total (color) and convective (gray) precipitation as a function of CWV binned at 0.5-mm intervals.

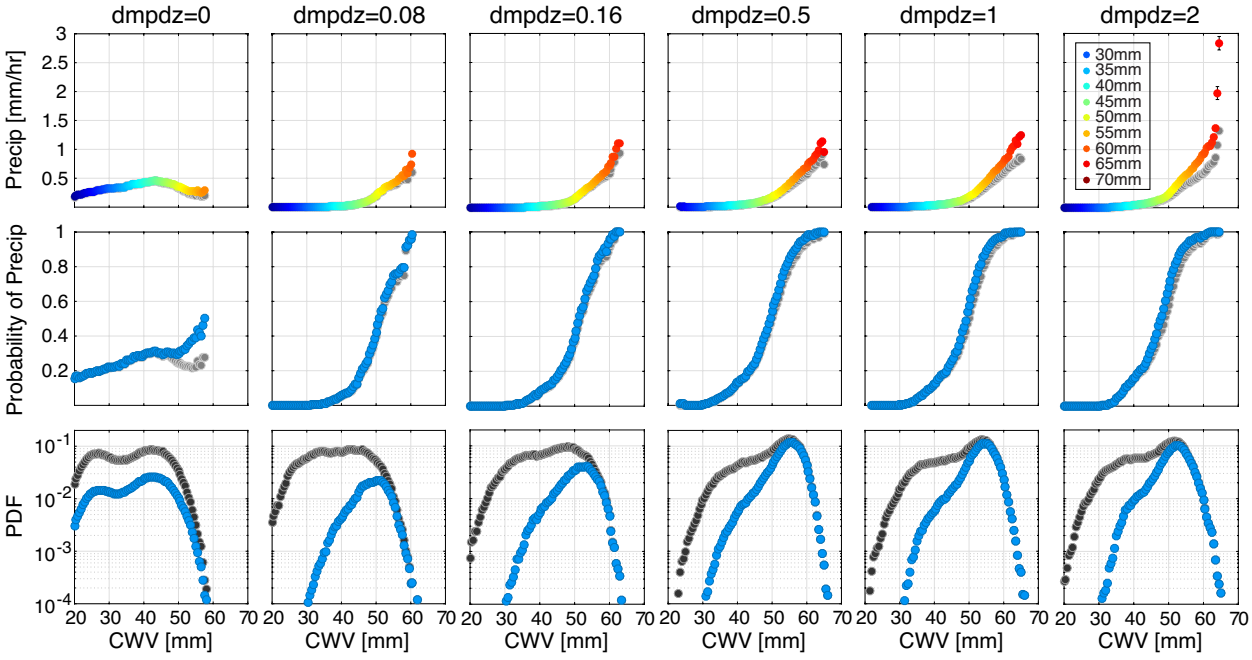

Figure 2.5: Same as in Fig.2.4, but using model output at the GOAmazon site. The standard errors associated with total precipitation rate are plotted if greater than that represented by the marker size.

The middle panels show the corresponding conditional probability of total (blue; $P > 0.1$ mm h^{-1}) and convective (gray; $P_c > 0.1$ mm h^{-1}) precipitation. The bottom panels show the probability distribution function (PDF) of CWV for all (dark gray) and precipitating (blue; $P > 0.1$ mm h^{-1}) events. Underpopulated bins (PDF $< 10^{-4}$) are trimmed and do not affect the discussion.

The convective transition statistics at tropical maritime and continental sites are qualitatively similar. For the standard case (dmpdz = 1), these statistics compare reasonably well to observed measures of the pickup. Observational comparisons are available from earlier studies at the ARM site at Nauru (0.5°S, 167°E; Holloway and Neelin 2009), and satellite microwave retrievals over the Tropical Western Pacific (Sahany et al. 2012, 2014). A direct comparison for the GOAmazon and Tropical Western Pacific ARM sites may be seen in the coordinated observational paper (Schiro et al. 2016). In particular, the precipitation rate sharply increases for CWV exceeding a threshold value, known as the critical CWV. The

accompanying conditional probability of precipitation picks up and the PDFs peak around this critical CWV. Quantitative discrepancies between model and observations do exist. For example, the simulated precipitation rates appear to be smaller than in observations, while the conditional probability derived from *in situ* data rarely reaches 80% (Schiro et al. 2016). Higher precipitation rates are noted in higher-resolution CESM runs (Sahany et al. 2012, 2014).

Drastic differences in the simulated convective transition statistics presented in Figs. 2.4 and 2.5 occur in the low entrainment range. For the no-entrainment case (dmpdz = 0) the precipitation pickup breaks down. At Manus Island, conditionally averaged precipitation increases only modestly over a broad range of CWV values (Fig. 2.4, leftmost column). Over land at the GOAmazon site (Fig. 2.5, leftmost column), the precipitation actually decreases at high CWV. The probability of precipitation exhibits very different behavior than for the standard case and the observations, and the PDF for precipitating events spreads across a large range of CWV.

As entrainment increases, precipitation rate and conditional probability both evolve towards increasing functions in CWV, and demonstrate clear signs of the observed pickup when subject to substantial entrainment. The precipitation rate and conditional probability curves shift towards higher CWV with increasing entrainment, consistent with the fact that larger entrainment results in a more sensitive dependence of entraining plume instability on environmental humidity. Larger entrainment also results in higher precipitation rates at the high end of CWV. The mean and mode of CWV, as being indicated by the PDF and reflected by the simulated climatology, increase as dmpdz increases from 0 to 0.5, and decrease slightly after that. This shift in climatology in response to varying entrainment matches that we see in Fig. 2.2. At high entrainment (dmpdz = 1.5 and 2), an even sharper increase of large-scale precipitation with reduced convective precipitation at very high CWV is noticed over some regions (e.g., the whole Tropical Western/Eastern Pacific basin, not shown), suggesting a shift from the deep convection regime to the large-scale saturation regime as the CWV is

driven to large-scale saturation.

It is clear that the model can reproduce the pickup only with substantial entrainment. These convective transition statistics are drastically altered as dmpdz increases from 0 to 0.08. Further increase in dmpdz above 0.16 causes relatively minor changes in the pickup behavior. These results apply for both maritime and continental tropics. The dependences of climatological values on entrainment we see in Fig. 2.2, together with the convective transition statistics shown in Figs. 2.4 and 2.5, clearly demonstrate the dominant direction in the fast-timescale precipitation-CWV relationship, indicating that entrainment results in the observed precipitation pickup, and the importance of environmental humidity to convective onset, in line with previous studies.

2.6 Effects of varying precipitation reevaporation

Reevaporation of precipitation could be hypothesized to affect the relationship between precipitation and CWV but via a different mechanism, i.e. greater reevaporation of hydrometeors in a drier environment reducing surface precipitation. Kim et al. (2011, Fig. 12) found an impact of reevaporation on pickup at daily timescale, in terms of CRH, in an earlier version of CAM (i.e., the precipitation picks up at lower CRH when subject to lower reevaporation rate). To evaluate the importance of this at the fast timescales most relevant to convection, we examine another set of CESM cases with varying reevaporation rate k_e. In the CAM, reevaporation is modeled following Sundqvist (1988), where the evaporation rate of convective precipitation is proportional to $(1-$ RH$)$ and a prescribed value of k_e. Here RH is the relative humidity at each level.

The simulated climatologies in the tropics are insensitive to reevaporation, except that the temperature decreases by about 1.5 K across the large range examined, and the precipitation rates over land decrease modestly, in response to increasing k_e (see Fig. 2.B.1). The corresponding convective transition statistics for the whole Tropical Western Pacific basin

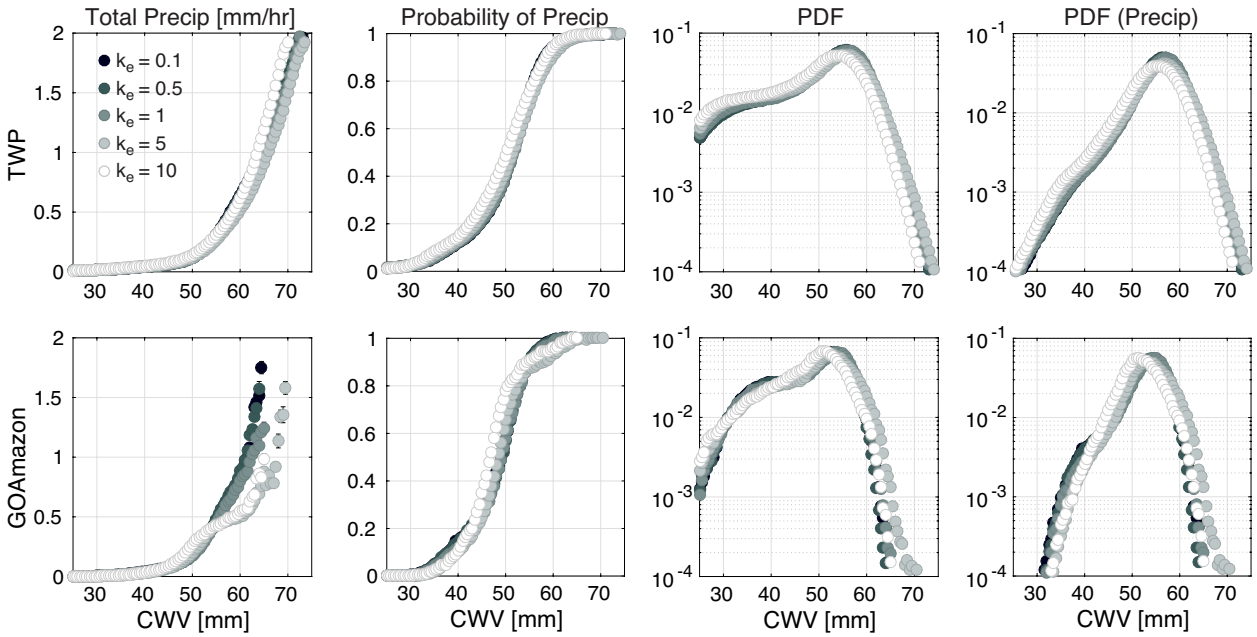

Figure 2.6: The CESM-simulated convective transition statistics in the Tropical Western Pacific (upper panels) and at the GOAmazon site (lower panels) for various reevaporation (k_e) cases. The plotted variables are the total precipitation rate conditioned on CWV, conditional probability of precipitation ($P > 0.1$ mm h^{-1}), and PDFs of CWV for all and precipitating ($P > 0.1$ mm h^{-1}) events. The standard errors associated with total precipitation rate are plotted if greater than that represented by the marker size. Underpopulated bins (PDF $< 10^{-4}$) are trimmed.

(TWP; west to 170°W) and for the GOAmazon site are compiled in Fig. 2.6. Much like the climatological responses, the precipitation pickup and the associated statistics (including convective precipitation, not shown) are insensitive to k_e across the two orders of magnitude tested here (from 0.1 to 10), except for large k_e values (5 and 10) for GOAmazon, where a slight reduction in the highest conditional average rain rates at high CWV may be noted. Though not the main focus here, the sensitivity noted in Kim et al. (2011) may be attributed to changing temperature in response to varying reevaporation (see Figs. 2.B.1 and 2.B.2).

Overall, the insensitivity to reevaporation shown in Fig. 2.6 suggests that reevaporation cannot be the primary cause for the precipitation pickup.

2.7 Temporal relation between CWV and precipitation revisited

Figure 2.7 shows the same composites as in Fig. 2.1, but for the no-entrainment case. In this case, one does not see an increase in CWV or CRH associated with the occurrence of high precipitation. At Manus Island, there is essentially no change in CWV, CRH or $\widehat{q_{sat}}$ when composited on precipitation. At the GOAmazon site for the no-entrainment case, the diurnal cycle overwhelmingly predominates the variations in precipitation as well as in CWV, CRH and $\widehat{q_{sat}}$. Without dependence on lower tropospheric environmental humidity set by entrainment, the influence of the diurnal cycle seems to be exaggerated. Diurnal cycle aside, composites for both tropical maritime and continental locations are consistent with the convective transition statistics (Figs. 2.4 and 2.5), showing that the precipitation and environmental humidity are no longer closely related when entrainment is turned off, and both the environmental humidity and temperature fail to serve as an indicator for precipitation.

2.8 Discussion

This chapter analyzes simulations from a set of parameter perturbation experiments in coupled CESM1 to determine the dominant direction of causality in the fast-timescale precipitation-water vapor relationship. The results presented here include composite time series centered at locally high precipitation (Figs. 2.1 and 2.7), the climatological responses at the largest tropical scales to varying entrainment (Figs. 2.2 and 2.3), and the dependences of the set of statistics associated with the transition to deep convection (referred to as convective transition statistics; Figs. 2.4, 2.5, and 2.6) on entrainment and reevaporation. The simulated convective transition statistics, in comparison to ground-based observations from ARM sites in the Tropical Western Pacific and from the GOAmazon campaign, as well as satellite microwave retrievals over tropical ocean basins lead us to conclude that entrainment results in the observed pickup of precipitation with CWV. This conclusion is in line with pre-

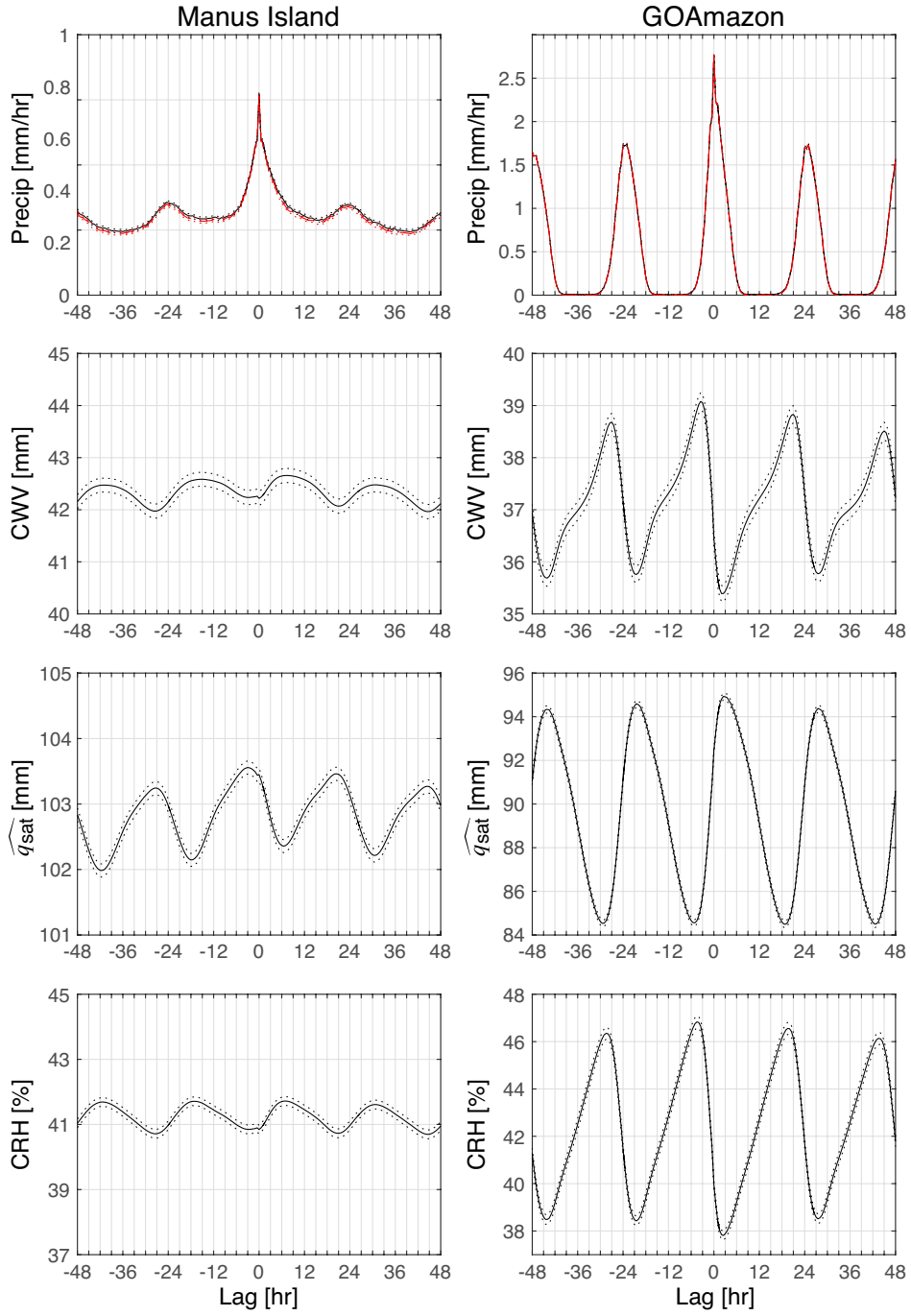

Figure 2.7: Same as in Fig. 2.1, but for the no-entrainment case (dmpdz = 0). Note that the scales of the ordinates for plots at the GOAmazon site are different from those at Manus Island or those shown in Fig. 2.1. At both sites, one can hardly differentiate total and convective precipitation, due to the lack of large-scale precipitation, and the composites centered at locally high convective and total precipitation are quantitatively similar in this case.

vious studies including the conditional instability calculations for entraining plumes. Unlike the offline entraining plume calculations, the CESM takes into account the two-way interaction between deep convection and environmental humidity, including moistening of the environment through detrainment and parameterized reevaporation of hydrometeors. When substantial entrainment is included in the deep convective parameterization, the composite time series (Fig. 2.1) show that the CWV increases prior to and decreases after (convective) precipitation maximum, akin to the observed (Fig. 2.A.1; Holloway and Neelin 2010) association with precipitation.

The high CWV associated with convection in these time series, and in the convective transition statistics has been hypothesized to be due to the impacts of environmental humidity on deep convection through entrainment in the lower free troposphere. The devil's advocate position, on the other hand, would be to postulate that these associations are simply due to the effect of convective moistening via detrainment or reevaporation. There is not sufficient asymmetry in the lead-lag relationship to rule out convective moistening as a major pathway. However, these parameter perturbation experiments add a new line of evidence for the causal role of entrainment. With low values of entrainment in the deep convective scheme (shallow convection is not affected), the convective transition statistics show a breakdown of the precipitation pickup, and the composite time series of CWV and precipitation are no longer tied together. Convection in this case occurs without preconditioning of environmental humidity, resulting in a dry and relatively warm atmosphere. In contrast, with substantial entrainment, the high CWV associated with convection in the corresponding composite time series and convective transition statistics indicate that convection cannot fire until the lower free-tropospheric environment is moistened due to the impact on buoyancy of turbulent entrainment of dry versus moist air, resulting in a moist and relatively cool atmosphere. The pathway through reevaporation is likely inconsequential to the existence of the pickup since varying the reevaporation rate by two orders of magnitude results in only minor variations in the convective transition statistics, although it can quantitatively affect

the climatology (Fig. 2.B.1).

As far as the precipitation-CWV relationship and its dependence on entrainment and reevaporation is concerned, the convective transition statistics at tropical maritime and continental sites are qualitatively very similar, though the convective transition statistics are more sensitive to reevaporation over land, where the influence of the diurnal cycle at low entrainment is also more significant.

Describing the convective transition statistics in terms of column-integrated values is primarily motivated by the availability of observational CWV products, including the ground-based radiometer data analyzed in the coordinated observational paper (Schiro et al. 2016). It retains information of environmental impacts on conditional instability of the deepest vertical structures of moisture variations, although not of more detailed vertical structure variations. Quantitative differences in the precipitation pickup (e.g., critical CWV and $\widehat{q_{sat}}$; not shown) are observed across different ocean basins and may be attributed to this. One way to quantify the uncertainties of convective transition statistics due to vertical structure is to treat these hidden factors as stochastic processes (e.g., Neelin et al. 2009) but ideally additional information about vertical structure should be included (i.e., explicitly distinguishing between boundary layer and lower free troposphere impacts on conditional instability). Convective transition statistics in GCMs (Sahany et al. 2012, 2014) require high-time resolution output or instantaneous samples of variables important for convection, which are not yet standard output in most models.

The results here are obtained with a single coupled GCM (CESM) that uses a particular convective parameterization. In this regard, our findings are model dependent. Nevertheless, our focus has been a specific process that is represented in a qualitatively similar way in other current convective parameterizations. Differences among various convective parameterizations include the vertical profile of entrainment rate. Other studies have analyzed simulations subject to different entrainment characteristics and have concluded that the entrainment profile can impact large-scale features such as double-ITCZ bias (e.g., Hirota

et al. 2014). The present chapter finds that the impacts of entrainment on the climatological simulation at the largest tropical scales, while substantial, are not as dramatic as those seen at the fast timescales analyzed here. This suggests that convective transition statistics can provide additional diagnostics of model performance, addressing behavior at timescales closer to the parameterized process. Examination of these fast-process statistics in perturbed physics experiments helps to determine which aspects of the underlying physics are being constrained by these metrics. This provides essential background as convective transition statistics are used to calibrate GCMs. Quantitative comparisons require quantification of dependence on temporal and spatial resolutions, as well as differences among reanalysis/satellite retrieval and ground-based observational products. However, qualitative conclusions such as the complete collapse of major features of the observations for low entrainment noted here are expected to be robust. More importantly, the model-based results can answer questions that cannot be addressed with observations alone, such as the relative importance of a particular physical process.

Acknowledgements

The content of this chapter had previously been published as Kuo et al. (2017), which was supported by the Office of Biological and Environmental Research of the U.S. Department of Energy grant DE-SC0011074, and by National Oceanic and Atmospheric Administration Grants NA14OAR4310274 and NA15OAR4310097 and National Science Foundation Grant AGS-1540518. U.S. Department of Energy Atmospheric Radiation Measurement (ARM) Climate Research Facility GOAmazon and Tropical West Pacific field campaign data are acknowledged. The author thanks Dr. K. A. Schiro for discussions in coordinating with her observational analysis, and for assistance with ARM site data, and J. Meyerson for graphical assistance. The author also thanks an anonymous reviewer for suggesting the addition of the reevaporation sensitivity experiments.

APPENDIX

2.A Lead-lag relationship between CWV and precipitation

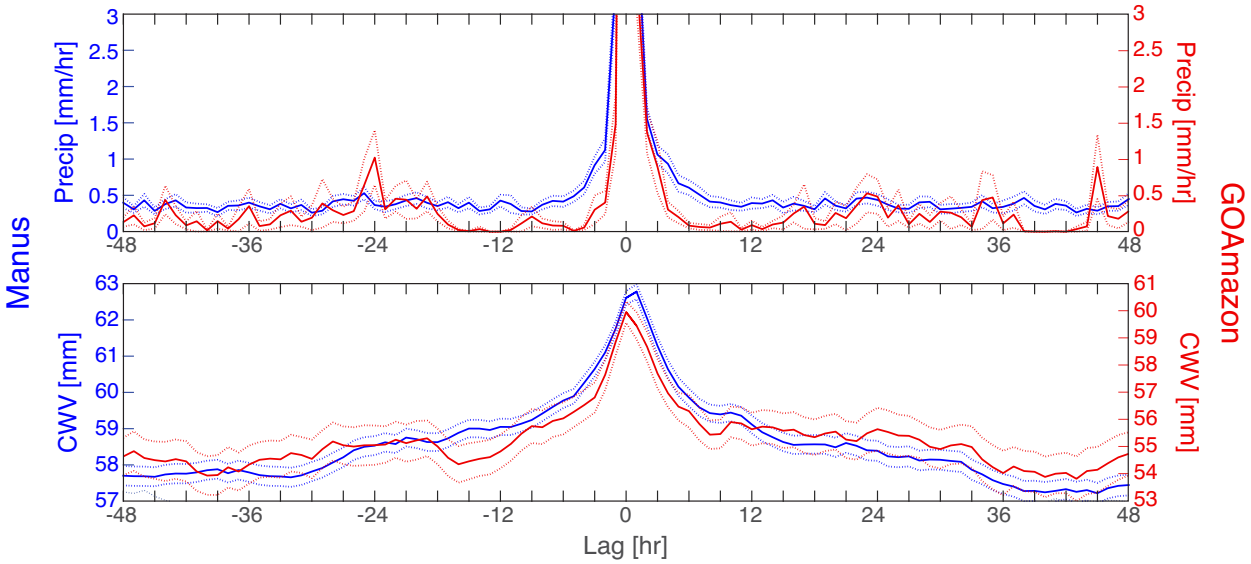

Figure 2.A.1: Composite time series for CWV and precipitation rate centered at locally high (total) precipitation rate calculated using radiometer and rain gauge data (hourly mean) collected for the period of 1998-2010 at Manus Island (blue), and for the period 10 January 2014 through 20 October 2015 at the GOAmazon site (red). The qualitative features indicated by these curves are robust with respect to the threshold defining heavy precipitation. The maximum of precipitation composites is about 19 mm h^{-1} at Manus, and about 18 mm h^{-1} at the GOAmazon site.

Figure 2.A.1 shows the composites centered at locally high total precipitation calculated using the radiometer and rain gauge data (hourly mean) collected from the ARM site for the period of 1998-2010 at Manus Island, and for the period from 10 January 2014 through 20 October 2015 during the GOAmazon campaign. Here high precipitation is defined as being greater than the mean precipitation rate averaged over all precipitating events with respect to the threshold value of 0.1 mm h^{-1}.

At both locations, CWV gradually increases (decreases) before (after) the precipitation

peaks, with more drastic variation occurs between ±6 hour time-lag, which could be attributed to mesoscale processes. It is clear that CWV has a longer autocorrelation timescale compared with precipitation. At the GOAmazon site, there are secondary precipitation peaks 24 hours before and after the main peak, hinting to the diurnal cycle. At Manus Island, the CWV slightly lags the precipitation maximum by about 7 min. (from the original higher-time resolution data, not shown), and the precipitation rate outside the main peak is invariant in time. Overall, the composites are rather symmetric.

The composites from the standard entrainment case (see Figs. 2.1 and 2.C.1) qualitatively capture the relationship between environmental humidity and precipitation seen from observations, although quantitative differences do exist. For instance, the simulated precipitation as well as the CWV variation associated with strong precipitation are smaller than in observations and have a longer timescale of increase prior and decrease after. The amplitudes of the simulated diurnal cycle are probably exaggerated. These discrepancies may due partly to the model resolution.

It is also worth noting that calculations of the simulated precipitation diurnal cycle using the 30-year-long history at the geographical location of the GOAmazon site exhibit numerical wiggles at 1-hour period (2 half-hour steps). These wiggles are not large enough to affect conclusions here but serve as a reminder that examining models for convective timescale processes can reveal imperfections in model numerics and implications for the fundamental underlying physics.

2.B Climatological responses to varying reevaporation

Figure 2.B.1 shows the simulated climatologies averaged over the tropics as a function of reevaporation rate k_e. As in Fig. 2.2, values for ocean and land points are calculated separately, and the corresponding values from observations/reanalysis are also provided for reference. Overall, the climatological responses to varying k_e across the range examined here

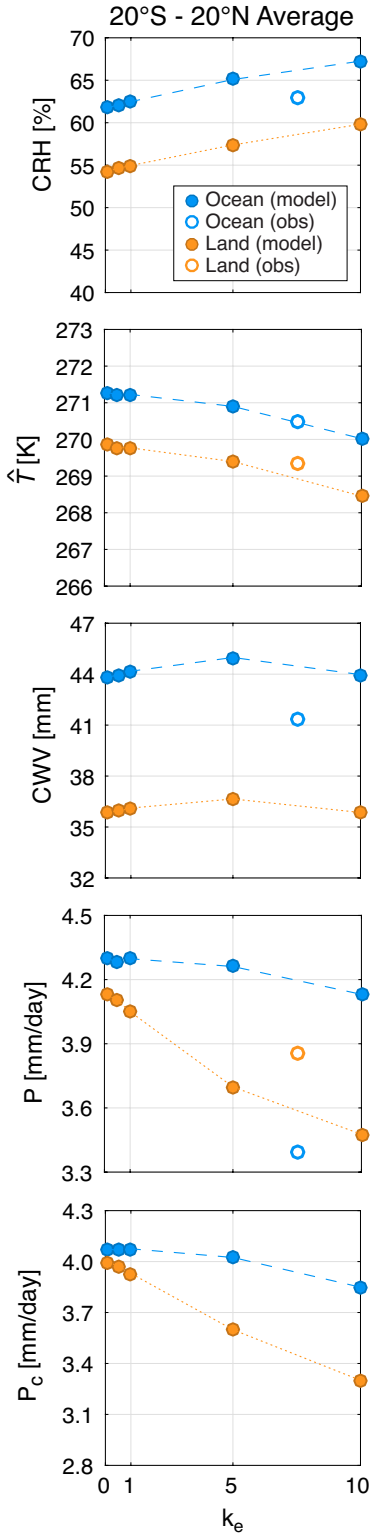

Figure 2.B.1: Same as in Fig. 2.2, but for different values of convective precipitation evaporation rate $k_e = 0.1, 0.5, 1, 5$ and 10.

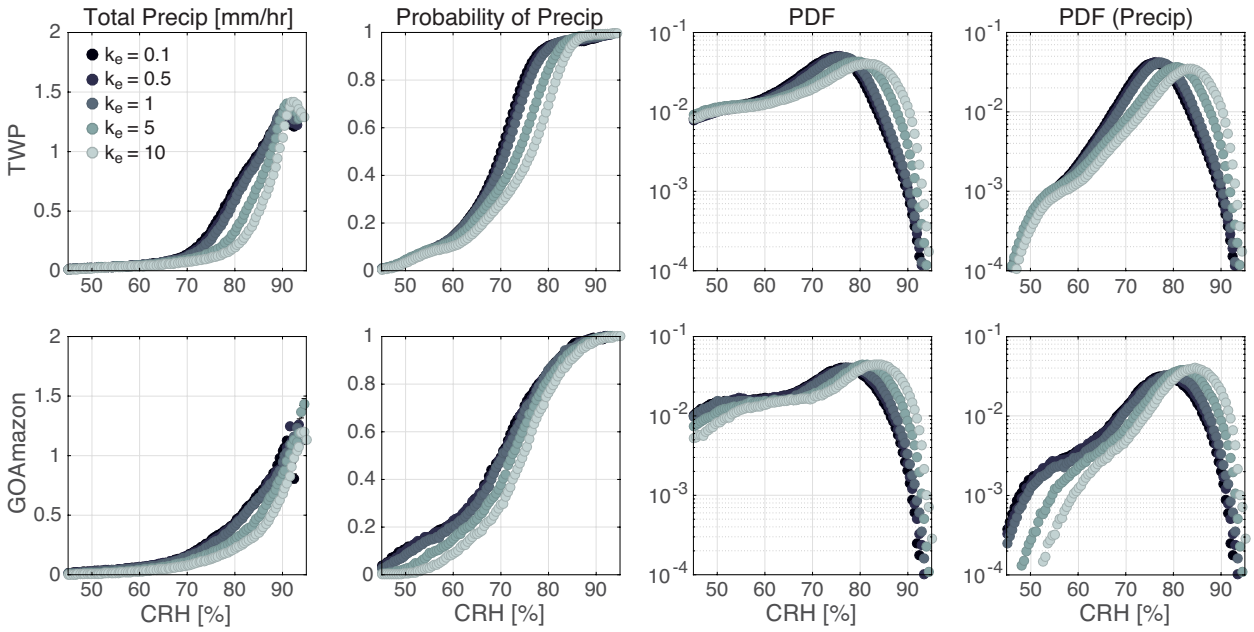

Figure 2.B.2: Same as in Fig. 2.6, but replace CWV with CRH.

are smaller compared with those for dmpdz as in Fig. 2.2. The average $\widehat{T}$ drops by about 1.5 K as k_e increases from 0.1 to 10, while CWV changes about 1 mm. At the same time, the average CRH increases by about 5%, associated with the changing temperature. Both the total and convective precipitation rates are insensitive to increasing k_e over ocean, but decrease modestly over land. The ratio of convective to total precipitation is almost constant ($74 \pm 1\%$), with slight reduction for $k_e = 10$ (71% over ocean versus 69% over land). Thus k_e does have nontrivial impacts on the climatology, especially over land.

The simulated fast-timescale statistics for various k_e values are compiled again in Fig. 2.B.2, but with CWV replaced by CRH. These statistics show modest sensitivity to reevaporation, but given the results in Figs. 2.6 and 2.B.1, this sensitivity is likely due to the change in temperature. We have not broken out the convective transition statistics with conditional averages on temperature, but previous results for observations and related versions of CESM (Sahany et al. 2014) show that convective onset is not well approximated by constant CRH—as $\widehat{q_{sat}}$ increases, the onset occurs at lower values of CRH. Thus the modest differences in

Fig. 2.B.2 relative to Fig. 2.6 are likely an artifact of using CRH versus CWV to characterize the impact of environmental humidity on conditional instability.

2.C Supplement

2.C.1 Lead-lag relationship between CWV and precipitation

Figure 2.1 shows the composite time series centered at locally high convective precipitation using model output at Manus Island and the GOAmazon site for the standard entrainment case. Figure 2.C.1 shows the model composites similar to Fig. 2.1, except that they refer to total precipitation. Here the composites are centered at locally high total precipitation (defined as being greater than the mean total precipitation rate averaged over all precipitating events with respect to the threshold value of 0.1 mm h^{-1}). There are some quantitative differences between composites in Figs. 2.1 and 2.C.1. For instance, the $\widehat{q_{sat}}$ variation at the GOAmazon site has larger amplitude when composited on convective precipitation. This suggests that in the continental tropics, the diurnal cycle has more pronounced influence on convection than on the overall precipitation. At Manus Island, the total precipitation time series is rather symmetric in time-lag, and CWV very slightly leads the total precipitation maximum. After the total precipitation peaks, both $\widehat{q_{sat}}$ and convective precipitation are smaller compared with before. Details aside, the behavior in Fig. 2.C.1 is highly consistent with the behavior seen in Fig. 2.1 based on convective precipitation.

2.C.2 Low-bias of NCEP Reanalysis CWV

It has been noted that the NCEP Reanalysis products consistently show a low bias for CWV over the tropical oceans (Trenberth and Guillemot 1998, Trenberth et al. 2005). Figure 2.C.2 shows the CWV climatology from RSS and Reanalysis-2 and their difference. Figure 2.C.3 shows the CRH climatology calculated using the Reanalysis-2 temperature together with

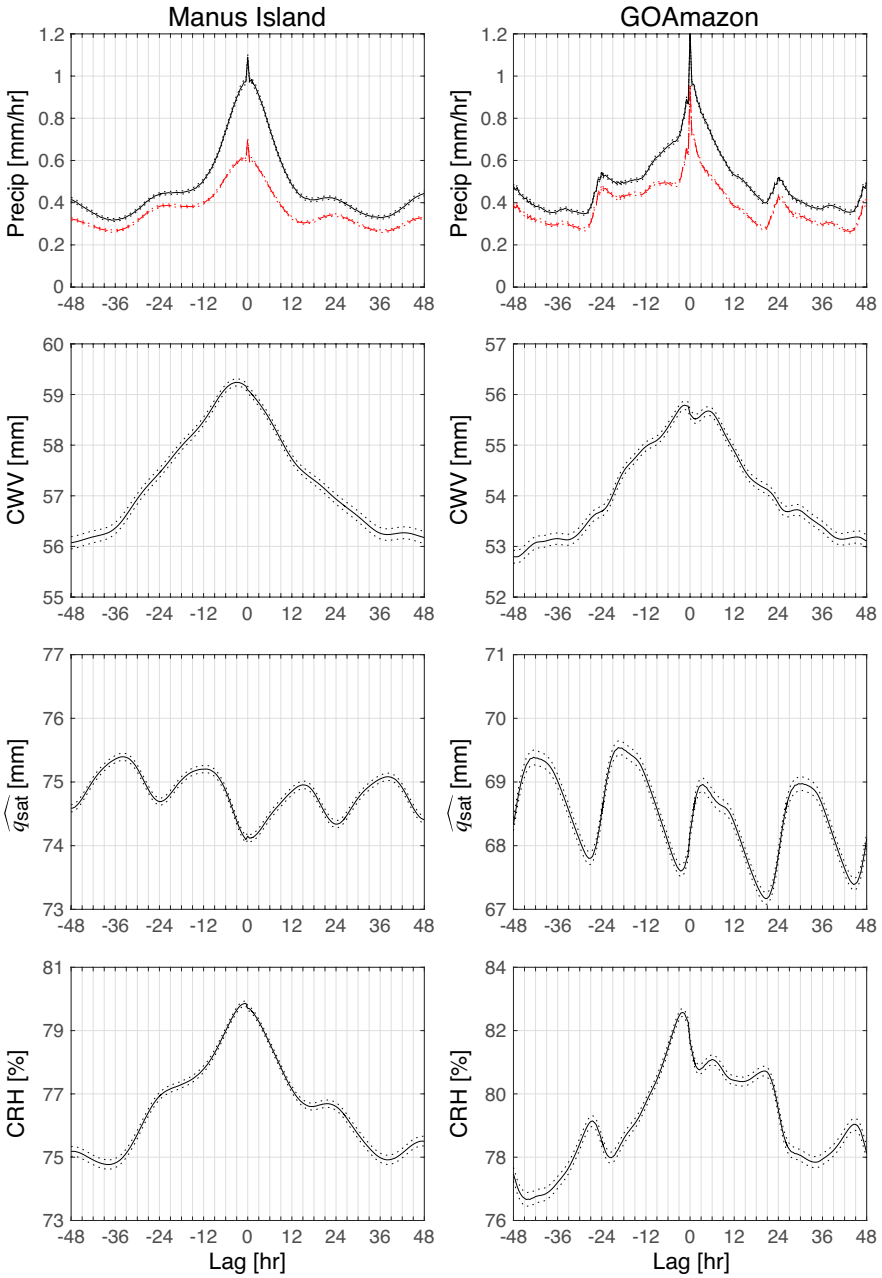

Figure 2.C.1: Model composite time series centered at locally high total precipitation (defined as being greater than the mean of all precipitating events with respect to the threshold of 0.1 mm h^{-1}) within a 96-hour window for standard entrainment case (dmpdz = 1). The top panels show the total (black) and convective (red) precipitation. Dotted curves in all panels represent ± 1 standard error. The qualitative features indicated by these curves are robust with respect to the threshold defining heavy precipitation.

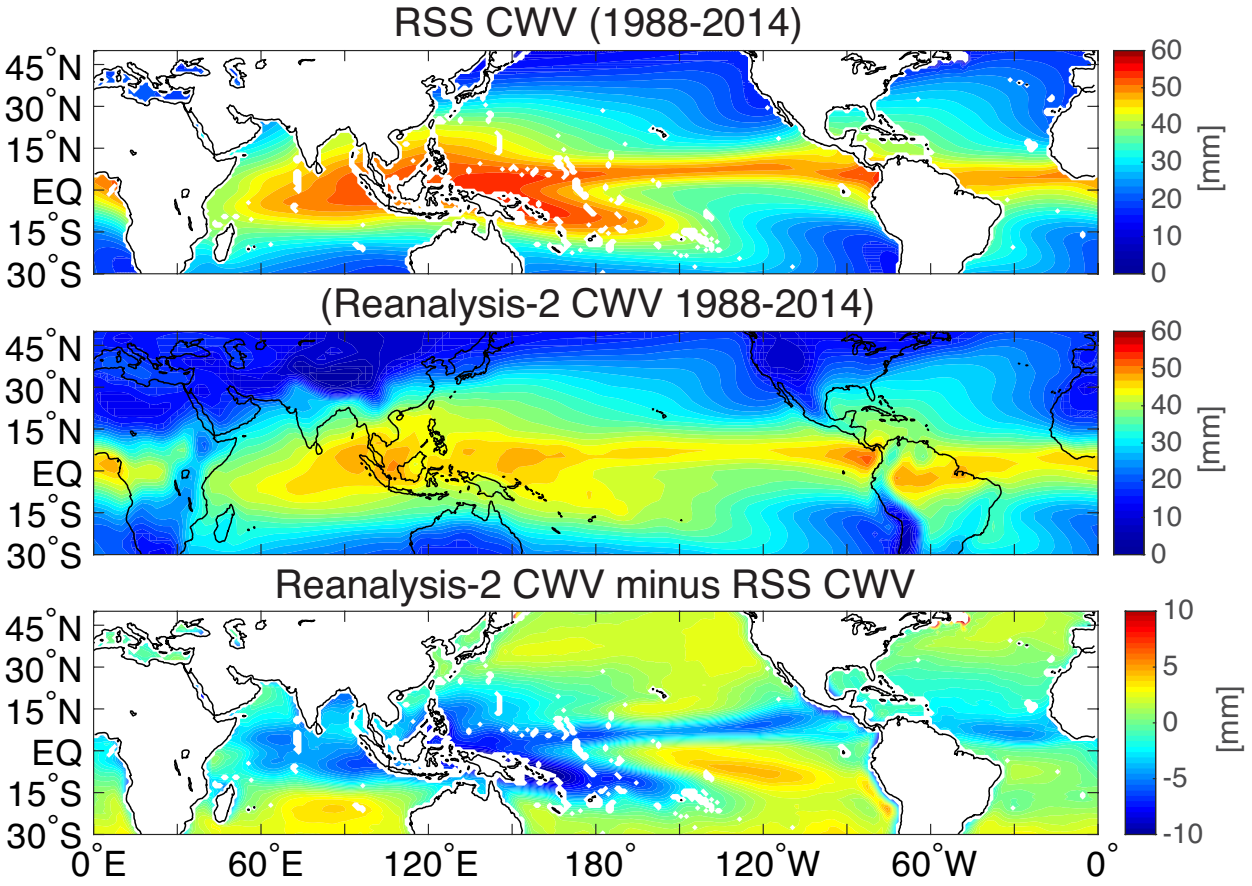

Figure 2.C.2: The climatology of CWV calculated using RSS CWV and Reanalysis-2 CWV (precipitable water). Their difference is plotted in the lower panel.

RSS and Reanalysis-2 CWV as well as the precipitation from the GPCP. From Figs. 2.C.2 and 2.C.3, regions with high (low) precipitation over the tropical oceans usually have high (low) CWV and CRH from satellite retrievals. Reanalysis-2 generally underestimates CWV in comparison with satellite microwave retrievals in regions where CWV is high, and slightly overestimates it in regions where CWV is low. This bias also results in the difference between Reanalysis-2 and RSS CRH. Overall, Reanalysis-2 underestimates CWV over the tropical oceans compared to satellite retrievals.

Given the evidence that the lack of entrainment in model physics leads to a drier atmosphere (see Figs. 2.2 and 2.3), we can conjecture that the low CWV bias in the NCEP

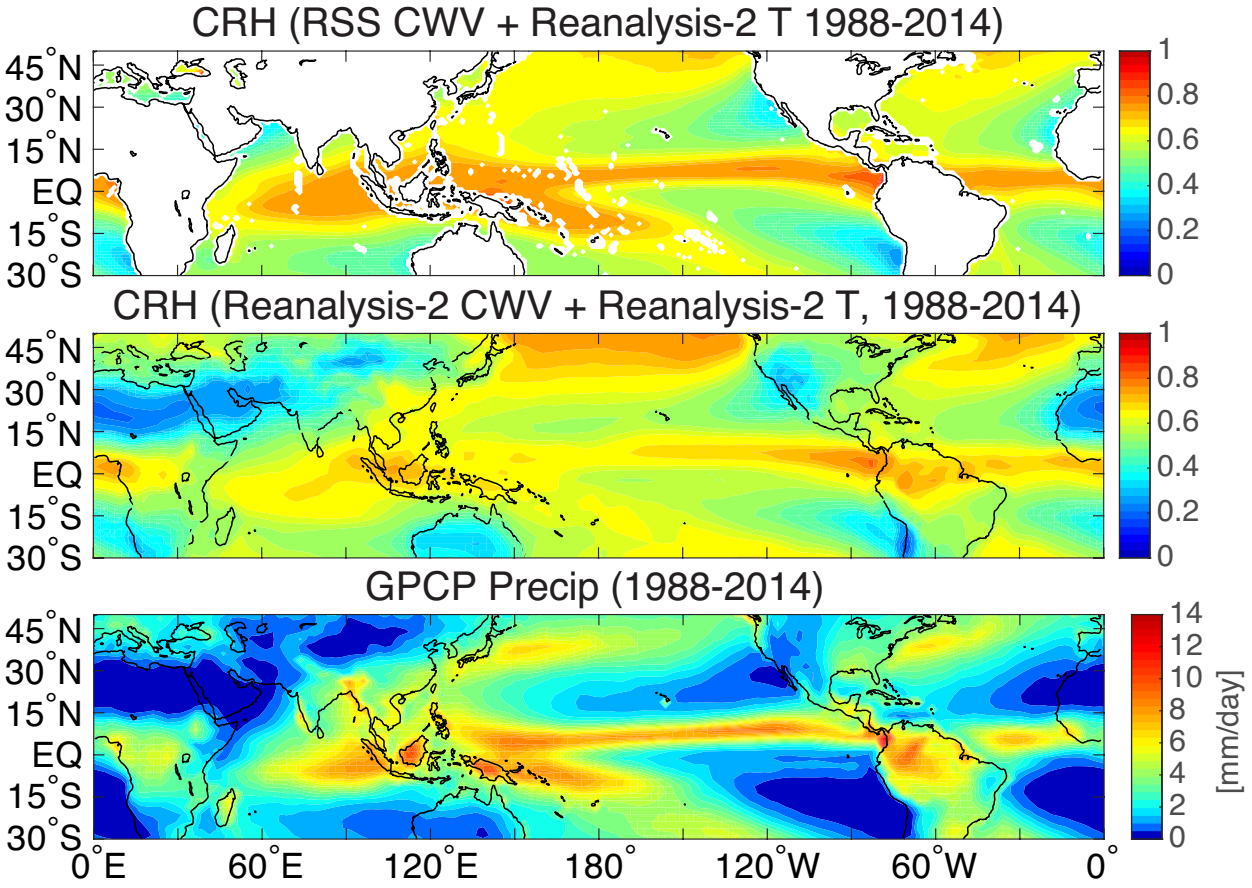

Figure 2.C.3: The climatology of CRH calculated using RSS and Reanalysis-2 datasets and precipitation from GPCP. The CRH values shown in the upper and middle panels are calculated using the RSS and Reanslysis-2 CWV, respectively. The Renalysis-2 temperature field is used for both calculations.

Reanalysis results from the entrainment process not being properly modeled in the Simplified Arakawa-Schubert scheme (or SAS scheme; Pan and Wu 1995) used in the atmospheric model component. In the SAS scheme, the level below 700 mb at which the moist static energy reaches local maximum is first found as the starting point (SP) of the convection in a model column. Then a parcel from the SP is taken upward, conserving its saturation moist static energy, to find the level of free convection (LFC, or cloud base). After the SP and LFC are found, the updraft mass flux is re-calculated by assuming that entrainment occurs only between the SP and LFC, and 50% of the mass flux at the LFC originates at the

SP. The parcel is assumed to be non-entraining above LFC up to the cloud top. Thus the entrainment process is confined within a rather shallow layer instead of through the whole column. This suggests that a revision of the entrainment process might help to improve this aspect of the NCEP model and thus the reanalysis.

CHAPTER 3

Convective transition statistics over tropical oceans for climate model diagnostics: Observational baseline

Abstract

Convective transition statistics, which describe the relation between column-integrated water vapor (CWV) and precipitation, are compiled over tropical oceans using satellite and ARM site measurements to quantify the temperature and resolution dependence of the precipitation-CWV relation at fast timescales relevant to convection. At these timescales, and for precipitation especially, uncertainties associated with observational systems must be addressed by examining features with a variety of instrumentation, and identifying robust behaviors versus instrument sensitivity at high rain rates. Here the sharp pickup in precipitation as CWV exceeds a certain critical threshold is found to be insensitive to spatial resolution, with convective onset occurring at higher CWV but at lower column relative humidity as bulk tropospheric temperature increases. Mean tropospheric temperature profiles conditioned on precipitation show vertically coherent structure across a wide range of temperature, reaffirming the use of a bulk temperature measure in defining the convective transition statistics. The joint probability distribution of CWV and precipitation develops a peak probability at low precipitation for CWV above critical, with rapidly decreasing probability of high precipitation below and near critical, and exhibits systematic changes under spatial-averaging. The precipitation pickup with CWV is reasonably insensitive to time-averaging up to several hours but is smoothed at daily timescales. This work demonstrates that CWV relative to critical serves as an effective predictor of precipitation with only mi-

nor geographic variations in the tropics, quantifies precipitation-related statistics subject to different spatial-temporal resolution, and provides a baseline for model comparison to apply these statistics as observational constraints on precipitation processes.

3.1 Introduction

Despite the ongoing improvement of weather and climate modeling in recent decades in terms of model resolution and number of simulated processes, convective parameterization remains a major contributor to the uncertainty of future projection (Sanderson 2011, Rowell 2012, Yokohata et al. 2012, Sherwood et al. 2014) and systematic biases in precipitation and clouds persist. A non-exhaustive list of persistent biases includes the double-ITCZ bias (Mapes and Neale 2011, Hirota et al. 2014), insensitivity of precipitation to environment humidity (Oueslati and Bellon 2013), low bias in tropospheric humidity (Gonzalez and Jiang 2017), failing to capture the amplitude and propagation of MJO (Kim et al. 2014, Jiang et al. 2016, Jiang 2017), unrealistic statistics and surface storm tracks for tropical cyclones (Booth et al. 2017), and incorrect precipitation diurnal cycle over land (Covey et al. 2016). These biases also impact model diagnosis for short-term forecasting purposes, since models adopted for weather forecasting or reanalysis share common components with climate models.

Many conventional diagnostics for climate models emphasize comparisons against long-term climatology or variability at different timescales, and the model performance examined by these metrics are affected by multiple factors. While sensitivity experiments with respect to such metrics are useful in identifying important processes (Benedict et al. 2013, 2014, Boyle et al. 2015, Bernstein and Neelin 2016, Langenbrunner and Neelin 2017), the contribution of certain processes can be difficult to isolate, making constraining model performance challenging. As such, there is an emerging need for diagnostics targeting processes and focusing on the most relevant timescales. This study presents an example of such process-oriented diagnostics—the convective transition statistics—which focus on the fast-timescale

deep convection in the tropics.

The sensitivity of moist convection to lower free-tropospheric humidity had been suggested by the analysis of TOGA COARE and operational sounding data for the tropical western Pacific (Brown and Zhang 1997, Sherwood and Wahrlich 1999, Parsons et al. 2000), and was subsequently affirmed by numerical experiments (Tompkins 2001, Redelsperger et al. 2002, Ridout 2002, Derbyshire et al. 2004). Later observational and modeling studies pointed to the importance of organized convective systems in determining the environment moisture field (Tao and Moncrieff 2009, Yano et al. 2012, Moncrieff et al. 2017). Bretherton et al. (2004) documented an empirical relationship between the column relative humidity (CRH) and precipitation over tropical oceans at daily and monthly timescales in SSM/I satellite retrievals. Based on the analysis of the same satellite observations at fast timescales, Peters and Neelin (2006) noted a sharp increase in precipitation as the column-integrated water vapor (CWV) exceeded a certain threshold, and, using the analogy to associated behavior in continuous phase transitions, showed consistent relations among a set of statistics including probability and variance of precipitation, and the distribution of CWV for precipitating events. Subsequent studies have examined the dependence on tropospheric temperature (Neelin et al. 2009) and how the statistics can be reproduced by simple stochastic models (Stechmann and Neelin 2011, 2014). The plume buoyancy calculations based on ground-based measurements at tropical ARM sites (Holloway and Neelin 2009, Schiro et al. 2016) and the NCAR CAM5 simulations (Sahany et al. 2012, Kuo et al. 2017) have demonstrated that entrainment is instrumental in explaining the observed precipitation-CWV relation, and that there is not a land-ocean contrast and the relation is qualitatively robust. These convective transition statistics characterize the dependence of tropical convection on bulk measures of the water vapor-temperature environment.

The robust rapid increase in conditionally-averaged precipitation and conditional probability of precipitation as CWV exceeds a certain threshold (the "pickup of precipitation") derived from the tropical ARM sites have been used to constrain the entrainment param-

eter in the NCAR CESM (Kuo et al. 2017). Given that precipitation-related statistics are sensitive to resolution (Chen and Dai 2018, Klingaman et al. 2017), to allow for a more quantitative comparison to model output subject to varying spatial resolution and temporal frequency, the dependence of the convective transition statistics on spatial-temporal resolution must be quantified. Moreover, the robustness to instrumentation, especially at high rain rate, should be addressed to ensure the reliability of such diagnostics. The purpose of this study is to quantify the resolution dependence and robustness of the statistics, provide an observational baseline for model comparison, and to expand the set of related properties that can be understood within this framework.

This chapter is organized as follows. Section 3.2 describes the datasets analyzed here. The basic convective transition statistics, which build on those introduced in previous work (e.g., Peters and Neelin 2006, Neelin et al. 2008), are presented in section 3.3 with the following additions: using newer datasets, assessing the spatial-resolution dependence of the statistics, testing the robustness to instrumentation and evaluating sensitivity to the choice of bulk measure of tropospheric temperature. Sections 3.4–3.6 explore new statistics characterizing the convective transition. Section 3.4 examines the geographic variations, or the lack thereof, of the effectiveness of CWV relative to critical as a predictor of precipitation, and the associated dependences on spatial-temporal resolution. The sensitivity of the statistics to time-averaging is discussed in section 3.5. The joint-PDF of CWV and precipitation, and its dependence on spatial resolution and instrumentation, are shown in section 3.6. Finally, section 3.7 summarizes the properties of convective transition statistics, and briefly discusses their potential as diagnostic tools.

3.2 Datasets

Compiling the convective transition statistics requires column-integrated water vapor CWV, precipitation rate P, column-integrated saturation humidity $\widehat{q_{sat}} \equiv \int q_{sat}[T(p), p]dp/g$ {here

$q_{sat}[T(p), p]$ is the saturation specific humidity with respect to liquid water as a function of temperature $T(p)$ and pressure $p\}$, and mass-weighted column-averaged temperature $\widehat{T}$.

The primary source of CWV and P here is the TRMM Microwave Imager (TMI) retrieval products processed by Remote Sensing Systems (RSS; algorithm v7.1; TMIv7.1 hereafter; Wentz et al. 2015). The retrieved values include gridded ($0.25° \times 0.25°$) snapshots of CWV (units: 0.3 mm) and P (units: 0.1 mm h^{-1}) over ocean, with no data available over land. The TRMM Precipitation Radar (PR) 2A25 (v7; TRMM 2011a) and TRMM 3B42 (v7; TRMM 2011b) Rainfall Rate products are used for comparison. The 2A25 data provides snapshots of P with resolution 5 km, and 3B42 provides gridded ($0.25° \times 0.25°$) P every 3 hours. Note that 3B42 is a merged product; as such, most values should be interpreted as instantaneous, since P is observed during a specific 3-hour window rather than a computed 3-hourly mean. Here, the TMIv7.1, 2A25, and 3B42 data for 01 Jun 2002–31 May 2014 are used.

The Microwave Radiometer (MWR) CWV and rain gauge P measurements collected from the DOE ARM sites at Nauru (0° 31' S, 166° 54' E) for 1999-2008 and at Manus (2° 3' S, 147° 25' E) for 1998-2010 in the tropical western Pacific @(both with optical rain gauge; Gaustad and Riihimaki 1996, 1998, Holdridge and Kyrouac 1997, 1998), and at the ARM Mobile Facility near Manaus (3° 7' S, 60° 1' W) for 10 Jan 2014–20 Oct 2015 during the GOAmazon campaign (with acoustic rain gauge; Schiro et al. 2016) are also used to study the sensitivity of the statistics to instrumentation and time-averaging.

For column-integrated/averaged $\widehat{q_{sat}}$ and $\widehat{T}$, with the column being defined as 1000-200 hPa, the 6-hourly 2.5° NCEP-DOE Reanalysis-2 (Kanamitsu et al. 2002) temperature is adopted with necessary interpolation. Since the spatial and temporal autocorrelation scales of temperature are expected to be large in the tropics, the interpolation is justified. To avoid potentially erroneous temperature values from spatial interpolation (e.g., around the Andes and New Guinea), data in the 2.5°-neighborhood of land pixels are excluded for some of the presented statistics.

Note that the CWV datasets often do not record a CWV value in the presence of pre-

cipitation, and thus gap-filling is required to re-construct missing data (see section 3.A for Supplement). For algorithm choices used for the TMIv7.1 data, the probability of missing CWV depends primarily on P, with the probability increasing from 0 to 1 almost linearly as P increases from 2 to 9 mm h^{-1}. This even affects the tropical mean precipitation, e.g., the annual mean precipitation over tropical oceans (20°S-20°N) is reduced from 3.1 to 2.1 mm day^{-1} by excluding precipitation without valid CWV retrievals. Therefore, it is necessary to gap-fill these missing CWV values; otherwise, the information comprising the desired statistics would be systematically distorted. Here the default is to simply fill the missing values using the available CWV value at the geographically nearest pixel. The sensitivity of the presented statistics to the gap-filling are included in Figs. 3.A.7-3.A.11. Similarly, the raw CWV time series from the tropical ARM site MWR measurements are recorded every 20 s, but exhibit gaps because of the "wet-window" effect. Gaps shorter than 6 hours are filled using linear interpolation as described in Schiro et al. (2016). The gap-filled time series are then used to calculate the mean time series at lower temporal frequencies (e.g., 5-min- or hourly-average). Precipitation observations are available in the CWV gaps and do not have to be interpolated.

Additionally, satellite CWV retrievals processed by RSS (including TMIv7.1) have a 75-mm cap set by the algorithm. While CWV rarely exceeds 75 mm, operational soundings occasionally record such events, e.g., weather stations in Ishigakijima (24° 20' N, 124° 10' E; station number 47918) and Taipei (25° 02' N, 121° 31' E; 58968) recorded 80.03 and 82.54 mm at 00Z and 12Z, respectively, on 21 Aug 2013 under the influence of Typhoon Trami (data from University of Wyoming Atmospheric Soundings). This serves as a reminder of the imperfect observational systems, and one must keep in mind the uncertainties when applying the presented statistics for model diagnosis.

3.3 Dependence of precipitation-CWV relation on tropospheric temperature and spatial resolution

3.3.1 Basic features of convective transition statistics

Figure 3.3.1 shows the basic convective transition statistics, including the precipitation rate (Fig. 3.3.1a), probability of precipitation (Fig. 3.3.1b; $P > 1.05$ mm h^{-1}), probability density functions (PDFs) of all events (Fig. 3.3.1c) and precipitating events (Fig. 3.3.1d) conditioned on CWV and $\widehat{q_{sat}}$ for the tropical western Pacific, along with results for other tropical ocean basins (Figs. 3.3.1e-3.3.1p). Here the statistics are compiled at 0.25° (colored markers) and 0.5° (dots), using $\widehat{q_{sat}}$ as the bulk tropospheric temperature (see Fig. 3.A.4 for the corresponding statistics compiled using $\widehat{T}$ as the bulk tropospheric temperature measure). The standard errors associated with the conditionally averaged precipitation (conditional precipitation hereafter) at 0.25° are smaller than the marker size, and thus omitted. To exclude light precipitation and focus on deep-convective events, a threshold of 1.05 mm hr-1 defining precipitating events is chosen, with a natural offset 0.05 since the TMIv7.1 precipitation is discretized by 0.1-mm h^{-1} units. Note that the PDFs of all events (e.g., Fig. 3.3.1c)—i.e., PDFs of CWV—are calculated from the joint-PDF of CWV and $\widehat{q_{sat}}$, normalized for each basin, by treating CWV as a continuous variable and $\widehat{q_{sat}}$ discretely. These PDFs, when multiplied by the corresponding conditional probabilities (Fig. 3.3.1b), give the PDFs for precipitating events (Fig. 3.3.1d). The jumps at 75 mm for the PDFs result from the CWV cap set by the retrieval algorithm. For sensitivity to gap-filling, see section 3.A.4 (Figs. 3.A.7-3.A.11).

For each $\widehat{q_{sat}}$, the conditional precipitation and probability (Fig.3.3.1; 1st and 2nd columns) pick up sharply as CWV exceeds a certain threshold, referred to as the "critical CWV," or w_c (defined in section 3.3.2), around which the PDF of precipitating events (4th column) peaks. The precipitation pickup occurs at higher CWV for higher $\widehat{q_{sat}}$, i.e., w_c is increasing with $\widehat{q_{sat}}$. The conditional probability would decrease with an increase in the threshold that

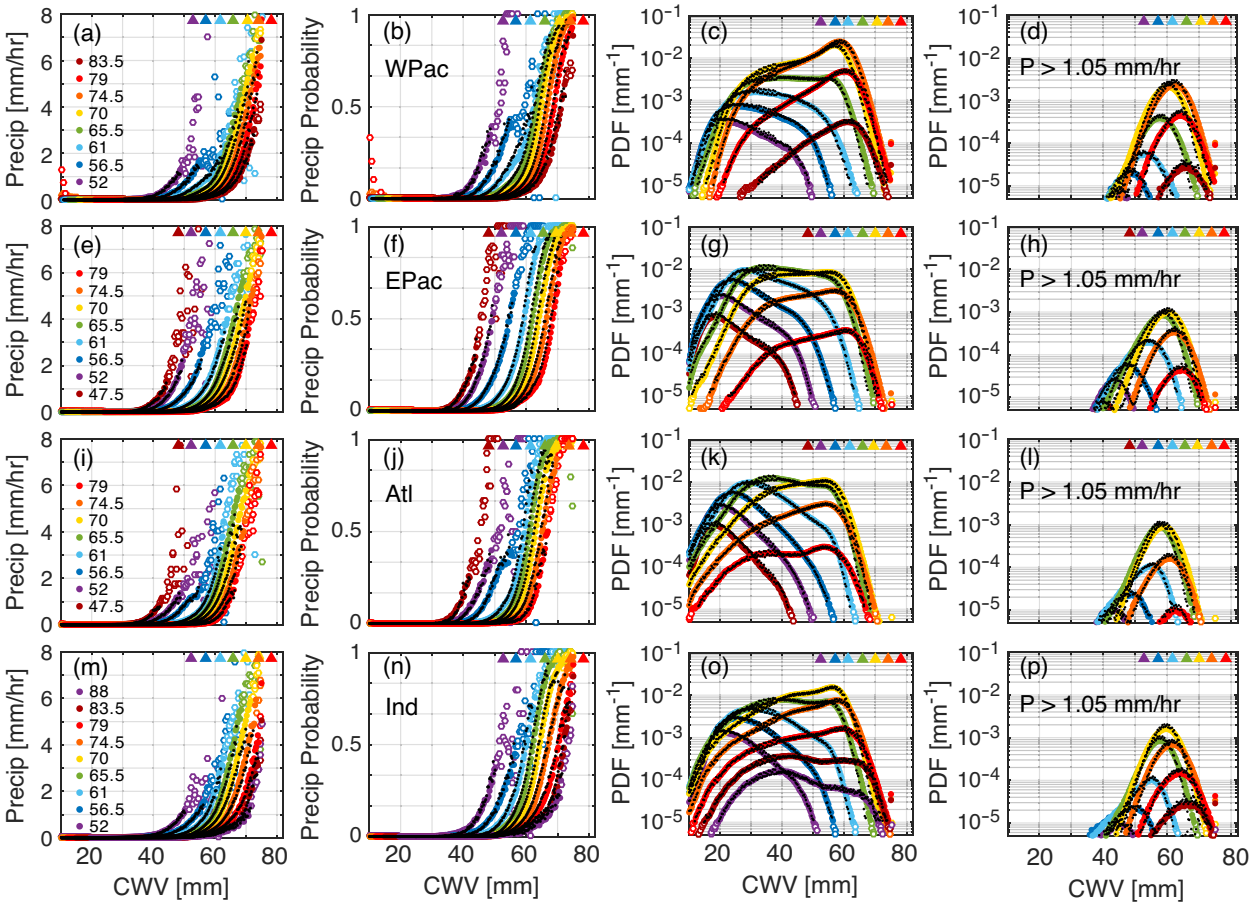

Figure 3.3.1: (a) Conditionally averaged precipitation rate; (b) conditional probability of precipitation; (c) probability density function of all events, and (d) precipitating events only as a function of CWV and $\widehat{q_{sat}}$ (units: mm) for the tropical (20°S-20°N) western Pacific. (e)-(h) Same statistics, but for the tropical eastern Pacific, (i)-(l) for Atlantic, and (m)-(p) for Indian Ocean. Results are shown using TMIv7.1 data and Reanalysis-2 temperature compiled at 0.25° (colored markers) and 0.5° (dots). Underpopulated bins at 0.25° (PDF $< 10^{-5}$) are indicated by open circles, and those for 0.5° are omitted. Triangles represent the corresponding $\widehat{q_{sat}}$ values. Here, precipitating events are defined by $P > 1.05$ mm h^{-1}. The CWV data is gap-filled using nearest available values, and data from pixels within 2.5° of land are excluded to avoid potentially erroneous temperature values arising from spatial interpolation. The standard errors associated with the conditional precipitation are smaller than the marker size, and omitted.

defines precipitating events; i.e., the probability curves would move towards higher CWV. The spacing between pickup curves (for conditional precipitation and probability) suggests

that the behavior for $\widehat{q_{sat}}$ bins ≥ 61 mm ($> 85\%$ of total occurrence over tropical oceans) is slightly different from that in lower $\widehat{q_{sat}}$ bins. Inspection of the geographical distribution of $\widehat{q_{sat}}$ occurrence suggests that low-$\widehat{q_{sat}}$ events are due mostly to systems originating from the extratropics (section 3.A.6).

The observed sharp increase in precipitation as CWV exceeds critical has been explained by entraining plume calculations, through which the deep-convective conditional instability can be estimated. As previously demonstrated (Holloway and Neelin 2009, Schiro et al. 2016, Kuo et al. 2017), CWV serves as a measure of the impact of environment moisture on plume buoyancy, and hence the instability, through the effects of mixing, as indicated by the precipitation pickup. The dependence of w_c on $\widehat{q_{sat}}$ can be explained through a similar approach (Sahany et al. 2012).

In Fig. 3.3.1, the dots (0.5°) match the colored markers (0.25°) in the 1st and 3rd columns; i.e., the conditional precipitation and PDF of CWV are insensitive to spatial resolution, with small but noticeable decreases in the PDF at highest CWV (above critical). This insensitivity is consistent with the assertion that the autocorrelation spatial scales of CWV and tropospheric temperature are much greater than that of precipitation. Nonetheless, to what extent this holds depends on the gap-filling (Figs. 3.A.9-3.A.11 in section 3.A.4). It is also consistent with Yano et al. (2012) which used a cloud-resolving model (CRM) and demonstrated that the conditional precipitation as a function of CWV is quantitatively robust to spatial resolution (up to $\sim$1°).

The conditional probability defined by a fixed nonzero threshold (1.05 mm h^{-1}; Fig. 3.3.1; 2nd column) slightly shifts toward lower CWV with spatial coarse-graining, consistent with the greater chances of observing precipitation over a larger area. However, with a much higher threshold (e.g., 15 mm h^{-1}, the practical maximum for TMIv7.1 precipitation in the tropics) or at even lower resolution (e.g., 2°), the dependence on spatial resolution may reverse for the rarer chances of seeing extreme over a larger area. These dependences indicate the underlying joint-PDF of CWV and P being resolution-sensitive, as will be discussed in

sectionn 3.6.

3.3.2 Critical CWV w_c and collapsed statistics

As described earlier, CWV measures the impact of environment moisture on conditional instability, and hence precipitation. For those $\widehat{q_{sat}}$ bins most relevant in the tropics ($\geq$ 61 mm), the pickup curves in Fig. 3.3.1 suggest the possibility of collapsing statistics by shifting CWV by w_c for each $\widehat{q_{sat}}$, i.e., the precipitation-CWV relation can be simplified by taking into account the dependence of w_c on temperature. To define w_c as a function of $\widehat{q_{sat}}$, it makes sense to do so based on conditional precipitation alone, for it, unlike the conditional probability, does not rely on any threshold and is insensitive to spatial resolution. This assumes that the conditional precipitation has the form of $f(cwv - w_c)$, with its $\widehat{q_{sat}}$-dependence implicitly built in through $w_c(\widehat{q_{sat}})$. See section 3.A.3 regarding details on finding w_c given the statistics as in Fig. 3.3.1.

Figures 3.3.2a-3.3.2d show the collapsed version of the original statistics for the tropical western Pacific in Fig. 3.3.1a-3.3.1d (other basins in Fig. 3.A.6). As in Fig. 3.3.2a, w_c is defined as the CWV value at which the best-fit for conditional precipitation (gray line) intersects with the CWV axis. For $\widehat{q_{sat}}$ bins $\geq$ 70 mm, the conditional precipitation, probability of precipitation (Fig. 3.3.2b), and PDF of precipitating events (Fig. 3.3.2d) collapse perfectly. For these $\widehat{q_{sat}}$ bins, there are below-critical precipitating events, many of which are weakly precipitating and excluded because of the 1.05-mm h^{-1} threshold adopted here, and are likely associated with the mature and decaying phases of convection (not shown). As $\widehat{q_{sat}}$ increases, $\widehat{q_{sat}} - w_c$ (triangles) increases, indicating critical deviates from column saturation. For lower $\widehat{q_{sat}} \leq$ 61 mm, both conditional precipitation and probability have slightly higher (lower) values for CWV right below (above) critical, with some underpopulated CWV bins (open circles) exceeding the corresponding column saturation (triangles), indicating minor inconsistency between the retrieval and reanalysis datasets. Furthermore, there is more below-critical precipitation as $\widehat{q_{sat}}$ decreases (Fig. 3.3.2d; even more when a

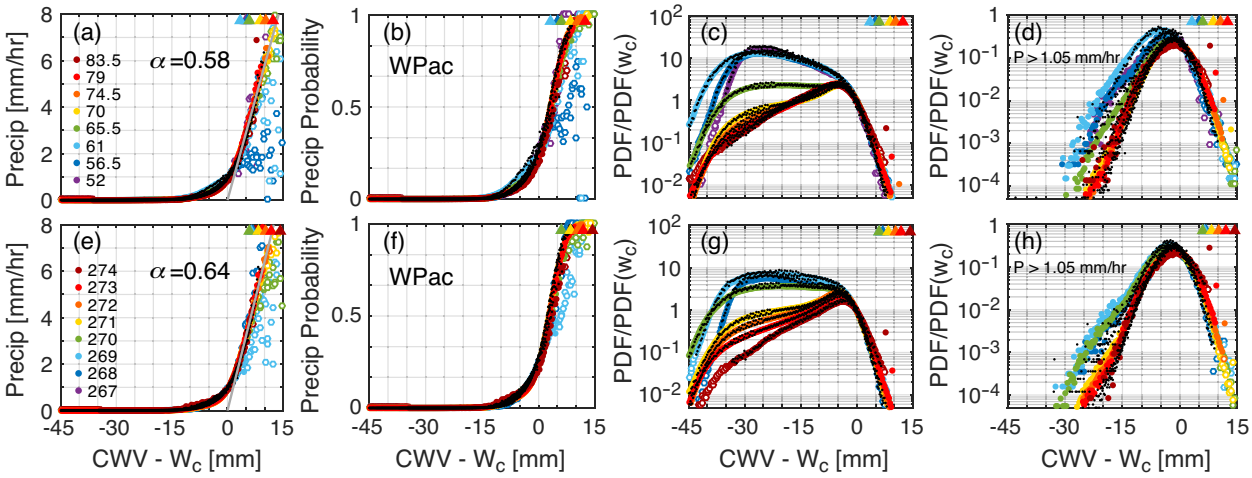

Figure 3.3.2: (a)-(d) Convective transition statistics for the tropical western Pacific as in Figs. 3.3.1a-3.3.1d for 0.25° (colored markers) and 0.5° (dots), but for each marker/dot shifted by the corresponding critical CWV $w_c(\widehat{q_{sat}})$ from Fig. 3c, and with PDFs scaled. The best-fit for conditional precipitation is shown as gray line in (a), with its slope indicated by α. (e)-(h) Same as (a)-(d), but using $\widehat{T}$ instead of $\widehat{q_{sat}}$ as the bulk tropospheric temperature measure. The colored triangles represent average $\widehat{q_{sat}}$ conditioned on $\widehat{T}$ and CRH ($\equiv$ CWV/$\widehat{q_{sat}}$) $> 60\%$, shifted by w_c. The corresponding plots for the other basins are in Figs. 3.A.5 and 3.A.6.

smaller precipitation threshold is adopted), consistent with cold events originating from the extratropics and exhibiting characteristics different from deep convection in the tropics.

The PDF of CWV in Fig. 3.3.2c also collapses around and above critical, with the PDF of non-precipitating events (including those with $P < 1.05$ mm h^{-1}) varying with $\widehat{q_{sat}}$ and basin. For CWV slightly lower than critical, the PDF of CWV starts to drop rapidly, and the PDF for precipitating events peaks. As demonstrated in simple stochastic models (Stechmann and Neelin 2011, 2014), moisture accumulates by surface evaporation and moisture convergence until CWV reaches critical, at which point precipitation becomes an effective sink, leading to the drop in the PDF for CWV above critical. Note that the PDF for all events has another peak at lower CWV because of the balance between surface evaporation and moisture divergence.

Earlier studies (Neelin et al. 2009, Sahany et al. 2014) have suggested scaling instead

of shifting by w_c, i.e., considering the form $f(cwv/w_c)$ instead of the shift $f(cwv - w_c)$, to collapse the statistics. Both are similar to leading order for small differences in w_c, but to second order have slightly different effects. Scaling preserves the zero CWV value, which can be important when examining PDFs across the entire CWV range, while shifting is preferred here because effects near critical seem to be affected by factors that do not scale with w_c. The two approaches may lead to different interpretations for warming climate, where some of the simplest arguments tend to rescale moisture by saturation (for a discussion surrounding saturation deficit vs relative humidity in projecting future tropical cyclone genesis frequency, see Camargo et al. 2014).

3.3.3 Dependence of critical on temperature

The collapsed conditional precipitation and probability of precipitation for the tropical western Pacific at 0.25° in Figs. 3.3.2a-3.3.2b are duplicated in Figs. 3.3.3a-3.3.3b, along with the critical CWV $w_c(\widehat{q_{sat}})$ (Fig. 3.3.3c) and critical column relative humidity (critical CRH) $w_c(\widehat{q_{sat}})/\widehat{q_{sat}}$ (Fig. 3.3.3d). Results for other basins are also shown. Here, we focus on the results derived using TMIv7.1 CWV and precipitation.

In Figs. 3.3.3a-3.3.3d, the precipitation pickup and the dependence of w_c on $\widehat{q_{sat}}$ are constant across basins, with slightly lower w_c for the tropical Atlantic. As noted earlier, a clear transition occurs around $\widehat{q_{sat}} = 61$ mm in Figs. 3.3.3c-3.3.3d. For lower $\widehat{q_{sat}}$, the precipitation pickup is less well-defined and scatters more, and so do the corresponding critical values, with approximately constant critical CRH. Above the transition $\widehat{q_{sat}}$, the critical values deviate from saturation as $\widehat{q_{sat}}$ increases, i.e., deep convective onset occurs at higher CWV but at lower CRH with increasing tropospheric temperature, as shown in Neelin et al. (2009). The critical CRH decreasing with $\widehat{q_{sat}}$ is expected to be robust as long as w_c is defined through collapsing statistics, for other reasonable definition of critical [e.g., assuming the functional form of $\log(1 + e^{\alpha(cwv - w_c)})$ for the conditional precipitation] would only introduce a $\widehat{q_{sat}}$-independent offset of w_c, preserving the slope of the $w_c - \widehat{q_{sat}}$

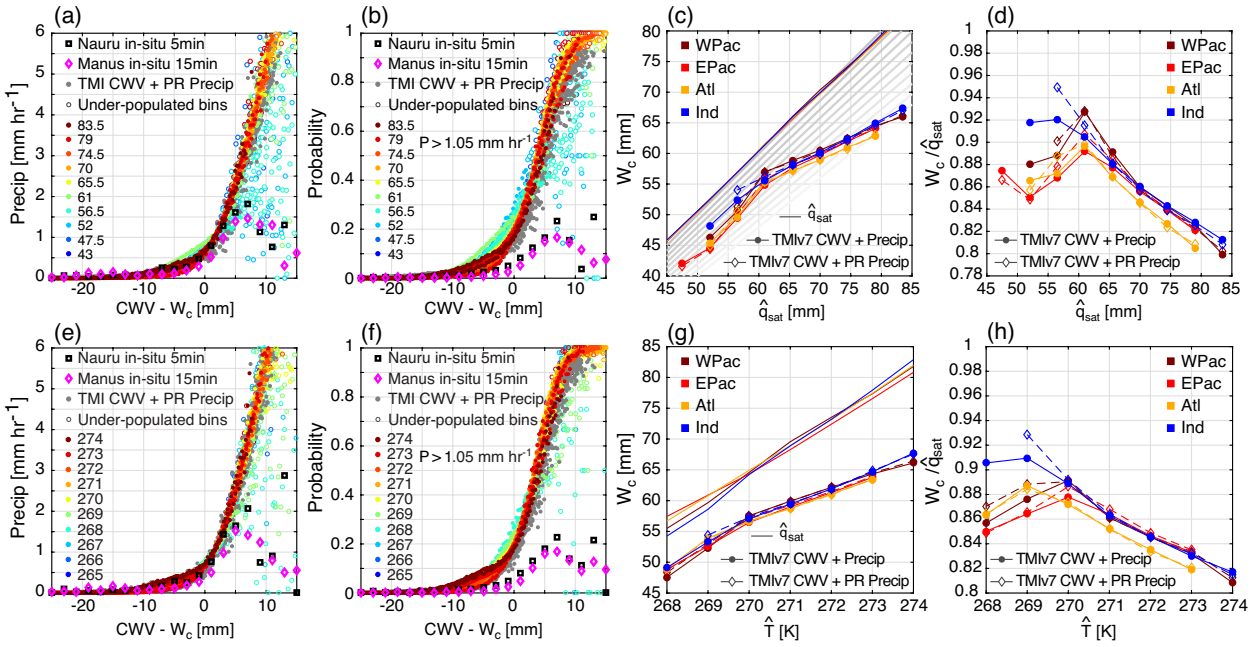

Figure 3.3.3: (a) Collapsed conditional precipitation and (b) probability of precipitation; (c) critical CWV w_c and (d) critical CRH ($\equiv w_c/\widehat{q_{sat}}$) for tropical oceans using $\widehat{q_{sat}}$ as the bulk tropospheric temperature measure. (e)-(h) Same as (a)-(d), but using $\widehat{T}$ instead of $\widehat{q_{sat}}$ as the bulk temperature. The conditional precipitation [(a), (e)] and probability of precipitation [(b), (f); $P > 1.05$ mm h^{-1}] are compiled for 3 combinations of datasets: (i) TMIv7.1 CWV and precipitation (colored dots) with underpopulated bins plotted as open circles, (ii) TMIv7.1 CWV and PR 2A25 precipitation (gray dots) excluding underpopulated bins, and (iii) ARM site CWV and precipitation measurements from Manus (diamonds) and Nauru (squares) Islands in the tropical western Pacific (WPac). Reanalysis-2 temperature is used for (i)-(iii). For (i) and (ii), bins from all four basins are plotted, with data at 0.25° resolution and coastal regions excluded. For (iii), the CWV values are shifted by the corresponding w_c given the temperature ($\widehat{q_{sat}}$ or $\widehat{T}$) time series according the w_c-temperature relation for WPac [as in (c) and (g)]. The critical CWV [(c), (g)] and critical CRH [(d), (h)] are calculated for combinations (i) and (ii), respectively. The colored solid lines in (c) and (g) represent $\widehat{q_{sat}}$ conditioned on temperature and CRH ($\equiv$ CWV/$\widehat{q_{sat}}$) $> 60\%$. This conditional $\widehat{q_{sat}}$ is also used in defining the critical CRH. The gray lines in (c) represent CRH from 100% to 8% with 2% spacing.

relation which, when compared with the constant CRH (gray) lines in Fig. 3.3.3c, indicates decreasing critical CRH with $\widehat{q_{sat}}$.

The transition from approximately constant to decreasing critical CRH with increasing

$\widehat{q_{sat}}$ marks the different precipitation regimes, i.e., convection-dominant in the tropics vs. large-scale saturation-driven in the extratropics.

3.3.4 Robustness to instrumentation

Before the convective transition statistics can be used for model diagnostics, their robustness and sensitivity to instrumentation must be quantified. Figures 3.3.3a-3.3.3d include the results derived using multiple datasets, including (i) TMIv7.1 CWV and precipitation, (ii) TMIv7.1 CWV and PR 2A25 precipitation, and (iii) ground-based measurements from Manus and Nauru ARM sites in the tropical western Pacific.

The statistics in Figs. 3.3.3a-3.3.3d are robust to TMIv7.1 vs. PR precipitation, with slightly more scatter for the conditional probability. Combining TMIv7.1 CWV and 3B42 precipitation results in quantitatively similar statistics except for a slightly smaller slope α of the best-fit for conditional precipitation (not shown).

In Fig. 3.3.3a, the conditional precipitation from Manus and Nauru ground-based measurements, collapsed using $w_c(\widehat{q_{sat}})$ for the tropical western Pacific (WPac; TMIv7.1 CWV + precipitation), are quantitatively consistent with those from satellite retrievals, with significant low bias at highest CWV (relative to critical; $cwv - w_c > 5$ mm); the corresponding conditional probability in Fig. 3.3.3b is uniformly lower than satellite retrievals because of the difference in spatial-resolution, with the similar low bias. Combining the ground-based CWV time series and 3B42 precipitation around Manus and Nauru shows the same bias at high CWV, indicating that the cause is due to the ground-based MWR CWV measurements (section 3.A.8). These have a "wet-window" problem, i.e., high CWV events associated with strong precipitation are missing in the raw CWV time series, and gap-filling can only partially compensate for this.

Though not the focus here, conditional precipitation and probability at the Manaus GOAmazon site (over land) exhibits quantitative differences from those over oceans as in

Fig. 3.3.3, despite the qualitative similarities we shall discuss in section 3.5.

The quantitative agreement among datasets examined here boosts our confidence in the reliability of the convective transition statistics as model diagnostic tools. Meanwhile, given that the same TMIv7.1 CWV and Reanalysis-2 temperature are used for compiling the statistics, we advise caution that the robustness of the statistics to TMIv7.1 vs. PR precipitation may simply reflect the efforts of calibration among datasets. As indicated by the minor difference in the collapsed conditional probabilities in Fig. 3.3.3b, and as we shall see in section 3.6, the two precipitation datasets do lead to quantitative differences in the distribution of precipitation, especially at high rain rate.

3.3.5 Robustness to bulk measure of temperature

Thus far, $\widehat{q_{sat}}$ appears to be a useful bulk measure of tropospheric temperature. As noted above, the critical value is not governed by $\widehat{q_{sat}}$ in a simple way, with critical CWV increasing and critical CRH decreasing with $\widehat{q_{sat}}$.

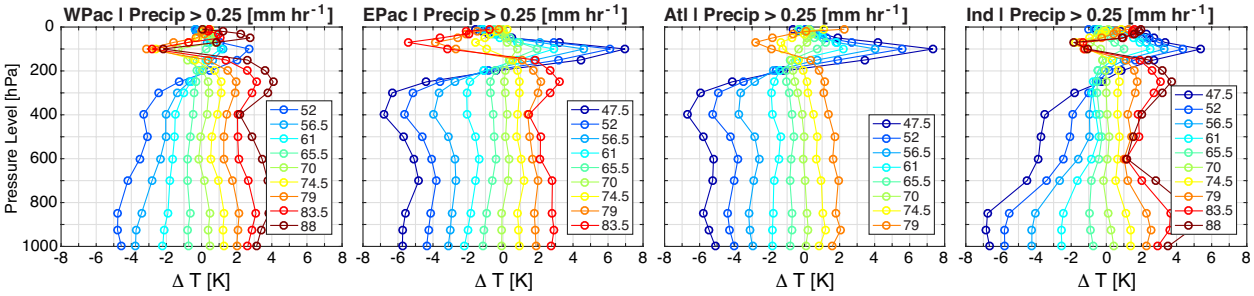

Figure 3.3.4: Reanalysis-2 temperature profiles conditionally averaged on TMIv7.1 precipitation and $\widehat{q_{sat}}$. Profiles are anomalies with respect to the mean profile averaged over all precipitating events ($P > 0.25$ mm h^{-1}) with coastal regions excluded.

Figure 3.3.4 shows the temperature profile, conditioned on precipitation and $\widehat{q_{sat}}$, relative to the mean profile (referred to as a perturbation). The perturbed profile evolves coherently in the vertical as a function of $\widehat{q_{sat}}$, explaining the usefulness of a bulk temperature measure such as $\widehat{q_{sat}}$, or the mass-weighted column-averaged temperature $\widehat{T}$ adopted in previous

studies (e.g., Holloway and Neelin 2007, Sahany et al. 2012). The profiles are similar across basins, except for the high- and low-$\widehat{q_{sat}}$ bins in the tropical Indian Ocean showing greater (smaller) anomaly in the lower (upper) troposphere. This is likely a consequence of the circulation pattern driven by the local land-ocean contrast, since both the warmest and coldest events in this domain tend to occur near the south Asian continent in the Bay of Bengal and Arabian Sea (Fig. 3.A.13). The resulting statistics in Figs. 3.3.1-3.3.3, nevertheless, do not reflect this difference in temperature structure. Replacing the condition on precipitation by CWV above critical, or replacing $\widehat{q_{sat}}$ by $\widehat{T}$, leads to similar profiles. For $\widehat{q_{sat}}$ higher than the most probable bin, the corresponding overall (perturbed + mean) temperature profiles are insensitive to conditions on precipitation or CWV, suggesting that high-$\widehat{q_{sat}}$ events result from previous or nearby convective activity, consistent with convection being the major heating mechanism in the tropical troposphere.

The two bulk measures $\widehat{q_{sat}}$ and $\widehat{T}$, both of which have similar properties in characterizing convection, are well-correlated because of the vertical coherence of temperature (section 3.A.2). It is nonetheless worth quantifying in detail their similarity as bulk temperature measures for the statistics because of the nonlinear dependence of precipitation statistics on the thermodynamic variables. The lower panels of Figs. 3.3.2-3.3.3 show the similar statistics corresponding to their upper-panel counterparts, but use $\widehat{T}$ instead as the bulk measure (other basins in Fig. 3.A.5). From these two figures, substituting one bulk measure by another only leads to minor quantitative differences, e.g., a slightly smaller slope α for conditional precipitation (Figs. 3.3.2a vs 3.3.2e), and slightly more precipitating events for CWV right below critical for cold bins when $\widehat{q_{sat}}$ is used (Figs. 3.3.2d vs 3.3.2h). This insensitivity to the bulk measure of temperature also holds for statistics presented in Figs. 3.4.1 and 3.6.1-3.6.3 below. Note that the vertically coherent temperature structure in the presence of convection guarantees that layered bulk measures (e.g., 850-500 hPa-integrated saturation humidity, etc.) can also be useful and would lead to similar statistics (e.g., Figs. 1 and 3 in Neelin et al. 2009), except for the PDF of all events for CWV significantly lower than

critical, which could differ qualitatively (not shown).

3.4 Geographical dependence of precipitation pickup

The statistics in Figs. 3.3.2-3.3.3 demonstrate that CWV above critical is a practical estimator of conditional instability, and hence precipitation, with the temperature dependence characterized by the w_c-temperature relation [$w_c(\widehat{q_{sat}})$ or $w_c(\widehat{T})$]. These relations seem to be universal across ocean basins, at basin scales. However, other factors contributing to conditional instability—vertical degrees of freedom of temperature and moisture structure not captured by the bulk measures used here, large-scale convergence/divergence, radiative forcing associated with existing clouds or the lack thereof, and triggering of convection because of cold pool expansion from organized systems or land-sea breeze in coastal regions—may vary geographically, causing geographic variations at regional scales (e.g., Torri et al. 2015, Bergemann and Jakob 2016, Ahmed and Schumacher 2017). As such, the effectiveness of CWV above critical as a predictor of precipitation at regional scales is examined in this section.

As background for our discussion, Fig. 3.4.1a shows the probability of precipitation ($P > 0.25$ mm h^{-1}; details in caption). The probability of high CWV (relative to critical; Fig. 3.A.14a) is included in section 3.A.7. These maps of probability of precipitation and high CWV reflect the climatology of precipitation (Fig. 3.A.14b), sharply contrasting the major convergence zones with regions elsewhere.

Figure 3.4.1b shows the corresponding conditional probability of precipitation given high CWV, formally defined as

$$\begin{aligned} &Prob(P > 0.25 \text{ mm h}^{-1} | \, cwv > w_c - 1.5 \text{ mm}) \\ &\quad \equiv \frac{\#\text{ of occurences with } P > 0.25 \text{ mm h}^{-1} \;\&\; cwv > w_c - 1.5 \text{ mm}}{\#\text{ of occurences with } cwv > w_c - 1.5 \text{ mm}}, \end{aligned} \tag{3.1}$$

as a function of geographical location. Here the critical value $w_c(\widehat{q_{sat}})$ is from Fig. 3.3.3c,

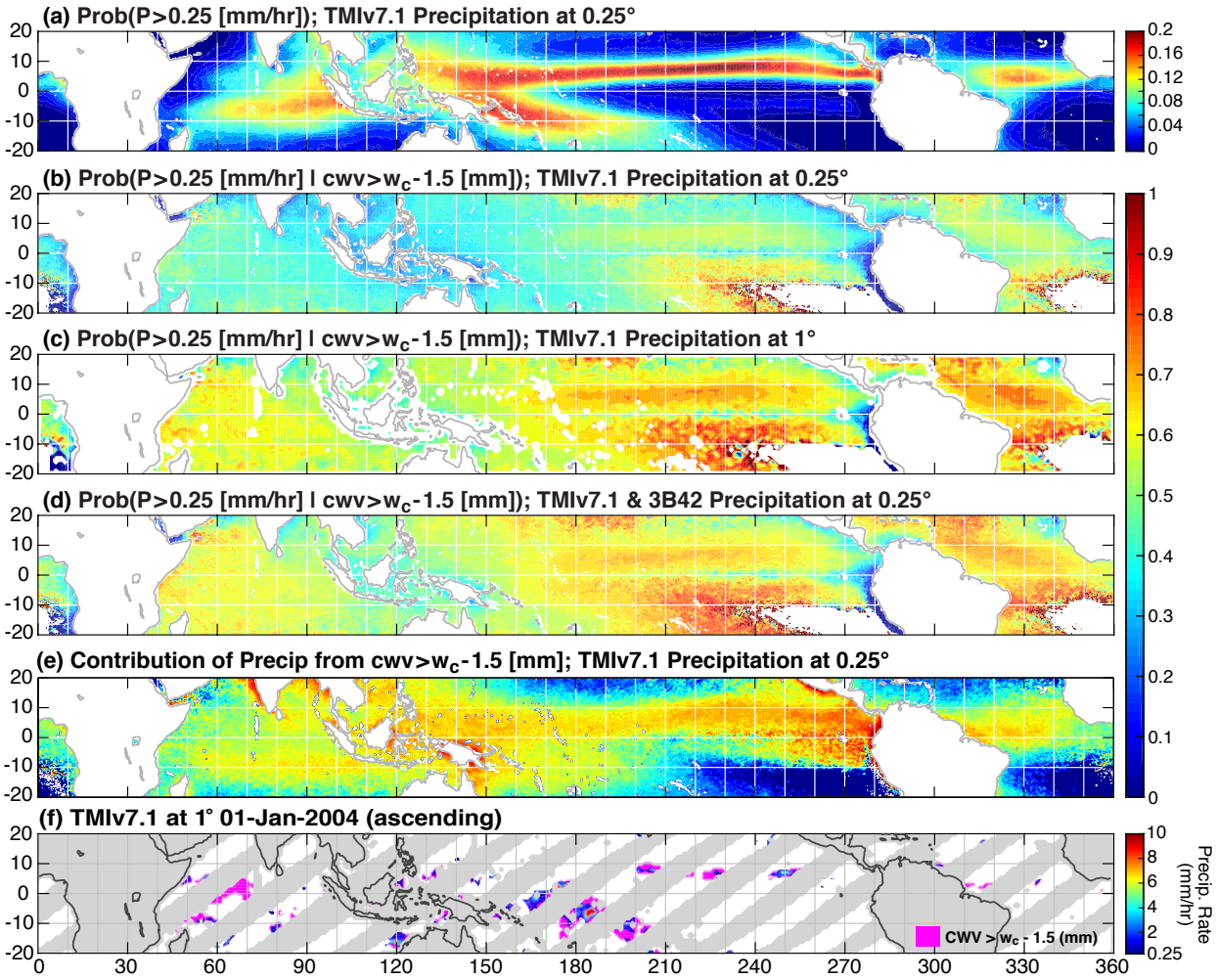

Figure 3.4.1: (a) The probability of precipitation as a function of geographical location, calculated using TMIv7.1 precipitation at 0.25° resolution. (b) The conditional probability of precipitation given CWV exceeding critical, calculated using TMIv7.1 CWV and precipitation, and Reanalysis-2 temperature at 0.25°. Here the conditional probability is calculated from the frequency binned by $cwv - w_c(\widehat{q_{sat}})$, P, and geographical location, with $w_c(\widehat{q_{sat}})$ as in Fig. 3.3.3c averaged over four basins. (c) Same as in (b) but at 1°. (d) Same as in (b), but with P defined as the maximum of the TMIv7.1 precipitation rate and two additional 3B42 precipitation rates that are closest in time to the TMIv7.1 measurement. (e) The fraction of total precipitation from events with CWV exceeding critical, calculated using data as in (b) at 0.25°. (f) Precipitation rate (for $P \geq 0.25$ mm h^{-1}) on top of regions of CWV exceeding critical using TMIv7.1 data at 1° for ascending orbits on 01 Jan 2004. Note that (f) is a realization of the conditional probability in (c) on a particular day. For (a)-(e), the precipitation threshold 0.25 mm h^{-1} is chosen for comparison across spatial resolution, and CWV offset -1.5 mm to include more events. The magnitudes of probabilities/fraction in these panels depend on the precipitation threshold and CWV offset, while the corresponding geographic patterns appear to be robust.

averaged over four basins (adopting basin-dependent critical values only introduces small discontinuities in w_c hence the conditional probability across basin boundaries). The most outstanding feature in Fig. 3.4.1b is that the conditional probability is far smoother than the probability of precipitation in Fig. 3.4.1a. To the extent that there are geographic variations, the conditional probability scarcely reflects the features of precipitation climatology. Thus, including CWV relative to critical and the dependence of critical on temperature has yielded a probability measure that is much less dependent on space.

To a first approximation, the CWV value relative to critical thus provides information that will apply reasonably well across a large portion of the tropics. Furthermore, compiling the statistics presented in Fig. 3.3.3 inside and outside regions with high seasonal precipitation yields quantitatively similar results (not shown; refer to Fig. 3.3.3 since the corresponding collapsed statistics and critical values are visually indistinguishable), reaffirming that these statistics focus on the occurrences of convection at fast timescales rather than long-term climatology.

Minor geographic variations may be noted in Fig. 3.4.1b, e.g., the contrast between the lower values around the Maritime Continent and along the equator in the eastern Pacific, and the higher values off the equator in the central-to-eastern Pacific and Atlantic. The conditional probability is not defined over dry regions covered by marine stratocumulus (there are not above-critical events occurring in these locations); where it is defined, there is large uncertainty associated with small sample size along the edges of the dry regions (e.g., along 10°S in the eastern Pacific). The extreme low values in some coastal regions ($\sim$2.5° in width, the resolution of Reanalysis-2 data) are due likely to the erroneously lower $\widehat{q_{sat}}$ (and hence w_c) and spurious occurrence of above-critical events arising from land-ocean temperature contrasts and spatial interpolation.

Figures 3.4.1c and 3.4.1d further quantify spatial and temporal dependence of this conditional probability. Figure 3.4.1c shows the same conditional probability as in Fig. 3.4.1b, but at 1°. Coarse-graining in space leads to the same spatial pattern (or the lack thereof)

and, with the 0.25-mm h^{-1} threshold adopted here, uniformly greater magnitude in conditional probability, consistent with the dependence on resolution shown in Figs. 3.3.1-3.3.2. That is, CWV above critical serves as a precipitation estimator with more certainty at scales comparable to or larger than the autocorrelation spatial scale of precipitation.

Figure 3.4.1d shows the conditional probability as in Fig. 3.4.1b, but incorporating 3B42 precipitation (details in caption). Here, including two additional 3B42 precipitation rate values effectively provides one more independent snapshot of precipitation taken in the period of 0 to 4.5 hours prior to or after the TMIv7.1 measurement is acquired. The resulting conditional probability in Fig. 3.4.1d therefore quantifies the probability of observing at least one precipitating event from the two datasets, consecutive in time but randomly separated by up to 4.5 hours, given that CWV exceeds critical. Note that here the CWV value relative to critical is treated as approximately constant because of the long autocorrelation timescales of CWV and temperature.

As expected, the conditional probability in Fig. 3.4.1d (at 0.25°) is everywhere greater than its counterpart in Fig. 3.4.1b, and a similar map compiled at 2° is uniformly greater than 85% over tropical oceans (not shown). These suggest that, at scales comparable to the autocorrelation spatial and temporal scales of CWV, an above-critical event is almost certainly accompanied by precipitation before decreasing to below-critical. While precipitation has much shorter autocorrelation timescales, the comparison of Figs. 3.4.1b and 3.4.1d has ruled out the simplest hypothesis that the two consecutive-in-time measurements of precipitation can be treated as independent random events (not shown).

Figure 3.4.1e shows the fraction of total precipitation from above-critical events, which are responsible for most of the precipitation over tropical oceans (except in dry regions). It also captures the seasonal shifts of convergence zones, e.g., the local maximum along 10° S in the Indian Ocean and between 0-10° S in the eastern Pacific results from events during the Southern Hemisphere raining seasons.

Note that Fig. 3.4.1e [and the conditional probability $Prob(cwv > w_c - 1.5 \text{ mm}| P >$

0.25 mm h^{-1}); Fig. 3.A.14d] has a geographic pattern similar to Fig. 17 in Tao and Moncrieff (2009, TM09; fraction of precipitation from mesoscale convective systems) with some coastal exceptions. This similarity suggests that organized systems are important contributors to precipitation above critical (see also Moncrieff et al. 2017). As we have seen in Figs. 3.3.1-3.3.2, the conditional precipitation and PDF of CWV are robust to spatial resolution (up to $\sim 1^{\circ}$)—in addition to the autocorrelation spatial scale of CWV being greater than that of precipitation, organized systems could play a role in this robustness.

Finally, Figure 3.4.1f shows an example for ascending orbits on a particular day, showing the regions where CWV is close to or above critical, i.e., a realization of the conditional probability in Fig. 3.4.1c for those snapshots on each orbit. Precipitation values exceeding 0.25 mm h^{-1} are overlaid. It may be seen that precipitation mainly occurs in the near- or above-critical regions sporadically, consistent with the probabilities shown in the earlier panels. Thus, the estimates of near- or above-critical CWV-temperature environment may have useful applications as predictors of precipitation (see also section 3.A.7), making the known association of precipitation with high CWV (e.g., Mapes et al. 2006) more quantitative.

3.5 Sensitivity to time-averaging

Satellite retrievals provide snapshots of CWV and precipitation covering basin-scale areas and, unlike most ground-based data, contain enough events for the compiled statistics to be stable, i.e., insensitive to noise. However, when these statistics apply to model diagnostics—given that most current models output at sub-daily frequencies (e.g., 6- or 12-hourly means) and higher frequency output (e.g., hourly or time-step mean/snapshot) are not standard yet—the validity of the model vs. retrieval comparison must be addressed. To quantify the dependence on coarse-graining in time, we turn to ground-based measurements that have more extensive time-domain information.

Figure 3.5.1 shows statistics from tropical ARM site measurements with different time-

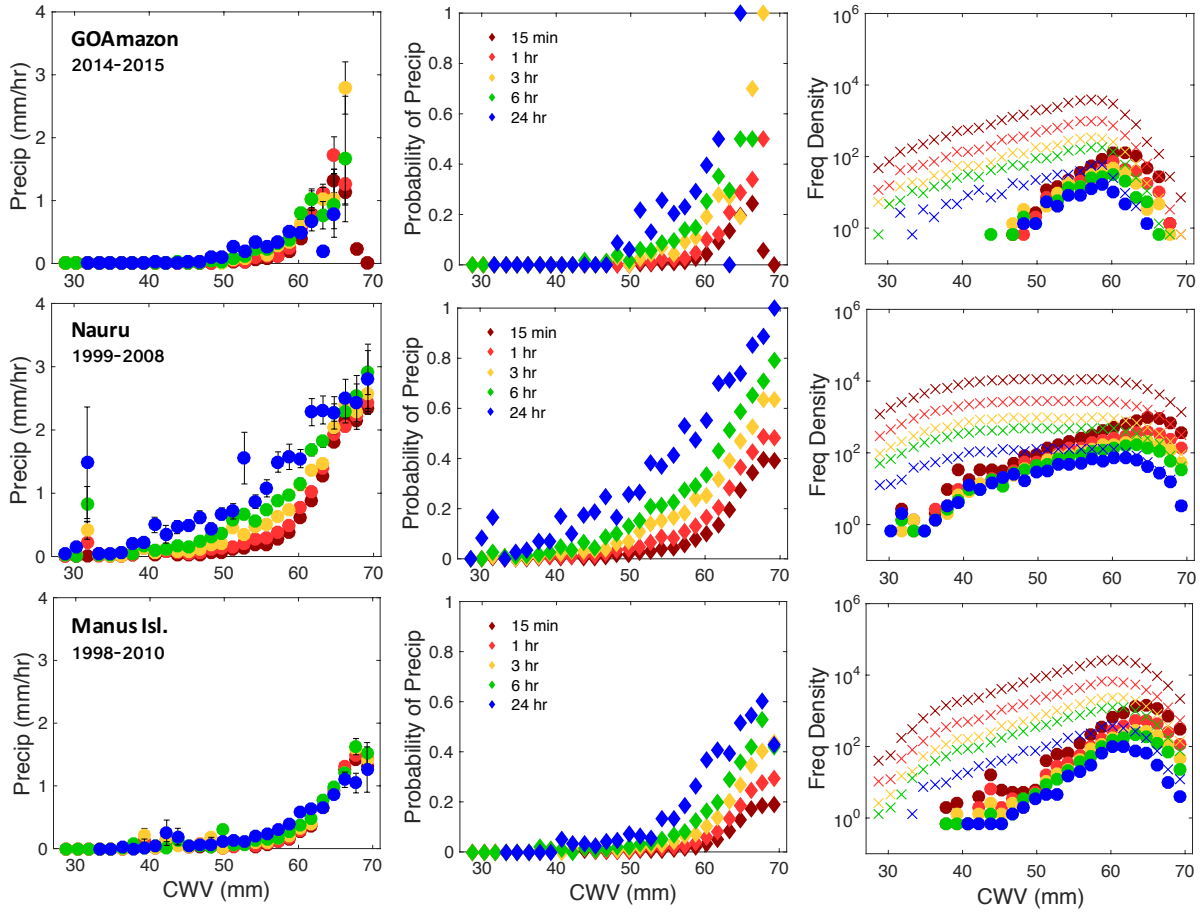

Figure 3.5.1: (Left) Precipitation rate with standard error as error bar, (center) probability of precipitation $P > 0.5$ mm h^{-1}, and (right) frequency density of all events (crosses) and precipitating events (circles), all conditioned on CWV using ARM site microwave radiometer CWV and precipitation data for the GOAmazon site in the Amazon (top), and for Nauru (middle) and Manus (bottom) Islands in the tropical western Pacific. Here the statistics are calculated using CWV and precipitation data time-averaged at 15-min (dark red), 1-h (red), 3-h (yellow), 6-h (green), and 24-h (blue) intervals. Conditional precipitation without error bar indicates a standard error smaller than the marker size.

averaging (not conditioned on temperature). At these sites, the temperature range in terms of $\widehat{T}$ is narrow, with ∼1-2 K variation, and hence the overall statistics are dominated by the most probable temperature bin. The conditional precipitation (1st column) and frequency density for all events (3rd column; crosses) are relatively insensitive to time-averaging up to

6 hours, with Nauru being more sensitive than the other two sites. Conditional probability (2nd column; $P > 0.5$ mm h^{-1}) increases with time-averaging, reflecting the sensitivity of the joint-PDF of CWV and precipitation. There are quantitative differences among these sites, but there is not a clear qualitative difference or contrast between oceanic vs. continental environments regarding the dependence on time-averaging. The sharpness of the pickup tends to be smoothed out by the averaging, resulting from averaging sub-daily instances of high CWV, high precipitation times with lower values. Overall, however, the results in Fig. 3.5.1 suggest that, while instantaneous or hourly data are desirable for insights into the fast-timescale behavior, statistics from 3- or 6-hourly mean data can be used for model comparisons, extending the applicability of using these statistics as diagnostic tools.

3.6 Joint-PDF of CWV and precipitation, and its resolution/instrument dependence

As mentioned in section 3.4, bulk measures like CWV and $\widehat{q_{sat}}$ (or $\widehat{T}$) can represent large-scale factors that affect conditional instability. However, given the same condition at large scales, one would still expect a distribution of precipitation because there are processes at smaller scales or large-scale factors that are unaccounted for by the bulk measures. In this section, we examine the joint-PDF of CWV and precipitation, and its dependence on spatial resolution and instrumentation, to quantify the uncertainty associated with the use of the bulk measures. This joint-PDF can be another useful metric for model diagnostics.

Figure 3.6.1a shows the joint-PDF of CWV (relative to critical) and precipitation rate P for the 70-mm $\widehat{q_{sat}}$-bin (2nd most probable) in the tropical western Pacific compiled using PR (2A25) precipitation at 0.25°. This $\widehat{q_{sat}}$ bin is chosen instead of the most probable bin (74.5 mm) because for the latter, the 75-mm cap of TMIv7.1 CWV results in the CWV value relative to critical being capped at ∼11 mm, and hence the PDF of the highest CWV is missing. The same joint-PDF is plotted in Fig. 3.6.1b on a log-log scale. Non-precipitating

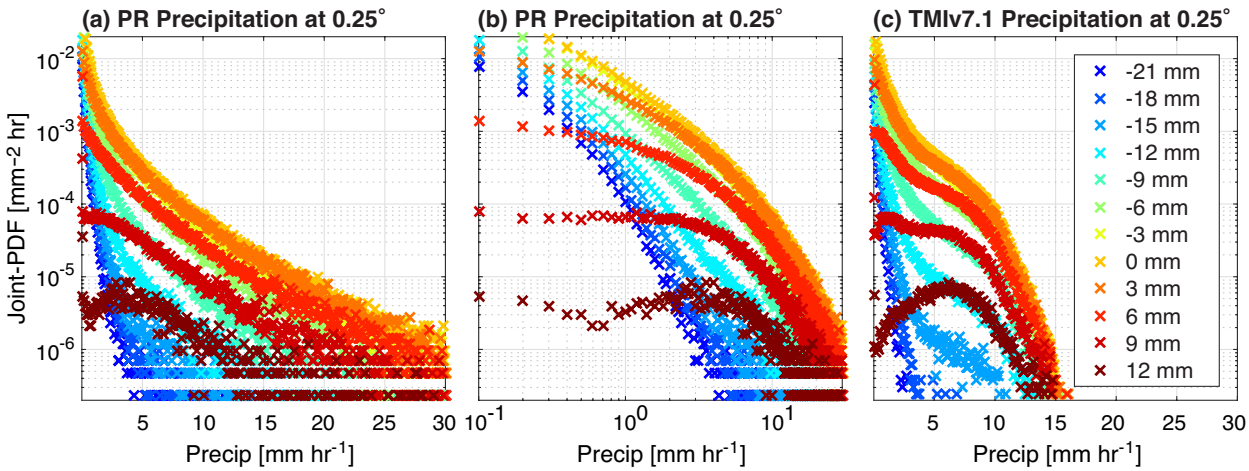

Figure 3.6.1: (a) Joint-PDF of CWV relative to critical and precipitation rate P for the 70-mm $\widehat{q_{sat}}$-bin in the tropical western Pacific compiled using TMIv7.1 CWV, Reanalysis-2 temperature and PR 2A25 precipitation at 0.25° by treating CWV and P as continuous variables with bin-width 3 mm, and 0.1 mm h^{-1} (0.05 for lowest bin), respectively. (b) Same as in (a), but on a log-log scale. (c) Same as in (a), but using TMIv7.1 precipitation (0.25°). The colors indicate the values of CWV relative to w_c.

bins ($0 \leq P < 0.05$ mm h^{-1}) aside, the joint-PDF is quantitatively similar across the $\widehat{q_{sat}}$ range and ocean basins (section 3.A.5).

For CWV below critical, the PDF in Fig. 3.6.1a drops sharply as P increases. As the CWV increases and approaches critical, the PDF increases for all $P > 0$ with long tails extending into high precipitation regime. This occurs until the CWV reaches critical, above which the PDF starts to decrease, with a local PDF maximum developing at a positive P ($\sim$3 mm h^{-1}) for the highest CWV bin. From Figs. 3.6.1a and 3.6.1b (the same joint-PDF on different scales), there is not a clear power-law or exponential dependence of the PDF on precipitation, although a possible functional form will be discussed further below.

Note that the distribution of P is asymmetric, with the most probable value being (close

to) zero even for CWV around critical. As such, any Gaussian-like distribution (Lin and Neelin 2003) or on-and-off precipitation model (Muller et al. 2009, Stechmann and Neelin 2014) with the observed conditional mean and variance would miss much of the distribution details.

The radar-based precipitation retrievals are probably more reliable than the passive microwave radiometer counterpart (including TMI) since the latter is based solely on a path-integrated signal without phase information (Chen et al. 2013). The conditional precipitation and probability of precipitation in Fig. 3.3.3 demonstrate that PR 2A25 and TMIv7.1 precipitation are consistent in terms of the mean and distribution of low-to-moderate precipitation. However, there are quantitative discrepancies for high precipitation between the two datasets. Figure 3.6.1c shows the similar joint-PDF as in Fig. 3.6.1a, but using TMIv7.1 precipitation instead. In Fig. 3.6.1c, there is a clear cutoff at $P \sim$ 10 mm h^{-1} and practically no events for > 15, despite the cap set by the algorithm is 25. This is an undesirable characteristic of the retrieval algorithm when applied to the tropics (there is no sign of a cutoff in the extratropics; not shown). Besides the cutoff, the joint-PDFs for $P < 10$ mm h^{-1} are similar for PR and TMIv7.1, with minor quantitative differences, e.g., the local PDF maximum at high CWV occurs at higher precipitation for TMIv7.1. Thus, we shall not emphasize the distribution of precipitation from TMIv7.1 precipitation, except for using it as an aid to study its dependence on spatial resolution.

Figure 3.6.2 shows the joint-PDF of CWV (relative to critical) and P compiled at different spatial resolutions (details in caption). The two panels for 0.25° show the same joint-PDFs as in Figs. 3.6.1a and 3.6.1c, but with a different CWV bin-width.

In terms of the general features, the joint-PDFs in Fig. 3.6.2 exhibit clear asymmetries between the low-CWV—low-precipitation regime and regime near critical. However, in the vicinity of critical (roughly ±3 mm), the joint-PDFs are roughly symmetric with respect to CWV, consistent with Figs. 3.3.2d and 3.3.2h. As CWV increases, the fraction of non-precipitating events decreases, as indicated by the conditional probability of precipitation

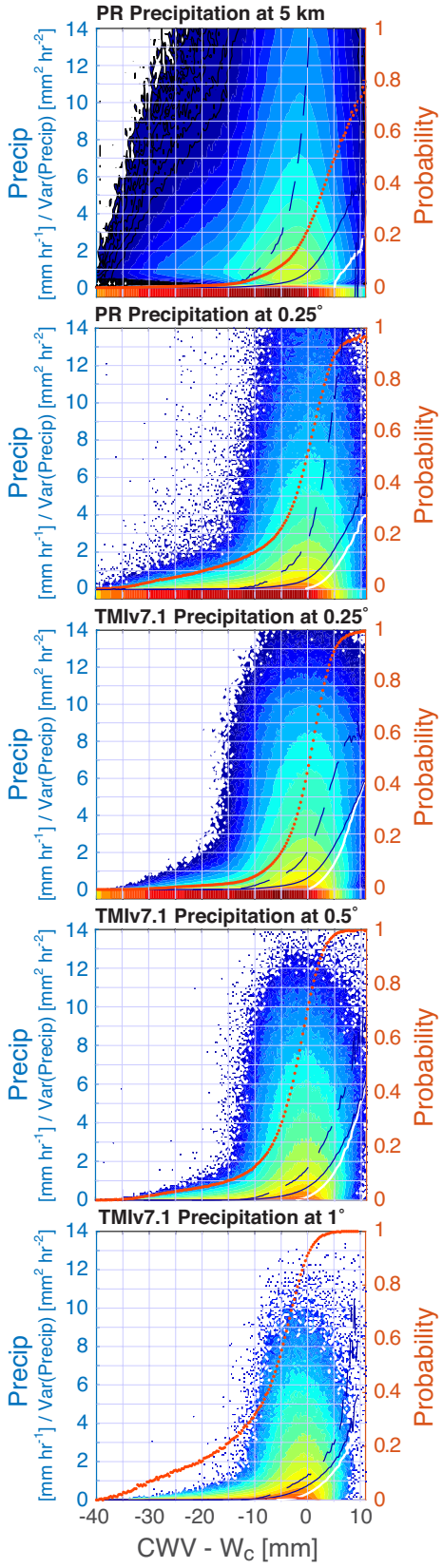

Figure 3.6.2: Color shading: Joint-PDF (units: mm^{-2} h), on a log10-scale, of CWV relative to critical and precipitation rate P for the 70-mm $\widehat{q_{sat}}$-bin in the tropical western Pacific compiled using TMIv7.1 CWV and Reanalysis-2 temperature, PR 2A25 (at 5 km and 0.25°) and TMIv7.1 (at 0.25°, 0.5°, and 1°) precipitation, by treating CWV and P as continuous variables. The spacing between the joint-PDF contours is 0.3, i.e., the color advances whenever the joint-PDF doubles ($10^{0.3} \sim 2$). The corresponding precipitation rate (blue solid line), probability of precipitation ($P > 0$ mm h^{-1}; orange dots), median (white solid line) and variance (blue dashed line) of precipitation, all conditioned on CWV, are also shown for reference. For PR (at 5 km and 0.25°) and TMIv7.1 (0.25°), the bands at the bottom indicate bins with $0 \leq P < 0.05$ mm h^{-1}. Note that the minimum nonzero P for raw PR data at 5 km is ~0.11 mm h^{-1}, and the TMIv7.1 precipitation at 0.25° is discretized with units 0.1 mm h^{-1}.

(orange dots; $P > 0$) and the bands at the bottom for the top 3 panels (PDFs for $0 \leq P < 0.05$ mm h^{-1}). This and the extension of PDF into high-precipitation around critical result in the sharp increase in the conditional mean (blue solid line), median (white solid), and variance (blue dashed) of precipitation. These 3 conditional statistics, when calculated by excluding non-precipitating pixels, would still show a sharp pickup around critical with slightly higher values for CWV below (not shown). Both the precipitation distribution for $P > 0$ and its contrast to non-precipitating events (i.e., $P > 0$ vs. $P = 0$) contribute to the overall variance of precipitation (Stechmann and Neelin 2011).

In addition to the differences of PR and TMIv7.1 shown in Fig. 3.6.1, the conditional probability for PR at 0.25° in Fig. 3.6.2 is noticeably higher than its TMIv7.1 counterpart for CWV lower than critical, partly because of the differences in instrument sensitivity and native resolution of the datasets. Recall in Fig. 3.3.3 that the conditional mean and probability (with respect to a different 1.05-mm h^{-1} threshold) from PR and TMIv7.1 are extremely close. Despite this, the two 0.25° panels in Fig. 3.6.2 show that the TMIv7.1 precipitation tends to underestimate the variance of precipitation for CWV around and above critical. Furthermore, the TMIv7.1 conditional median approaches mean at high CWV, implying a more symmetric distribution of precipitation, consistent with the corresponding PDFs in Fig. 3.6.1c.

As for the dependence on spatial resolution shown in Fig. 3.6.2, there are more weakly precipitating events (e.g., $0 < P < 2$ mm h^{-1}) in the expense of non-precipitating and heavily precipitating events at lower resolutions, consistent with spatial-averaging, which also results in the conditional probability increasing and variance decreasing with resolution.

Figure 3.6.3 shows the precipitation contribution as a function of CWV and P for the 70-mm $\widehat{q_{sat}}$-bin in the tropical western Pacific on different scales. In Fig. 3.6.3a, the areas under the curve integrated to the mean precipitation rate for this $\widehat{q_{sat}}$. While the largest contributions come from near critical, values below or above critical still contribute substantially. The relatively linear range in Fig. 3.6.3b appears to suggest that a $P^{-1}e^{-\beta P}$

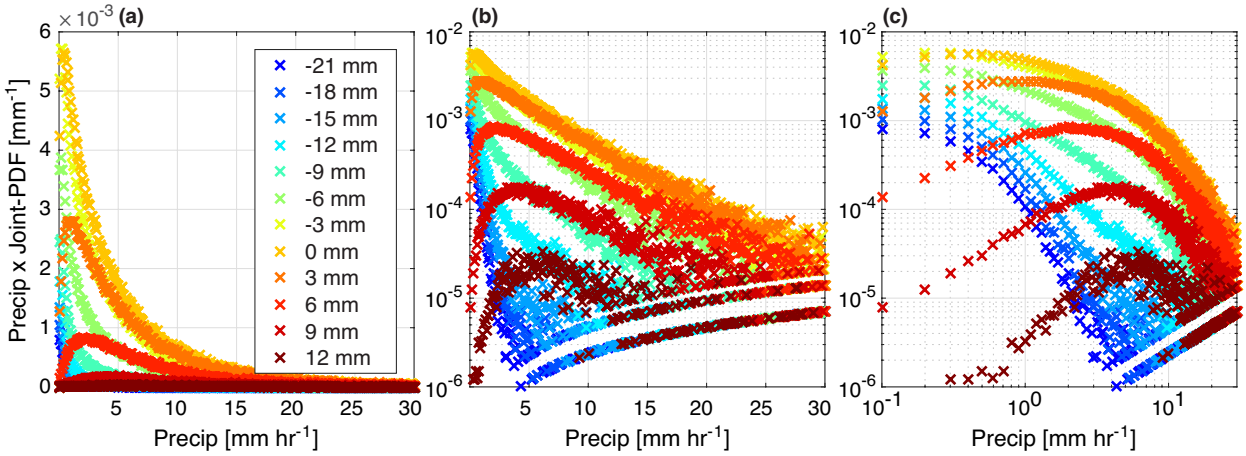

Figure 3.6.3: Precipitation rate-weighted Joint-PDF of CWV relative to critical and precipitation rate P, i.e., the precipitation contribution as a function of CWV and P, for the 70-mm $\widehat{q_{sat}}$-bin in the tropical western Pacific. (a) linear axes; (b) log-linear axes; (c) log-log axes. The data correspond to the Joint-PDF of CWV relative to critical and P in Fig. 3.6.1a, using PR 2A25 precipitation at 0.25°. The colors indicate the values of CWV relative to w_c.

dependence with $\beta \sim 0.16$ (mm h^{-1})$^{-1}$ might be a reasonable approximation for moderate to high precipitation for a wide range of CWV. In both Figs. 3.6.3b and 3.6.3c, the value of P at which the precipitation contribution is a maximum moves towards higher P as CWV increases.

Overall, the distributions of precipitation discussed in this section underline the importance of considering the dependence of the precipitation PDF on where the CWV-temperature environment is relative to critical, rather than as a single PDF for total precipitation.

3.7 Summary and discussion

In this chapter, the convective transition statistics over tropical oceans are compiled using satellite retrievals and ARM site measurements to quantify the dependence of precipitation on the water vapor and tropospheric temperature environment, and to provide an

observational baseline for comparison in using these statistics as model diagnostics at fast (convective) timescales.

The mean tropospheric temperature profiles conditioned on precipitation ($P > 0.25$ mm h^{-1}; Fig. 3.3.4) show vertically coherent structure, justifying the use of bulk tropospheric temperature measures like column-integrated saturation humidity $\widehat{q_{sat}}$, mass-weighted column average temperature $\widehat{T}$, or other layered equivalents as the leading order description of temperature in defining the convective transition statistics. Using these temperature measures yields quantitatively similar statistics, e.g., those shown in Figs. 3.3.2-3.3.3, including the conditional precipitation and probability of precipitation, critical CWV w_c, and PDFs of CWV for precipitating events, though the PDFs of CWV for all events below critical may differ significantly, reflecting the differences in the climatology of these temperature measures. Because of the narrow temperature range in the tropics, the conversion among these temperature measures can be carried out using simple linear relations found by regression.

Among the robust features of the precipitation-CWV relation is the conditional precipitation as a function of CWV and tropospheric temperature, which is insensitive to spatial resolution (Figs. 3.3.1-3.3.3) and time-averaging (Fig. 3.5.1), consistent with the assertion that the autocorrelation spatial and temporal scales of CWV and temperature are much greater than that of precipitation. This is particularly useful for model comparison since model output is subject to varying spatial-temporal resolution. Because of this insensitivity, w_c and the slope α characterizing the precipitation pickup are defined through the conditional precipitation. Both w_c and α are approximately constant across ocean basins, with the latter being insensitive to temperature over the most common range in the tropics. The dependence of the precipitation-CWV relation on temperature is completely characterized by w_c in the sense that shifting CWV by w_c collapses the convective transition statistics and the joint-PDFs of CWV and precipitation. The dependence of w_c on temperature is, however, not a simple relation. Convective onset occurs at higher CWV but at lower column relative humidity (CRH) with increasing temperature, as noted in Neelin et al. (2009), and

is consistent with the entraining plume calculations by Sahany et al. (2012). At low temperatures, which lie along the subtropical margin of the domain, critical values could plausibly be approximated by a constant CRH within a small regime. This regime likely corresponds to the subtropical expression of mid-latitude frontal systems. For the most common behavior in the tropical domain, we underline that using CRH as a variable, without separately quantifying the water vapor-temperature dependence, would yield a poor characterization of the statistics, as expected because of the dominance of conditional instability as a source of tropical convective events.

Robustness of the presented statistics to instrumentation is examined by comparing various datasets, including precipitation radar, microwave retrievals and *in situ* data. A major source of uncertainty in the convective transition statistics is the measurement of CWV in the presence of precipitation. Sensitivity to CWV gap-filling is quantified, which primarily affects probability distributions at very high CWV (above critical). Despite the differences in precipitation distribution, especially at high rain rate, associated with different datasets as indicated by the joint-PDFs (Figs. 3.6.1-3.6.2), both conditional precipitation and probability of precipitation are robust to instrumentation (including ground-based measurements of the former; Fig. 3.3.3). This consistency likely reflects the calibration among precipitation datasets, and emphasizes the reliability of these statistics as observational references for model diagnostics.

At the timescale of the individual retrieval, the tendency of precipitation to coincide with high CWV has been observed. Here, this is quantified more precisely by including the dependence on tropospheric temperature. Specifically, CWV relative to critical ($cwv - w_c$) appears to be a useful predictor of precipitation over tropical oceans. Unlike the climatology of precipitation or CWV that shows sharp contrast between major convergence zones and regions elsewhere, the conditional probability of precipitation given CWV exceeding critical shows only minor geographic variations (Fig. 3.4.1). In other words, the convective transition statistics created from individual convective events conditioned on two bulk mea-

sures of the temperature—water-vapor environment apply reasonably universally through the tropics even at the individual space-time point. Small departures are noted that are presumably due to other vertical degrees of freedom impacting convection. At larger spatial scales and sub-daily timescales, events of high CWV relative to critical are almost certainly associated with convection, leading to a potential application of using CWV above critical as a precipitation predictor. A connection between above-critical events and mesoscale convective systems (Fig. 3.4.1e vs. TM09's Fig. 3.6.1) is noted, which could contribute to the robustness of conditional precipitation to spatial resolution (up to $\sim 1^{\circ}$). A recent analysis of the GOAmazon campaign data also points to the potential importance of organized flow in creating the dependence of deep convection on lower tropospheric water vapor through a deep layer (Schiro et al. 2018) that is seen here as the CWV dependence of precipitation.

It is common to discuss probability distributions of precipitation and to compare models to these (e.g., Figs. 8 and 13 in Klingaman et al. (2017)). However, the strong dependence of the statistics on CWV relative to critical suggests that much of the important dynamics depend on the temperature–water-vapor environment of the precipitating system. We extend the scope of the precipitation-CWV relation to include the joint-PDF of CWV relative to critical and precipitation rate P. This joint-PDF is quantitatively similar in the most common temperature range across tropical ocean basins. For low CWV (relative to critical) the PDF drops rapidly as P increases. As CWV increase, the PDF extends into high precipitation regime, and develops a peak at a non-zero P ($\sim$3 mm h^{-1}) for the highest CWV (Fig. 3.6.1a), with most of the precipitation contribution from CWV around and above critical (mostly $P < 10$ mm h^{-1}; Fig. 3.6.3a).

Examination of the precipitation contributions suggests that the conditional distribution of precipitation in the PR 2A25 data can be approximated by the functional form $P^{-1}e^{-\beta P}$ with $\beta \sim 0.16$ (mm h^{-1})$^{-1}$ for sufficiently high P, for a wide range of CWV (Fig. 3.6.3b). This would correspond to a gamma distribution at the limit of its range of validity, except that there is a clear low-precipitation cutoff in the precipitation contribution that changes

systematically as a function of CWV above critical. This apparently simple observational relationship in precipitation distributions as a function of CWV relative to critical can potentially provide an interesting target for theoretical work.

The joint-PDF does exhibit dependence on spatial averaging, with the joint-PDF exhibiting more light precipitation at the expense of non-precipitating and heavily precipitating events, at lower spatial resolution (Fig. 3.6.2). This resolution dependence results in the dependence of conditional probability of precipitation on resolution, as in Figs. 3.3.1-3.3.3. There is not enough observational data to compile the joint-PDF at resolutions most common for current models ($\sim 1^{\circ}$) without losing information for the highest CWV, but qualitative dependence of the joint-PDF on distance above critical can be used as an auxiliary diagnostic tool for the evaluation of modeled convective parameterizations.

Overall, in addition to providing an observational baseline with quantified robustness and resolution dependence of the basic convective transition statistics for model comparison, the ability to summarize statistics in terms of CWV relative to critical enables additional diagnostics. The dependence of precipitation probability on this quantity expands the set of related properties that exhibit common behavior for precipitation throughout the tropics.

Acknowledgements

The content of this chapter had previously been published as Kuo et al. (2018), which was supported by National Oceanic and Atmospheric Administration Grants NA15OAR4310097 and NA14OAR4310274, the Office of Biological and Environmental Research of the U.S. Department of Energy Grant DE-SC0011074, and National Science Foundation Grant AGS-1540518. U.S. Department of Energy Atmospheric Radiation Measurement (ARM) Climate Research Facility GOAmazon and tropical western Pacific field campaign data are acknowledged. The author thanks J. Meyerson for graphical assistance, and Dr. M. W. Moncrieff and an anonymous reviewer for insightful review comments.

APPENDIX

3.A Supplement

3.A.1 Gap-filling methods for TMIv7.1 CWV

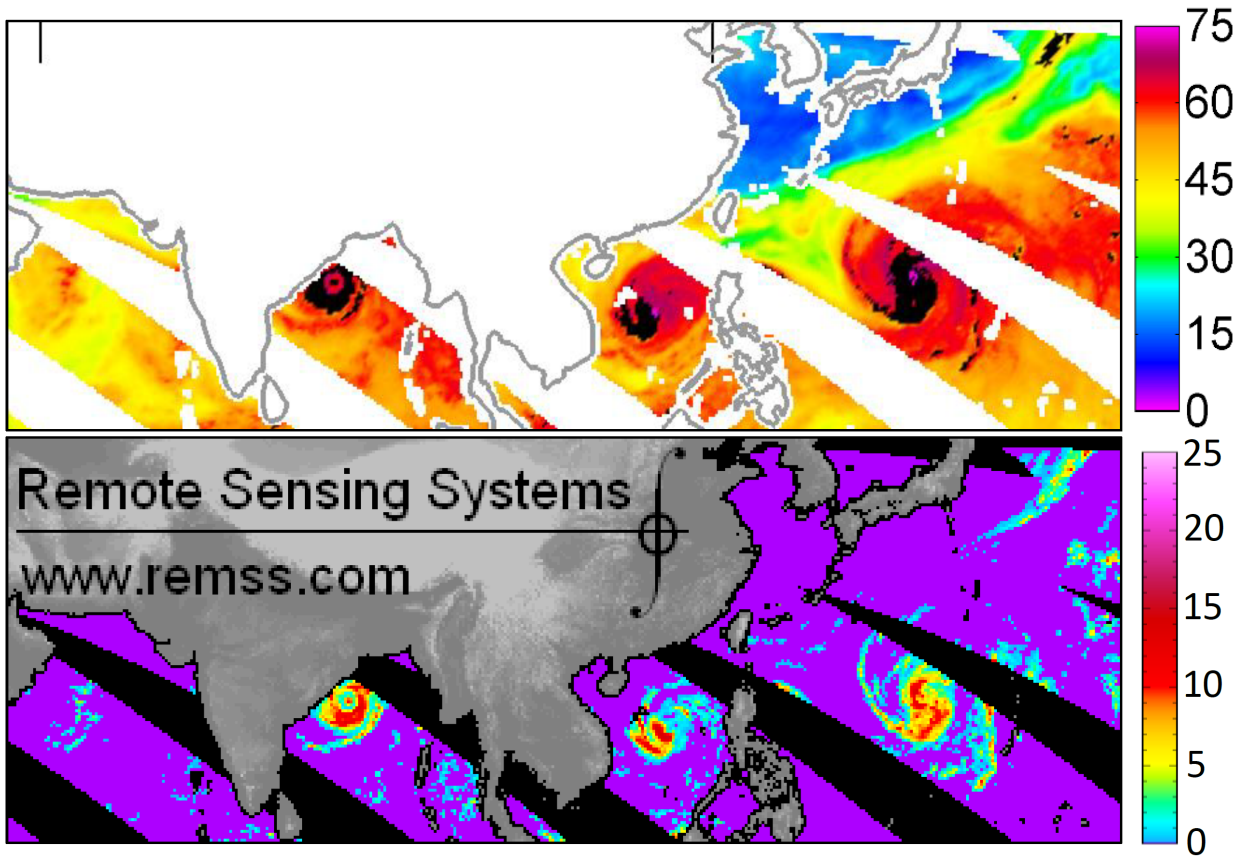

Figure 3.A.1: TMIv7.1 CWV (upper; units: mm) and precipitation rate (lower; units: mm h^{-1}) for TRMM descending passes on 12 October 2013. In the upper panel, regions of missing CWV are shown by black. The image in the lower panel is directly downloaded from the RSS website. The three tropical cyclones, from left to right, are Phailin, Nari, and Wipha.

The latest algorithm (version 7.1) adopted by the Remote Sensing Systems (RSS; Wentz et al. 2015) for column-integrated water vapor (CWV) and precipitation retrievals occasionally does not return a CWV value in the presence of precipitation. Figure 3.A.1 shows an

example of this (chosen to illustrate a severe case, as opposed to a typical situation). One may note that regions with missing CWV, as indicated by black in the upper panel, coincide with regions of high precipitation, as indicated by warm colors in the lower panel.

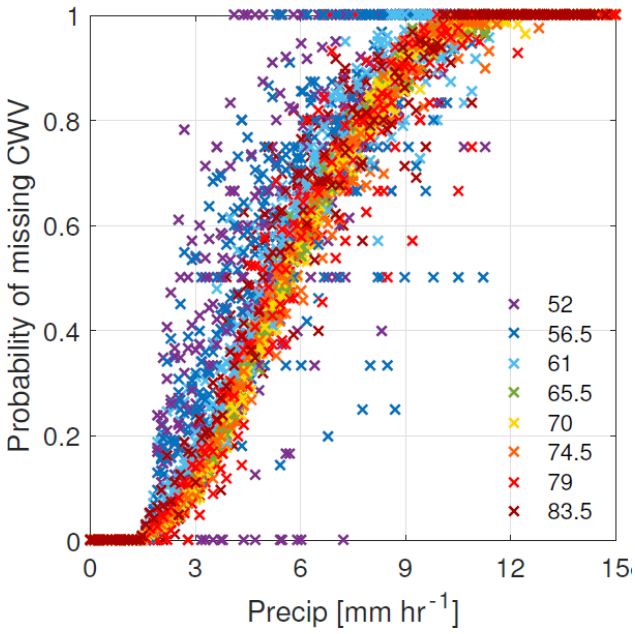

Figure 3.A.2: Probability of missing CWV as a function of precipitation rate and $\widehat{q_{sat}}$ (colors; units: mm) for four tropical ocean basins calculated using TMIv7.1 CWV and precipitation, and Reanalysis-2 temperature for 2005.

The probability of missing CWV is shown in Fig. 3.A.2. The probability depends primarily on precipitation rate and shows little sensitivity to bulk tropospheric temperature and basin. There is also no noticeable annual variability (not shown). Because the missing values are associated with higher precipitation, the raw TMIv7.1 data product has significant biases. This applies even to the climatology, for instance, when precipitation values without CWV retrievals are excluded, the annual mean precipitation rate over tropical oceans calculated using the TMIv7.1 data is reduced from ∼3.1 to 2.1 mm h^{-1}. As such, it is necessary to gap-fill the missing CWV values to avoid distortion of the desired precipitation-CWV relation.

Three gap-filling methods are tested. The first approach fills the missing values using

the available CWV value at the geographically nearest pixel. When there are multiple such pixels, the maximum among the available CWV values is used. This method, referred to as "Nearest" here, is our default choice for CWV gap-filling. The second approach starts with identifying "holes" of missing CWV. For all pixels in each hole, we then fill missing values with the maximum CWV value on the circumference. This approach is referred to as "Max." The third method, "Mean," is similar to Max, but uses a mean instead. Among these three methods, Max assigns more high CWV values, and Mean assigns less high CWV values, while Nearest lies somewhere in between. A fourth method based on biharmonic spline interpolation provided by MATLAB (see https://www.mathworks.com/help/matlab/ref/griddata.html; option 'v4') has also been tested; the results are similar to Max, and hence is not presented here.

The sensitivity of the convective transition statistics (and their spatial-resolution dependence) to gap-filling is discussed in section 3.A.4 (Figs. 3.A.7-3.A.11).

3.A.2 Bulk measures of tropospheric temperature

In the presence of convection, the tropospheric temperature tends to exhibit vertically coherent structure (as in Fig. 3.3.4). Therefore, bulk measures of tropospheric temperature, such as the column-integrated saturation humidity $\widehat{q_{sat}}$ (units: mm) and mass-weighted column average temperature $\widehat{T}$ (units: K) are expected to be useful in characterizing convection, and different bulk measures are expected to yield similar characterization. To verify this assertion directly, Fig. 3.A.3 shows that the joint-PDF of $\widehat{q_{sat}}$ and $\widehat{T}$ over tropical oceans are clearly well-correlated.

Figure 3.3.1 shows the convective transition statistics conditioned on $\widehat{q_{sat}}$. The corresponding statistics conditioned on $\widehat{T}$ are shown in Fig. 3.A.4. As expected, statistics in these two figures demonstrate similar behaviors.

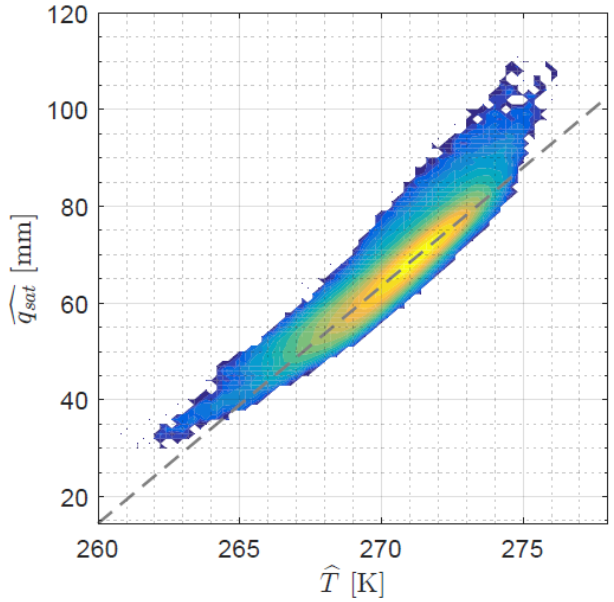

Figure 3.A.3: Joint-PDF (log10) of $\widehat{q_{sat}}$ and $\widehat{T}$ over tropical oceans calculated using Reanalysis-2 temperature for 2005. The color advances when the values of the joint-PDF doubles ($10^{0.3} \sim 2$). The gray dashed line represents the linear regression with slope ~ 4.9 mm K^{-1}.

3.A.3 Estimating critical CWV

The critical CWV w_c is used to characterize the location of the strong increase in conditionally average precipitation and probability of precipitation, and related drops in probability of CWV. Here we detail how this is estimated from the statistics presented in Figs. 1 and S4. Throughout this study, we use the following estimator for w_c: the CWV value at which the asymptote of the conditional precipitation curve intersects with the CWV-axis, with the asymptote being approximated by the best-fit line of a segment of the precipitation pickup (recall Fig. 3.3.2). In practice, the curves for some temperature bins may not reach the high precipitation regime so that their asymptotes (and hence the best-fit lines) are not sufficiently well-sampled for robust estimation. We thus work with the assumption that the precipitation pickup curves can be collapsed by shifting CWV by a suitable amount depending on the temperature, and the slope of the best-fit line does not depend strongly on temperature. One can refer to Figs. 2-3 in the main text, and Figs. S5-S11 below to

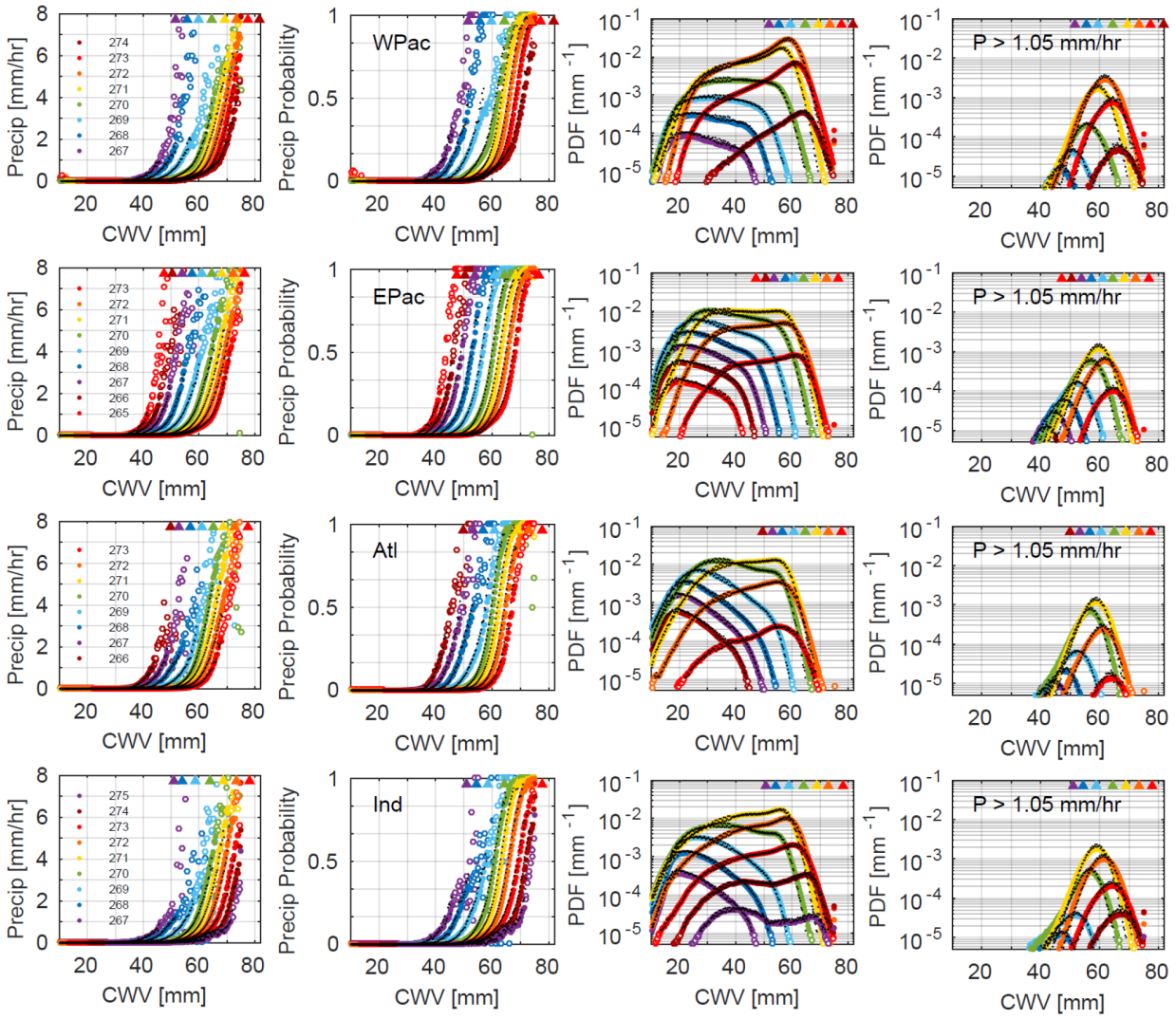

Figure 3.A.4: Similar to Fig. 3.3.1 of the main text but conditioned on $\widehat{T}$ instead of $\widehat{q_{sat}}$ as the measure of tropospheric temperature. Conditionally averaged precipitation rate (1st column from left), conditional probability of precipitation (2nd column), probability density function of all events (3rd column) and precipitating events only (4th column) as a function of CWV and $\widehat{T}$ (units: K) for four tropical ocean basins (20°S-20°N): western Pacific (WPac; 1st row), eastern Pacific (EPac; 2nd row), Atlantic (Atl; 3rd row), and Indian Ocean (Ind; 4th row). Results are shown using TMIv7.1 data and Reanalysis-2 temperature for the period of 01 Jun 2002–31 May 2014 compiled at 0.25° (colored markers) and 0.5° (black dots). Underpopulated bins at 0.25° (PDF $< 10^{-5}$) are indicated by open circles, and those for 0.5° are omitted. Triangles represent the corresponding $\widehat{q_{sat}}$ values. Here, precipitating events are defined by $P > 1.05$ mm h^{-1}. The CWV data is gap-filled using nearest available values, and data from pixels within 2.5° of land are excluded to avoid potentially erroneous temperature values arising from spatial interpolation.

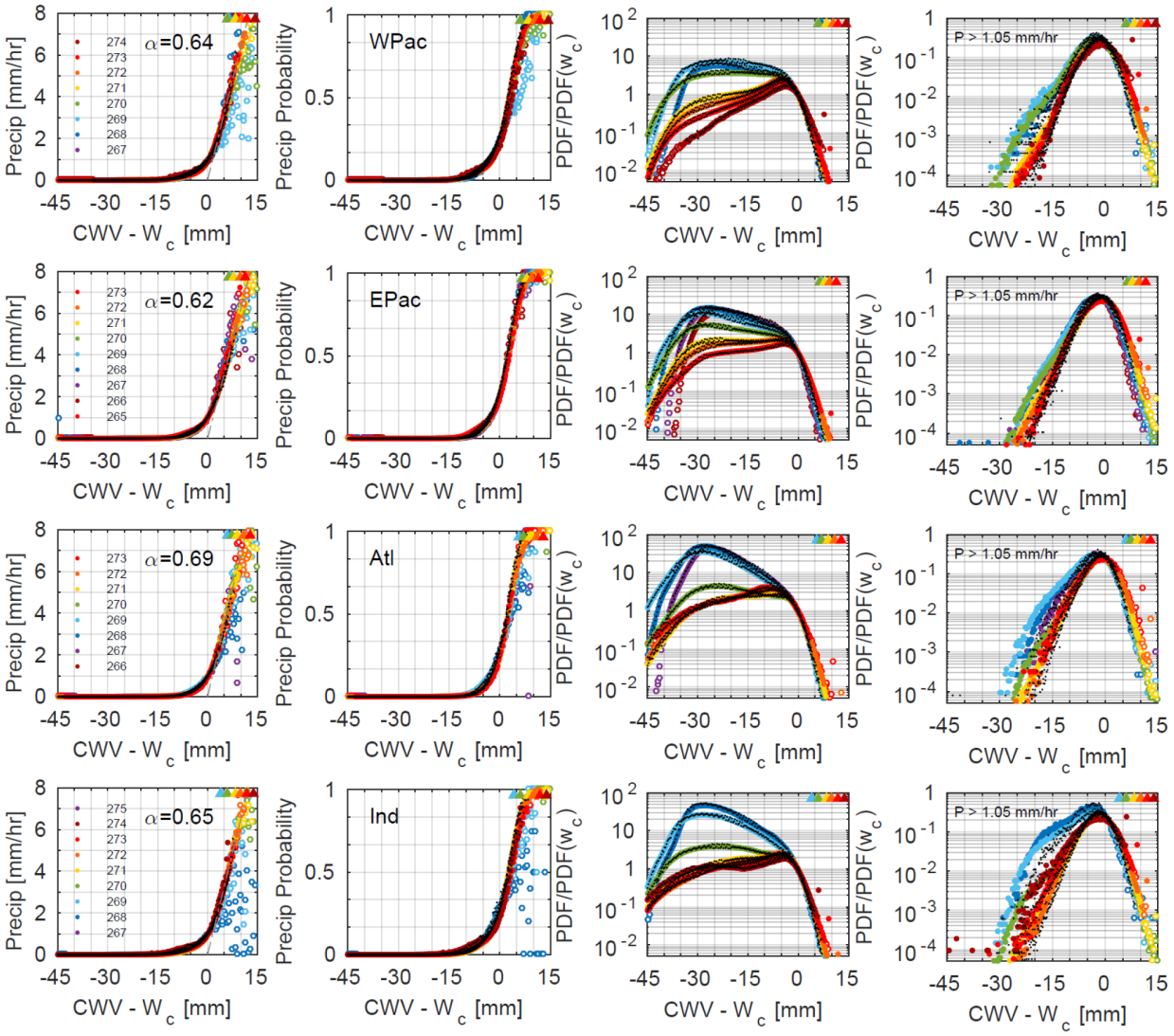

Figure 3.A.5: Convective transition statistics for each ocean basin, as in Fig. 3.A.4 for 0.25° (colored markers) and 0.5° (dots), but for each $\widehat{T}$ shifted by the corresponding critical CWV w_c (as in Fig. 3.3.3g), and with PDFs scaled. The best-fit lines for conditional precipitation rates (leftmost column) are shown as gray dash-dot line, with slope indicated by α. The top row is identical to the bottom row in Fig. 3.3.2.

assess the validity of this assumption. Consider the case where $\widehat{q_{sat}}$ is used as the bulk temperature measure. We start with choosing a fixed reference precipitation rate P_r (say, 1.05 mm h^{-1} as used here). For each $\widehat{q_{sat}}$, we can find the reference CWV w_r at which the conditional precipitation equals P_r. Having found $w_r(\widehat{q_{sat}})$, the assumption implies that the

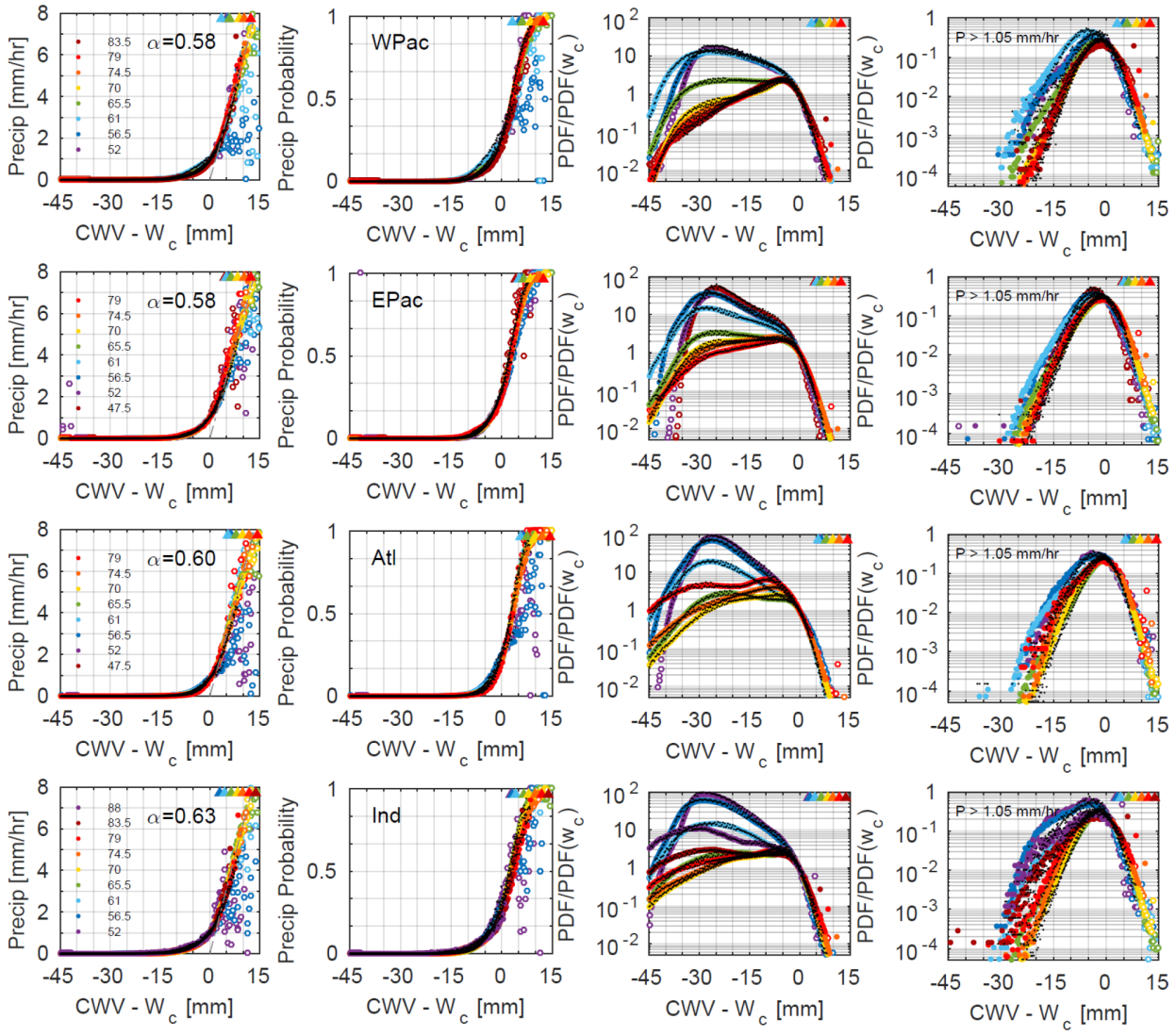

Figure 3.A.6: Same as Fig. 3.A.5, but conditionally averaged by $\widehat{q_{sat}}$ as in Fig. 3.3.1. The top row is identical to the top row in Fig. 3.3.2.

precipitation pickup curves can be collapsed by shifting CWV by $w_r(\widehat{q_{sat}})$ for each $\widehat{q_{sat}}$, i.e., expressing statistics as a function of $cwv - w_r(\widehat{q_{sat}})$ instead. After the curves collapse into a single cluster, one can then take a segment of the cluster with the precipitation rate falling within a certain range (here, $3 < P < 5$ mm h^{-1}) to find the best-fit line and its (shifted) CWV-intercept. Note that the difference between $w_r(\widehat{q_{sat}})$ and $w_c(\widehat{q_{sat}})$ under this procedure is independent of $\widehat{q_{sat}}$, and is typically around 1.75 mm (given by P_r divided by the slope of

the pickup curve, α). The value of w_r would correspond approximately to the measure of critical used in Sahany et al. (2014). The critical values found by the procedure just outlined, and hence the resulting collapsed statistics, are reasonably insensitive to the reference P_r and the specified precipitation range. There are, however, occasions for which special care is necessary. An example of such occasion (but without the proper care for demonstration purposes) is shown in Figs. S8 and S11 below for the 274-K $\widehat{T}$-bin in the tropical western Pacific (WPac). In this case, the conditional precipitation as a function of CWV (gap-filled by Mean) has an irregular behavior for precipitation rate around P_r, leading to a w_r sensitive to P_r, and hence an unsatisfactory collapse. In this particular case, a set of carefully chosen P_r (and precipitation range in some other cases) can resolve the issue. There are, however, cases where the precipitation pickup is too irregular compared with observation (e.g., non-monotonic as a function of CWV) and the procedure outlined above would simply fail (e.g., output from a model with ill-constrained convective parameterization; not shown). Note that in some of the figures presenting the collapsed statistics, the colored markers and black dots represent statistics compiled at different resolutions using the same gap-filling method (Figs. 3.3.2, 3.A.5-3.A.6, and 3.A.9-3.A.11), respectively, and represent statistics using different gap-filling at the same resolution in the others (Figs. 3.A.7-3.A.8). Figures 3.A.5-3.A.6 show the same statistics as in Fig. 3.3.2 in the main text, but include other basins. In all of these figures, the black-dot statistics are collapsed by using the critical values calculated for the colored-marker statistics. Since the lower-resolution conditional precipitation usually does not reach the high precipitation regime, this approach enables us to collapse the lower-resolution (black-dot) statistics without choosing a different range of precipitation, and still leads to a satisfactory collapse. One can assess this last assertion, and the sensitivity of the critical values and the collapsed statistics to the resolution/gap-filling as indicated by the differences between the color-marker and black-dot statistics, by referring to these figures (with the exception of the 274-K $\widehat{T}$-bin for WPac in Fig. 3.A.8).

3.A.4 Sensitivity of convective transition statistics (and their spatial-resolution-dependence) to gap-filling

In this subsection, we examine the sensitivity of the convective transition statistics (and their dependence on spatial-averaging) to the adopted gap-filling method. As mentioned in section 3.A.3, in Figs. 3.A.7-3.A.11, the black-dot statistics are collapsed by using the critical values calculated for the colored-marker statistics.

Figures 3.A.7 shows the (collapsed) statistics at 0.25° compiled using TMIv7.1 data with CWV gap-filled by Max (colored markers) and Nearest (default; black dots). The two methods lead to very similar results. Noticeable differences include the slope of the precipitation pickup and the PDF at high CWV—the former method results in a steeper pickup in terms of conditional precipitation and probability, and more frequent occurrences of CWV exceeding critical. Figure 3.A.8 is similar to Fig. 3.A.7, but with statistics for Max replaced by Mean. The latter method leads to a less steep precipitation pickup, and slightly less frequent occurrences of CWV above critical.

To further examine how the gap-filling method impacts the sensitivity of the statistics to spatial resolution, Figs. 3.A.9-3.A.11 show the collapsed statistics compiled using TMIv7.1 CWV data gap-filled by Max (0.25° and 1.5°), Nearest (0.25° and 1°), and Mean (0.25° and 0.5°), respectively. The choices of resolution for Max and Nearest are the lowest resolution up to which a noticeable difference starts to appear. Here we should leave aside the conditional probability and PDF of precipitating events since they are expected to be sensitive to resolution. Max leads to the conditional precipitation most robust to spatial resolution, with the slope of the asymptote being almost invariant up to 1.5°, while Mean results in the least robust conditional precipitation and a noticeable reduction in the slope for 0.5° compared to 0.25°. Overall, Max assigns more high CWV values and leads to statistics most robust to spatial-averaging, Mean is at the other end of the spectrum, and Nearest lies somewhere in between. For comparison purposes, Nearest is chosen as the default gap-filling method

for this study. Although currently available observational datasets cannot provide sufficient information to favor one method over another, Yano et al. (2012) analyzed output from a cloud-resolving model (CRM) and concluded that the conditional precipitation as a function of CWV is indeed very robust to spatial-averaging. In light of the CRM study, our default choice of gap-filling may be too conservative, and Max leads to statistics more consistent with the CRM simulation in terms of being insensitive to spatial resolution.

3.A.5 Joint-PDF of CWV relative to critical and precipitation for different temperature and basin

Figure 3.A.12 shows the joint-PDF of CWV relative to critical and precipitation rate given different $\widehat{q_{sat}}$ bins and tropical ocean basins. Note that the 70-mm panel for the tropical western Pacific (WPac) is identical to Fig. 3.6.1a in the main text. These joint-PDFs are similar across the most common range of $\widehat{q_{sat}}$ and basins.

3.A.6 Geographic distribution of bulk tropospheric temperature

Figure 3.A.13 shows the probability of occurrences of $\widehat{T}$ (bin-width 1 K) as a function of geographical location. The most probable $\widehat{T}$-bin is 271 K in all tropical ocean basins but the tropical western Pacific, where the most probable $\widehat{T}$ is 272 K. Events with $\widehat{T}$ lower than 270 K mostly occur at latitudes around or higher than 20°, but occasionally in the tropical eastern Pacific and Atlantic. These cold events in the tropics, judged from their geographical distribution, are likely due to systems from the extratropics. Some of the coldest and warmest events in the tropics tend to happen near the south Asian continent in the Bay of Bengal and Arabian Sea, likely caused by the circulation pattern driven by the local land-sea contrast.

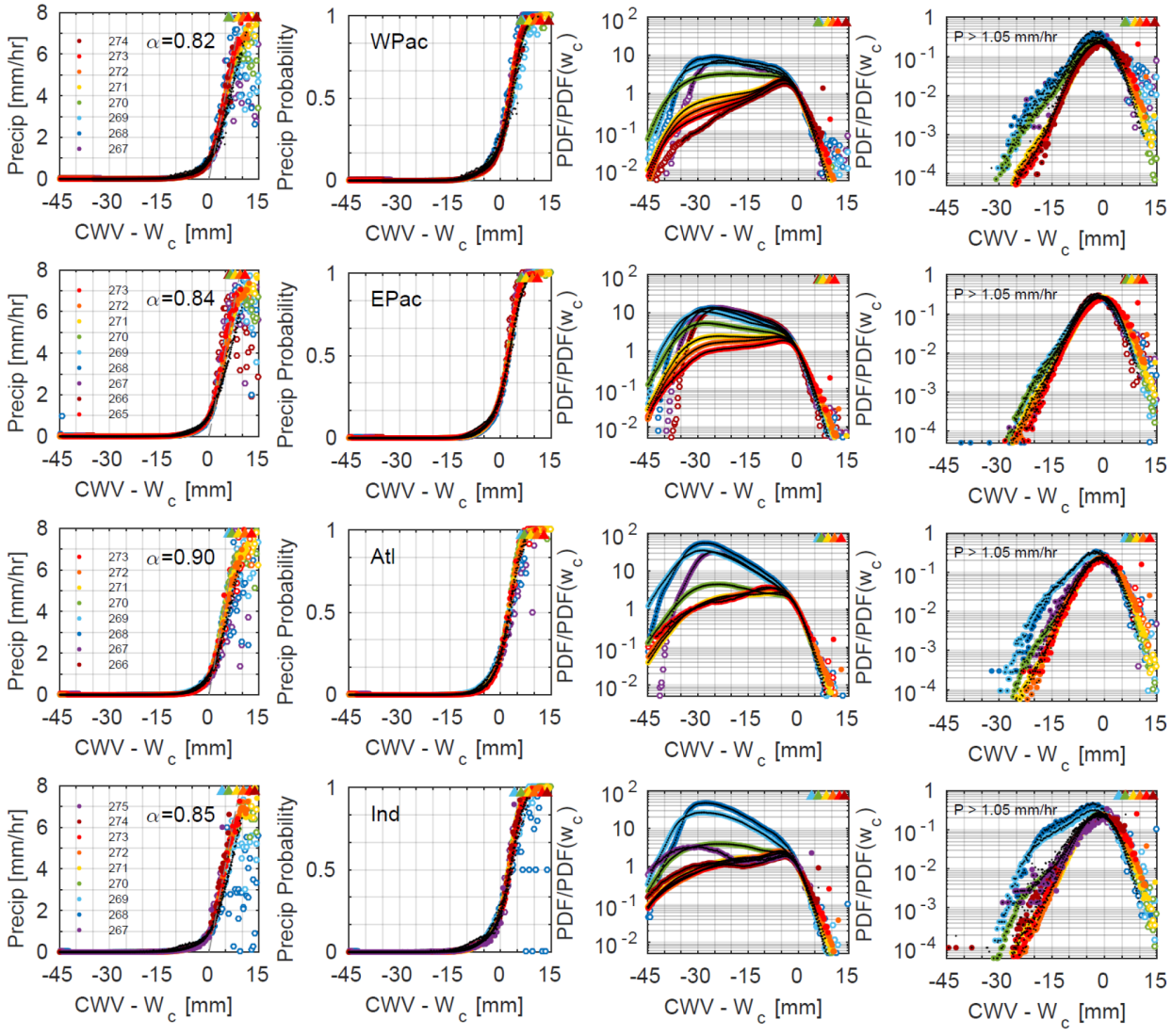

Figure 3.A.7: Convective transition statistics as in Fig. 3.A.4 for 0.25° (colored markers), but with CWV gap-filled using Max. The black dots are a duplication of the colored markers in Fig. 3.A.4 (the statistics for 0.25° with CWV gap-filled using Nearest).

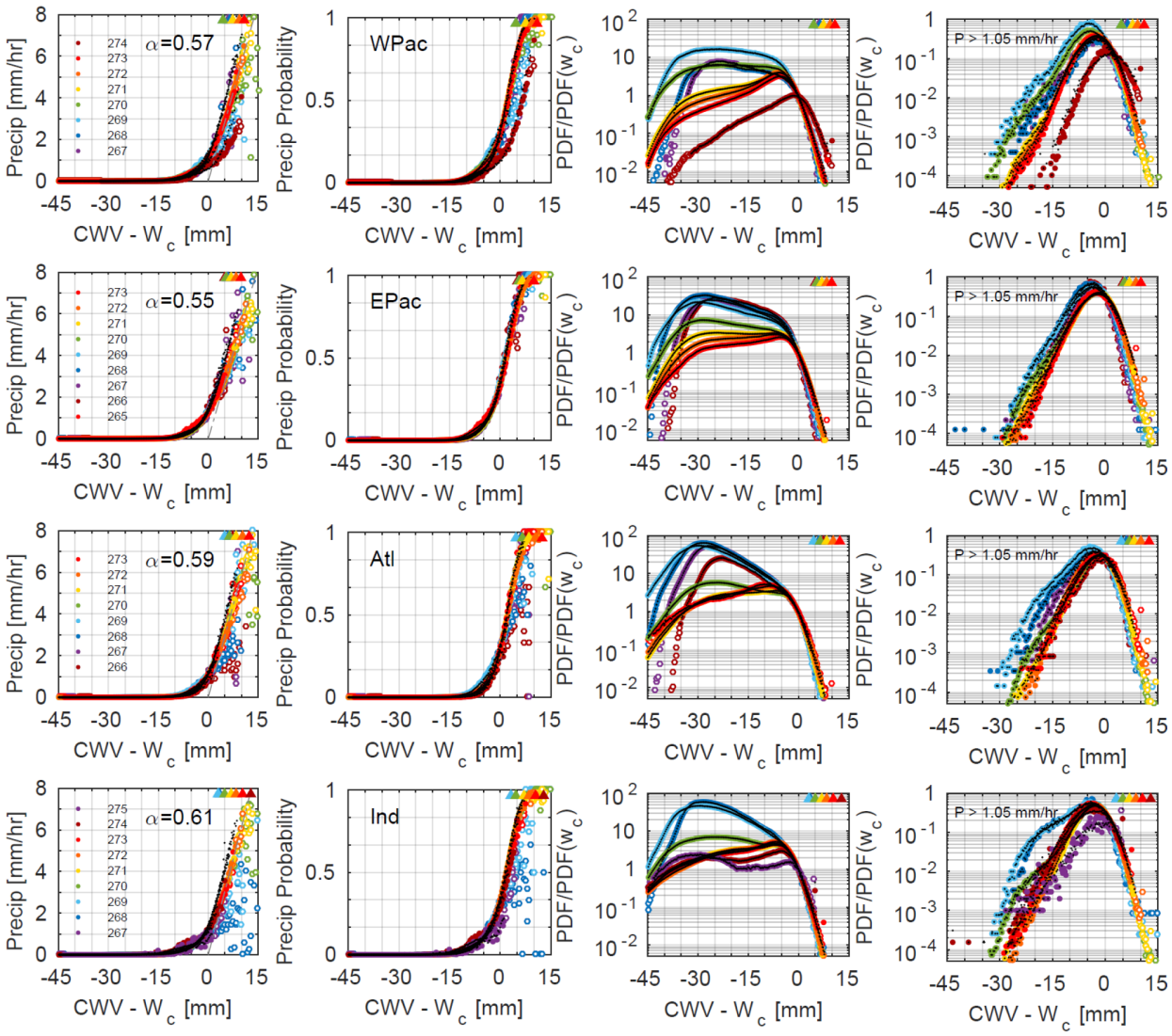

Figure 3.A.8: Convective transition statistics as in Fig. 3.A.4 for 0.25° (colored markers), but with CWV gap-filled using Mean. The black dots are a duplication of the colored markers in Fig. 3.A.4 (the statistics for 0.25° with CWV gap-filled using Nearest). The 274-K $\widehat{T}$-bin for WPac requires the additional effort of choosing a larger P_r to collapse the statistics, which is not done here for illustration purpose (section 3.A.3).

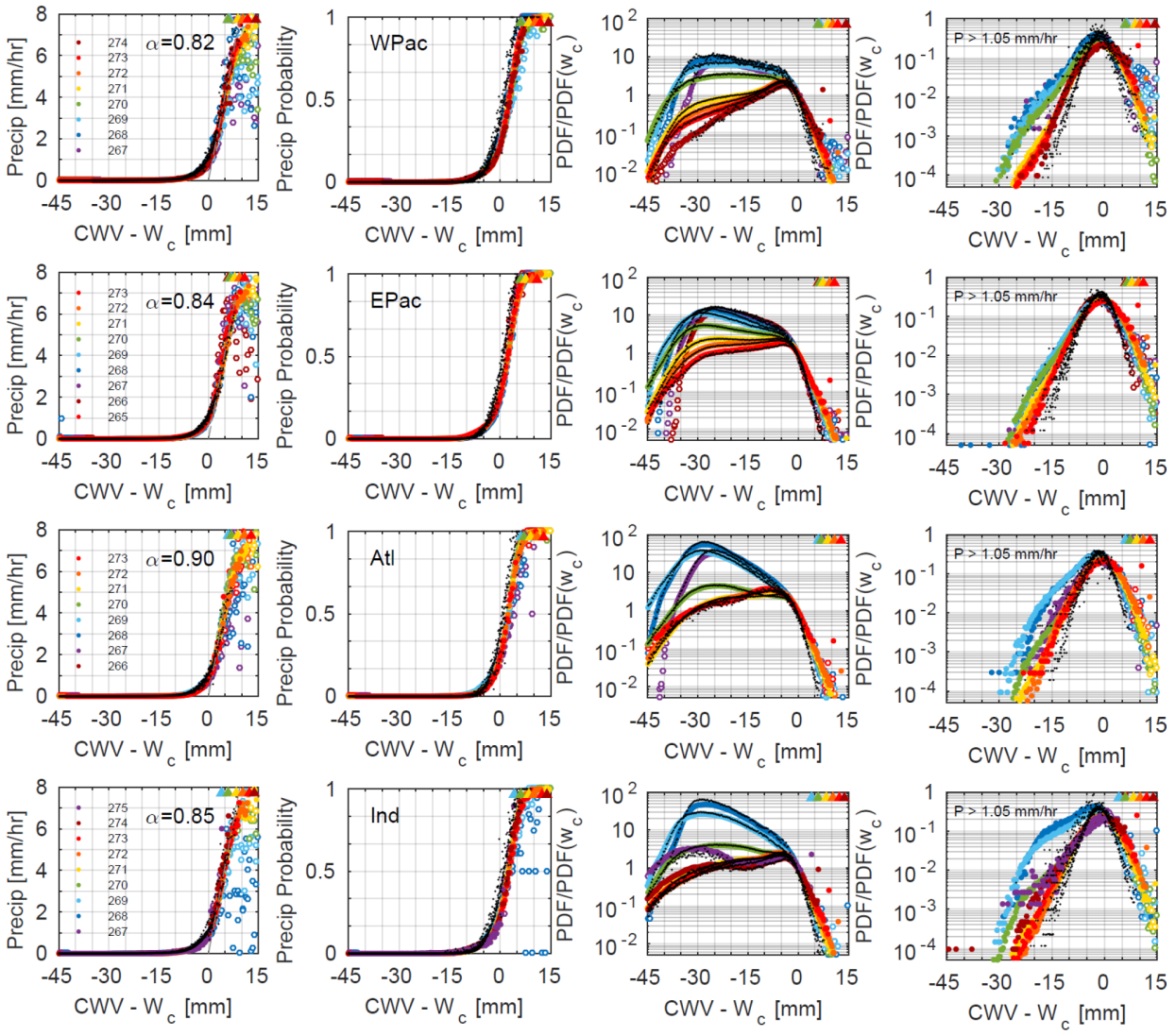

Figure 3.A.9: Convective transition statistics as in Fig. 3.A.5 for 0.25° (colored markers) and 1.5° (black dots), both with CWV gap-filled using Max.

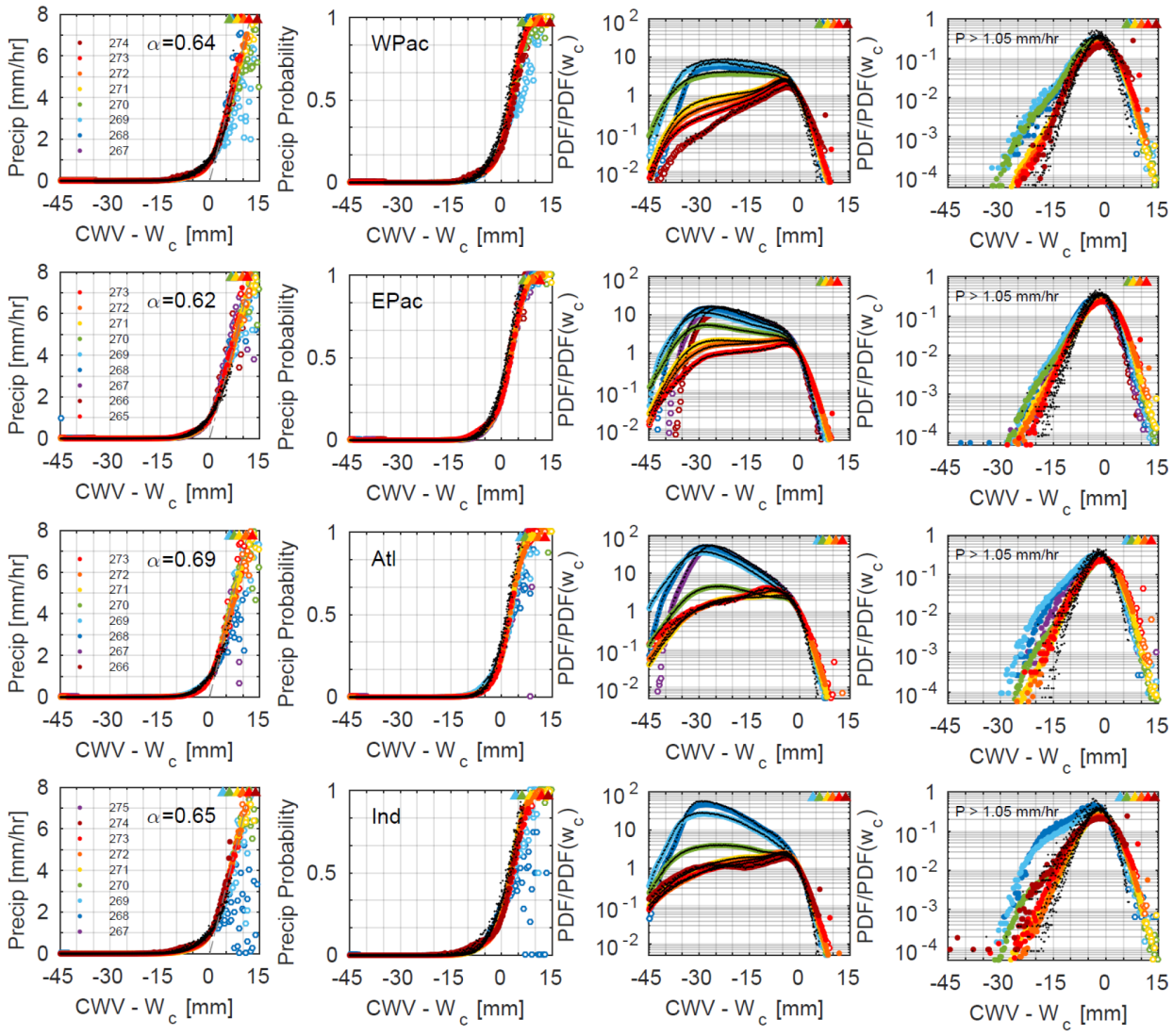

Figure 3.A.10: Convective transition statistics as in Fig. 3.A.55 for 0.25° (colored markers) and 1° (black dots), both with CWV gap-filled using Nearest.

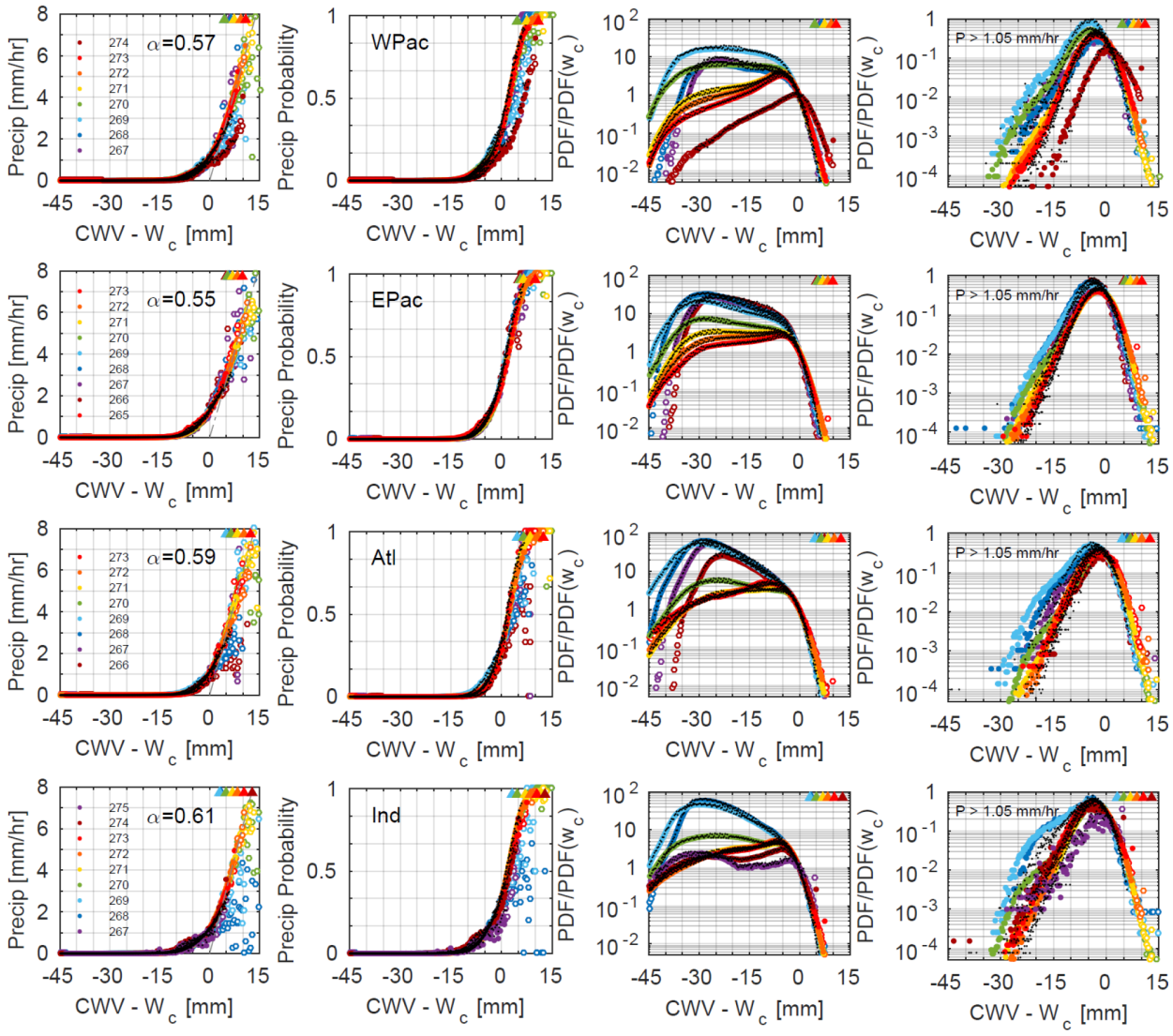

Figure 3.A.11: Convective transition statistics as in Fig. 3.A.5 for 0.25° (colored markers) and 0.5° (black dots), both with CWV gap-filled using Mean. The 274-K $\widehat{T}$-bin for WPac requires the additional effort of choosing a larger P_r to collapse the statistics, which is not done here for illustration purpose (section 3.A.3).

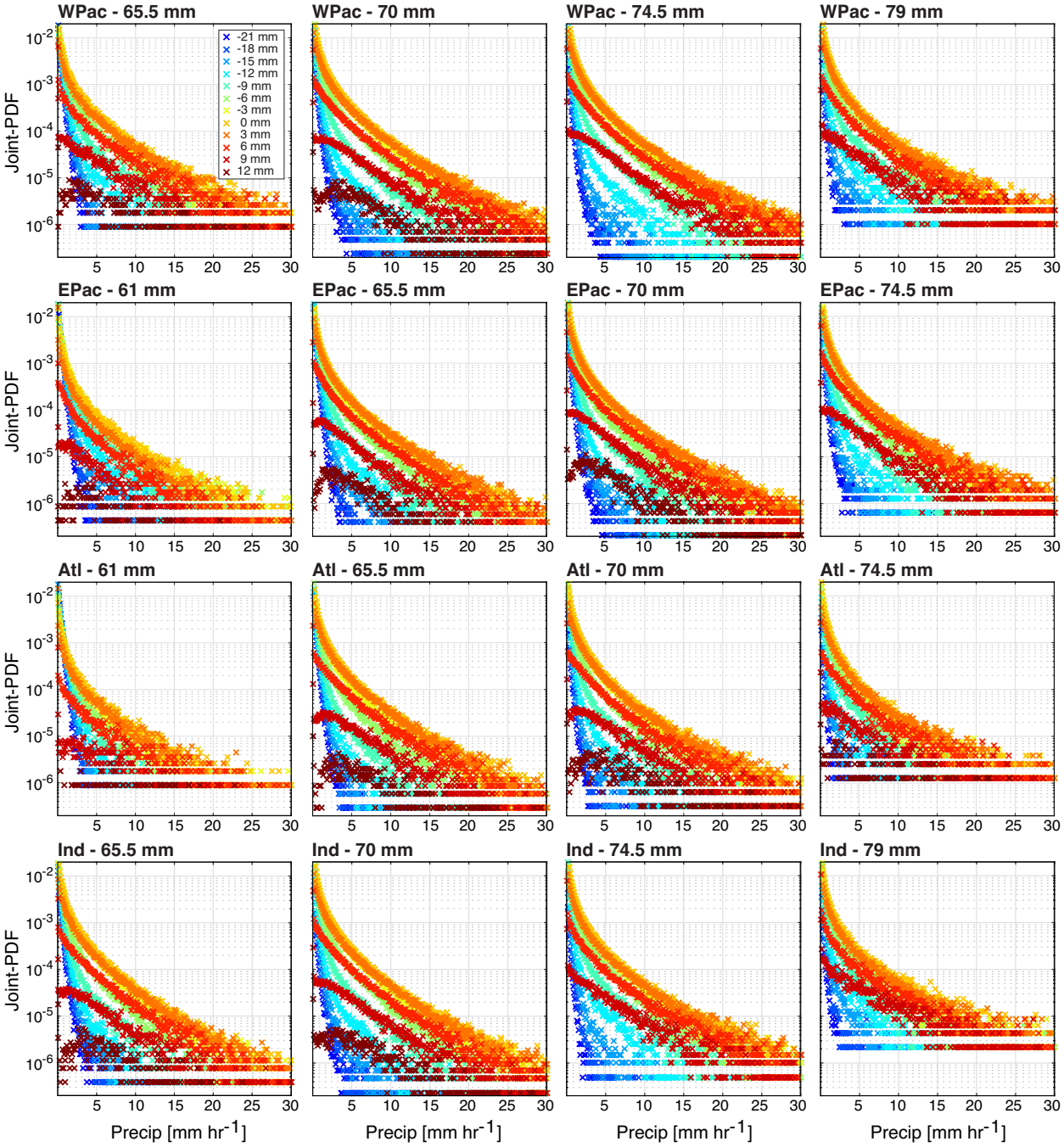

Figure 3.A.12: Joint-PDF of CWV relative to critical (colors) and precipitation rate for the four most probable $\widehat{q_{sat}}$ bins for each tropical ocean basin. The joint-PDF is normalized for each $\widehat{q_{sat}}$.

3.A.7 CWV relative to critical as an indicator of precipitation

Section 3.4 (with Fig. 3.4.1) in the main text discusses how CWV relative to critical can be used as an indicator of precipitation. This section provides additional information com-

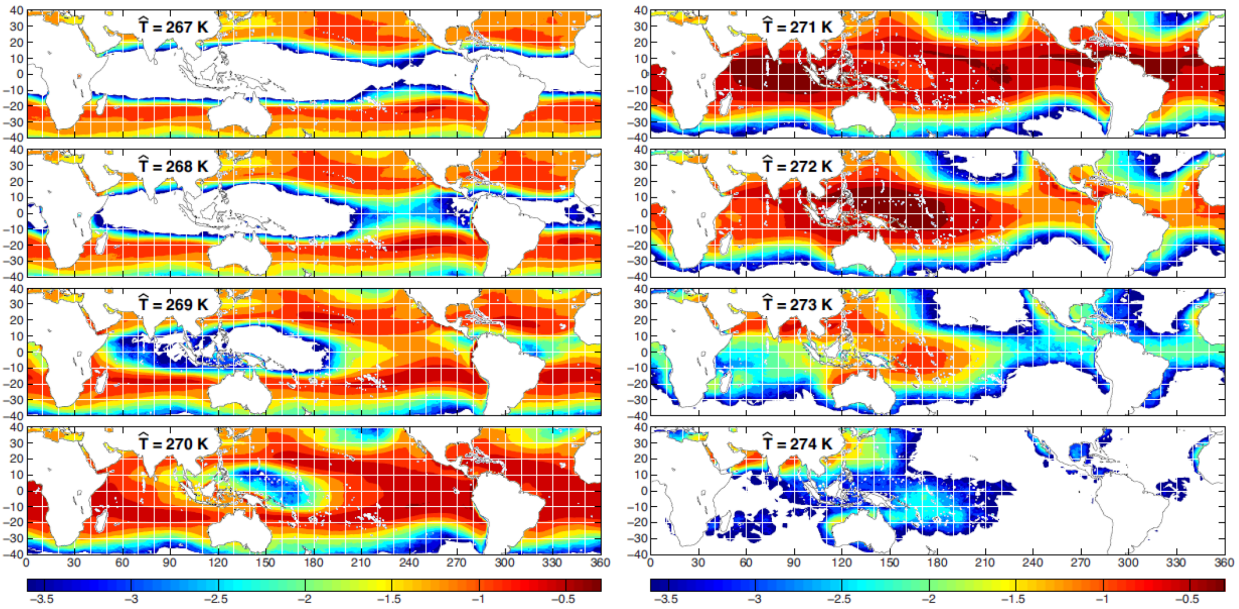

Figure 3.A.13: PDF of $\widehat{T}$ on a log10-scale as a function of geographical location calculated using Reanalysis-2 temperature for the period of 1 June 2002–31 May 2014. The color advances whenever the PDF doubles ($10^{0.3} \sim 2$). The sum of the PDFs over all $\widehat{T}$ (including < 267 K and > 274 K) equals one.

plementing that discussion. Note that the geographical patterns (not the magnitudes) in Figs. 3.4.1 and 3.A.14 are robust to the CWV offset and precipitation threshold.

Figure 3.A.14a shows the probability of CWV exceeding critical (offset by -1.5 mm; to be consistent with Fig. 3.4.1), exhibiting a geographical pattern similar to that of the probability of precipitation (Fig. 3.4.1a) and precipitation climatology (Fig. 3.A.14b). The most outstanding feature here is the sharp contrast between the major convergence zones and other regions. Note that the corresponding CWV climatology in Fig. 3.A.14c, without taking into account the dependence of the critical CWV on temperature, reveals a gentler spatial variation, although the overall pattern still resembles that of precipitation.

While it has been demonstrated that CWV relative to critical is a useful proxy for precipitation, given that the chances of CWV exceeding critical are low ($\sim$ 25% in the major convergence zones as in Fig. 3.A.14a), and that there are below-critical precipitating events, the contribution of above-critical events to the overall precipitation still has to be

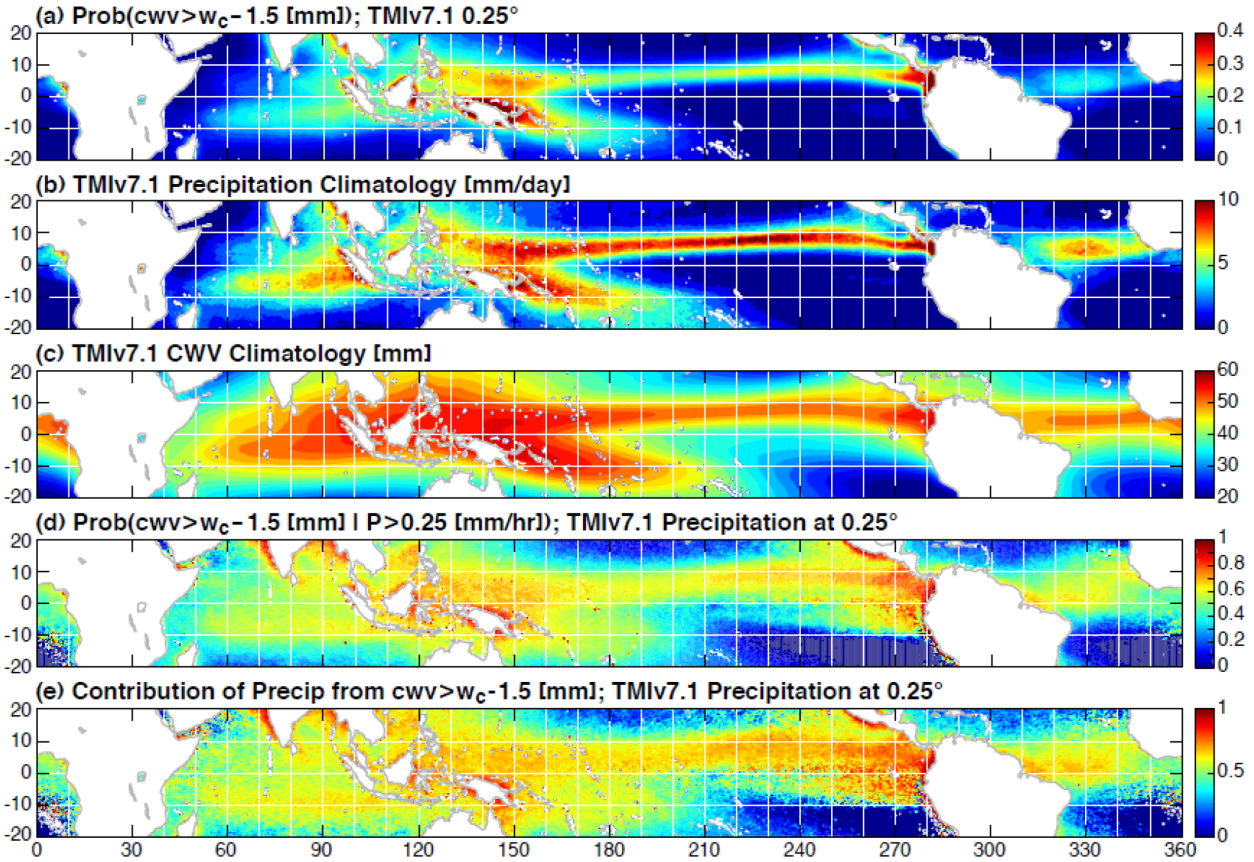

Figure 3.A.14: (a) The probability of CWV exceeding critical (offset by −1.5 mm) as a function of geographical location, calculated using TMIv7.1 CWV and Reanalysis-2 temperature. (b) The precipitation climatology calculated using TMIv7.1 precipitation. (c) Same as in (b) but for CWV. (d) The conditional probability $[Prob(cwv > w_c - 1.5 \text{ mm} | P > 0.25 \text{ mm h}^{-1})]$ calculated using TMIv7.1 data and Reanalysis-2 temperature. Here, (a)-(d) are for the same period 01 Jun 2002–31 May 2014 and resolution 0.25°, and the critical CWV $w_c(\widehat{q_{sat}})$ is as in Fig. 3.3.3 (top center; in the main text) averaged over four basins.

quantified. Figure 3.A.14d shows the conditional probability of CWV exceeding critical given precipitation, which exhibits a geographical pattern and magnitude similar to the fraction of total precipitation from above-critical events shown in Fig. 3.4.1e. In most places in the tropics, the conditional probability and fraction are higher than 60%, indicating that above-critical events are indeed the major contributor to precipitation. The spatial pattern, when compared to that of the precipitation climatology, shows much weaker spatial contrast, and

seems capable of capturing the seasonal shift of precipitation. For instance, one may notice the high values in Figs. 3.A.14d and 3.4.1e in the tropical eastern Pacific between 0° and 10°S, reflecting the occurrences of deep convective events in this region during the boreal spring (not shown). Since these events are rare, they barely make a dent in Figs. 3.A.14a and 3.A.14b (255°-275°).

Figure 3.4.1f in the main text demonstrates a potential application of using CWV relative to critical as a predictor of precipitation. The false positive rate of this (i.e., the conditional probability of no precipitation given CWV exceeding critical) is given by the conditional probability shown in Figs. 3.4.1b, 3.4.1c, and 3.4.1d (more precisely, one minus the conditional probability), and varies weakly with geographical location. The actual magnitude of the false positive rate depends on the spatial-temporal resolution of precipitation in which one is interested, as well as the CWV offset and precipitation threshold. The false negative rate (the chances of having precipitation given CWV below critical) is given by (one minus) the conditional probability in Fig. 3.A.14d. While the exact magnitude of the false negative rate depends on the resolution, CWV offset, and precipitation threshold, it is expected to be lower than 40% in regions including the major convergence zones based on Fig. 3.A.14d. There are regions with high false negative rates, but mostly inside regions with climatologically low precipitation.

3.A.8 Low bias of conditional precipitation associated with ground-based CWV measurements

In Fig. 3.3.3 of the main text, the conditional precipitation and probability of precipitation compiled using the ARM site data from Manus and Nauru show significant low bias for the highest CWV bins (relative to critical; $cwv - w_c > 5$ mm) compared to those from the satellite retrievals. To test whether the bias results from the "wet-window" problem associated with the ground-based MWR CWV measurements, Fig. 3.A.15 shows the conditional precipitation and conditional probability as in Figs. 3.3.3a-3.3.3b, but with the ground-based

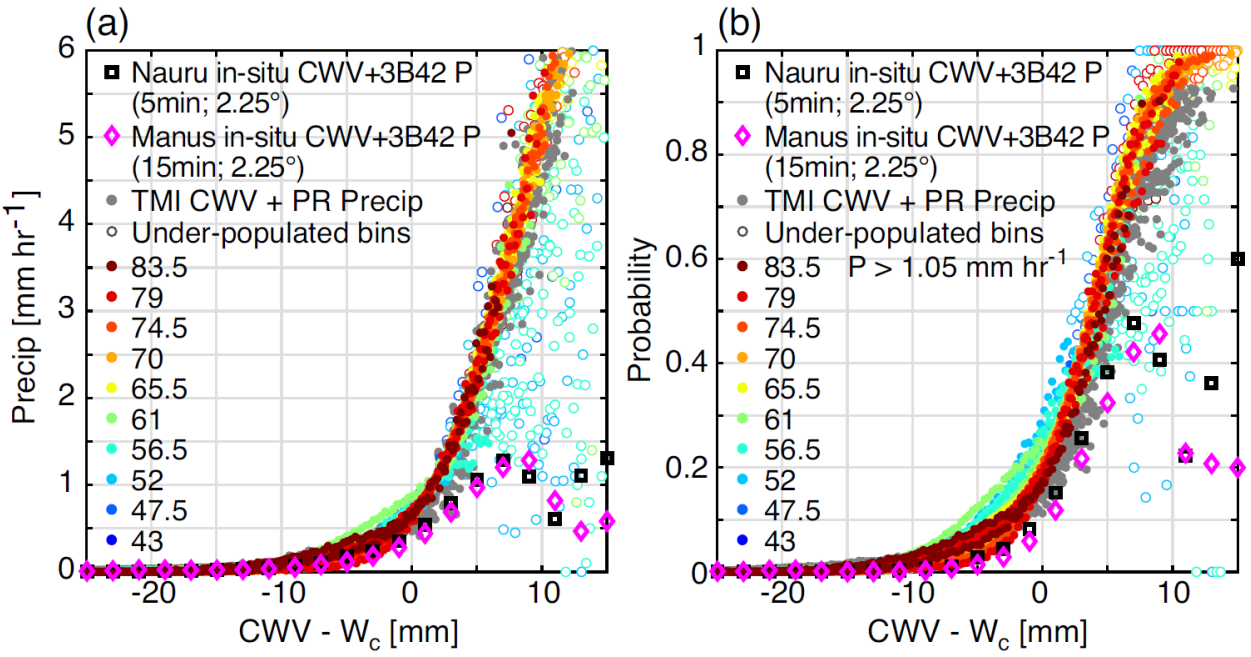

Figure 3.A.15: Similar to Fig. 3.3.3 of the main text but with the ground-based precipitation from the Manus and Nauru ARM sites replaced by the TRMM 3B42 precipitation averaged around the sites (2.25° × 2.25°). (Left) Collapsed conditional precipitation complied using different datasets, including (i) TMIv7.1 CWV and precipitation (colored dots) with underpopulated bins plotted as open circles, (ii) TMIv7.1 CWV and PR 2A25 precipitation (gray dots) excluding underpopulated bins, and (iii) ARM site CWV and 3B42 precipitation (2.25°-averaged) for Manus (diamonds) and Nauru (squares) Islands in the tropical western Pacific (WPac). Reanalysis-2 temperature is used for (i)-(iii). For (i) and (ii), bins from all four basins are plotted, with data at 0.25° resolution for 01 Jun 2002–31 May 2014 and coastal regions excluded. For (iii), the curves are shifted by the corresponding w_c given the temperature $\widehat{q_{sat}}$ or $\widehat{T}$) time series according the w_c-temperature relation for WPac. (Right) Same as in the left panel, but for conditional probability of precipitation defined by $P > 1.05$ mm h^{-1}.

precipitation at Manus and Nauru being replaced by 3B42 precipitation around the 2 islands (a 2.25° × 2.25°-average). Since the ground-based data and 3B42 have different temporal frequency/averaging, the necessary interpolation/matching has been performed. In Fig. 3.A.15, the low bias for the statistics for Manus and Nauru persists.

An additional combination of TMIv7.1 CWV and 3B42 precipitation gives results quantitatively similar to those shown in Figs. 3.3.1-3.3.3, except for the slope of the precipitation

pickup is slightly smaller (not shown), with no signs the low bias for the highest CWV bins. Given this, and the low bias for Manus and Nauru in Figs. 3.3.3 and 3.A.15, we conclude that this bias must be caused by the ground-based CWV measurements, and very likely, the "wet-window" problem. Specifically, high CWV events (relative to critical) with strong precipitation are missing from the CWV timeseries, and the gap-filling, through interpolation, assigns to these events CWV values lower than that happened, while high CWV events associated with weak/no precipitation are not affected as much, resulting in the low bias for the highest $cwv - w_c$ bins. The results here further suggest (i) the adopted gap-filling for ground-based CWV time series cannot satisfactorily restore the missing information; (ii) for $cwv - w_c > 5$ mm, the CWV data is no longer trustworthy, and (iii) the temperature dependence of critical must be considered in determining this trustworthiness.

CHAPTER 4

Convective transition statistics over tropical oceans for climate model diagnostics: GCM evaluation

Abstract

To assess deep-convective parameterizations in a variety of GCMs and examine the fast-timescale convective transition, a set of statistics characterizing the pickup of precipitation as a function of column water vapor (CWV), PDFs and joint-PDFs of CWV and precipitation, and the dependence of the moisture-precipitation relation on tropospheric temperature is evaluated using the hourly output of two versions of GFDL AM4, NCAR CAM5 and superparameterized CAM (SPCAM). The 6-hourly output from the MJOTF/GEWEX Atmospheric System Study (GASS) project is also analyzed. Contrasting statistics produced from individual models that primarily differ in representations of moist convection suggest that convective transition statistics can substantially distinguish differences in convective representation and its interaction with the large-scale flow, while models that differ only in spatial-temporal resolution, microphysics, or ocean-atmosphere coupling result in similar statistics. Most of the models simulate some version of the observed sharp increase in precipitation as CWV exceeds a critical value, as well as that convective onset occurs at higher CWV but at lower column RH as temperature increases. While some models quantitatively capture these observed features and associated probability distributions, considerable inter-model spread and departures from observations in various aspects of the precipitation-CWV relationship are noted. For instance, in many of the models, the transition from the low-CWV, non-precipitating regime to the moist regime for CWV around and above critical

is less abrupt than in observations. Additionally, some models overproduce drizzle at low CWV, and some require CWV higher than observed for strong precipitation. For many of the models, it is particularly challenging to simulate the probability distributions of CWV at high temperature.

4.1 Introduction

Simulating deep convection in GCMs has been a longstanding challenge despite progress in computer power and model complexity. The tropical precipitation simulated by GCMs is often at odds with the observed and targeted studies have identified limitations of simulated convection as a likely contributor to major biases in climatology and large-scale modes of tropical variability—e.g. the MJO (Del Genio et al. 2012, Zhu and Hendon 2015, Jiang 2017), the diurnal cycle of precipitation (Del Genio and Wu 2010, Rio et al. 2009, Hourdin et al. 2013, Covey et al. 2016), and the double ITCZ (Mapes and Neale 2011, Hwang and Frierson 2013, Oueslati and Bellon 2013, Hirota et al. 2014). Tropical precipitation also exhibits great intermodel spread in the context of future change projection (Biasutti and Sobel 2009, Biasutti 2013, Voigt et al. 2016, Su et al. 2017, Maloney et al. 2019a). As a result, model diagnostic efforts targeting deep convection are central to several model improvement efforts across scales. Recent approaches seek process-oriented diagnostics that target improvements to physical parameterizations by investigating coordinated statistics for relationships among variables aimed at giving insight into underlying processes (Eyring et al. 2019, Maloney et al. 2019b). Such efforts include, for example, diagnostics for Moist Static Energy (MSE) variance budget analysis (Wing and Emanuel 2014), MJO propagation (Kim et al. 2014, Gonzalez and Jiang 2017), MJO midlatitude teleconnection (Henderson et al. 2017), ENSO-related SST anomalies for seasonal to interannual predictability (Annamalai et al. 2014), warm rain processes (Suzuki et al. 2015), and tropical cyclone simulations (Kim et al. 2018).

Here we focus on convective transition statistics that serve as model diagnostics for the

parameterization of deep convection (Peters and Neelin 2006, Neelin et al. 2009; Kuo et al. 2018, content included in chapter 3). These statistics characterize the PDFs of CWV for precipitating points, the pickup of precipitation as a function of CWV, and the dependence of the moisture-precipitation relation on tropospheric temperature. The moisture-precipitation relation is representative of the relation between observed deep convection and the buoyancy available for deep convection (Holloway and Neelin 2009, Schiro et al. 2016, Ahmed and Neelin 2018), applying to both mesoscale-organized and smaller-scale convection (Schiro et al. 2018, 2019). The relationship to convective instability has been examined in a single GCM (Sahany et al. 2012, 2014, Kuo et al. 2017). Here we systematically evaluate the performance of multiple GCMs in simulating key features of tropical precipitation and deep convection with such diagnostics.

Chapter 3 has detailed observational aspects of the convective transition statistics over tropical oceans using satellite retrievals and ground-based measurements, providing a baseline. Here, the same set of statistics are compiled for 3 sets of high-frequency (hourly and 6-hourly) GCM output and compared to observations to address a fundamental question: whether these statistics can target specific processes and differentiate the relevant parameterization schemes adopted by each GCM, namely deep-convective parameterizations. The first set consists of hourly output from a pair of uncoupled GFDL AM4 and AM4 modified to include multiple deep plumes. The second set, also hourly output, is from the uncoupled NCAR CAM5.3 and the superparameterized CAM (SPCAM), which share the same dynamic core but differ in representations of moist convection. These 2 pairs of model comparison demonstrate that the convective transition statistics can reveal model characteristics directly relevant to the moist-convective representations in contrast to the conventional diagnostic metrics based on long-term climatology and variability. The third set consists of 6-hourly output from a subset of models participating in the MJO Task Force/GEWEX Atmospheric System Study (GASS) multimodel comparison project on the Madden-Julian Oscillation (hereafter MJOTF/GASS; Petch et al. 2011, Jiang et al. 2015), which further enables us

to perform similar assessment but for a selection (16 models/configurations) of mainstream GCMs.

This chapter is organized as follows. Section 4.2 describes the observational and model data. Section 4.3 briefly summarizes the observational aspects of the basic convective transition statistics, with the corresponding model comparisons in section 4.4. The joint PDFs of CWV and precipitation, and the derived statistics, are presented in section 4.5. Summary and conclusions are given in section 4.6.

4.2 Data and model descriptions

4.2.1 Observational datasets

Compiling the desired statistics requires the column-integrated water vapor (CWV), precipitation rate P, and 1000-200 hPa column-integrated saturation humidity $\widehat{q_{sat}} \equiv \int q_{sat}[T(p),p]dp/g$ $\{q_{sat}[T(p),p]$ is the saturation specific humidity with respect to liquid water$\}$. Here, $\widehat{q_{sat}}$ is used as the bulk measure of tropospheric temperature (see chapter 3 for comparison to vertically-averaged tropospheric temperature).

To be consistent with previous studies, the 6-hourly 2.5° NCEP-DOE Reanalysis-2 temperature (Kanamitsu et al. 2002) is adopted for calculating $\widehat{q_{sat}}$ with interpolation as needed. Newer reanalysis products (e.g., ERA-Interim) give similar results (not shown). Our primary source of CWV and P is the TRMM Microwave Imager (TMI) retrievals processed by Remote Sensing Systems (version 7.1; TMIv7.1 hereafter; Wentz et al. 2015) for the period of 1 June 2002 through 31 May 2014. The TMIv7.1 data contains gridded (0.25°) snapshots of CWV and P (at 0.3-mm and 0.1-mm h^{-1} increments, respectively) over ocean. The CWV is capped at 75 mm and often records missing values in the presence of heavy precipitation (with increasing probability of missing values starting around $P = 2$ mm h^{-1} and recording almost nothing above 9 mm h^{-1}). We gap-fill the missing values using the available values at the nearest pixel to restore substantial coverage, but one should not overlook the uncertainty

associated with the CWV counts at high P (see chapter 3 for sensitivity to gap-filling). The TMIv7.1 P exhibits a spurious cutoff around 10 mm h^{-1}. Thus, for studying the PDFs of P, the TRMM Precipitation Radar (PR) 2A25 (v7; TRMM 2011a) Rainfall Rate containing snapshots of P at $\sim$5 km resolution is utilized. At its native resolution, the lowest value the PR can distinguish is $\sim$0.11 mm h^{-1}.

4.2.2 Model descriptions

Part of the model data analyzed here are from the Timeslice Experiments performed by the NOAA MAPP Model Diagnostic Task Force (Maloney et al. 2019b), which include 2-year-long high-frequency output under the AMIP settings. The relevant data consists of hourly snapshots of temperature and humidity, for calculating $\widehat{q_{sat}}$ and CWV, and hourly average precipitation. The available models include uncoupled $\sim$1° GFDL AM4 (Zhao et al. 2018a,b, AM4G9 hereafter), and AM4 modified to include multiple deep plumes and convective mesoscale circulations (Donner et al. 2011, AM4B6), and the uncoupled $\sim$1° NCAR CAM5.3 (Neale et al. 2012). The two AM4 configurations, running through 2009-2010, primarily differ in the convective parameterizations—double-plume convective scheme (Zhao et al. 2009) for AM4G9 vs Donner convective scheme (Donner 1993) for AM4B6—with associated tuning differences, but otherwise share most model components.

The CAM5.3, running through 1990-1991, uses the Zhang-McFarlane deep-convective parameterization Zhang and McFarlane (1995) as updated by Neale et al. (2008) and Richter and Rasch (2008). For comparison, our analysis also includes another set of 10-year-long hourly output from the uncoupled $\sim$2° superparameterized CAM (SPCAM; the atmospheric component of the SP-CESM, version 1.1.1; prescribed monthly mean SST over 1982-2001), in which the moist-convective processes are explicitly simulated by a 2D cloud-resolving model (Khairoutdinov and Randall 2003) instead of being parameterized. The SPCAM is run with the CAM4 physics. CAM5 (and CAM5.3) differs from CAM4 primarily in updated parameterization schemes and incorporating aerosol-cloud interactions, leaving most of the

dynamic components unchanged. Thus, one major difference between the SPCAM and CAM5.3 lies in the representations of moist convection, which is expected to be the key difference for the statistics analyzed here.

	Model Name	Institute	Resolution (lon×lat), Vertical Levels	References
1	AM4G9	*Geophysical Fluid Dynamics Laboratory, NOAA*	1.25° × 1°, L32	*Zhao et al., 2018a, 2018b*
2	AM4B6		1.25° × 1°, L48	*Zhao et al., 2018a, 2018b*
3	CAM5.3	*National Center for Atmospheric Research*	1.25° × 0.9°, L30	*Neale et al., 2012*
4	SPCAM	*Colorado State University*	GCM: 2.5° × 1.9°, L26 CRM: 4km × 32 col., L24	*see note*[a]
5	CAM5	*National Center for Atmospheric Research*	1.25° x 0.9°, L30	*Neale et al., 2012*
6	CAM5-ZM	*Lawrence Livermore National Laboratory*	1.25° x 0.9°, L30	*Song and Zhang, 2011*
7	CNRM-AM	*Centre National de la Recherche Scientifique / Météo-France*	T127 (1.4°), L31	*Voldoire et al., 2013*
8	CNRM-CM			
9	CNRM-ACM			
10	ECEarth3	*Rossby Center, Swedish Meteorological and Hydrological Institute*	T255 (80km), L91	*see note*[b]
11	BCC-AGCM2.1	*Beijing Climate Center, China Meteorological Administration*	T42 (2.8°), L 26	*Wu et al., 2010*
12	CanCM4	*Canadian Centre for Climate Modelling and Analysis*	2.8°, L35	*Merryfield et al., 2013*
13	NavGEM1	*US Naval Research Laboratory*	T359 (37km), L42	*see note*[c]
14	MRI-AGCM3	*Meteorological Research Institute, Japan*	T159, L48	*Yukimoto et al., 2012*
15	MIROC5	*AORI / NIES / JAMSREC, Japan*	T85 (1.5°), L40	*Watanabe et al., 2010*
16	GISS-E2	*Goddard Institute for Space Studies, NASA*	2.5° × 2.0°, L40	*Schmidt et al., 2014*
17	GEOS5	*Global Modeling and Assimilation Office, NASA*	0.625° × 0.5°, L72	*Molod et al., 2012*
18	CWB-GFS	*Central Weather Bureau, Taiwan*	T119 (1°), L40	*Liou et al., 1997*
19	FGOALS-s2	*Institute of Atmospheric Physics, Chinese Academy of Sciences*	R42 (2.8° ×1.6°), L26	*Bao et al., 2013*
20	ISUGCM	*Iowa State University*	T42 (2.8°), L18	*Wu and Deng, 2013*

[a]Here the SPCAM is the atmospheric component of the superparameterized Community Earth System Model (SP-CESM), version 1.1.1, in which the embedded cloud-resolving model (CRM) is the System for Atmospheric Modeling (SAM; Khairoutdinov and Randall 2003). For more regarding the SPCAM configuration for the examined simulation, see Kuo et al. (2019).

[b]Hazeleger et al. (2012) describes an earlier version of the EC-EARTH model, while here we have used a newer version based on ECMWF's IFS model cy36r4. The main differences between these model versions are an improved radiation scheme (Morcrette et al., 2008) and a new cloud microphysics (Forbes et al., 2011).

[c]The NAVGEM version 1.0 model used here, for which there is no published reference, differs from NAVGEM 1.1 (Hogan et al., 2014) in that it lacks prognostic cloud water and that it uses the radiation scheme of Harshvardhan et al. (1987).

Table 4.2.1: Analyzed models with resolutions and references. Simulations 1-3 are provided by the NOAA MAPP MDTF Timeslice Experiments. Simulations 1-4 output hourly data. Simulations 5-20 are provided by the 20 year climate simulation component of the MJOTF/GASS Global Model Comparison Project, with 6-hourly data regridded to 2.5° × 2.5° resolution. The descriptions of the MJOTF/GASS models follow (Jiang et al. 2015, Table 1).

To survey the convective transition in a variety of models, we also analyze the 6-hourly output of 16 models/configurations participating in the MJOTF/GASS Global Model Comparison Project, the 20 year climate simulation component. Here, the precipitation is 6-

hourly average, and all the data have been regridded to 2.5° × 2.5° resolution prior to our analysis (Jiang et al. 2015). This MJOTF/GASS ensemble further provides an opportunity for two case studies of the sensitivity of the convective transition statistics on (a) time-averaging and convective-cloud microphysics through two additional CAM5 instances (referred to as CAM5 and CAM5-ZM), and on (b) coupling/forcing configurations through three CNRM instances (CNRM-AM, CNRM-CM, and CNRM-ACM; section 4.4.2.3).

See Table 4.2.1 and reference therein for details regarding the examined models.

4.3 A summary of the observational aspects of convective transition statistics over tropical oceans

In this section, we briefly summarize the observed characteristics of convective transition over tropical oceans synthesized by chapter 3.

Figures 4.3.1a-4.3.1d show the basic statistics compiled using the TMIv7.1 data and Reanalysis-2 temperature at 1° resolution, including the conditionally-averaged precipitation rate (conditional precipitation hereafter; calculated by including all events; Fig. 4.3.1a), conditional probability of precipitation ($P > 0.25$ mm h^{-1}; Fig. 4.3.1b), PDFs of CWV for all events (Fig. 4.3.1c) and for precipitating events (Fig. 4.3.1d), all as a function of CWV and $\widehat{q_{sat}}$ for the tropical western Pacific (WPac; 20°S-20°N, west of 180°). Here, $\widehat{q_{sat}}$ is used as a proxy for the bulk tropospheric temperature. The PDFs in Fig. 4.3.1c together represent the normalized joint distribution of CWV and $\widehat{q_{sat}}$, reflecting the CWV-$\widehat{q_{sat}}$ climatology in this basin. Multiplying these PDFs by the corresponding conditional probabilities in Fig. 1b leads to the PDFs for precipitating events in Fig. 4.3.1d.

The conditional precipitation and probability (Figs. 4.3.1a and 4.3.1b) sharply increase as CWV exceeds a certain threshold known as the critical CWV w_c (defined through Fig. 4.3.1e later). w_c increases with $\widehat{q_{sat}}$. For low $\widehat{q_{sat}}$ bins, the PDFs of CWV in Fig. 4.3.1c exhibit a characteristic shape, i.e., a peak at low CWV below which the PDF drops sharply, and above

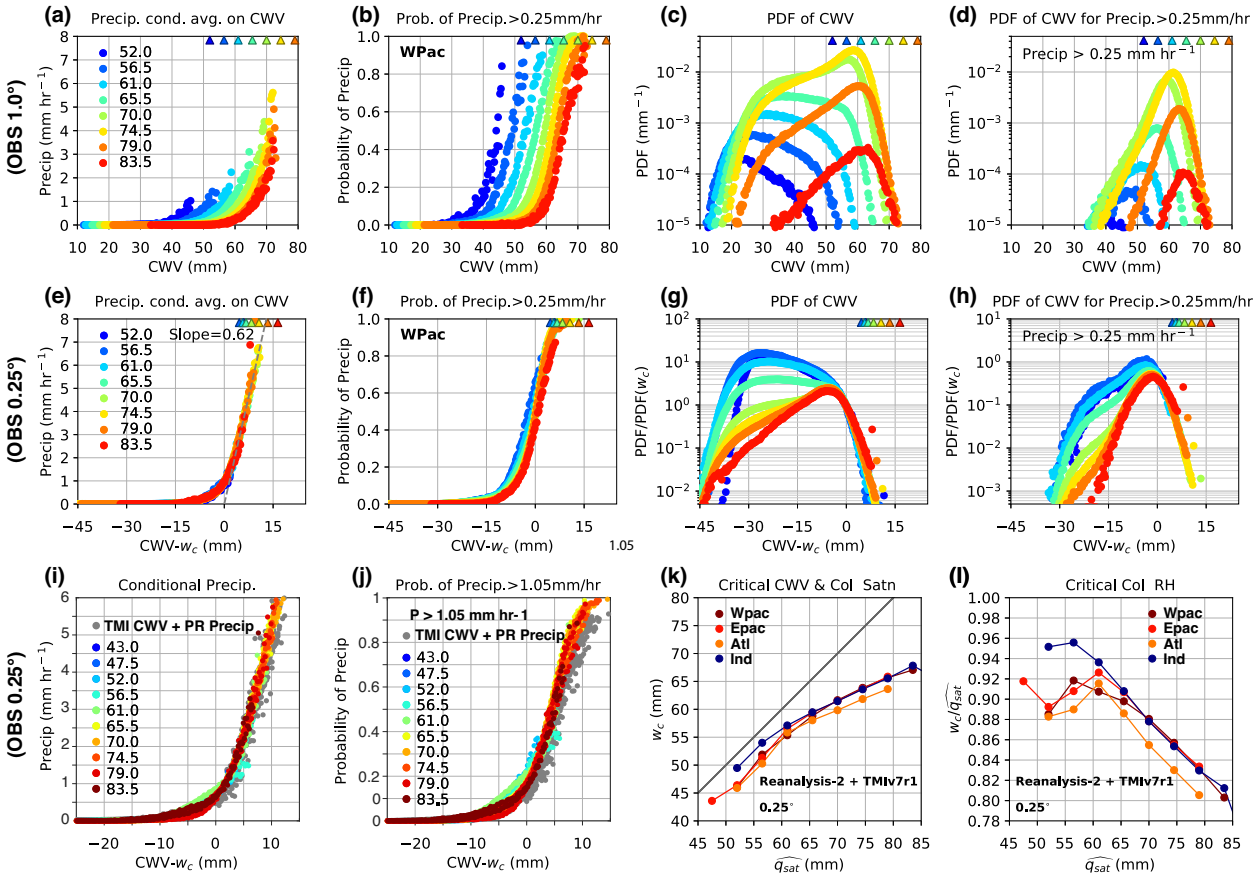

Figure 4.3.1: Conditionally averaged precipitation rate (a), conditional probability of precipitation (b), PDFs of all events (c), and PDFs for precipitating events as a function of CWV and $\widehat{q_{sat}}$ (colors; units: mm) (d) for the tropical western Pacific (20°S-20°N, west of 180°). In (a)-(d), results are using TMIv7.1 precipitation rate and CWV and Reanalysis-2 temperature compiled at 1° (colored markers). Triangles represent corresponding $\widehat{q_{sat}}$ values, which indicate where the column is approximately saturated, and underpopulated bins (PDF $< 10^{-5}$) are omitted. (e)-(h) Same statistics as in (a)-(d) but at 0.25° to include more events, and with the statistics collapsed by shifting CWV for each $\widehat{q_{sat}}$ by the corresponding critical CWV w_c from (k), and with the PDFs scaled by values at w_c. (i) Collapsed conditionally averaged precipitation rate at 0.25° as in (e) but with data from three additional tropical (20°S-20°N) ocean basins (colored dots) and with TMIv7.1 precipitation rate replaced by PR 2A25 precipitation rate (gray dots). (j) Same as in (i) but for conditional probability of precipitation [$P > 1.05$ mm h^{-1}; different from the 0.25-mm h^{-1} threshold for (b) and (f)]. (k) Critical CWV w_c as a function of $\widehat{q_{sat}}$ for the four tropical ocean basins, with the gray line indicating the $\widehat{q_{sat}}$ value where the column is approximately saturated. (l) Critical column RH defined as $w_c/\widehat{q_{sat}}$. In (k)-(l), the values of w_c are calculated by fitting the conditionally averaged precipitation rate in the range 3-5 mm h^{-1} using TMIv7.1 data and Reanalysis-2 temperature compiled at 0.25°.

which the PDF decreases slowly until reaching a cutoff around critical. As $\widehat{q_{sat}}$ increases, another peak develops at high CWV around critical with the low-CWV peak diminishing. Neelin et al. (2009) has noted that low-CWV/high-CWV events tend to occur over ocean with colder/warmer SST, which is closely related to the locations of the descending/ascending branches of the general circulation. Stechmann and Neelin (2011, 2014) have also demonstrated through a stochastic framework that the CWV PDFs are sensitive to processes like surface evaporation, precipitation, and moisture convergence. These observations suggest that the CWV PDFs are determined by the large-scale flow interacting with convective physics.

In chapter 3, we noted that, because of the large spatial autocorrelation scales of temperature and CWV compared with that of precipitation, the conditional precipitation (Fig. 4.3.1a) and CWV PDF (Fig. 4.3.1c) are insensitive to the spatial resolution at which the statistics are compiled, while the conditional probability (Fig. 4.3.1b) and PDF of precipitating events (Fig. 4.3.1d) are more sensitive. It thus makes sense to define w_c through conditional precipitation alone so that it provides a resolution-independent metric. Following chapter 3, we define w_c as the CWV value at which a linear fit for conditional precipitation (in the range 3-5 mm h^{-1}) intersects with the CWV axis. This is depicted in Fig. 4.3.1e, which shows the conditional precipitation as in Fig. 4.3.1a, but for 0.25° resolution and is collapsed by shifting CWV by w_c for each $\widehat{q_{sat}}$. Here, the resolution 0.25° is chosen instead of 1° to include more events, making the fitting numerically stable. The collapsed conditional probability and re-scaled CWV PDFs corresponding to those in Figs. 4.3.1b-4.3.1d are shown in Figs. 4.3.1f-4.3.1h, and the values of w_c and critical column RH $w_c/\widehat{q_{sat}}$ in Figs. 4.3.1k-4.3.1l.

From Figs. 4.3.1k-4.3.1l, the slopes of w_c and $w_c/\widehat{q_{sat}}$ exhibit a clear transition around $\widehat{q_{sat}} = 61$ mm separating tropical convection from events originating from extratropics (indicated by the geographical distribution of $\widehat{q_{sat}}$; low-$\widehat{q_{sat}}$ occurrence mostly along the edge of tropics, sometimes reaching the equator in the central-eastern Pacific; see chapter 3, Fig. 3.A.13). As $\widehat{q_{sat}}$ exceeds around 61 mm, w_c increases but $w_c/\widehat{q_{sat}}$ decreases, i.e., convec-

tive onset occurs at higher CWV but at lower column RH. This w_c–$\widehat{q_{sat}}$ relation completely characterizes the dependence of precipitation pickup on tropospheric temperature in the sense that the conditional precipitation and probability (Figs. 4.3.1e and 4.3.1f) collapse well without exhibiting additional temperature dependence. For $\widehat{q_{sat}}$ bins $\geq$ 70 mm, the PDFs for precipitating events (Fig. 4.3.1h) peak right below critical with a common near-Gaussian core, i.e., precipitation mostly occurs within a characteristic (and relatively narrow) CWV range around critical. Also, there are more precipitating events below critical for lower $\widehat{q_{sat}} \leq 65.6$ mm, consistent with the slightly higher probability in Fig. 4.3.1f.

The conditional precipitation and probability in Figs. 4.3.1e and 4.3.1f are reproduced in Figs. 4.3.1i and 4.3.1j together with the results from the other tropical ocean basins (20°S-20°N; colored markers). Here, the statistics from all 4 basins collapse, and are thus indistinguishable. The corresponding values calculated using the PR (2A25) precipitation are also shown (gray dots). Note that Fig. 4.3.1j uses a 1.05-mm h^{-1} threshold. The PR and TMI precipitation yield consistent statistics despite that the two instruments slightly differ in sensitivity to low precipitation < 1.05 mm h^{-1}. For $\widehat{q_{sat}}$ above the transition ($\sim$61 mm), the pickup of conditional precipitation and probability shows little variation across the $\widehat{q_{sat}}$ range and ocean basins (Figs. 4.3.1i and 4.3.1j), and so do the critical values (Figs. 4.3.1k and 4.3.1l). For $\widehat{q_{sat}}$ below the transition, on the other hand, precipitation exhibits a gentler pickup, and the critical values scatter over a wider range. Although not shown here, the qualitative features of the CWV PDFs (for all events and precipitating events) for WPac noted above also apply to other ocean basins.

It is worth noting that the CWV PDFs vary considerably across basins and seasons (not shown), reflecting differences in the CWV–$\widehat{q_{sat}}$ climatology. However, there is not a clear interannual variability (e.g., ENSO vs non-ENSO years). The conditional precipitation, probability, and the critical values, on the other hand, are robust and exhibit little variation.

We caution the readers to interpret Fig. 4.3.1 carefully, especially for results at the highest CWV. The TMIv7.1 CWV retrievals are capped at 75 mm and often contain missing values in

the presence of heavy precipitation ($P > 2$ mm h^{-1}). Here, we adopt the gap-filling method tested in chapter 3 prior to compiling the statistics. The gap-filling partially restores the missing information but inevitably leads to uncertainty, e.g., in the distribution of CWV above critical for highest $\widehat{q_{sat}}$ bins.

The tropical ARM site data had also been examined to quantify the dependence of convective transition on temporal averaging (not shown). Based on the analysis of satellite retrievals and ground-based measurements in chapter 3, the conditional probability of precipitation defined through a reasonable threshold (e.g., $P > 0.25$ mm h^{-1}) would shift towards lower CWV for (1) lower spatial resolution, (2) longer temporal averaging, or (3) lower precipitation threshold, with the shift being less than 10 mm for spatial resolution changing from 0.25° to 2° and/or temporal resolution from snapshot to 6-hourly averaging. This dependence on resolution would not hold for an extreme precipitation threshold (e.g., $P > 10$ mm h^{-1}). In contrast, the conditional precipitation and CWV PDF are insensitive to spatial averaging and less sensitive to temporal averaging.

For more information regarding observed convective transition, see chapter 3. Below we summarize key aspects of the basic statistics. In the next section, we will examine the performance of the chosen models with these in mind:

a. The conditional precipitation and probability sharply increase as CWV exceeds the critical CWV w_c.

b. As the bulk tropospheric temperature $\widehat{q_{sat}}$ increases, w_c increases, but the critical column RH $w_c/\widehat{q_{sat}}$ decreases.

c. The critical values exhibit little variation across ocean basins.

d. The conditional precipitation and probability can be collapsed by shifting the CWV by w_c.

e. The collapsed conditional precipitation and probability exhibit little variation across the $\widehat{q_{sat}}$ range and ocean basins.

f. The CWV PDF exhibits a characteristic shape (the low- vs high-CWV peak) which depends on $\widehat{q_{sat}}$.

g. For CWV above critical, the CWV PDF drops rapidly for all $\widehat{q_{sat}}$. *This part of the PDF can be collapsed by shifting the CWV and re-scaling the PDF.*

h. The PDF of CWV for precipitating events, for the most common $\widehat{q_{sat}}$ *bins over tropical oceans, can be collapsed and shares a common near-Gaussian core.*

4.4 Simulated convective transition statistics in GCMs

4.4.1 Convective transition statistics distinguishing convective parameterizations

To assess whether the convective transition statistics can apply as a diagnostic tool targeting convective processes and distinguish the realism of convective parameterizations adopted by models, in this subsection, we examine the basic statistics compiled using the hourly data from two pairs of GCMs. The configurations/models within each pair differ primarily in their representations of moist convection, which is expected to be the key difference for the examined statistics analyzed here.

The first pair of GCMs consists of two $\sim 1^{\circ}$ configurations of the latest global model AM4 (Zhao et al. 2018a,b) developed by the GFDL that are equipped with different convective schemes, namely the AM4G9 with the double-plume convective scheme (Zhao et al. 2009), and the AM4B6 with the Donner convective scheme (Donner 1993).

The second pair is based on the CAM developed by the NCAR, namely the CAM5.3 ($\sim 1^{\circ}$; Neale et al. 2012) with the default Zhang-McFarlane convective parameterization (Zhang and McFarlane 1995), and the SPCAM ($\sim 2^{\circ}$) with a 2D CRM for simulating moist convection (Khairoutdinov and Randall 2003). Both models share the same dynamic core. Like the observed statistics in Fig. 4.3.1, Figs. 4.4.1-4.4.4 show the same sets simulated in the models

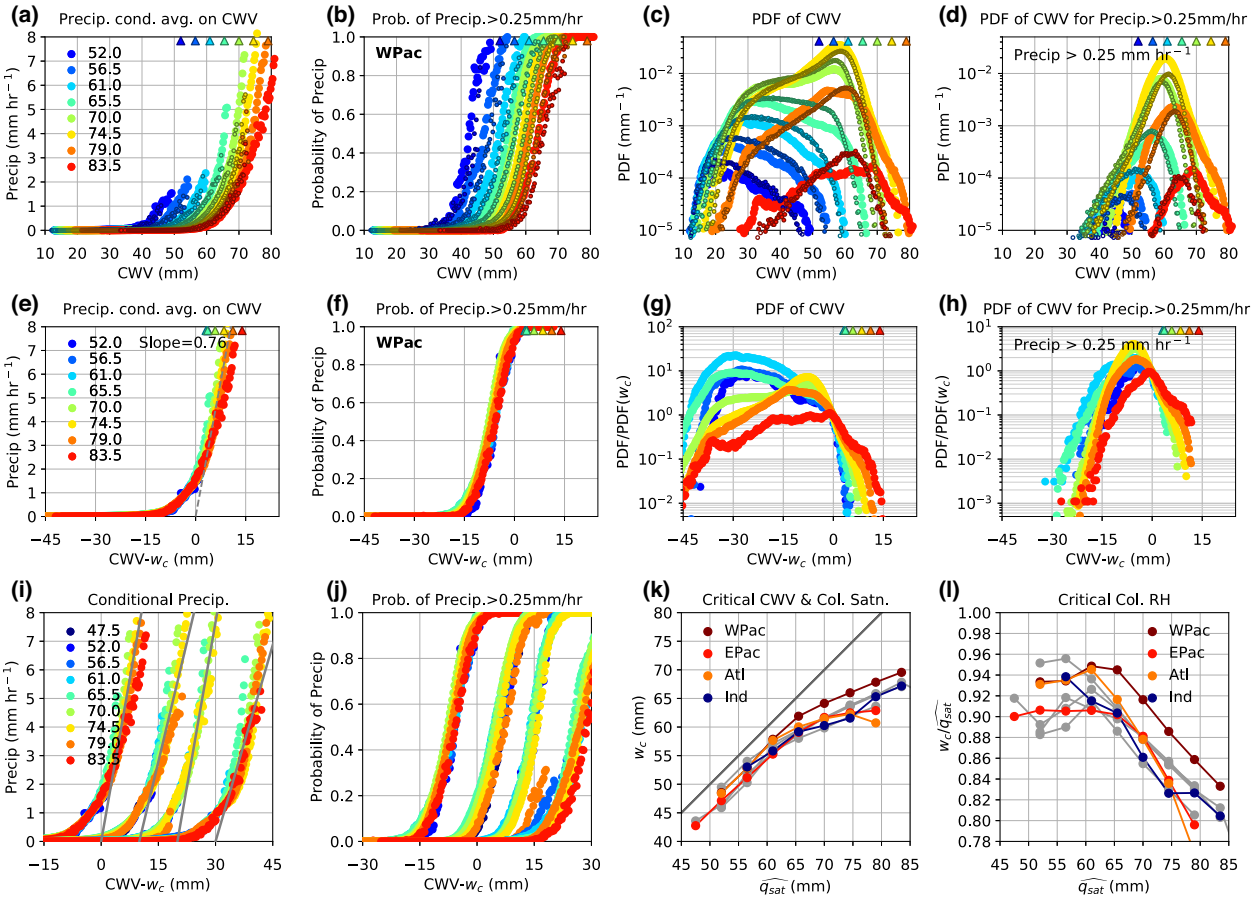

Figure 4.4.1: Same as in Fig. 4.3.1 but compiled using the AM4G9 model output (∼1°, hourly). Statistics in Figs. 4.3.1a-4.3.1d are reproduced as smaller markers in (a)-(d) here for visual reference, and critical values in Figs. 4.3.1k-4.3.1l reproduced in (k)-(l) as gray makers. In (i)-(j), statistics from the four tropical ocean basins are shifted with 10-mm increments for ease in viewing.

listed above. The observed statistics in Figs. 4.3.1a-4.3.1d are reproduced as small markers for visual reference in Figs. 4.4.1a-4.4.1d; the simulated statistics in Figs. 4.4.1i and 4.4.1j are shifted for ease in viewing [with 10-mm increments; from left to right: tropical western (WPac) and eastern Pacific (EPac), Atlantic (Atl) and Indian Ocean (Ind)]; the observed critical values in Figs. 4.3.1k and 4.3.1l are reproduced in gray in Figs. 4.4.1k and 4.4.1l; same for the corresponding panels in Figs. 4.4.2-4.4.4. We note in Fig. 4.4.4 (SPCAM), because of lower precipitation rates, the range of the linear fit in Figs. 4.4.4e and 4.4.4i had to be reduced to 1.5-2.5 mm h^{-1} (as opposed to 3-5 mm h^{-1} for observations and other models).

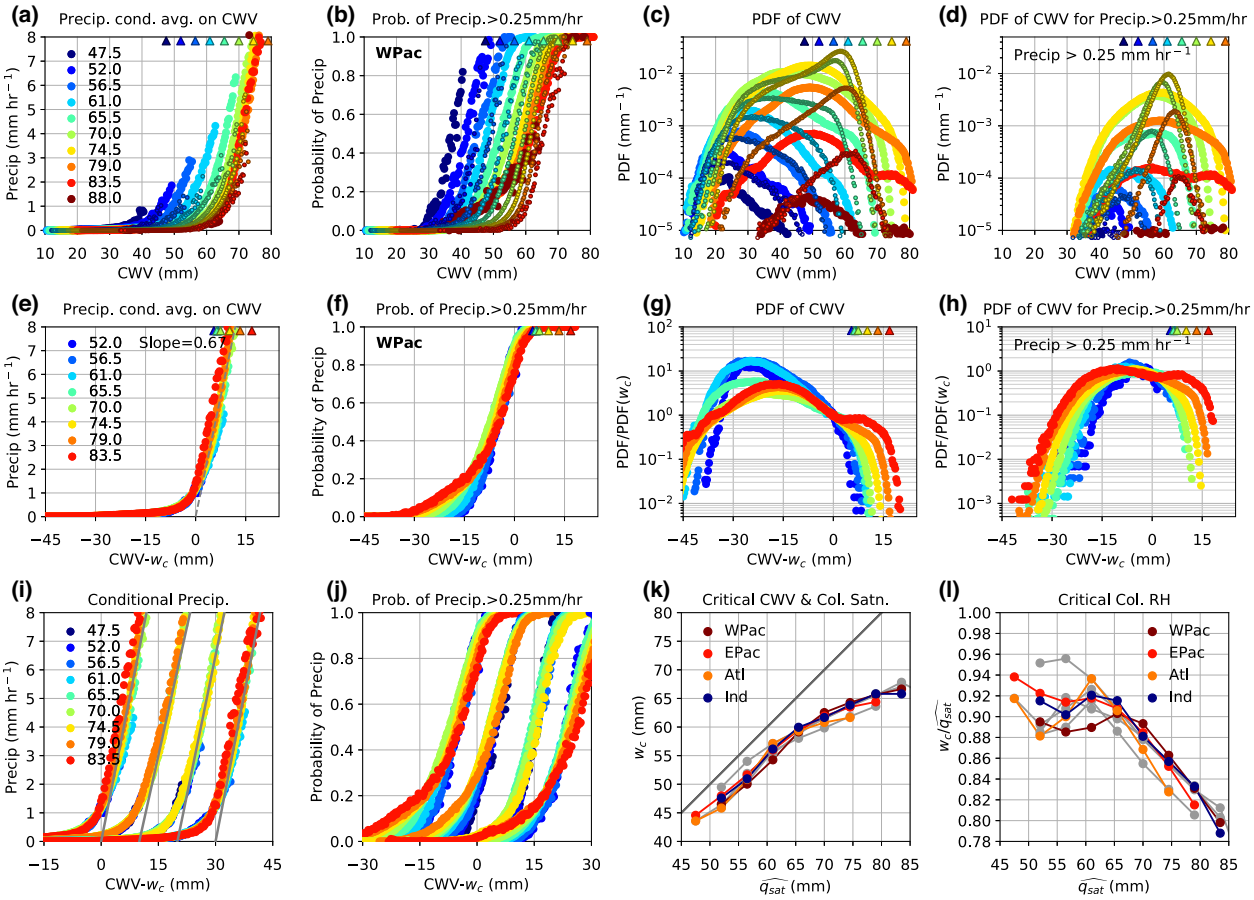

Figure 4.4.2: Same as in Fig. 4.4.1 but compiled using the AM4B6 model output (∼1°, hourly).

All 4 models capture the observed pickup of precipitation and probability; they also capture the observed dependence of the critical CWV and critical column RH as a function of $\widehat{q_{sat}}$ (Figs. 4.4.1-4.4.4k,l). However, the simulated conditional probability (Figs.4.4.1-4.4.4b,f,j) shows departures from observations to varying extents, reflecting the disagreement in the joint distribution of CWV and precipitation rate P (discussed later in section 4.5). The collapsed version of the simulated statistics in panels e-j also demonstrate that the w_c–$\widehat{q_{sat}}$ relation does not completely characterize the temperature dependence in these models, e.g., the slope of the best-fit to the conditional precipitation and the conditional probability show sensitivity to $\widehat{q_{sat}}$ (Figs. 4.4.1-4.4.4e,f,i,j); Additionally, the CWV PDFs for high $\widehat{q_{sat}}$ do not drop rapidly around critical (Figs. 4.4.1-4.4.4g,h), i.e., more above-critical events than

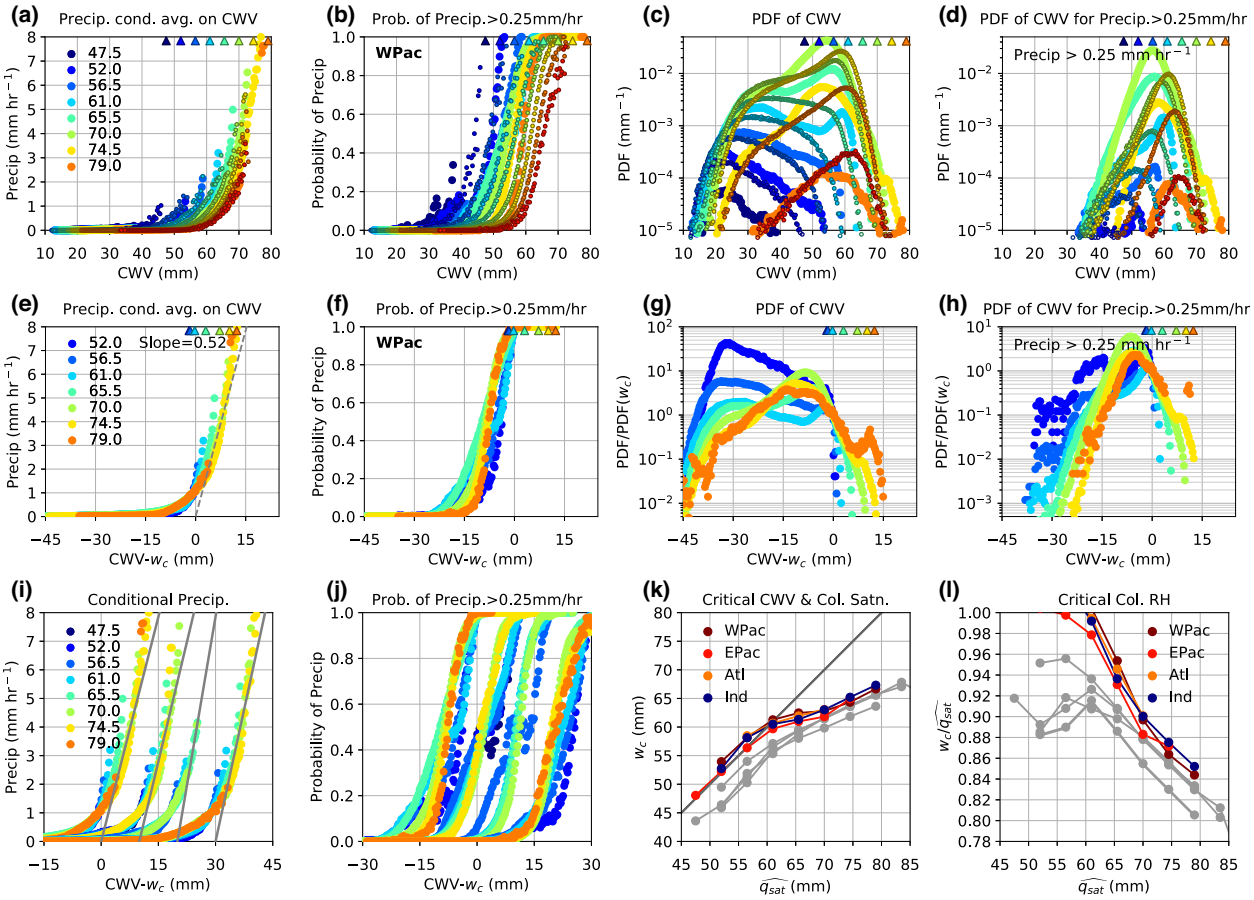

Figure 4.4.3: Same as in Fig. 4.4.1 but compiled using the CAM5.3 model output (∼1°, hourly).

observed, indicating a tendency of excessive moisture convergence or surface evaporation during precipitation in models. The following sections examine each model in greater detail.

4.4.1.1 AM4G9 (Double-plume convective scheme)

According to Fig. 4.4.1, the simulated conditional precipitation by AM4G9 quantitatively agrees with observations (Fig. 4.4.1a), with the slope of the best-fit being slightly higher than observed (Figs. 4.4.1e vs 4.3.1e) but still within the range of observational uncertainty (e.g., caused by CWV gap-filling). The slope also modestly varies with $\widehat{q_{sat}}$ (Fig. 4.4.1e) and across ocean basins (Fig. 4.4.1i). The simulated conditional probability has a steeper pickup occurring at slightly lower CWV (Fig. 4.4.1b). The simulated CWV PDF (Fig. 4.4.1c),

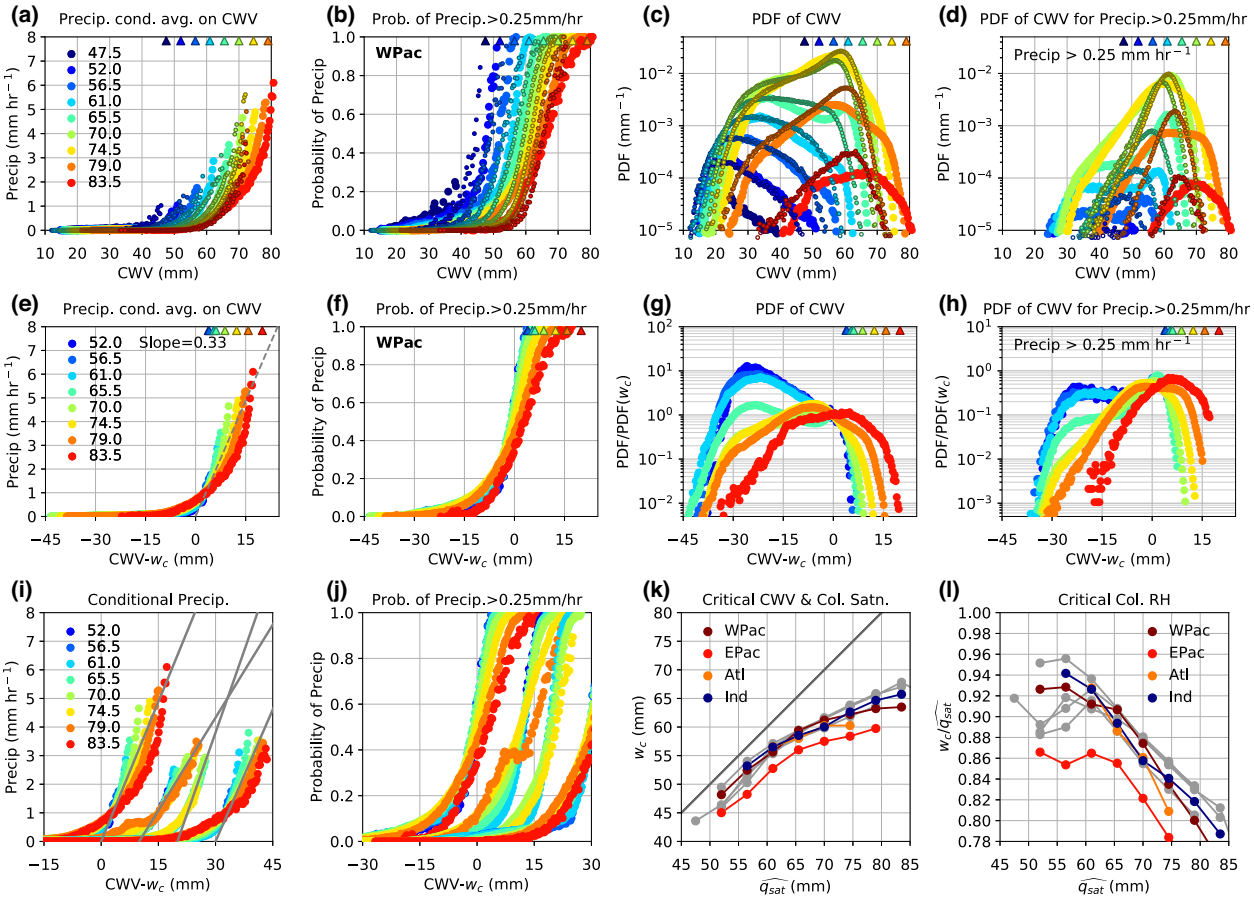

Figure 4.4.4: Same as in Fig. 4.4.1 but compiled using the SPCAM model output (∼2°, hourly). In (k)-(l), the values of w_c are calculated by fitting the conditionally averaged precipitation rate in the range 1.5-2.5 mm h^{-1}.

i.e., the joint PDF of CWV and $\widehat{q_{sat}}$, matches observations but also exhibits modestly more above-critical events for highest $\widehat{q_{sat}}$ bins (Fig. 4.4.1g). However, given the uncertainty in the CWV retrievals at high values, it is inconclusive at this time whether this mismatch in the PDF implies the model misbehaving. The simulated PDF for precipitating events shows that there are more below-critical precipitating events for low $\widehat{q_{sat}}$, resembling observations (Figs. 4.4.1h and 4.3.1h). The simulated critical values (Figs. 4.4.1k and 4.4.3l) exhibit a clear transition around $\widehat{q_{sat}} = 61$ mm and are consistent with observations, with slightly higher values for WPac.

4.4.1.2 AM4B6 (Donner convective scheme)

In Fig. 4.4.2, the simulated conditional precipitation by AM4B6 roughly matches observations for $\widehat{q_{sat}}$ bins ≥ 70 mm (Fig. 4.4.2a), with the best-fit slope slightly increasing with $\widehat{q_{sat}}$ (Fig. 4.4.2e). The simulated critical values (Figs. 4.4.2k and 4.4.2l) agree with observations and display a transition around $\widehat{q_{sat}} = 61$ mm. However, discrepancies exist in the simulated conditional probability and CWV PDFs. The collapsed conditional precipitation shows little variation across basins (Fig. 4.4.2i), but its pickup is gentler than observed (Fig. 4.4.2b) and exhibits dependence on $\widehat{q_{sat}}$ for CWV below critical (Fig. 4.4.2f), i.e., there are more below-critical precipitating events for high $\widehat{q_{sat}}$ compared to observations (Figs. 4.4.2h vs 4.3.1h). While the characteristic shape of the simulated PDFs of CWV (Fig. 4.4.2c) for low-$\widehat{q_{sat}}$ bins is consistent with observations, the high-CWV peak around critical fails to develop as $\widehat{q_{sat}}$ increases. Furthermore, the simulated CWV PDF extends into the above-critical range for highest $\widehat{q_{sat}}$ bins (Fig. 4.4.2g), implying the moisture convergence in warm, moist environments is stronger than suggested by observations.

An additional set of output from the 0.5° version of AM4B6 has also been analyzed, and the resulting statistics closely resemble those for 1° shown in Fig. 4.4.2, with minor quantitative differences (not shown). This is indicative that comparing models of different resolution may still be relevant for diagnosis of convective transition.

4.4.1.3 CAM5.3 (Zhang-McFarlane convective scheme)

In Fig. 4.4.3, the simulated conditional precipitation by this version of CAM5.3 picks up at higher CWV than observed (Fig. 4.4.3a), resulting in higher critical values (especially for lower $\widehat{q_{sat}}$ bins; Figs. 4.4.3k and 4.4.3l). The best-fit slope is slightly lower than observed (but still within the observational uncertainty) and exhibits weak dependence on $\widehat{q_{sat}}$ (Fig. 4.4.3e) with modest variation across basins (Fig. 4.4.3i). On the other hand, the simulated conditional probability picks up at lower CWV (Fig. 4.4.3b; $P > 0.25$ mm h^{-1}). The collapsed

conditional probability also exhibits dependence on $\widehat{q_{sat}}$ with slightly steeper pickup for higher $\widehat{q_{sat}}$ (Fig. 4.4.3f), and exhibits noticeable irregularities, i.e., non-monotonic in CWV for $\widehat{q_{sat}} = 47.5$ mm in EPac and for $\widehat{q_{sat}} = 56.5$ mm in Atl (Fig. 4.4.3j). The simulated CWV PDFs (Fig. 4.4.3c) reveal a cold bias in the model with 70-mm instead of 74.5 being the most probable $\widehat{q_{sat}}$ for WPac, and this cold bias also appears in other tropical ocean basins. The characteristic shape of the PDFs generally agrees with observations (Fig. 4.4.3c), but also exhibits more above-critical events for highest $\widehat{q_{sat}}$ bins, subject to the uncertainty of the CWV retrievals at high values (Fig. 4.4.3g; like Fig. 4.4.1g for AM4G9). In Fig. 4.4.3c, the CWV PDF for $\widehat{q_{sat}} = 61$ mm has two peaks, implying a bimodal distribution of SST (Neelin et al. 2009) instead of a smoother transition from cold to warm SST (or low-level divergence to convergence) suggested by observations.

4.4.1.4 SPCAM (Superparameterization using a 2D cloud-resolving model)

In Fig. 4.4.4, the simulated precipitation-CWV relationship by SPCAM is decent despite the lower resolution ($\sim 2^\circ$) for the host GCM grid (note the grid spacing of the 2D CRM is 4 km). The pickup of the simulated conditional precipitation and probability is less steep compared with observations (Figs. 4.4.4a and 4.4.4b) and exhibits a $\widehat{q_{sat}}$-dependence with gentler pickup for higher $\widehat{q_{sat}}$ (Figs. 4.4.4e and 4.4.4f). Note that in Fig. 4.4.4b, as CWV increases from below-critical, the simulated conditional probability for $\widehat{q_{sat}}$ bins ≤ 74.5 mm increases roughly linearly until reaching a probability of ~ 0.15, and then sharply increases with further CWV increment, exhibiting a 2-step pickup. The pickup also displays a great variation across basins (Figs. 4.4.4i and 4.4.4j), and irregular behavior of the simulated conditional probability can be noted for $\widehat{q_{sat}} = 79$ mm in EPac. On the other hand, the simulated critical values generally agree with observations, with lower values for EPac (Figs. 4.4.4k and 4.4.4l). For low $\widehat{q_{sat}}$ bins ≤ 61 mm, the simulated CWV PDFs are consistent with observations (Fig. 4.4.4c), with a bimodal PDF for $\widehat{q_{sat}} = 65.5$ mm (like Fig. 4c, 61-mm bin). For even higher $\widehat{q_{sat}}$ bins, the high-CWV peak around critical is less distinctive compared to observations, and the

PDF also extends into the above-critical regime (like Fig. 4.4.2g for AM4B6). The statistics presented in Fig. 4.4.4 are from an SPCAM simulation with prescribed SST. Another SPCAM run coupled with a slab ocean model (SOM; Bitz et al. 2012) leads to similar statistics with a slightly shifted joint PDF of CWV and $\widehat{q_{sat}}$, reflecting changes in the mean climate state (not shown). This is indicative that coupling with different model components (e.g., ocean model) does not alter the simulated convective transition which primarily depends on the representation of convective physics. This is also supported by a set of CNRM simulations discussed later in subsection 4.4.2.3. Also note that the statistics exhibit little sensitivity to doubling the CRM domain size (4 km $\times$ 64 column vs 32 column) to permit more organized convective events (not shown).

4.4.2 Convective transition in MJOTF/GASS models

The last subsection has demonstrated that hourly model data is suitable for the diagnosis of fast-timescale convective transition. However, most high-frequency output from the recent CMIP5 are daily or 6-hourly, and higher frequencies are uncommon. To establish that 6-hourly data can also be useful for diagnosing convective transition, and to survey the performance of current mainstream GCMs, in this subsection we sample the basic statistics for particular $\widehat{q_{sat}}$ bins using the 6-hourly output (snapshot for CWV and $\widehat{q_{sat}}$, average for precipitation; regridded to 2.5° $\times$ 2.5° resolution) from a subset of models (simulations 5-20 in Table 4.2.1) from the MJOTF/GASS project.

Figure 4.4.5 shows the conditional precipitation and probability of precipitation ($P > 0.25$ mm h^{-1}) for the 70-mm $\widehat{q_{sat}}$-bin for WPac sampled from the MJOTF/GASS models, together with observations (TRMM OBS; as in Fig. 4.3.1) and hourly 1° CAM5.3 (as in Fig. 4.4.3). The corresponding CWV PDFs are presented in Figs. 4.4.6a-4.4.6c for different $\widehat{q_{sat}}$ bins from low to high relative to the most probable $\widehat{q_{sat}}$ in each case (bins chosen to contrast differences). A single $\widehat{q_{sat}}$ is sufficient to demonstrate the typical behavior for the precipitation pickup, while three $\widehat{q_{sat}}$ values illustrate the typical behavior of the PDFs. For the complete set of

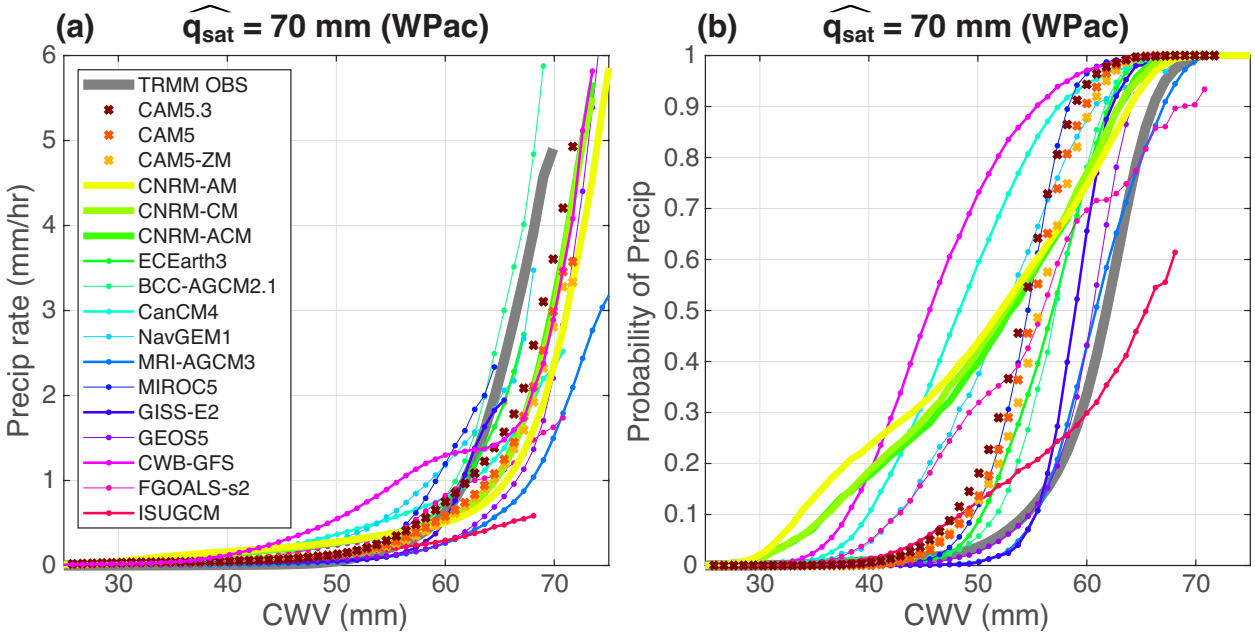

Figure 4.4.5: (a) Conditionally averaged precipitation rate for $\widehat{q_{sat}} = 70$ mm in the tropical western Pacific sampled from the MJOTF/GASS ensemble. (b) Same as in (a) but for conditional probability of precipitation ($P > 0.25$ mm h^{-1}). Here, the TRMM OBS is reproduced from Figs. 4.3.1a-4.3.1b, and CAM5.3 from Figs. 4.4.3a-4.4.3b for visual reference. The MJOTF/GASS model data are 6-hourly (average for precipitation) and had been regridded to 2.5° resolution prior to our analysis. See Fig. 4.A.1 for MJOTF/GASS ensemble statistics for other $\widehat{q_{sat}}$ bins.

statistics for the MJOTF/GASS models, see Fig. 4.A.1.

4.4.2.1 General overview

Figure 4.4.5a displays considerable variation across models. Most models produce a qualitatively reasonable pickup of precipitation above some threshold in CWV, but the exact value varies considerably. Qualitative departures from the observed behavior can be noted for some models. For instance, CWB-GFS and FGOALS-s2 exhibit a two-step pickup, and precipitation in the ISUGCM is relatively insensitive to CWV. The pickup of precipitation in many models occurs at higher CWV compared to observations. In contrast, the simulated conditional probability (Fig. 4.4.5b) in most models sharply increases at CWV much

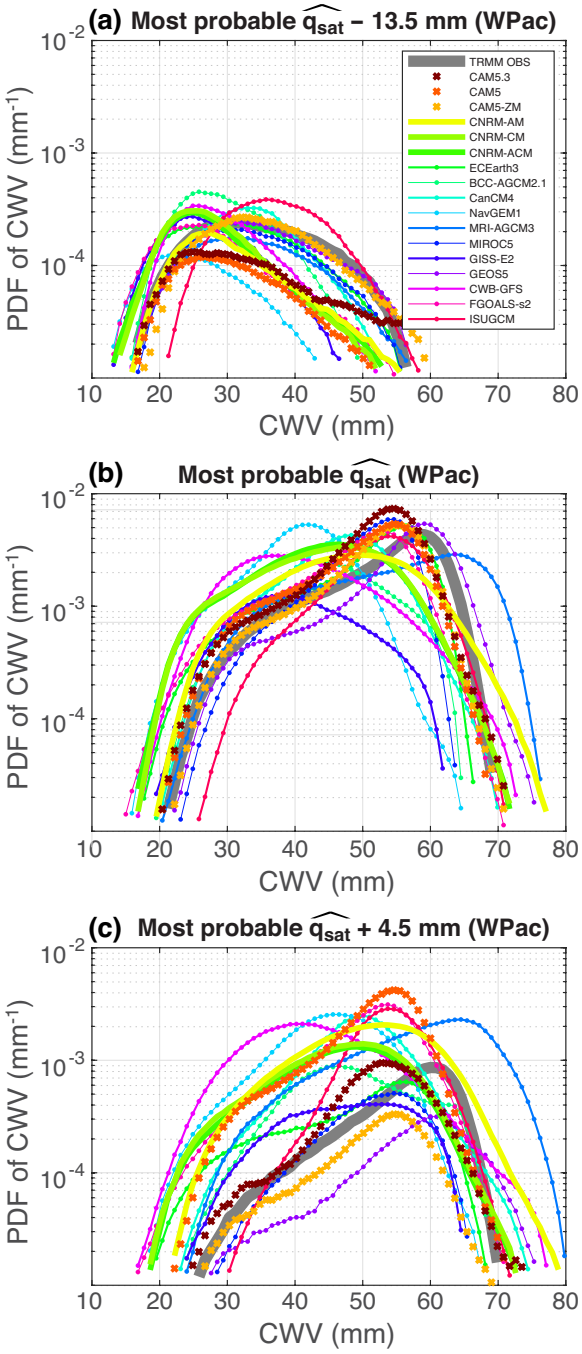

Figure 4.4.6: (a) PDFs of CWV for the most probable $\widehat{q_{sat}}$ − 13.5 mm (i.e., a relatively cold bin) in the tropical western Pacific sampled from the MJOTF/GASS ensemble. (b) Same as in (a) but for the most probable $\widehat{q_{sat}}$ bin. (c) Same as in (a), but for the most probable $\widehat{q_{sat}}$ + 4.5 mm (i.e., a relatively warm bin). Here, the most probable $\widehat{q_{sat}}$ value is found separately for each case. The TRMM OBS is reproduced from Fig. 4.3.1c, and CAM5.3 is reproduced from Fig. 4.4.3c for visual reference. See Fig. 4.A.1 for MJOTF/GASS ensemble statistics for other $\widehat{q_{sat}}$ bins.

lower than observed, and this departure from observations is too large to be explained by the dependence of conditional probability on spatial- and time-averaging (1° snapshot for observations vs 2.5° 6-hourly average for MJOTF/GASS models). Following section 4.3, the estimated shift caused by averaging is on the order of 5-10 mm or smaller compared to the shifts of up to 20 mm exhibited here. The low conditional precipitation and high conditional probability (for $P > 0.25$ mm h^{-1}; well above detection limit of the TMI and PR; TRMM 2011; Wentz et al. 2015) at CWV below critical in these models imply a widespread problem with excessive occurrence of low rain rates—which for brevity we refer to as a drizzle problem at subdaily timescales (not to be confused with the conventional drizzle problem for daily mean, e.g., Dai 2006).

Turning to the CWV PDF, as noted in section 4.3 (Fig. 4.3.1c), at low $\widehat{q_{sat}}$, the PDF peaks at low CWV below which the PDF drops sharply, and above which the PDF decreases slowly. As $\widehat{q_{sat}}$ increases, another peak develops at high CWV around critical with the low-CWV peak diminishing. In Fig. 4.4.6a, the simulated PDFs for low $\widehat{q_{sat}}$ by all models qualitatively resemble the observed low-CWV peak. But the transition to high-CWV peak as $\widehat{q_{sat}}$ increases (Figs. 4.4.6b and 4.4.6c) is correctly captured only by some of the models (e.g., CAM5 cases, MRI-AGCM3 and GEOS5). In the other models, the high-CWV peak has a wider spread (CanCM4, NavGEM1, and CNRM cases) or fails to develop (CWB-GFS). Note that whether a model can capture this transition of PDF at high $\widehat{q_{sat}}$ is in part related to its ability to simulate precipitation pickup, with models that have a less sharp pickup tending to have PDFs that have insufficiently sharp peaks for the most common $\widehat{q_{sat}}$. However, this relationship is not perfect; for instance, ISUGCM has a very slow pickup, but while the pickup peak occurs at too low CWV, the excessive breadth of its PDF is not as bad as might be anticipated from its simulation of the pickup.

Next, we concentrate on two subsets of models for which we have multiple instances: the CAM5 and CNRM.

4.4.2.2 CAM5 comparisons

There are three CAM5 instances (represented by crosses in Figs. 4.4.5 and 4.4.6): CAM5.3, CAM5, and CAM5-ZM. CAM5.3 and CAM5 primarily differ in spatial (1° vs 2.5°; originally simulated at same resolution) and temporal resolution (hourly vs 6-hourly average), which presumably lead to the minor differences in Fig. 4.4.5 (a small shift in CWV) and PDFs in Fig. 4.4.6. However, the precipitation pickup in CAM5.3 and CAM5 closely resemble each other (see also Fig. 4.A.1), which is consistent with the insensitivity to spatial- and time-averaging noted in observations (section 4.3; chapter 3). This demonstrates that conventional 6-hourly model data is useful for fast-timescale convective transition diagnosis, thus extending the applicability of such metrics.

For CAM5 vs CAM5-ZM, the latter configuration adopted a modified Zhang-McFarlane deep-convective parameterization with a new microphysics scheme for convective clouds (Song and Zhang 2011). Nevertheless, the resulting statistics in Figs. 4.4.5 and 4.4.6 are very similar, suggesting that the formulation of entraining plume and mass flux closure are more important than microphysics to the convective transition (see Fig. 4.A.1. Small differences between the two most probable $\widehat{q_{sat}}$ bins in the CAM5 and CAM5-ZM lead to apparent differences in the magnitude of the peak in Fig. 4.4.6, while the shapes are similar.) Whether this will hold for other models requires further investigation.

4.4.2.3 CNRM comparisons

There are three CNRM instances (thick solid lines in Figs. 4.4.5-4.4.6): CNRM-AM, CNRM-CM, and CNRM-ACM. Here the suffixes AM and CM stand for atmosphere-only and coupled simulations, and ACM for atmosphere-only run forced by the monthly mean SST and sea ice output from the coupled simulation (Jiang et al. 2015). That is, they differ in coupling or forcing through lower boundary.

CNRM-CM and CNRM-ACM produce almost identical statistics in Figs. 4.4.5 and 4.4.6.

The uncoupled version, CNRM-AM, quantitatively differ in CWV PDF from the other two, tending to be shifted towards higher values in Fig. 4.4.6. However, the pickup of precipitation (Fig. 4.4.5) and qualitative features of the CWV PDF (Figs. 4.4.6 and 4.A.1) are alike for all 3 cases, and the most common $\widehat{q_{sat}}$ value, 65.5 vs 70 mm, indicates that the coupled/forced versions are residing overall at lower temperatures. These differences are consistent with the fast-timescale convective transition operating similarly among these versions, as in the SPCAM comparisons (section 4.4.1.4), while the overall effects of the coupling and forcing through lower boundary affect the probability distribution of temperature and water vapor, associated with differences in climatology.

4.4.3 Summary of model behavior

Sections 4.4.1 and 4.4.2 are suggestive that the basic statistics can distinguish convective parametrizations and are less sensitive to other model components, e.g., cloud microphysics, coupling and forcing configurations. Furthermore, the qualitative features of the basic statistics are reasonably robust to spatial- and time-averaging, making it possible to leverage the existing CMIP effort for such fast-timescale diagnosis. Across the tested models there is great variation in various aspects, which must be examined separately to comprehensively assess parameterization schemes.

The observed precipitation-CWV relationship has been attributed to the impact of tropospheric moisture on conditional instability through entrainment (Holloway and Neelin 2009, Schiro et al. 2016, Kuo et al. 2017). The exact functional forms of simulated conditional precipitation and probability vary considerably, but all models capable of simulating precipitation pickup can reproduce the dependence of critical CWV w_c and critical column RH $w_c/\widehat{q_{sat}}$ on $\widehat{q_{sat}}$ (including those from the MJOTF/GASS project; not shown), although quantitative differences are noted in the values of w_c. This could be consistent with the observed w_c–$\widehat{q_{sat}}$ relation arising from entrainment, as demonstrated by offline entraining plume calculations (Sahany et al. 2012) and perturbed physics experiments (Kuo et al. 2017), since

the models differ in their entrainment representations. However, we cannot exclude other intermodel differences as potentially contributing to this spread.

The conditional probability in most models picks up at below-critical CWV lower than observed, which cannot be fully explained by the difference in spatial- and time-averaging of the data, revealing a widespread drizzle problem at subdaily/hourly timescales. The traditional use of the term 'drizzle problem' concerns excessive occurrence of low daily mean intensities (Dai 2006) without specifying the underlying thermodynamic environment. Here, conditioned on the bulk parameters $(CWV, \widehat{q_{sat}})$ that tend to vary slowly compared with subdaily/hourly timescales, the statistics indicate misrepresented precipitation processes in many of the models.

In the model for which we have a direct comparison of different microphysics schemes (CAM5.3 vs CAM5-ZM), only very small impact on the drizzle problem was noted. On the other hand, perturbed physics experiments (Kuo et al. 2017) indicate that the entrainment value can strongly affect this issue, since low entrainment yields insufficient dependence on free tropospheric moisture and thus overly frequent occurrence of rainfall. Analysis of such perturbed physics experiments across a wide set of convective parameters, combined with conceptual modeling, would be useful to further understand such intermodel differences.

Some of the models qualitatively capture the form of the PDFs of CWV and the dependence of these on temperature seen in observations, but many do poorly in this comparison. The PDF in the dry (non-precipitating) regime is expected to be influenced by dynamics other than the convective physics alone. The PDFs at colder temperatures, which reflect more of the dry regime, tend to be better simulated than the high-temperature, high-CWV range that has stronger dependence on the convective physics. Comparison of models with coupled vs uncoupled versions and different coupling/forcing settings through lower boundary (SPCAM and CNRM cases) indicates that the shapes of the PDFs tend to be similar, but shifts in climatology are reflected in the probability distribution of temperatures and water vapor.

Note that small errors in the onset of precipitation could have significant implications. For instance, the values of critical CWV determine the CWV PDF peak locations in observations and some of the models. Thus, a bias of a few millimeters in the critical values, compared with the observed climatological mean of ∼41 mm over tropical oceans, and more generally, biases in the CWV PDFs, could substantially alter the longwave radiation budget.

Overall the spread among the models and departures from observations in these fast-process diagnostics to which they have not previously been compared is of considerable concern for model development. But the existence of some models that do well at these diagnostics is encouraging.

4.5 Joint probability distributions of precipitation and CWV

In this section, we further examine the joint PDF of precipitation rate P and CWV (relative to critical, $cwv - w_c$) compiled from observations and hourly data of the AM4G9, AM4B6, CAM5.3, and SPCAM. Recall that the former two AM4 instances adopt different convective parameterizations, and the latter two are CAM cases sharing the same dynamic components but differing in moist-convective representations (parameterizations vs 2D CRM). To help interpret the joint PDF, consider the decomposition:

$$Prob(P, cwv - w_c) = Prob(P|\, cwv - w_c) Prob(cwv - w_c), \tag{4.1}$$

where the three Prob terms from left to right represent, respectively, the joint PDF of P and $cwv - w_c$, the conditional probability distribution of P given $cwv - w_c$, and the PDF of $cwv - w_c$. Each of these quantities potentially depends also on bulk tropospheric temperature $\widehat{q_{sat}}$ and ocean basin, but these are omitted from the notation for simplicity. $Prob(P|cwv - w_c)$ characterizes the probability distribution of precipitation for a given large-scale temperature-moisture environment (with temperature entering via w_c). $Prob(cwv - w_c)$ reflects the interaction of the large-scale environment with convective physics (to the extent this environment is captured by CWV and $\widehat{q_{sat}}$). Note that even if a model permits an

accurate estimate of precipitation given a large-scale temperature-moisture environment [e.g., with a correct $Prob(P|\, cwv - w_c)$], the joint PDF would still be affected by $Prob(cwv - w_c)$, which is expected to be more vulnerable to large-scale flow interacting with convective physics and subsequent feedbacks.

Below, we first examine the joint PDFs in Fig. 4.5.1, and then Figs. 4.5.2-4.5.3 for a quantitative breakdown of these distributions.

4.5.1 Joint PDF of precipitation and CWV relative to critical

Figure 4.5.1a (color shading) shows the joint PDF of P and $cwv - w_c$ for the most probable $\widehat{q_{sat}}$ bin (74.5 mm) in the tropical western Pacific (WPac) compiled at 1° using the PR precipitation, TMIv7.1 CWV and Reanalysis-2 temperature. Here, the color increments correspond to a doubling of the PDF value. The "non-precipitating" bins ($0 \leq P \leq 0.05$ mm h^{-1}) are enlarged in the vertical along the bottom for visual clarity, and the orange dotted lines represent the conditional probability of $P > 0.05$ mm h^{-1}, providing an alternate display of the ratio of the non-precipitating bins. The gray shading indicates CWV > 75 mm at which the TMIv7.1 CWV is capped. The corresponding conditional mean (blue solid), variance (blue dashed), and median (magenta solid) of precipitation are also shown for reference. The same set of statistics compiled using the TMIv7.1 precipitation is displayed in Fig. 4.5.1b, and those simulated by models in Figs. 4.5.1c-4.5.1f. Compared to PR, the TMIv7.1 precipitation has a spurious cutoff around $P \sim 10$ mm h^{-1} (presumably retrieval-dependent; see Figs. 4.5.2b vs 4.5.2a) but contains more events than the PR when coarse-grained to 1°. Hence both are included in Fig. 4.5.1.

In Fig. 4.5.1a, an abrupt transition from the dry to moist regime occurs around $cwv - w_c \sim -10$ mm below which only weak precipitation is permitted, and above which strong precipitation becomes frequent. However, this transition occurs considerably lower than critical, implying that the rapid increase of the conditional precipitation (blue solid) near critical is partly contributed by the decreasing ratio of non-precipitating vs precipitating events

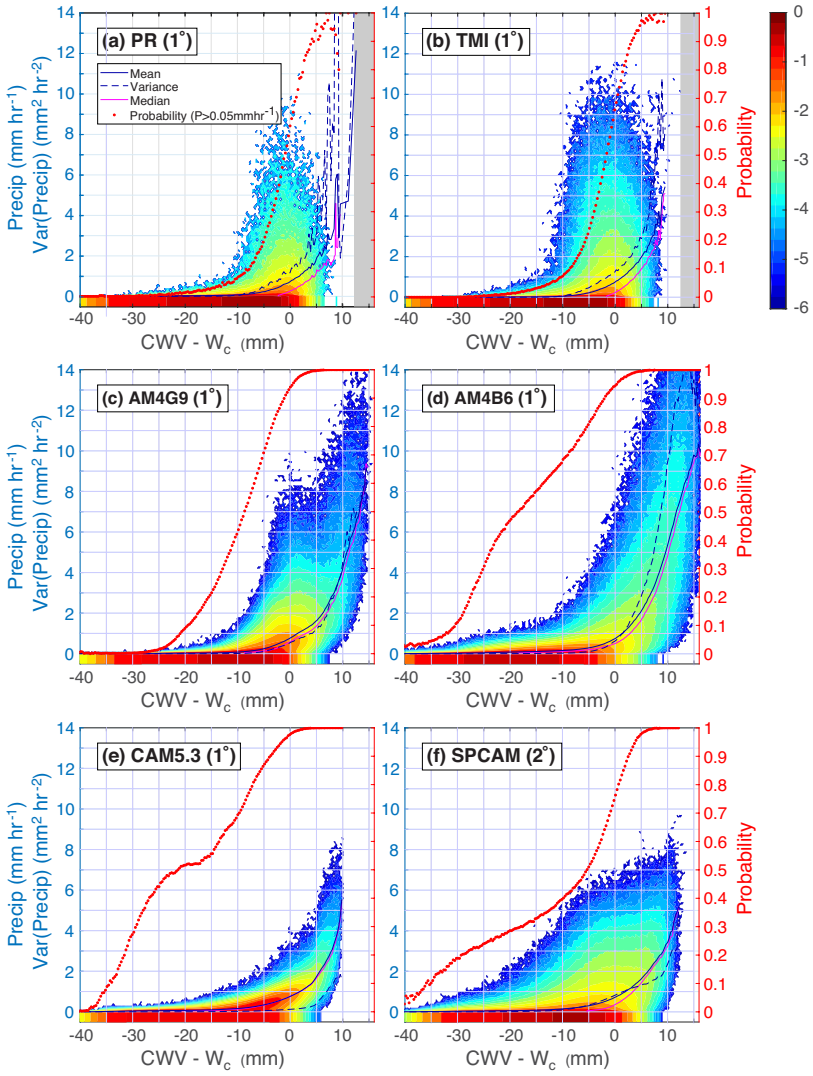

Figure 4.5.1: (a) Joint-PDF (color shading; units: mm^{-2} h), on a log10-scale, of CWV relative to critical and precipitation rate P for the 74.5-mm $\widehat{q_{sat}}$-bin in the tropical western Pacific compiled at 1° using the PR 2A25 precipitation rate, TMIv7.1 CWV and Reanalysis-2 temperature. The color increments correspond to a doubling of the PDF value ($10^{0.3} \sim 2$). The "non-precipitating" bins ($0 \leq P \leq 0.05$ mm h^{-1}) are enlarged in the vertical along the bottom for visual clarity. The conditional mean (solid blue), median (solid magenta), variance (dashed blue), and probability of precipitation ($P > 0.05$ mm h^{-1}; orange dots), all as a function of CWV, are also displayed for reference (note separate y-axes for precipitation and probability; variance is on the same axis as precipitation, although in different units). (b) Same as in (a) but with the PR 2A25 precipitation rate replaced by TMIv7.1 precipitation rate. (c)-(f) Same as in (a) but compiled using the hourly output from the AM4G9, AM4B6, CAM5.3, and SPCAM, respectively. In (a)-(b), the gray shading represent where the TMIv7.1 CWV value is capped at 75 mm and is hence unavailable.

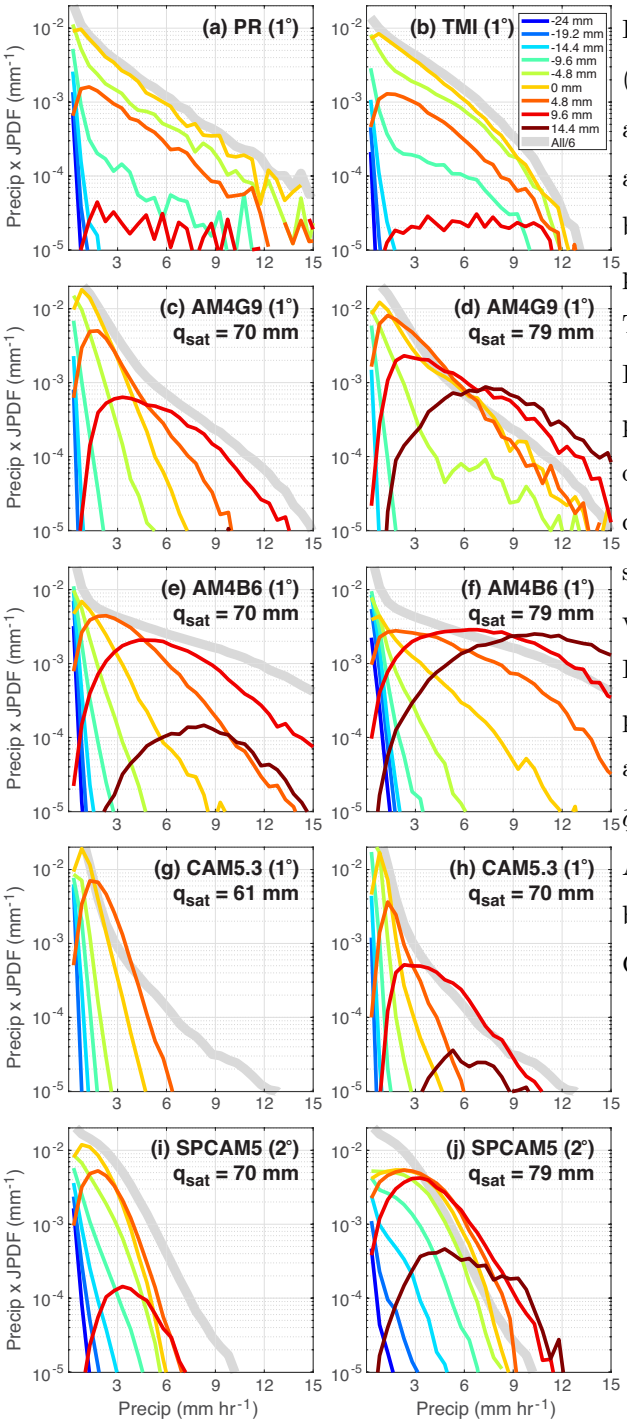

Figure 4.5.2: (a) The precipitation contribution (i.e., precipitation rate-weighted joint-PDF), as a function of precipitation rate P and CWV relative to critical (colors), for the 74.5-mm $\widehat{q_{sat}}$-bin in the tropical western Pacific (WPac) compiled at 1° using the PR 2A25 precipitation rate, TMIv7.1 CWV and Reanalysis-2 temperature. Here, the calculation uses the joint-PDF displayed in Fig. 4.5.1a. The gray line represent the overall (i.e., including all CWV and $\widehat{q_{sat}}$) precipitation contribution for WPac (units: dimensionless) shifted downwards by a factor of 6 for visual reference. (b) Same as in (a) but with the PR 2A25 precipitation rate replaced by TMIv7.1 precipitation rate. (c)-(d) Same as in (a) but for a relatively cold $\widehat{q_{sat}}$-bin and a relatively warm $\widehat{q_{sat}}$-bin, respectively, compiled using the hourly AM4G9 model output. (e)-(j) same as in (c)-(d) but using the hourly output from the AM4B6, CAM5.3, and SPCAM, respectively.

as CWV increases and exceeds critical. This is also reflected by the pickup of conditional probability (orange dotted) and median (magenta solid) around the same location. One can contrast the conditional precipitation which sharply increases with the more detailed behavior of the joint PDF. From slightly below critical to slightly above critical, a roughly exponential tail toward high precipitation values may be seen, and the properties of this tail do not change dramatically as a function of CWV in this range (see also Fig. 4.5.2a). The joint PDF exhibits the highest probability of high precipitation near critical, partly because the CWV PDF peaks around critical. The statistics in Fig. 4.5.1b generally agree with those in Fig. 4.5.1a (differences may be noted later in Figs. 4.5.2b vs 4.5.2a).

The model-simulated joint PDFs in Figs. 4.5.1c-4.5.1f qualitatively capture many features of the observations, but the dry-to-moist transition is less drastic than observed. Another notable difference seen to some extent in all models is in the behavior of the tail of the PDF extending to high precipitation as a function of CWV. The tail tends to extend further towards strong precipitation as CWV increases above critical ($cwv - w_c > 5$ mm), indicating departures from observations in $Prob(P|\, cwv - w_c)$ and/or $Prob(cwv - w_c)$. One can also see the conditional precipitation tending to coincide more closely with the conditional median in the models, implying a relatively symmetric P distribution at odds with the observed asymmetry. Variations among the models in these differences relative to observations may be noted: AM4G9 and SPCAM can produce strong precipitation for CWV around or right below critical, while AM4B6 and CAM5.3 can not. All 4 models underestimate the conditional P variance, but CAM5.3 is the most serious one.

Chapter 3 has noted that the observed joint PDF shows little variation across the $\widehat{q_{sat}}$-range and ocean basins (except the ratio of precipitating vs non-precipitating events for below-critical CWV may vary significantly). That is, the value of $cwv - w_c$ alone characterizes the probability distribution of precipitation in the moist regime, and this precipitation-CWV relation does not exhibit additional dependence on $\widehat{q_{sat}}$. As such, only the results for the most probable $\widehat{q_{sat}}$ are displayed in Figs. 4.5.1a and 4.5.1b (and the qualitative characteristics

noted in Figs. 4.5.1c-4.5.1f are generally valid). However, the model-simulated distributions exhibit spurious dependence on $\widehat{q_{sat}}$, as shown in Fig. 4.5.2.

4.5.2 Precipitation contributions

Figures 4.5.2a and 4.5.2b show the amount of total rainfall accumulation contributed by each P intensity, or precipitation contribution (i.e., P-weighted joint-PDF), for various values of $cwv - w_c$ (colors) calculated using the same joint PDFs in Figs. 4.5.1a and 4.5.1b, with different bin width. The gray lines represent the overall (i.e., including all CWV and $\widehat{q_{sat}}$) precipitation contribution for WPac (units: dimensionless; shifted downwards by a factor of 6 for visual reference). The corresponding results simulated by models are in Figs. 4.5.2c-4.5.2j, with panels on the left displaying a low $\widehat{q_{sat}}$ bin (the most probable $\widehat{q_{sat}} - 4.5$ mm), and panels on the right displaying a high $\widehat{q_{sat}}$ bin (the most probable $\widehat{q_{sat}} + 4.5$ mm).

The individual colored lines in Fig. 4.5.2a from PR precipitation represent $P{\cdot}Prob(P|cwv-w_c)Prob(cwv-w_c)$ for different values of $cwv-w_c$. The shape of the curve at moderate to high P is primarily determined by $Prob(P|\, cwv - w_c)$. These precipitation contributions vanish at zero because of P, which does not otherwise greatly alter the profiles of $Prob(P|\, cwv - w_c)$ for $P > 3$ mm h^{-1}. The lowest $cwv - w_c$ values only permit low $P < 2$ mm h^{-1}. Around critical (yellow line), an approximately exponential tail may be noted above $P \sim 2$ mm h^{-1} extending to the highest precipitation values for which sufficient data is available. The slope of this tail is insensitive to $cwv - w_c$ over a wide range ($-9.6{\sim}4.8$ mm). As CWV exceeds critical, the precipitation contribution develops a maximum at a positive P, which shifts slightly toward higher P with further increase in CWV [this evolution of maximum can also be seen in $Prob(P|\, cwv - w_c)$ and is more pronounced for higher spatial resolution; see chapter 3]. At the highest $cwv - w_c$ (9.6 mm; red), the precipitation contribution exhibits a broad spread in P, indicating that strong precipitation is more frequent given very high CWV values. However, the contribution from the highest $cwv - w_c$ is only a small fraction of the overall contribution (gray) which roughly matches that at critical (yellow)

because of the modulation by $Prob(cwv - w_c)$. The corresponding statistics in Fig. 4.5.2b are consistent with those in Fig. 4.5.2a but display a faster decay at high P caused by the (retrieval-dependent) cutoff $\sim$10 mm h^{-1} in the TMIv7.1 precipitation.

We evaluate the model-simulated precipitation contributions in Figs. 4.5.2c-4.5.2j. For low $\widehat{q_{sat}}$ [left column: (c), (e), (g), (i)], the models capture some aspects of the observed dependence of precipitation on CWV to an extent that varies among models. For instance, the precipitation contribution drops rapidly for CWV below critical, and the contribution from high precipitation values increases with CWV. Around critical (yellow line), a local maximum of the precipitation contribution can be seen at a positive P. This local maximum occurs at higher P with its magnitude decreasing as CWV further increases because of $Prob(cwv - w_c)$. The contributions tend to be less asymmetric in P around the local maximum compared to observations (especially for AM4B6, CAM5.3, and SPCAM). These less asymmetric contributions explain why the conditional average of precipitation tends to coincide with the median noted in Fig. 4.5.1.

Other departures from observations can also be noted. Each model exhibits some range that appears qualitatively consistent with an exponential tail toward high precipitation. However, the tail slope (in log-Y coordinates), where it exists, varies substantially among models and does not quantitatively match observations. The tail slope ends to be shallower for higher $cwv - w_c$ values, i.e., strong precipitation is more frequent given higher CWV. Comparing the low-$\widehat{q_{sat}}$ contributions to their high-$\widehat{q_{sat}}$ counterparts [right column: (d), (f), (h), (j)], high-($cwv - w_c$) events (red and brown) are more frequent for high $\widehat{q_{sat}}$, reflecting that there are more above critical evens as noted in section 4.4.1. Using the overall precipitation contribution (gray) as a reference, the high-$\widehat{q_{sat}}$ contributions tend to decay slower than the low-$\widehat{q_{sat}}$ ones. These indicate that both $Prob(P|\ cwv - w_c)$ and $Prob(cwv - w_c)$ exhibit spurious dependence on $\widehat{q_{sat}}$, inconsistent with observations.

Figure 4.5.3 shows the precipitation contribution from a different angle, i.e., as a function of $cwv - w_c$ for different $\widehat{q_{sat}}$ bins (indicated by colors) for WPac, with the top/bottom

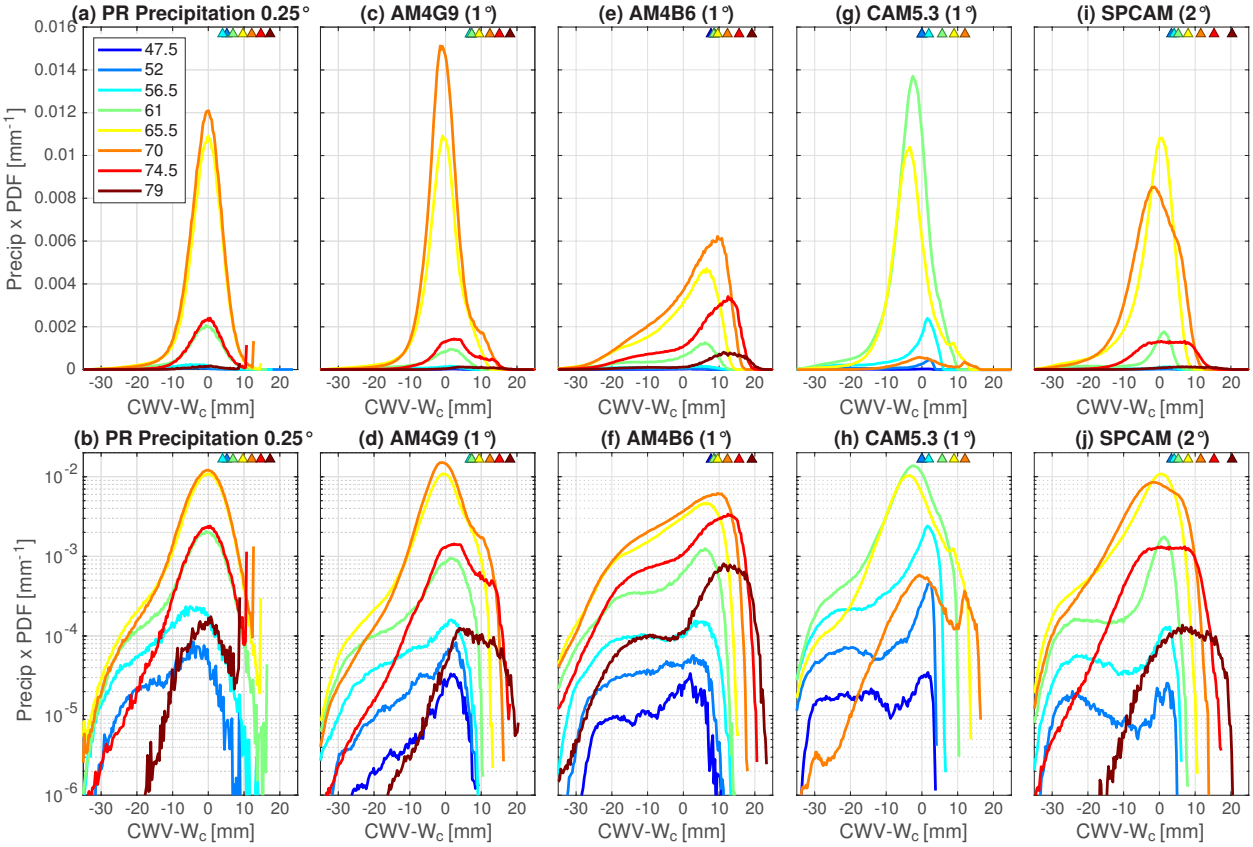

Figure 4.5.3: (a) The precipitation contribution (i.e., precipitation rate-weighted CWV PDF), on a linear scale, as a function of CWV relative to critical and $\widehat{q_{sat}}$ (colors) in the tropical western Pacific compiled at 0.25° using the PR 2A25 precipitation rate, TMIv7.1 CWV and Reanalysis-2 temperature. Here the triangles represent the values of $\widehat{q_{sat}}$ relative to the critical CWV, which indicate where the column is approximately saturated. (b) Same as in (a) but on a log10-scale. (c)-(j) Same as in (a)-(b) but using the hourly output from the AM4G9, AM4B6, CAM5.3, and SPCAM.

panels in a linear/log-Y scale. Here the area under each curve represents the precipitation contributed by each $\widehat{q_{sat}}$.

The observed contributions (Fig. 4.5.3a) for the most common $\widehat{q_{sat}}$ values peak around critical with a common near-Gaussian core (Fig. 4.5.3b). Variations can be noted for CWV below critical (< -15 mm) which clearly deviates from Gaussian, presumably affected by dry-regime dynamics and non-convective rain. For low $\widehat{q_{sat}}$ bins ≤ 56.5 mm, the contributions peak slightly below critical with a wider spread in CWV, contrasting tropical vs extratropical

precipitation.

The precipitation contributions simulated by the AM4G9 (Figs. 4.5.3c and 4.5.3d) and SPCAM (Figs. 4.5.3i and 4.5.3j) also peak around critical but tend to shift and spread toward higher CWV relative to critical as $\widehat{q_{sat}}$ increases. For CAM5.3 (Figs. 4.5.3g and 4.5.3h), the contributions peak around critical but do not exhibit consistent dependence on $\widehat{q_{sat}}$, and the contribution for the highest $\widehat{q_{sat}}$ (70 mm) is bimodal, consistent with the CWV PDF in Fig. 4.4.3g. The greatest departure from observations are noted for the AM4B6 (Figs. 4.5.3e and 4.5.3f), with the contributions spreading across a wide range of CWV, and the peak clearly shifting with $\widehat{q_{sat}}$. These features display the dependence of precipitation on $\widehat{q_{sat}}$ that generally agree with Fig. 4.5.2. We note that the differences from observations are exhibited even around critical, near the peak of the distribution, and are thus likely to be robust to any retrieval issues at high precipitation.

Overall, the precipitation contributions in Figs. 4.5.2-4.5.3 show that the models exhibit many qualitative features of the observations, but also exhibit substantial quantitative deviations. These combine with biases in the PDF of $cwv - w_c$, in which the models overproduce above-critical events (especially at high temperature) to yield the errors in the joint PDF seen in Fig. 4.5.1.

4.6 Summary and discussion

Most of the models examined simulate some version of the observed precipitation pickup with CWV. However, significant intermodel spread and departures from observations in multiple aspects of the convective transition statistics suggest these provide a challenging observational constraint. Examining these aspects separately using the 6-hourly and higher frequency model output provides a comprehensive assessment for deep-convective parameterizations with clues for improvements. Below we briefly summarize the comparisons of these aspects.

4.6.1 Precipitation pickup and CWV relative to critical

In observations, the conditionally averaged precipitation, as a function of CWV for a given bulk tropospheric temperature $\widehat{q_{sat}}$, sharply increase as CWV exceeds the critical threshold w_c (Fig. 4.3.1a). w_c increases with $\widehat{q_{sat}}$ but the corresponding critical column RH $w_c/\widehat{q_{sat}}$ decreases (Figs. 4.3.1k and 4.3.1l). Offline calculations have suggested that the dependence of w_c and $w_c/\widehat{q_{sat}}$ on $\widehat{q_{sat}}$ is a generic consequence of including entrainment in the estimation of buoyancy in convective updraft (Sahany et al. 2012). The conditionally averaged precipitation exhibits little variation across ocean basin (Fig. 4.3.1i) and is insensitive to spatial-averaging (chapter 3). Furthermore, when viewed as a function of $cwv - w_c$, its functional form shows little dependence on $\widehat{q_{sat}}$ (Figs. 4.3.1e and 4.3.1i). This reaffirms the interpretation that $cwv - w_c$ combines the impacts of tropospheric moisture and temperature on conditional instability, through entrainment, into a single measure (Holloway and Neelin 2009, Schiro et al. 2016; chapter 3).

Among the examined models, AM4B6 (Fig. 4.4.2a) satisfactorily simulates the conditionally averaged precipitation which exhibits modest sensitivity to $\widehat{q_{sat}}$ (Fig. 4.4.2e) and little variation across ocean basin (Fig. 4.4.2i). The corresponding critical values match observations (Figs. 4.4.2k and 4.4.2l). However, the conditionally averaged precipitation simulated by the other models (Figs. 4.4.1, 4.4.3, 4.4.4, and 4.4.5a), tends to exhibit sensitivity to $\widehat{q_{sat}}$ (Fig. 4.4.4e) and basins (Fig. 4.4.4i), or results in different critical values (Figs. 4.4.3k and 4.4.3l). Figure 4.4.5a further demonstrates a significant intermodel spread in the critical values (where the precipitation picks up) or in the functional form of precipitation. For instance, the precipitation in the ISUGCM fails to pick up, likely because of the lack of entrainment in its convective scheme. The precipitation in CWB-GFS shows a two-step pickup, likely results from a built-in precipitation trigger that explicitly depends on environment humidity.

Most models that can simulate a decent precipitation pickup also capture the observed qualitative dependence of critical values on $\widehat{q_{sat}}$ (w_c increases and $w_c/\widehat{q_{sat}}$ decreases; not

shown), indicating that entrainment is the essential mechanism.

4.6.2 Probability of precipitation and drizzle problem

The observed conditional probability of precipitation (defined relative to a threshold of precipitation rate P) also exhibits a sharp pickup for CWV around critical (Figs. 4.3.1b and 4.3.1f). Its functional form can be approximated using an error function with standard deviation ∼4 (units: mm; not shown). Lower $\widehat{q_{sat}}$, lower P threshold, and lower spatial resolution (at which the statistics are computed) all lead to higher values of conditional probability without altering its functional form, i.e., the conditional probability curve would shift slightly towards lower CWV (chapter 3). Like the conditional average, the conditional probability can also be expressed as a function of $cwv - w_c$, which exhibits little variation across the $\widehat{q_{sat}}$ range and basins (Figs. 4.3.1f and 4.3.1j).

As an example, we consider two GFDL AM4 cases with different convective parameterizations, one among the best and one among the poorest simulations in this measure. In the AM4G9, the conditional probability of precipitation closely resembles the observed values with a slightly steeper pickup (Fig. 4.4.1b) which starts at lower CWV relative to critical (Figs. 4.4.1f vs 4.3.1f). It also exhibits modest variation across basins (Fig. 4.4.1j). The simulated conditional probability picking up at lower CWV relative to critical may result from and is consistent with the difference in the temporal resolution of P (hourly average for AM4G9 vs snapshot for satellite retrievals). Despite the superior performance of AM4B6 in simulating conditionally averaged precipitation, the conditional probability in AM4B6 deviates considerably from observations (Fig. 4.4.2b). The pickup of conditional probability is gentler and shows a clear dependence on $\widehat{q_{sat}}$ (Fig. 4.4.2f), i.e., higher probability of precipitation at low CWV relative to critical especially at high $\widehat{q_{sat}}$, indicating a drizzle problem in a warm environment (see also the CNRM instances in Fig. 4.4.5). This contrast in AM4B6's ability to simulate conditional average and probability of precipitation serves as a reminder that different aspects of the convective transition statistics must be examined separately.

Regarding the other models, the simulated conditional probability exhibits sensitivity to $\widehat{q_{sat}}$ (Figs. 4.4.3f and 4.4.4f) and variation across basins (Figs. 4.4.3j and 4.4.4j), and even non-monotonic behavior. Figure 4.4.5b shows a substantial intermodel spread and that the conditional probability in most models picks up at CWV values lower than observed, many of which cannot be explained by the difference in the temporal resolution of P alone.

4.6.3 PDF of CWV

The observed CWV PDFs have $\widehat{q_{sat}}$-dependent characteristic shapes with two peaks/cut-offs at low and high CWV values (Fig. 4.3.1c), and are relatively insensitive to resolution. For low $\widehat{q_{sat}}$, the PDF peaks at a low CWV value above which the PDF decreases gradually until reaching a high-CWV cut-off right below critical (Fig. 4.3.1g). As $\widehat{q_{sat}}$ increases, the high-CWV cut-off develops into a peak. The pickup of precipitation suggests that the behavior for CWV above critical is governed by the moist-regime dynamics, i.e., conditional instability. Consequently, the (properly normalized) CWV PDF exhibits little variation across $\widehat{q_{sat}}$ range (Fig. 4.3.1g) and ocean basins (chapter 3). Stochastic models suggested that the functional form of the CWV PDF in this regime is primarily controlled by precipitation removal balancing low-level convergence of moisture (Stechmann and Neelin 2011, 2014). In contrast, at low CWV, the PDF and fraction of non-precipitating events vary considerably (Fig. 4.3.1g), suggesting other factors influencing the dry regime, e.g., prevailing subsidence and extratropical events intruding into the tropics (chapter 3).

For low $\widehat{q_{sat}}$, the CWV PDFs are primarily determined by the dry-regime dynamics, and all the models simulate this aspect in reasonable agreement with observations (Figs. 4.4.1-4.4.4c,g and Fig. 4.4.6a). But when moist-regime dynamics becomes dominant as $\widehat{q_{sat}}$ increases, the simulated CWV PDFs by many of the models depart from the observed (Figs. 4.4.6b and 4.4.6c), e.g., the PDF has a broad spread around intermediate CWV values (CNRM cases). Some of the models overproduce very-high-CWV events especially at high $\widehat{q_{sat}}$ values (Figs. 4.4.2g and 4.4.4g) which may result from small gross moist stability during

precipitation. Note that the CWV PDFs for highest $\widehat{q_{sat}}$ values in the AM4G9 (Fig. 4.4.1g) and CAM5.3 (Fig. 4.4.3g) seemingly indicate more above-critical events, but still fall within the observational uncertainty.

4.6.4 PDF of CWV for precipitating events

The CWV PDF for precipitating events here is defined as the product of the CWV PDF and conditional probability. Consequently, it modestly depends on the P threshold and resolution. In observations, the CWV PDFs for precipitating events for $\widehat{q_{sat}} \geq 70$ mm display a common near-Gaussian core (Fig. 4.3.1h), indicating convection favors specific thermodynamic conditions with a narrow water vapor range. For lower $\widehat{q_{sat}}$ values, the corresponding PDFs coincide with the high-$\widehat{q_{sat}}$ PDFs for CWV around and above critical, but also indicate greater probability of precipitation given CWV below critical. The geographical distribution of $\widehat{q_{sat}}$ suggests these low-$\widehat{q_{sat}}$ below-critical precipitation occurrences are in part associated with extratropical events resulting from other mechanisms, e.g., large-scale saturation (chapter 3).

Among the examined models, the AM4G9 and CAM5.3 can reproduce the common near-Gaussian core to some extent (Figs. 4.4.1h and 4.4.3h), but the contrast in below-critical precipitation for high- vs low-$\widehat{q_{sat}}$ is less pronounced as observed. The SPCAM, on the other hand, seems more capable of simulating this contrast but the PDF spreads over a broader range of CWV (Fig. 4.4.4h). The AM4B6 performs poorly in this regard (Fig. 4.4.2h) as a result of the biased CWV PDF and conditional probability (Figs. 4.4.2f and 4.4.2g). See also Fig. 4.A.1 for CWV PDFs in the MJOTF/GASS models.

4.6.5 Joint PDF of precipitation and CWV relative to critical

In observations, the joint PDF of P and $cwv - w_c$ exhibits an abrupt transition from the dry, non-precipitating regime into the moist regime as CWV increases from below critical

(Fig. 4.5.1a). In the moist regime, a robust exponential tail toward high precipitation can be noted in the PDF of P for CWV around critical (Fig. 4.5.2a), and the accumulated precipitation is mostly contributed by events in this regime (Fig. 4.5.3a and 4.5.3b). The slope of the exponential tail, and more generally, the PDF of P, depend on spatial averaging (chapter 3). The joint PDF shows little variation across the $\widehat{q_{sat}}$ range ≥ 61 mm and ocean basins (chapter 3).

The four models for which we examined joint PDFs with hourly data, AM4G9, AM4B6, CAM5.3 and SPCAM, can simulate the transition from the dry to moist regime to some extent (Figs. 4.5.1c-4.5.1f). However, the simulated transitions are less abrupt than observed. High precipitation tends to occur at above-critical CWV values but is less likely for around- and below-critical CWV than in the observed. The CAM5.3 especially underestimates the variability of precipitation (Fig. 4.5.1e). At relatively low $\widehat{q_{sat}}$, the simulated PDFs of P seem to exhibit some version of the asymptotic tail into high precipitation (Figs. 4.5.2c, 4.5.2e, 4.5.2g, 4.5.2i). The tails at critical CWV drop more rapidly than observed. Moreover, the simulated tails display dependence on CWV and indicate that strong precipitation favors high $\widehat{q_{sat}}$, i.e., a warm troposphere (Figs. 4.5.2d, 4.5.2f, 4.5.2h, 4.5.2j). These spurious dependencies on CWV and $\widehat{q_{sat}}$ lead to biased precipitation contribution. For instance, the above-critical contribution of precipitation at high $\widehat{q_{sat}}$ values is slightly exaggerated in the AM4G9 (Figs. 4.5.3c and 4.5.3d), and the AM4B6 precipitation is contributed over a broader range and mostly from above-critical CWV (Figs. 4.5.3e and 4.5.3f). This identifies the high-precipitation, high-CWV range as a regime demanding greater scrutiny as further discussed below.

4.6.6 Additional inferences based on the ensemble

Several comparisons are available in individual models with multiple instances differing in some specific components, permitting additional inferences regarding using the convective transition statistics as diagnostic tools:

1) Where the model (AM4 and CAM5.3 vs SPCAM) is available with alternative representations of moist convection, the statistics distinguish different instances in multiple aspects, despite all the model instances having been calibrated against typical diagnostic metrics.

2) Different cloud microphysics in the convective parameterizations in the same model (CAM5) only cause minor variations in the joint distribution of CWV and $\widehat{q_{sat}}$, but otherwise do not notably alter the statistics examined here.

3) Where the same model (CAM5) is examined at hourly and 6-hourly time-averaging (of precipitation), the results are comparable. Although output at model timestep or hourly timescale are preferable, the analysis can apply with more conventional subdaily output.

4) Where the model (CNRM and SPCAM) is available in uncoupled vs coupled versions, or with different forcing settings through the lower boundary, the major difference appears in the probability distribution of $(cwv, \widehat{q_{sat}})$ associated with climate drift caused by coupling/forcing configuration. Other aspects of the statistics, e.g., the precipitation pickup and CWV PDF are less sensitive.

These cases in this ensemble of opportunity further indicate that the convective transition statistics substantially discriminate between convective parameterizations and are reasonably robust to subdaily time-averaging i.e. can be used with conventional model data.

4.6.7 Possible action items for model revision and diagnostic development

While these diagnostics help identify the relationship between tropical precipitation and its thermodynamic environment in considerable detail, the diagnostics presented here can lead to suggestions for specific revisions of a given convective parameterization. The link is not direct, however. Analysis and improvement necessarily involve specifics of each model's set of parameterizations and can involve interaction of these parameterizations with emergent behavior of the dynamics. While it is not possible to cover detailed analysis for each model

in the ensemble, here we discuss process hypotheses and suggestions for further diagnostic development, broken out by type of error. These are all offered with the caveat that changes to improve model performance under one set of diagnostics can often erode the performance under other measures (Kim et al. 2011, Langenbrunner and Neelin 2017).

4.6.7.1 Errors in position/shape of onset

For models exhibiting errors in the functional form of conditional precipitation, the leading candidate for adjustment can be the entrainment assumptions in the convective scheme, since these are known to impact the critical values simulated by models (Sahany et al. 2012) or even the existence of a sharp pickup in precipitation Kuo et al. (2017). Plume calculations with higher entrainment are more sensitive to the free tropospheric environmental humidity, resulting in precipitation tending to pick up at higher CWV. Changes in a vertically constant entrainment rate can impact circulation or vertical distribution of cloud (Mapes and Neale 2011, Qian et al. 2018, Schiro et al. 2019). Recent analysis of observations and reanalysis (Schiro et al. 2018, Ahmed and Neelin 2018) point to a large influence of the environment on convective plume through a deep lower tropospheric layer contributing relatively uniformly to the updraft mass flux from all levels. This may be consistent with certain representations of entrainment (e.g., Siebesma et al. 2007), although if it occurs substantially through dynamical entrainment (Suselj et al. 2019) the strong effects may be confined to the lower troposphere.

This suggests that models that fail to simulate a strong precipitation pickup (e.g., ISUGCM) may benefit from increased lower tropospheric entrainment. Some models in the ensemble exhibit a multi-step pickup (CWB-GFS) because precipitation is triggered with respect to a certain humidity threshold. Apparently, this kind of trigger must be designed with caution to match the observed precipitation-moisture relationship and may not be necessary if entrainment is reasonably represented.

4.6.7.2 Errors in water vapor/precipitation PDFs

We note the following aspects of errors:

I. Errors in shape of water vapor PDF

The shape of the CWV PDF is largely controlled by the dominant moisture budget balance. Statistics from observations clearly distinguish between the wet, precipitating regime and the dry, non-precipitating regime. The overprediction of drizzle frequency in some of the models can be thought of as a spurious sink term of moisture at low CWV, contributing to biases in CWV PDF. In the wet regime, a longer convective adjustment timescale can be a factor tending to limit the rate at which the convective scheme removes moisture. In response, the environment reaches saturation more often and results in a higher fraction of precipitation occurring by grid-scale condensation associated with convection (e.g., Jiang et al. 2016).

II. Too much precipitation below main onset (drizzle problem) & Precipitating PDF too wide

Increasing entrainment can alleviate the drizzle problem over tropical oceans (but not over land, in CESM1; Kuo et al. 2017). Models produce precipitation through contributions by various parameterizations (e.g., cloud microphysics, shallow- and deep-convective) under different circumstances. Identifying precipitation types in varying thermodynamic conditions using radar rainfall products may help modelers coordinate parameterization schemes and quantify conditional instability given the tropospheric temperature-moisture state, e.g., in terms of entraining CAPE or general cloud work functions.

III. Joint PDF follows conditionally averaged precipitation too closely & Precipitation PDF/contribution tail errors at high precipitation

Several features of the joint PDF described in section 4.6.5 can be summarized as the model joint-PDF tending to follow the pickup of the conditionally average precipitation, with smaller spread about this than in observations. This suggests that for a given thermody-

namic environment, the precipitation is too deterministic. This is consistent with simulated extreme precipitation being improved by explicitly incorporating a stochastic component (Plant and Craig 2008, Wang et al. 2017). It could also be consistent with representation of additional sources of variability including effects of subgrid scale moisture variability, gustiness, downdrafts, cold pools, or organized systems (e.g., Hourdin et al. 2013, Harrop et al. 2018, Mapes and Neale 2011).

The longer-than-Gaussian tail of the observed precipitation distribution/contribution at high P is insensitive to the bulk measures of water vapor and temperature in the retrieval datasets used here. Given the importance of model projections of changes in extreme precipitation under global warming, the departures of the model precipitation PDFs from the observed in the high-precipitation, high-CWV regime as a function of temperature is of concern. Independent observational datasets, for instance from radio occultation (Padullés et al. 2018), could be used to further constrain the behavior in this regime; process modeling could be used to better identify sources of differences among models; and this regime can be an important target for cloud resolving models.

4.6.8 Concluding remarks

The statistics presented here are available as the Convective Transition Diagnostic Module associated with the Model Diagnostics Task Force (MDTF) Diagnostics Package (Maloney et al. 2019b, available at https://www.gfdl.noaa.gov/mdtf-diagnostics/). As applied to the set of models analyzed here, the convective transition statistics summarized above reveal substantial departures from observations and intermodel spread, especially for CWV within the moist regime, reflecting the current status of model representations of moist convection and its interaction with the large-scale flow. Although several models performed poorly with respect to the measures introduced here, it is encouraging that for the basic statistics (i.e., pickup of precipitation and probability, CWV PDF and CWV PDF for precipitating points) a few cases—including AM4G9, ECEarth3, GEOS5, and CAM5—performed well. This is

particularly noteworthy as in almost all cases the models had not previously been assessed with respect to these measures so have clearly not been in any way tuned to achieve these results. For a model to do well, the parameterization must reasonably capture multiple aspects of the triggering of deep convection associated with conditional instability. From related work, there is evidence that this requires a reasonable representation of the dependence on lower free tropospheric humidity by entrainment into the deep convective plumes. It also implies that the parameterization of convective heating as a function of buoyancy is operating well, and that the overall effects in the model yielding large-scale variations with which the convection interacts are of a suitable magnitude—on the one hand driving the system into the high-moisture, high-precipitation regime, and on the other causing event (i.e., precipitation) termination—with each occurring at a reasonable frequency. However, even in models that perform well, the high-temperature, high-CWV, high-precipitation regime is flagged as challenging to simulate in detailed comparison to the observations at these fast timescales.

Acknowledgements

The content of this chapter had previously been published as Kuo et al. (2020), which was supported by National Oceanic and Atmospheric Administration (NOAA) Grants NA15OAR4310097 and NA18OAR4310280, National Science Foundation (NSF) Grant AGS-1540518, and the Office of Biological and Environmental Research of the U.S. Department of Energy Grant DE-SC0011074. The author thanks J. Meyerson for graphical assistance, and the reviewers for insightful comments

APPENDIX

4.A Supplement

4.A.1 Basic convective transition statistics for MJOTF/GASS models

Figure 4.A.1 displays the basic statistics for the tropical western Pacific basin compiled using the 6-hourly model output (average for precipitation) from a subset of the MJOTF/GASS ensemble, as in Figs. 4.4.1-4.4.4a-d. The statistics presented in Fig. 4.A.1, from left to right, are the conditionally averaged precipitation rate, conditional probability of precipitation ($P > 0.25$ mm h^{-1}), PDFs of all events, and PDFs for precipitating events as a function of CWV and $\widehat{q_{sat}}$ (colors; units: mm). Triangles represent corresponding $\widehat{q_{sat}}$ values, which indicate where the column is approximately saturated, and underpopulated bins (PDF $<$ 10^{-5}) are omitted.

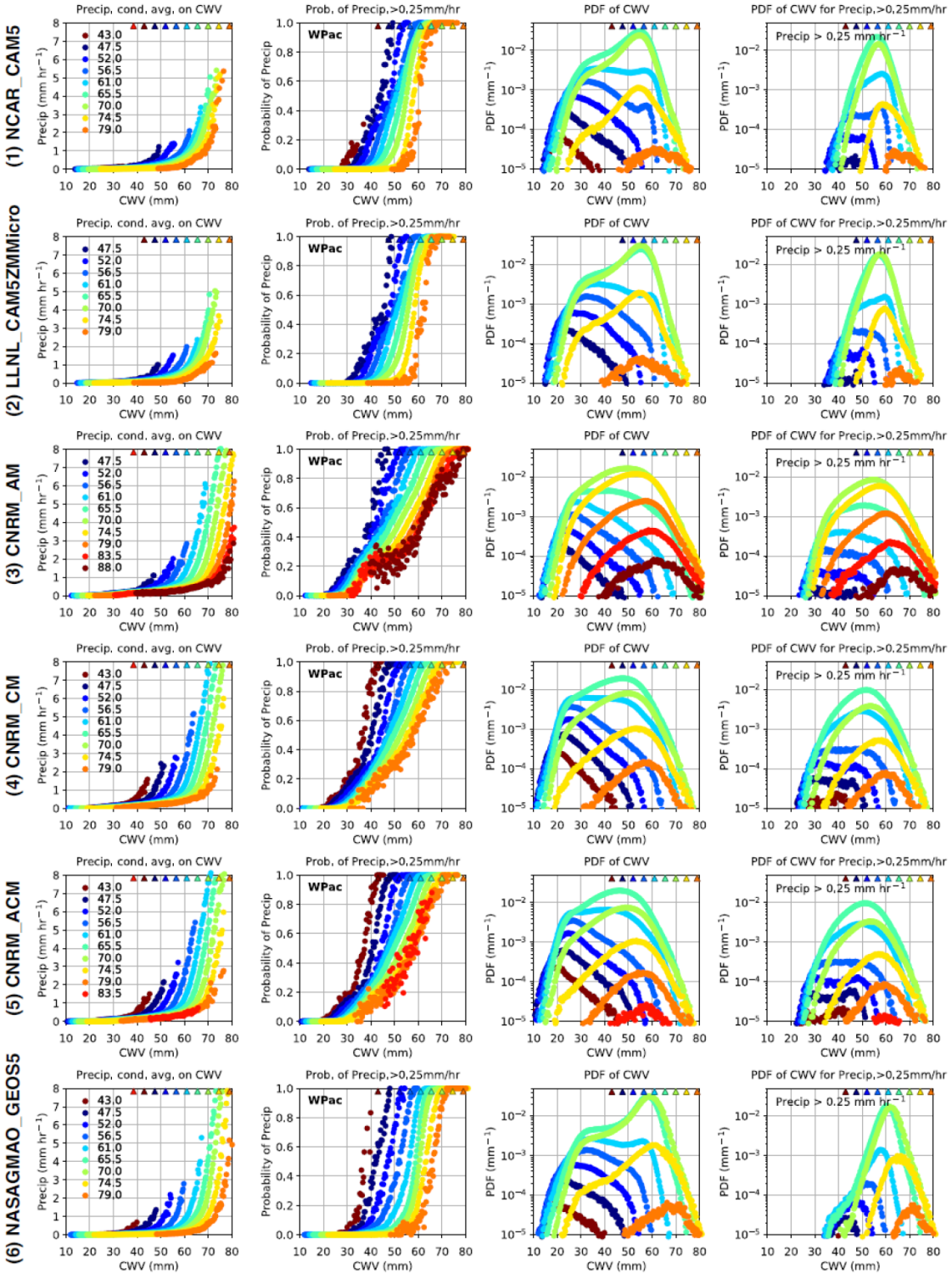

Figure 4.A.1: Basic convective transition statistics in the tropical western Pacific compiled using the 6-hourly output (average for precipitation) from the MJOTF/GASS models.

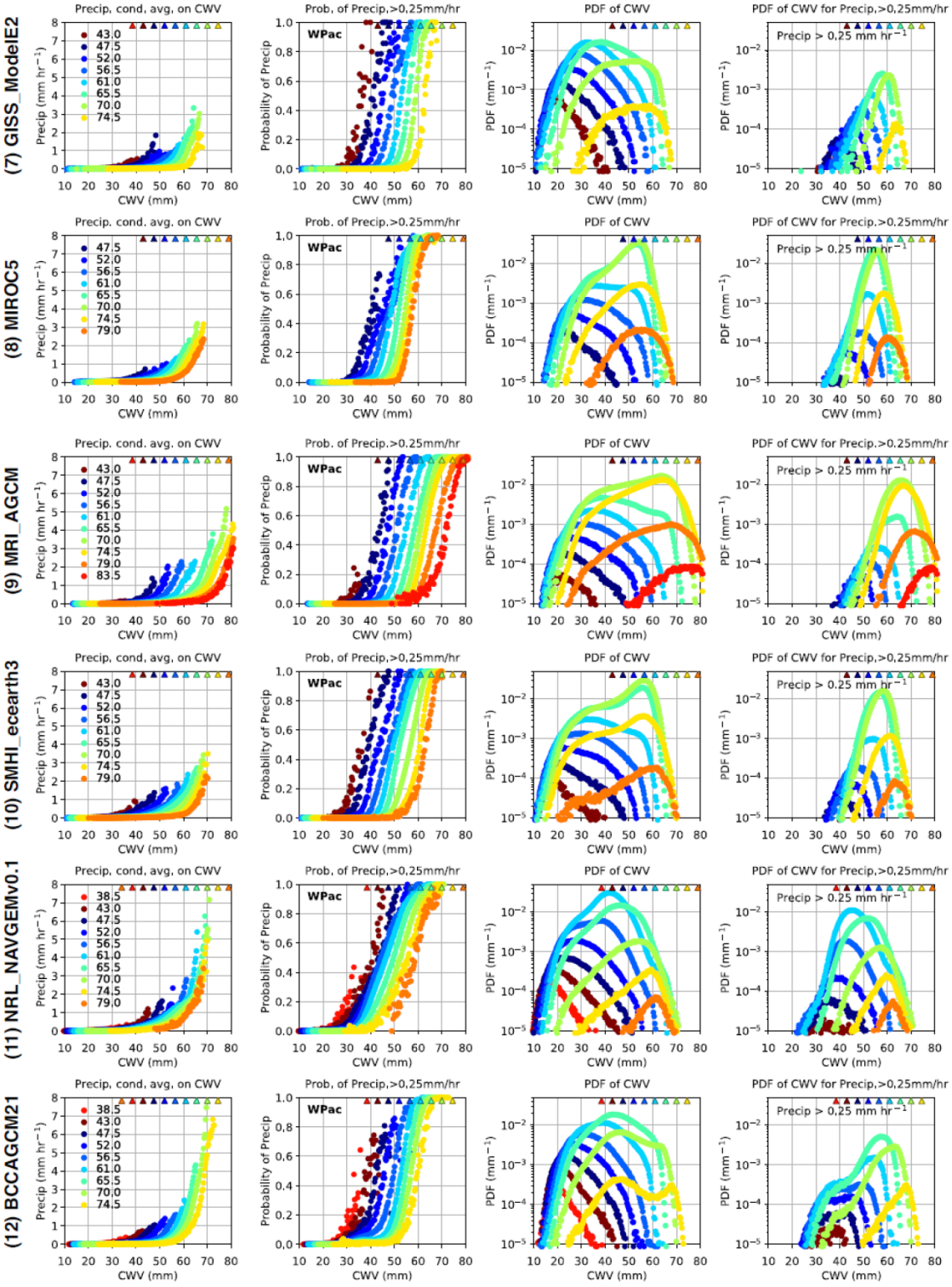

Figure 4.A.2: Figure 4.A.1 continued.

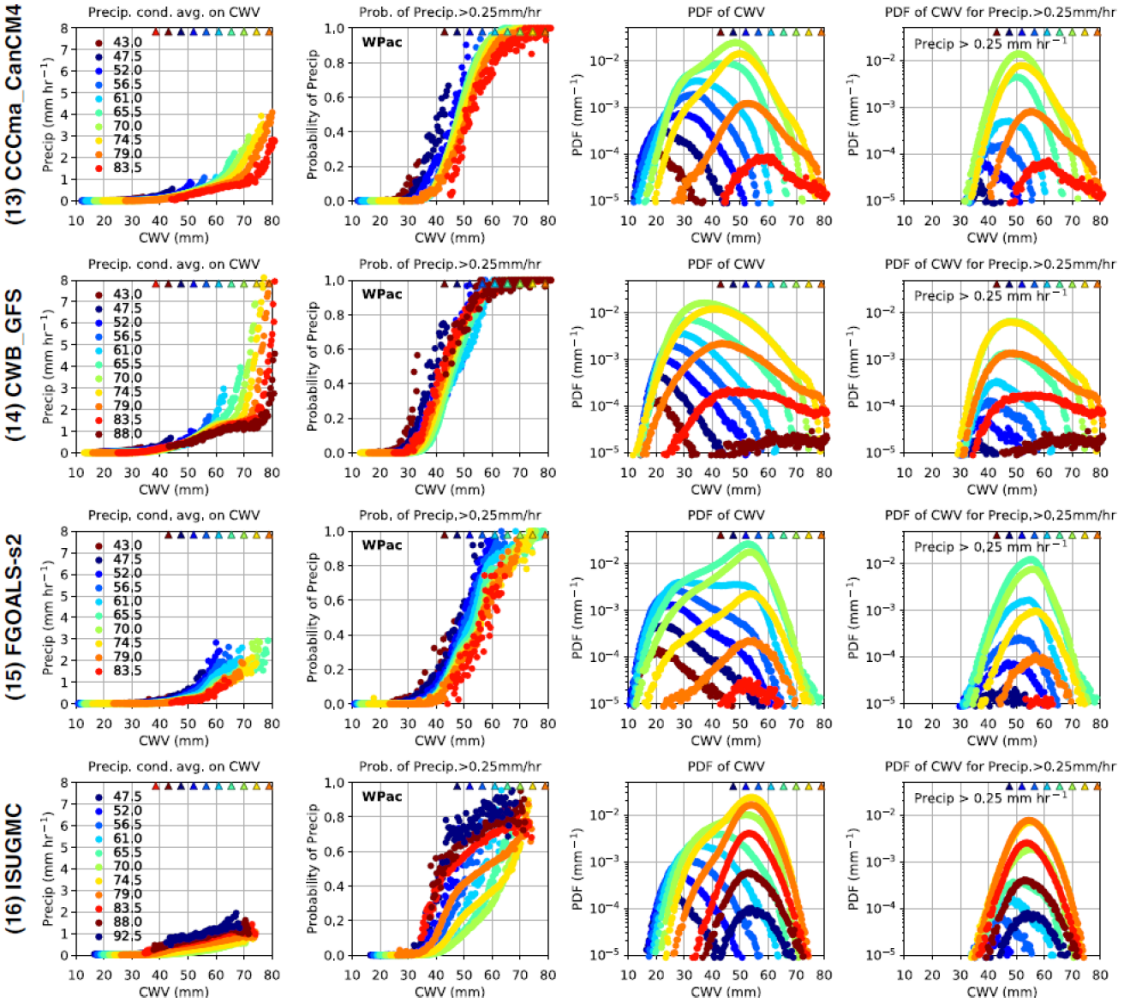

Figure 4.A.3: Figure 4.A.1 continued.

CHAPTER 5

Conditions for convective deep inflow

Abstract

Strong convective precipitation comes from a range of scales, from isolated cumulonimbus to mesoscale convective systems (MCSs). Representations of deep convection (comparable in depth to the troposphere) in climate models still typically rely on plume models in which rising cloud parcels, modified by small-scale turbulent mixing, are compared locally to their environment. There is a growing recognition from field observations and cloud-resolving simulations that a convective updraft structure that draws mass from a deep layer (0–4 km) in the lower troposphere occurs over a wide range of conditions. This "deep inflow" can also be reverse-engineered from the observed dependence of precipitation on the thermodynamic environment. Surprisingly, it occurs for both MCS and less-organized convection, raising the question: Is there a simple, universal characteristic governing the deep inflow? Here we show that horizontally and vertically nonlocal dynamics of the response to buoyancy are key to this behavior. For precipitating deep-convective features including horizontal scales comparable to or exceeding a substantial fraction of the troposphere depth, the response to buoyancy tends to yield deep inflow into the updraft mass flux. Precipitation features in this range of scales are found to dominate contributions to observed convective precipitation for both MCS and less-organized convection. The importance of such nonlocal dynamics implies thinking beyond small-scale turbulence for representation of convection in climate models. Superparameterizations incorporate these effects via subgrid cloud-resolving models but are computationally costly. Solutions here lend support to investment in parameterizations at a

complexity between conventional and superparameterization.

5.1 Introduction

Deep-convective clouds produce much of the Earth's precipitation and strongly constrain the atmospheric circulation especially in the tropics (Houze 2014, Emanuel et al. 1994). Through self-aggregation (Holloway et al. 2017, Wing et al. 2017), convective cells can organize into extensive storms known as mesoscale convective systems (MCSs) that have sizable upper cirriform anvils and rainfall over large areas, accounting for a significant fraction of precipitation in the tropics and midlatitudes (Houze 2004, Nesbitt et al. 2006). MCSs also form constituent parts of synoptic-scale features and impact large-scale disturbances like the Madden-Julian Oscillation (Yang et al. 2019, Chen et al. 2021). Understanding the interaction between convection and large-scale environment aids the projection of precipitation extremes under warming scenarios (O'Gorman and Schneider 2009, Abbott et al. 2020, Martinez-Villalobos and Neelin 2021). Indeed, reliable forecasting of weather and climate depends on adequate representations of deep convection in general circulation models (GCMs). This—especially in regards to organized convection (Yano and Moncrieff 2016, Moncrieff et al. 2017)—remains a challenging subject (Kuo et al. 2020, Yano and Plant 2020, Feng et al. 2021) even with the advances in cloud-resolving models (CRMs) and machine learning (Wing et al. 2020, Yuval and O'Gorman 2020).

A primary source of uncertainty in the parameterization of convection is the entrainment process of environmental air entering in-cloud updrafts (Plant 2010, Sherwood et al. 2014). The traditional view assumes a plume/parcel rising from near the surface that is modified by its immediate surroundings via localized, small-scale turbulent mixing (Arakawa and Schubert 1974, Kain and Fritsch 1990, Zhang and McFarlane 1995). This motivated efforts to quantify a postulated local entrainment rate (Siebesma et al. 2003, Del Genio and Wu 2010, Romps 2010, Masunaga and Luo 2016)—primarily by indirect means—from which mass flux

can be derived for plume models in parameterization schemes (De Rooy and Pier Siebesma 2010, Morrison 2017). At odds with the above conceptual model, a range of turbulent scales contributes to the mixing within actual convective entities (Becker et al. 2018), and features of larger scales are instrumental for nonlocal transport by convection (Siebesma et al. 2007). Field measurements of convective updrafts during aircraft campaigns and by radar wind profilers (LeMone and Zipser 1980, Lucas et al. 1994, Kumar et al. 2015, Schiro et al. 2018), in accordance with CRM simulations (Robe and Emanuel 1996, Li et al. 2008), identify a common mass flux structure that gradually increases throughout the lower troposphere. Contributions to this can occur through organized inflow (Moncrieff 1992)—termed dynamic entrainment (Houghton and Cramer 1951, Ferrier and Houze 1989, Lecoanet and Jeevanjee 2019)—in contrast with the traditional paradigm of small-scale mixing. Deep-inflow profiles, with environmental air entering the updraft through a deep lower-tropospheric layer, can also be inferred from the dependence of precipitation on the temperature-moisture environment as a function of lower-tropospheric layer (Ahmed and Neelin 2018). The deep-inflow profile is in general agnostic as to whether inflow occurs by spatially coherent flow, small-scale turbulence, or both.

Given the importance of mass flux in convective parameterizations, the occurrence of simple vertical structures demands explanation, particularly since any potential for directly constraining such structures could aid in bypassing the elusive task of determining vertical dependence of entrainment rate (Kuang and Bretherton 2006, Han and Bretherton 2019, Peters et al. 2021). The apparent widespread occurrence of deep-inflow structures, together with the surprising observation that such structures occur similarly for both MCS and less-organized deep convection (Schiro et al. 2018), raises the question of whether there is some universal characteristic governing the dynamics of deep inflow.

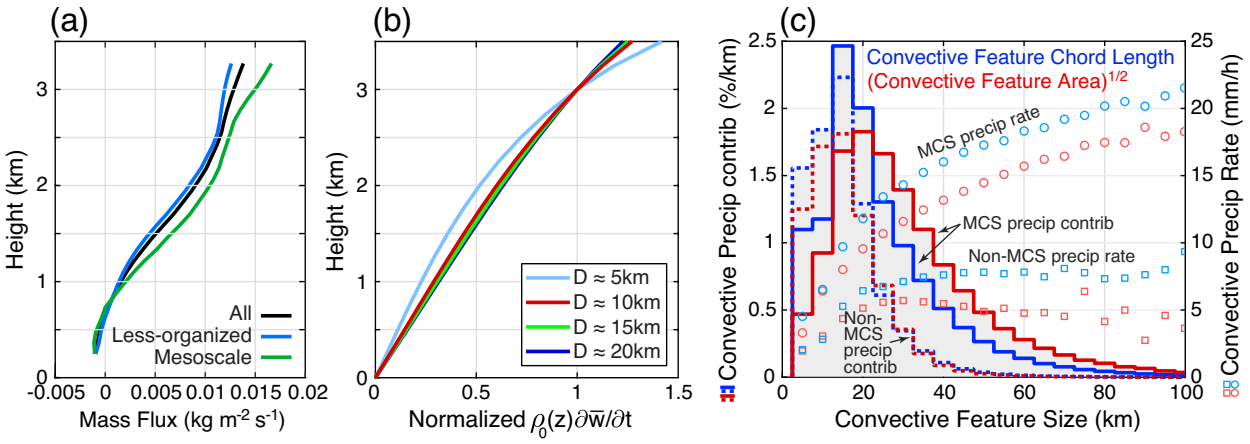

Figure 5.2.1: (a) Mean deep-convective mass flux profiles in the lower troposphere for mesoscale, less-organized, and all precipitating convective events estimated from radar wind profiler during the GOAmazon campaign adapted from (Schiro et al. 2018). (b) Theoretical response of convective mass flux to buoyancy tartares of vertical extent $4 \leq z \leq 8$ km and varying horizontal diameter D. The tartares consist of randomly generated small cylindrical bubbles with a 7:3 warm-to-cold bubble ratio (see Fig. 5.4.1a). The response profiles are the mean within the diameter D and averaged over an ensemble of 10 tartare realizations, then normalized using values at $z = 3$ km. (c) Convective precipitation contribution (curves) and precipitation rate (markers), for MCS and non-MCS features, conditioned on convective feature size measured by chord length (blue) and square root of area (red). The areas under the MCS and non-MCS precipitation contribution curves sum to unity. Feature size is solely based on contiguous *convective* precipitation pixels.

5.2 Convective precipitation feature scales and inflow

Fig. 5.2.1 provides an overview of key ingredients of this problem and of the proposed solution. First, Fig. 5.2.1a summarizes the observed deep-convective updrafts in the lower troposphere (Schiro et al. 2018). The gradual increase of mass flux with height implies horizontal convergence of environmental air into the updrafts through much of the lower troposphere. Such mass flux profiles are characteristic of both MCS and less-organized convection.

Second, Fig. 5.2.1b provides a thumbnail of key results from the nonlocal response to buoyancy elaborated below. For localized net-positive buoyancy structures of horizontal diameter D and vertical extent $4 \leq z \leq 8$ km, the nonlocal response of mass flux $\partial_t(\rho_0 \bar{w})$

averaged within the diameter yields a deep-inflow profile through the lower troposphere. This tends to converge to a roughly linear increase for a broad range of reasonable conditions when D is comparable to the depth of the tropospheric layer under consideration.

Third, in Fig. 5.2.1c we quantify the claim that much of the deep convective precipitation comes from features that include such horizontal scales. Contiguous features of convective precipitation are identified from satellite precipitation radar (PR) retrievals (section 5.A.5). The contribution to total convective precipitation is shown as a function of feature size estimated two different ways: by cord length of the feature and by square root of the area of the feature. The contribution to convective precipitation is further separated by features that meet common criterion for MCS (section 5.A.5), and features that do not (i.e., less organized). Note that stratiform precipitation is *not* included, since we wish to focus on the scales of features of the deep-convective precipitation. For both MCS and less-organized convection, the precipitation contribution peaks around 15 km, and $> 70\%$ of the total convective rain is from events of this scale or greater for both feature size measures. That is, convective rain is mostly from deep-convective features whose horizontal extent is comparable to the depth of the troposphere (Louf et al. 2019). MCS features tend to have greater contribution to convective rain at large sizes than do less-organized features. While the conditionally averaged convective precipitation rate for less-organized features (squares) levels off as size exceeds $\sim$25 km, the MCS precipitation rate (circles) continues to increase asymptotically as roughly the 1/4-th power of feature size.

The convective precipitation region is not necessarily identical to that of the buoyancy, but provides a rough measure of the existence of strong updrafts and downdrafts indicative of buoyancy anomalies. The spatial and temporal coverage of the satellite PR provides regions and periods extensive enough to identify typical characteristics of convection. We also note that the satellite PR resolution $\sim$5 km coarse-grains smaller scale variations, but suffices to support that localized features containing substantial convective rain occur over a broad range of scales. The nonlocal effects discussed below also help justify such coarse-graining.

We thus have 1) observational evidence that much of the convective rain in both MCS and less-organized systems comes from features with characteristic scales of the convection exceeding 10 km; and 2) a theoretical basis for how the nonlocal nature of the response to buoyancy tends to yield deep inflow on such scales.

5.3 Nonlocal response to buoyancy

We follow the anelastic framework (Ogura and Phillips 1962, Lipps and Hemler 1982) to derive the diagnostic equation for the response to buoyancy. The anelastic approximation assumes a horizontally homogeneous, time-invariant atmospheric density $\rho_0(z)$, which allows the governing system to filer acoustic waves and retain nonhydrostatic solutions relevant for deep convection with $O(1)$ aspect ratio. Thus the anelastic approximation has been widely adopted by CRMs (Bryan and Fritsch 2002, Khairoutdinov and Randall 2003, Jung and Arakawa 2008).

5.3.1 Anelastic response to buoyancy field

One can use the vorticity and anelastic continuity equations and derive the following (section 5.A.1)

$$\nabla_h^2 a + \frac{\partial}{\partial z}\left[\frac{1}{\rho_0}\frac{\partial}{\partial z}(\rho_0 a)\right] = \nabla_h^2 B + \mathcal{D}, \tag{5.1}$$

where $a \equiv \partial_t w$ is the vertical acceleration (z-direction), B the buoyancy, $\mathcal{D}$ a quadratic function of spatial derivatives of velocity $\mathbf{u}$ (i.e., associated with flow kinematics) that vanishes when $\mathbf{u} \equiv 0$. The influences of buoyancy and kinematics on a can thus be separately diagnosed via Eq. 5.1. Here we focus on the response to buoyancy, which allows a direct contrast to conventional parameterizations.

In Eq. 5.1, the operator acting on a is elliptic, one thus expects a global response even for localized forcing. The response is accompanied by adjustment to horizontal convergence to ensure mass conservation. Note that buoyancy drives acceleration via $\nabla_h^2 B$, i.e., the flow

field evolves following horizontal variation of buoyancy (Wu et al. 2015).

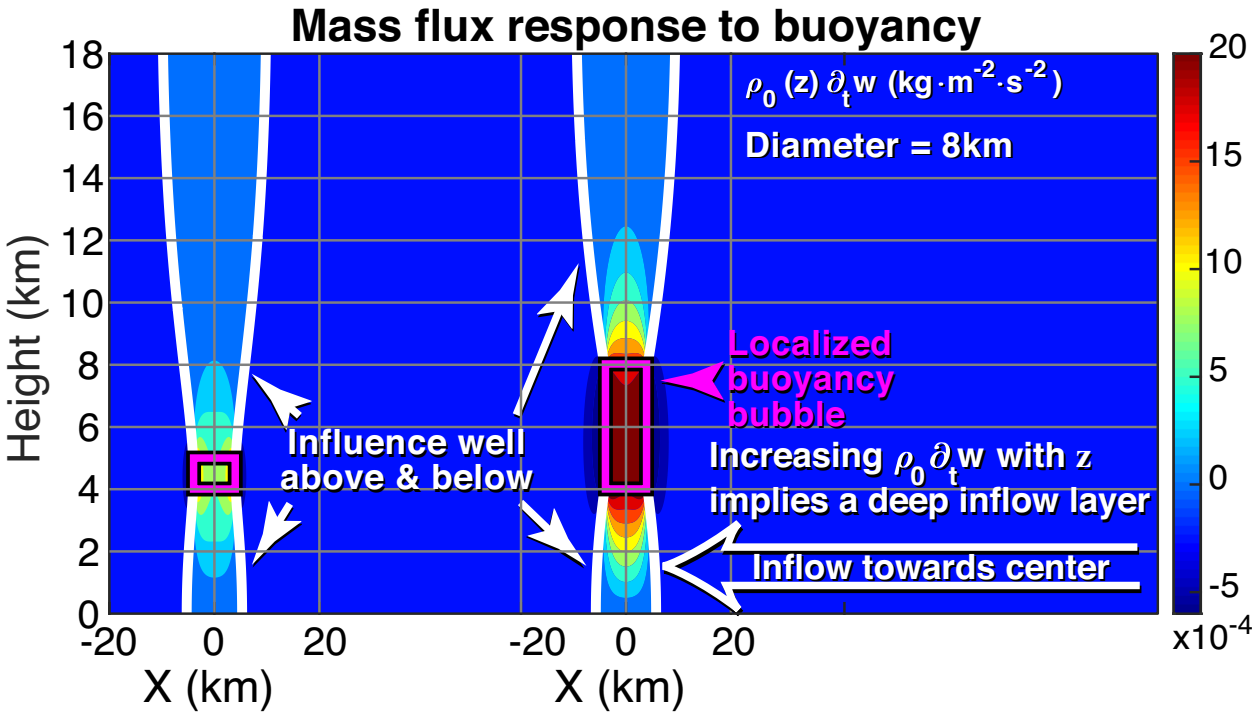

Figure 5.3.1: Cross section of vertical mass flux response (color shading; kg/m^{2}s^2) to idealized buoyancy forcing with constant $B = 0.01$ m/s^2 in cylindrical bubbles of 8-km diameter and varying vertical extent (magenta contours). The white contours indicate zero response. The colorbar range is chosen to highlight details below and above the bubbles.

To give a concrete sense of the nonlocal dynamics, Fig. 5.3.1 demonstrates two examples of the mass flux response $\rho_0 a$ (color shading) to an idealized cylindrical buoyancy bubble of 8-km diameter and different vertical extent (magenta contours). Here a is from solving Eq. 5.1 (with $\mathcal{D} \equiv 0$) for the two bubbles separately. The localized buoyancy generates strong upward acceleration within its diameter, accompanied by weak, broad downward acceleration in the surroundings to conserve mass. The extensive response reaches well below and above the bubble, driving a layer of flow into the convective region in the lower troposphere, as a consequence of gradually increasing $\rho_0 a$ with height, and outflow aloft from decreasing $\rho_0 a$. For the same magnitude of buoyancy, deeper bubbles generally result in greater responses.

The nonlocal responses in Fig. 5.3.1 are consistent with the operator in Eq. 5.1 being

elliptic. The anelastic approximation filtering acoustic solutions implies that the nonlocal behavior is the result of rapid adjustment by acoustic waves (if these were resolved, the adjustment timescale yielding the solutions would be on the order of 10 s). Since the propagation of acoustic waves is not sensitive to atmospheric stability, neither is the nonlocal behavior. In particular, the response above or below a buoyancy anomaly can occur for a broad range of conditions regardless of background stratification.

We do not intend to discuss in depth the buoyancy response to vertical motion here, but note the following. In the atmosphere, updrafts associated with buoyancy anomalies cause adiabatic cooling and possibly condensation. If the condensational heating is not available to balance the work against stratification—e.g., in the upper troposphere or lower stratosphere with low water vapor concentration—the cooling, i.e., production of negative buoyancy can be a probable source of phenomena like the convective cold top (Holloway and Neelin 2007) and convective overshoot (Houze 2014).

5.3.2 Analytic vertical structures

For a more detailed characterization of the nonlocal dynamics, we apply a Fourier transform to Eq. 5.1

$$-4\pi^2(k^2+\ell^2)\widehat{a} + \frac{\partial}{\partial z}\left[\frac{1}{\rho_0}\frac{\partial}{\partial z}(\rho_0\widehat{a})\right] = -4\pi^2(k^2+\ell^2)\widehat{B}, \tag{5.2}$$

where $a \sim \widehat{a}(z;k,\ell)e^{2\pi i(kx+\ell y)}$ and $B \sim \widehat{B}(z;k,\ell)e^{2\pi i(kx+\ell y)}$. We denote the horizontal wavelength by $L \equiv (k^2+\ell^2)^{-1/2}$.

Consider a simple buoyancy structure with $\widehat{B}(z) \equiv$ constanst within a layer and vanishing elsewhere—general profiles can be approximated by superposition. We can analytically solve Eq. 5.2 (section 5.A.3) for the homogeneous solutions

$$\widehat{a}^{\pm}(z;k,\ell) \sim e^{\pm 2\pi z/L}, \tag{5.3}$$

and for the particular solution within the buoyant layer

$$\widehat{a}^{p}(z;k,\ell) \approx \widehat{B}(z;k,\ell). \tag{5.4}$$

The monochromatic solutions can then be constructed as a piecewise linear combination of $\widehat{a}^{\pm}$ and $\widehat{a}^{p}$ by matching across layer boundaries. Therefore, each horizontal wavelength gives rise to an e-folding scale $H_s \equiv L/2\pi$ in the vertical, i.e., there is a greater range of nonlocal influence for longer wavelength.

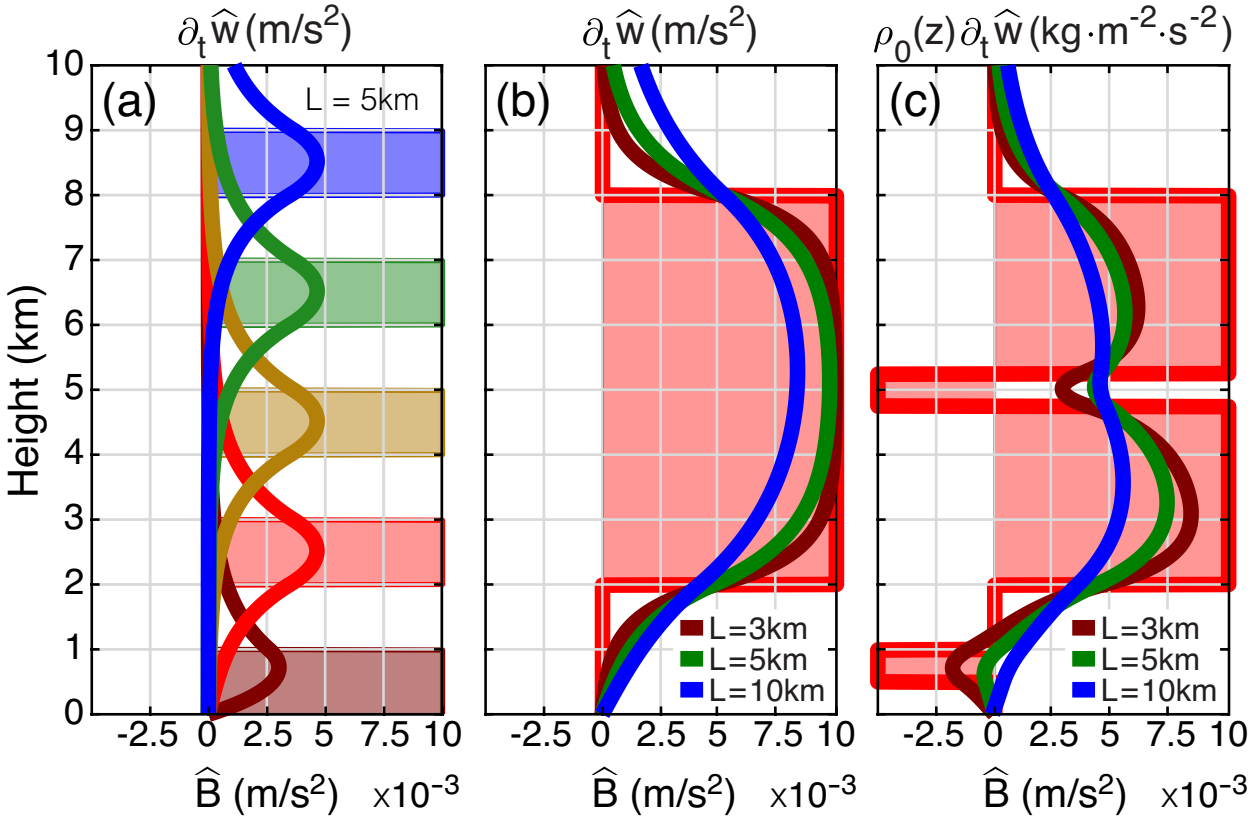

Figure 5.3.2: (a) Monochromatic solutions of vertical velocity response (lines) to individual buoyant layers located at different heights (shadings) with horizontal wavelength $L = 5$ km. (b) As in (a), for a deeper layer (red) and varying L. (c) As in (b), with additional thin layers of negative buoyancy, for vertical mass flux response.

Fig. 5.3.2a shows examples of $\widehat{a}$ (lines) given a buoyant layer of depth $H_B = 1$ km and $\widehat{B} = 0.01$ m/s^2 (shadings) at various heights with $L = 5$ km. Above the buoyancy, the vanishing condition requires that $\widehat{a} \sim e^{-2\pi z/L}$. Below the buoyancy for layers away from the surface (compared with H_s), $\widehat{a} \sim e^{+2\pi z/L}$, and the overall profiles appear to be symmetric in z with maximum occurring in the middle of the layers. But for a layer at low altitude (e.g., brown

line in Fig. 5.3.2a), the surface boundary condition results in $\widehat{a} \approx c_1 e^{+2\pi z/L} - c_2 e^{-2\pi z/L}$—adding $\widehat{a}^p$ if the layer reaches the surface—causing an approximately linear dependence on height below the maximum as well as an overall weaker response magnitude. This surface control is generally important for sufficiently long wavelength (see also Fig. 5.3.2b, blue line). As a limiting case, note that $\widehat{a} = 0$ for $k = \ell = 0$ or $L = \infty$.

To further illustrate how the layer depth and horizontal wavelength affect the solutions, consistent with prior studies (Jeevanjee and Romps 2016, Morrison 2016), Fig. 5.3.2b includes additional examples for a deeper layer of buoyancy ($H_B = 6$ km; red) and varying L. Short wavelength ($L/H_B \ll 1$) leads to limited nonlocal influence, mostly confined in the vicinity of the layer boundaries (brown line). Conversely, long wavelength or relatively shallow ($L/H_B \gg 1$) layer would yield solutions extending well outside the buoyant layer (blue line; also contrast with Fig. 5.3.2a). Note that the inflow can also continue for a characteristic vertical scale $\sim H_s$ within the buoyant layer. The mass flux response corresponding to the accelerations in Figs. 5.3.2a,b are similar but bottom-heavy since ρ_0 decreases with height.

For a more sophisticated case, Fig. 5.3.2c shows the mass flux responses $\rho_0 \widehat{a}$ (lines) to an idealized deep-convective structure with the addition of a near-surface convective inhibition (CIN) layer and a thin negatively-buoyant layer representing, for instance, effects of melting near freezing level (red). For short wavelength, the response tracks the variation of buoyancy (e.g., brown line). But for sufficient horizontal scales, the solution due to net-positive buoyancy has no difficulty tunneling through vertically restricted layers of negative buoyancy or near-surface CIN layer.

This last observation—based on monochromatic argument but also supported by the tartare results presented below—has practical implications. First, this helps understand why a nighttime CIN layer may not prevent pre-existing storms from moving into a region, e.g., over the Mississippi basin or the Amazon (Burleyson et al. 2016, Houze 2018): the layer depth plus surface interactions limit the effect of CIN. This may also be relevant to elevated MCSs (Parker 2008, Marsham et al. 2011). Second, it addresses a common issue in

parcel computations of convective available potential energy (CAPE) that have to contend with small layers in which parcel buoyancy goes negative (e.g., similar to the buoyancy in Fig. 5.3.2c)—this can give rise to an underestimate of the energy actually available to convective storms; the results here indicate why updrafts in large storms easily penetrate such layers.

To briefly summarize the monochromatic dependence on scales: 1) the horizontal wavelength L determines the range of nonlocal vertical influence; small L yields the familiar limit of vertically localized response, while buoyancy layers that are thin compared to $L/2\pi$ yield response of limited magnitude. 2) L comparable to or exceeding a substantial fraction of the tropospheric depth or of the height of the buoyant layer above the surface yields roughly linear profiles below the buoyancy.

5.4 Buoyancy Tartare—robustness to fine structure

Two important modifications occur as one moves from considering a single wavelength to more realistic cases. First, the buoyancy associated with convective updrafts tends to be localized. Features of a finite horizontal size D and net-positive buoyancy consist of Fourier component contributions from a broad range of wavelength, primarily $L \gtrsim D$ (see section 5.A and Fig. 5.B.1). This includes nonlocal effects beyond what one would anticipate from the monochromatic considerations above, and is in contrast with prior studies that emphasized on the contribution from $L \approx D$ (Jeevanjee and Romps 2016, Jeevanjee 2017). Second, robustness to complex buoyancy structures associated with imperfectly mixed turbulent flow must be assessed.

To address this, we build net-positive buoyancy patches from an ensemble of smaller elements, using the shorthand "tartare" to describe these constructions of larger scale D from raw ingredients of scale $d \ll D$. Figs. 5.4.1a,c display two such tartares of diameter $D \approx 10$ km consisting of warm (red) and cold (blue) bubbles of $d = 1$ km and depth 0.5 km.

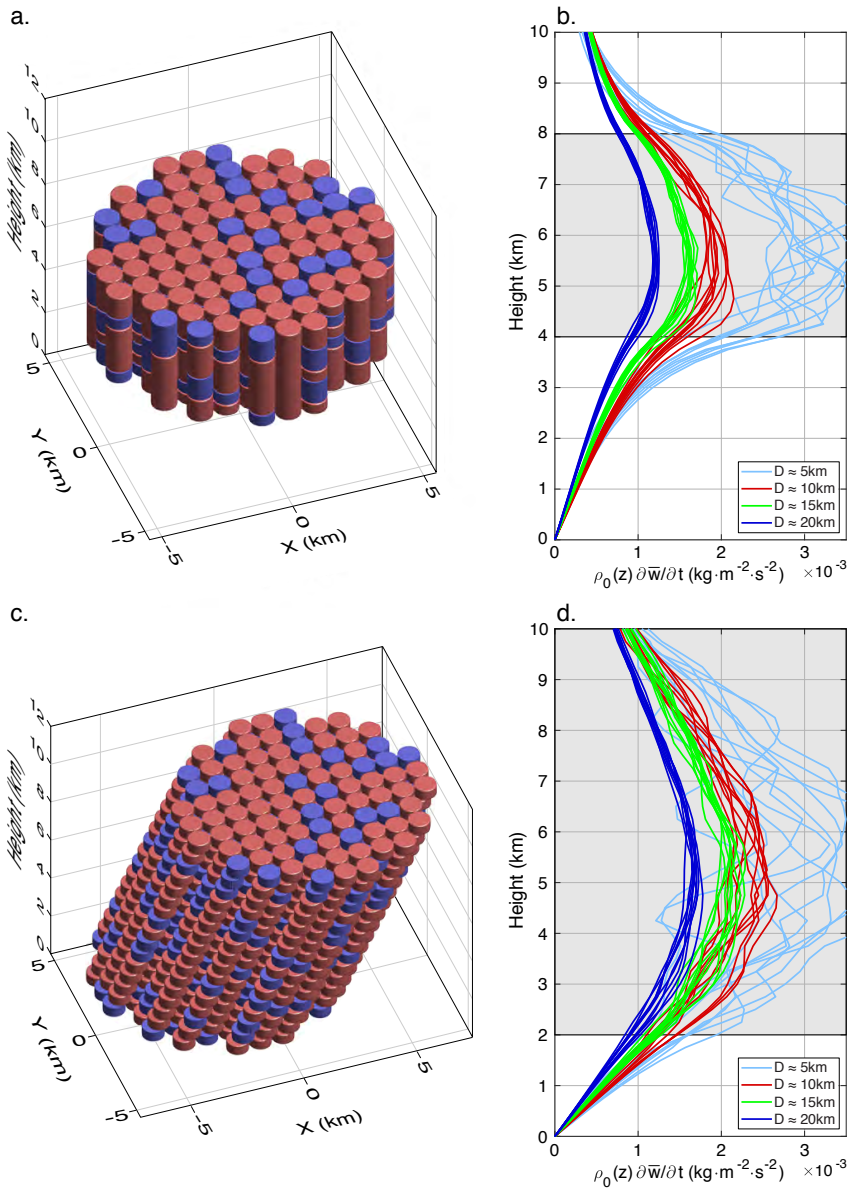

Figure 5.4.1: (a) A realization of a net-positive buoyancy tartare—an aggregate of stochastically generated smaller positive (red) and negative (blue) buoyancy elements—of horizontal diameter $D \approx 10$ km and vertical extent $4 \leq z \leq 8$ km. Buoyancy value within individual element is approximately constant, and of equal strength for warm and cold elements. The ratio of numbers of warm to cold elements is set to 7:3. (b) Theoretical response of convective mass flux to an ensemble of 10 tartare realizations as in (a), for varying D. The average buoyancy over each tartare is rescaled to $+0.01$ m/s^2. Each curve represents the mean profile within the tartare diameter. (c) As in (a), with vertical extent $2 \leq z \leq 10$ km and tilt $\approx 27°$ ($\Delta z/\Delta x \equiv 2$). (d) As in (b), but for vertically tilted tartares as in (c).

In the first set of examples (as in Fig. 5.4.1a) the tartares are constructed to illustrate the nonlocal influence below the buoyancy by placing them at a distance from the surface. The mean mass flux responses to 10 randomly generated tartares for each D are demonstrated in Fig. 5.4.1b (depth indicated by gray shading). Through interference, the integral of individual d-bubbles results in primary Fourier contributions from $L \gtrsim D$ for each D-tartare (Fig. 5.B.1). Thus for larger D and/or further below the buoyancy forcing, the responses converge towards linear dependence on height; see also Fig. 5.2.1b. For smaller D (e.g., $D \approx 5$ km) and closer to the forcing, the vertically localized behaviors—i.e., more rapid increase with height near the tartare base—from the smaller-scale $1 \lesssim L \lesssim 5$ km Fourier components can be distinguished from the nonlocal, roughly linear solutions at lower height ($z < 2.5$ km) dominated by contributions from $L \gtrsim 5$ km.

Figs. 5.4.1c,d offer additional examples for vertically tilted tartares—to mimic convective clouds under wind shear—with a greater depth and lower base. The tilt does not greatly alter the nonlocal behavior for D exceeding a substantial fraction of the tropospheric depth. Since the tartare base is at $z = 2$ km, the responses appear roughly linear even for $D \approx 5$ km. In a more comprehensive setup where the evolution of buoyancy is included, the tilt impacts the location of rain, hence cooling by evaporation of raindrops relative to latent heating. Here, the point is simply that tilted convective systems are subject to the same nonlocal dynamics.

Compared with idealized bubbles of the same dimensions and constant buoyancy (not shown), the tartare responses are weaker by a small fraction but otherwise exhibit similar profiles. This is consistent with the nonlocal dynamics being robust to small-scale variations and depending primarily on large-scale integral measures for the features of interest. The fine structures within the buoyant region give rise to localized intense accelerations. The effects of this on the horizontal average in Figs. 5.4.1b,d may be seen in variations among instances of the tartare. Below the buoyant region, however, the nonlocal effects create relatively smooth structure even for individual instances. Furthermore, this horizontal-average mass flux is

equivalent to the horizontal convergence of air entering the feature, bringing in unmodified air from the far field and thus tending to dominate the effect of the environment on the feature.

5.5 Discussion

Aspects of nonhydrostatic nonlocal solutions have been studied in recent years with different focuses (Jeevanjee and Romps 2016, Jeevanjee 2017). For instance, the rate of entrainment of individual updrafts as a function of updraft size has been examined for dry plumes (Lecoanet and Jeevanjee 2019). Relationships of entrainment and plume scale have been incorporated into recent convective parameterizations for preliminary testing (Morrison 2017, Peters et al. 2021). Such approaches are similar to modifying the idealized monochromatic response as in Fig. 5.3.2 as building blocks for constraining mass flux profiles. Although results here are aimed at explaining a feature of observations, they have implications for such parameterization efforts. In particular, they underline that the leading-order flow response to a buoyant region of a finite size includes contributions from a range of wavelengths. This is key to the robustness of nonlocal dynamics at the larger scales involved in convection—those less amenable to treatment by moment closures or traditional turbulent assumptions—especially when one has in mind the formulation for organized ensembles of smaller structures (Moncrieff et al. 2017). Superparameterizations include representations of all these effects by partially resolving them with CRMs embedded into GCM grid-boxes (Khairoutdinov and Randall 2001, Slawinska et al. 2015, Chern et al. 2016, Jansson et al. 2019). The nonlocal effects whose importance is emphasized here are thus likely captured, even if small-scale turbulence is not resolved—but superparameterization remains computationally expensive. Approaches such as Moncrieff et al. (2017), Morrison (2017), and Lecoanet and Jeevanjee (2019) may be promising if generalized to include the nonlocal effects underlined here both vertically and horizontally. Overall, leveraging anelastic solutions such as Jeevanjee and

Romps (2016), Jeevanjee (2017) and those here can help move parameterizations away from the idealization of entrainment as determined purely locally by a single parameter.

In light of these results, what can be considered universal regarding the convective mass flux profile? Not so much a specific profile shape, but the inherent vertically and horizontally nonlocal effects tending to yield a deep contribution to the mass flux. The nonlocal dynamics is effective at integrating over heterogeneous buoyancy (as in the tartare solutions), and can generate deep inflow robustly under a wide range of conditions. Variations in the distribution of buoyancy can create departures from this. In particular, a layer of negative buoyancy can yield reductions in the vertical increase of mass flux, or even a low-level layer of negative vertical velocity at small scales. Yet because the nonlocal dynamics operates persistently, deep-inflow profiles tend to appear in averages of mass flux over many convective instances.

The observationally motivated hypothesis that there is a common explanation for the deep inflow into heavily precipitating unorganized convection and mesoscale-organized convection indeed has a simple explanation: the nonlocal dynamics entailing interaction between the buoyant layer and the surface. The robustness of this effect especially at scales relevant for both large cumulonimbus and MCSs, supports the potential for parameterizing aspects of these systems. Although it implies the need to include nonlocal, anelastic dynamics in convective parameterizations, the overall effect is to simplify key aspects of the interaction with the thermodynamic environment for large convective entities.

Acknowledgements

The content of this chapter has been prepared for publication, and the research was supported by National Science Foundation grant AGS-1936810 and National Oceanic and Atmospheric Administration grant NA21OAR4310354. This work was partly motivated by prior work of Drs. D. M. Romps and N. Jeevanjee. The author thanks Dr. C.-M. Wu for discussions regarding cloud-resolving simulations and J. Meyerson for graphical assistance.

The author also thanks Drs. S. W. Nesbitt, M. W. Moncrieff, and J. Jeevanjee for their valuable comments.

APPENDIX

5.A Materials and Methods

The 3D velocity and vorticity are denoted by $\mathbf{u} = (\mathbf{u}_h, w) = (u, v, w)$ and $\omega \equiv \nabla \times \mathbf{u} = (\xi, \eta, \zeta)$, respectively (subscript h for horizontal components). We use ρ and θ for atmospheric density and potential temperature, and subscript 0 for hydrostatic reference states that are time-invariant, horizontally homogeneous. Relevant constants for dry air used here include the gas constant $R_d = 287$ J/kg/K, specific heat at constant pressure $c_{pd} = 1005$ J/kg/K and at constant volume $c_{vd} = 718$ J/kg/K (Yau and Rogers 1996). Also, $g = 9.81$ m/s^2.

5.A.1 Governing equation for response

From the definitions of ξ and η, $\partial_y \xi - \partial_x \eta = \nabla_h^2 w - \partial_z(\nabla_h \cdot \mathbf{u}_h) = \nabla_h^2 w + \partial_z[\rho_0^{-1} \partial_z(\rho_0 w)]$ (Jung and Arakawa 2008). The last equality follows the anelastic continuity equation $\nabla_h \cdot (\rho_0 \mathbf{u}_h) + \partial_z(\rho_0 w) = 0$. Apply ∂_t to both sides of the equation and substitute $\partial_t \xi$, $\partial_t \eta$ using the vorticity equation, it is straightforward to derive Eq. 5.1 with

$$\begin{aligned} B &\equiv g\left(\frac{\theta'}{\theta_0} + 0.61 q_v - q_c\right), \\ \mathcal{D} &\equiv -\frac{\partial}{\partial z} \nabla \cdot [\mathbf{u} \times (\omega + \mathbf{f})] + \nabla^2 (u\eta - v\xi), \end{aligned} \tag{5.5}$$

where B is the buoyancy, θ' the potential temperature deviation from θ_0, q_v and q_c the mixing ratios of water vapor and condensate, $\mathbf{f}$ the Coriolis parameter pointing along the vertical z-direction. Note that $(u\eta - v\xi)$ is the z-component of $\mathbf{u} \times \omega$. Furthermore, Eq. 5.1 is similar to the decomposition adopted by Jeevanjee and Romps (2016) in that both capture the nonlocal nature and have the identical response to buoyancy. $\mathcal{D}$ can become a significant modifier in strong flow regimes, but spatial filtering by the nonlocal solutions to Eq. 5.1 would apply to forcing by $\mathcal{D}$ as well.

5.A.2 Atmospheric density

In practice, $\rho_0(z)$ is often determined by a prescribed reference potential temperature $\theta_0(z)$ assuming hydrostatic balance. Here to facilitate our analytic approach, we assume

$$\rho_0(z) \equiv \frac{P_0}{R_d \Theta_0} \left(1 - \frac{z}{H}\right)^{\beta}, \tag{5.6}$$

with the reference pressure P_0 and potential temperature Θ_0 at $z = 0$ (values set to 1000 hPa and 292.8 K so that $H \equiv c_{pd}\Theta_0/g \equiv 30$ km throughout this chapter), and $\beta = c_{vd}/R_d \approx 2.5$ for an isentropic atmosphere (i.e., $\theta_0 \equiv \Theta_0$). Note that the atmospheric stability can be adjusted by slightly varying β, which will not alter our key findings (neither will a more general ρ_0).

5.A.3 Analytic solutions

We introduce the changes of variables

$$\begin{aligned} s &\equiv 1 - \frac{z}{H}, \\ A(s) &\equiv \sqrt{\rho_0}\, \widehat{a}, \end{aligned} \tag{5.7}$$

with which Eq. 5.2 becomes

$$A'' - \lambda(s)^2 A = -F(s). \tag{5.8}$$

Here $(\cdot)'$ denotes d/ds, and

$$\begin{aligned} F(s) &\equiv \lambda_0^2 \sqrt{\rho_0} \widehat{B}, \\ \lambda(s) &\equiv \lambda_0 \left(1 + \frac{\gamma}{\lambda_0^2 s^2}\right)^{1/2}, \\ \lambda_0 &\equiv 2\pi H/L, \\ \gamma &\equiv \frac{\beta}{2}\left(\frac{\beta}{2} + 1\right). \end{aligned} \tag{5.9}$$

A WKB approach gives approximate homogeneous solutions to Eq. 5.8

$$A^{\pm}(s) = e^{\mp\lambda(s)s} \left(\frac{\lambda(s)s - \sqrt{\gamma}}{\lambda(s)s + \sqrt{\gamma}}\right)^{\mp\sqrt{\gamma}/2} \lambda(s)^{-1/2}, \tag{5.10}$$

leading to $\widehat{a}^{\pm}(z)$ in Eq. 5.3. When $\widehat{B}$ is slow-varying—e.g., a polynomial in z of degree ≤ 2—so that $O(F''/\lambda^2) \ll O(F)$ allows iteratively approximating the particular solution

$$A^p(s) = \frac{1}{\lambda(s)^2}\left[F(s) + \frac{F''(s)}{\lambda(s)^2}\right], \tag{5.11}$$

leading to $\widehat{a}^p(z)$ in Eq. 5.4.

The monochromatic solutions in Fig. 5.3.2 are evaluated using Eqs. 5.10 and 5.11. The value and first derivative of the solutions are matched across the jumps of buoyancy in the vertical. This requires inverting regular yet ill-conditioned (because of the exponentials) linear systems for which symbolic computations are employed.

The monochromatic responses to a single layer of buoyancy at various height and for different L form a basis that is used for building responses to more general buoyancy configurations in Fig. 5.4.1. The solutions built this way are consistent with those obtained by numerically solving Eq. 5.1. For general ρ_0, Eqs. 5.7 and 5.8 still apply though with different $\lambda(s)$ and approximate solutions.

5.A.4 Numerical evaluations of responses

Denote the normal cumulative distribution function by $\mathcal{N}(\tau, \tau_0, \sigma) \equiv \frac{1}{2} erfc(-\frac{\tau-\tau_0}{\sqrt{2}\sigma})$. In Fig. 5.3.1, the idealized cylindrical bubbles of buoyancy (units: m/s^2) are given by $B \equiv 10^{-2} \times [1 - \mathcal{N}(r, 4, 0.2)] \times \mathcal{N}(z, z_B, 0.1)[1 - \mathcal{N}(z, z_T, 0.1)]$, where $r \equiv \sqrt{x^2 + y^2}$, $z_B = 4$, and $z_T = 5$, 8 (in km). Here instead of directly solving Eq. 5.1, we consider a domain doubly periodic in the horizontal $-16 \leq x$, $y \leq 16$ km, and solve Eq. 5.2 for $\widehat{a}(z; k, \ell)$ numerically with vanishing conditions at $z = 0$, 20 km for all admissible (k, ℓ), then reconstruct a via inverse Fourier transform. The horizontal and vertical grid spacings used are 125 and 6 m.

The tartares in Fig. 5.4.1 consist of raw elements having buoyancy of the form $B = \pm\frac{1}{2} erfc\left(\frac{r-0.5}{0.02}\right) \times \mathcal{H}(z - z_B)\mathcal{H}(z_B + 0.5 - z)$ with r, z, z_B in km, and $\mathcal{H}$ denoting the Heaviside function. When building a tartare of diameter $\approx D$, the $\pm$ signs are randomly assigned with $7:3$ probabilities. Then the integral buoyancy of each tartare is rescaled to that of $10^{-2} \times$

$\frac{1}{2}erfc\left(\frac{r-D/2}{0.2}\right)\times\mathcal{H}(z-z_B)\mathcal{H}(z_T-z)$ (≈ 0.01 m/s^2 on average within the tartare of depth $z_T - z_B$). The overall responses to buoyancy tartares are computed utilizing the monochromatic basis in a 64 km $\times$ 64 km doubly-periodic horizontal domain with grid spacing 62.5 m. Using the analytic expressions for vertical structures, the accuracy of solutions is not affected by the vertical grid spacing. For tilted tartares, the tartare cross section for $5.5 \leq z \leq 6$ km is centered at $x = y = 0$. The profiles in Fig. 5.4.1d are from averaging over $x^2 + y^2 \leq D/2$.

5.A.5 Convective precipitation feature scales and MCS identification

For convective precipitation features, we use the TRMM 2A25 data (TRMM 2011a) for the period of June 2002 through May 2014 that include PR retrievals of surface rain rate ($rain$) and type ($rainType$) at 5 km $\times$ 5 km resolution covering 40°S-40°N. The values of $rainType$ consist of three numerical digits, and here we consider 2X0 (X = 0, 2, 3, 4) convective. Note that these are different from shallow-convective and have $rain \geq 0.11$ mm/h—the minimum detectable by the PR. For each 2A25 file (i.e., one orbit) we identify all contiguous areas and/or along-track chords consisting of convective raining pixels for the two measures of convective feature size. We further associate each area/chord with MCS or non-MCS depending on whether the feature overlaps with an MCS identified as outlined below. We do not attempt to correct for the finite PR swath—this would lead to biases toward small features and so would not impact our conclusion regarding the importance of large features in the size distribution.

We follow (Mohr and Zipser 1996) for simple MCS criteria. With the 10.8 μm brightness temperature (TB_{11}) from the Merged IR product (Janowiak et al. 2017), for each IR snapshot, we identify MCS as an area with $TB_{11} < 250$ K of at least 2,000 km^2 and an enclosed minimum < 225 K.

5.B Horizontal features of finite size and their Fourier spectrum

In section 5.4, we asserted that net-positive buoyancy features of a finite horizontal size d consist of Fourier component contributions primarily from wavelength $L \gtrsim d$. Here we provide a heuristic argument of why this should be the case, and demonstrate by examples for more realistic instances.

5.B.1 Heuristic proof

The heuristic argument goes as follows. Consider an idealized feature of size d in a large 1D domain

$$B_H(x) \equiv \begin{cases} 1, & |x| \le d/2, \\ 0, & \text{elsewhere}, \end{cases} \tag{5.12}$$

and its Fourier coefficient (omitting the normalization factor that varies with domain size and the precise convention one adopts)

$$\widehat{B_H}(k) \equiv \int B_H(x) e^{-2\pi i k x} dx. \tag{5.13}$$

When $L \equiv 1/|k|$ is comparable to or smaller than d, the sign of the integrand changes. The positive and negative contributions to the integral tends to cancel, resulting in $\widehat{B_H}(k)$ of small magnitude. In contrast, when L exceeds d (or $2d$ to be conservative), the integrand tends to be of the same sign, leading to a substantial $\widehat{B_H}(k)$.

Indeed, for this idealized case, the integral can be readily evaluated

$$\widehat{B_H}(k) = \begin{cases} \frac{d}{k\pi d} \sin(k\pi d), & k \neq 0, \\ d, & k = 0. \end{cases} \tag{5.14}$$

Normalize $\widehat{B_H}$ by its value at $k = 0$. The magnitude of $\widehat{B_H}$ is bounded by the envelope $1/|k|\pi d \equiv L/\pi d$, i.e., the size d quantifies the primary Fourier component contribution.

While the possibility of pathological counterexamples cannot be ruled out, the assertion

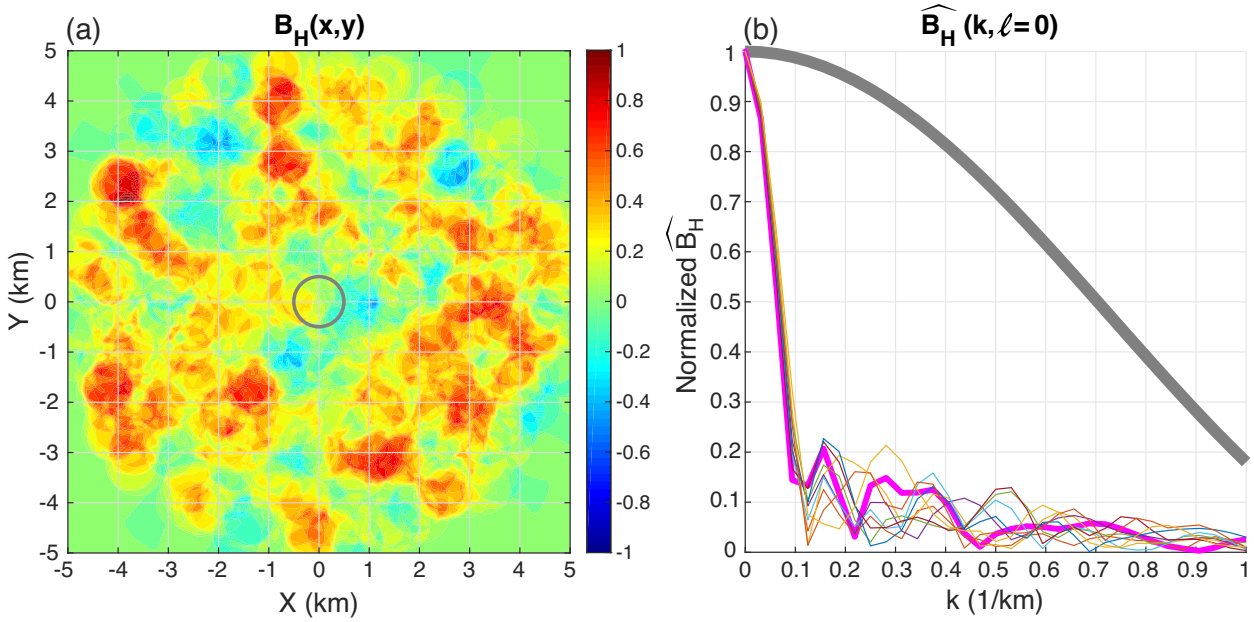

Figure 5.B.1: (a) An idealized buoyancy pattern b_h of diameter 1 km (gray contour) and a realization of stochastically-generated net-positive pattern of diameter $\approx$ 10 km (color shading). The latter is constructed using 1,000 copies of b_h, with their centers randomly spread within a circle of diameter 10 km, magnitudes uniformly distributed in $[0, 1]$, and 7:3 positive-to-negative sign ratio. (b) The Fourier coefficients of b_h (gray thick) and 10 realizations of the stochastically-generated net-positive patterns (colors) for wavenumbers $k \geq 0$, $\ell = 0$. The Fourier coefficient of the pattern in a is indicated by the thick magenta line. Here, the Fourier coefficients are computed in a 32 km$\times$32 km doubly-periodic domain, normalized by their values at $k = \ell = 0$.

is likely to hold for a broad range of conditions relevant to atmospheric convection, as elaborated below.

5.B.2 More realistic demonstration

In 2D, consider the following idealized pattern

$$b_H(x, y) \equiv \frac{1}{2} erfc\left(\frac{r - 0.5}{0.02}\right), \tag{5.15}$$

where $r \equiv \sqrt{x^2 + y^2}$ (units: km). $b_H \sim 1$ for $r < 0.5$ km and vanishes elsewhere with a smooth transition over a width ~ 0.06 km. In Fig. 5.B.1, the pattern of b_h and its Fourier

coefficient

$$\widehat{b_H}(k,\ell) \equiv \iint b_H(x,y)e^{-2\pi i(kx+\ell y)}dxdy \tag{5.16}$$

are represented by gray lines. b_h has its primary Fourier contribution from $|k| \lesssim 1$ (km^{-1}), or $L \gtrsim 1$ km.

Using b_h, we construct more complicated net-positive patterns as

$$B_H(x,y) \equiv \sum_{n=1}^{1000} s_n m_n b_H(x-x_n, y-y_n), \tag{5.17}$$

where $s_n = \pm 1$ with 7:3 positive-to-negative ratio, m_n the magnitude uniformly distributed in $[0,1]$, and (x_n, y_n) the center of b_h uniformly spread within a circle of diameter 10 km. Figure 5.B.1a shows one such realization, which seems plausible for convection. Its Fourier coefficient for $k \geq 0$, $\ell = 0$ is included in Fig. 5.B.1 (magenta thick) together with the results for nine more realizations. These examples demonstrate that when an ensemble of 1-km patterns form larger-scale net-positive features of diameter 10 km, the primary Fourier contributions are from $|k| \lesssim 1/10$ (km^{-1}), or $L \gtrsim 10$ km

Bibliography

Abbott, T. H., T. W. Cronin, and T. Beucler, 2020: Convective dynamics and the response of precipitation extremes to warming in radiative–convective equilibrium. *Journal of the Atmospheric Sciences*, **77 (5)**, 1637–1660.

Adams, D. K., S. I. Gutman, K. L. Holub, and D. S. Pereira, 2013: GNSS observations of deep convective time scales in the Amazon. *Geophysical Research Letters*, **40 (11)**, 2818–2823.

Adler, R. F., and Coauthors, 2003: The version-2 global precipitation climatology project (GPCP) monthly precipitation analysis (1979–present). *Journal of hydrometeorology*, **4 (6)**, 1147–1167.

Ahmed, F., and J. D. Neelin, 2018: Reverse engineering the tropical precipitation–buoyancy relationship. *Journal of the Atmospheric Sciences*, **75 (5)**, 1587–1608.

Ahmed, F., and C. Schumacher, 2017: Geographical differences in the tropical precipitation-moisture relationship and rain intensity onset. *Geophysical Research Letters*, **44 (2)**, 1114–1122.

Annamalai, H., J. Hafner, A. Kumar, and H. Wang, 2014: A framework for dynamical seasonal prediction of precipitation over the Pacific islands. *Journal of climate*, **27 (9)**, 3272–3297.

Arakawa, A., and W. H. Schubert, 1974: Interaction of a cumulus cloud ensemble with the large-scale environment, Part I. *Journal of Atmospheric Sciences*, **31 (3)**, 674–701.

Bechtold, P., J.-P. Chaboureau, A. Beljaars, A. Betts, M. Köhler, M. Miller, and J.-L. Redelsperger, 2004: The simulation of the diurnal cycle of convective precipitation over land in a global model. *Quarterly Journal of the Royal Meteorological Society: A journal of the atmospheric sciences, applied meteorology and physical oceanography*, **130 (604)**, 3119–3137.

Bechtold, P., M. Köhler, T. Jung, F. Doblas-Reyes, M. Leutbecher, M. J. Rodwell, F. Vitart, and G. Balsamo, 2008: Advances in simulating atmospheric variability with the ECMWF model: From synoptic to decadal time-scales. *Quarterly Journal of the Royal Meteorological Society: A journal of the atmospheric sciences, applied meteorology and physical oceanography*, **134 (634)**, 1337–1351.

Becker, T., C. S. Bretherton, C. Hohenegger, and B. Stevens, 2018: Estimating bulk entrainment

with unaggregated and aggregated convection. *Geophysical Research Letters*, **45 (1)**, 455–462.

Benedict, J. J., E. D. Maloney, A. H. Sobel, and D. M. Frierson, 2014: Gross moist stability and MJO simulation skill in three full-physics GCMs. *Journal of Atmospheric Sciences*, **71 (9)**, 3327–3349.

Benedict, J. J., E. D. Maloney, A. H. Sobel, D. M. Frierson, and L. J. Donner, 2013: Tropical intraseasonal variability in version 3 of the GFDL atmosphere model. *Journal of Climate*, **26 (2)**, 426–449.

Bergemann, M., and C. Jakob, 2016: How important is tropospheric humidity for coastal rainfall in the tropics? *Geophysical Research Letters*, **43 (11)**, 5860–5868.

Bernstein, D. N., and J. D. Neelin, 2016: Identifying sensitive ranges in global warming precipitation change dependence on convective parameters. *Geophysical Research Letters*, **43 (11)**, 5841–5850.

Biasutti, M., 2013: Forced Sahel rainfall trends in the CMIP5 archive. *Journal of Geophysical Research: Atmospheres*, **118 (4)**, 1613–1623.

Biasutti, M., and A. H. Sobel, 2009: Delayed Sahel rainfall and global seasonal cycle in a warmer climate. *Geophysical Research Letters*, **36 (23)**.

Bitz, C. M., K. Shell, P. Gent, D. Bailey, G. Danabasoglu, K. Armour, M. Holland, and J. Kiehl, 2012: Climate sensitivity of the community climate system model, version 4. *Journal of Climate*, **25 (9)**, 3053–3070.

Booth, J. F., Y.-O. Kwon, S. Ko, R. J. Small, and R. Msadek, 2017: Spatial patterns and intensity of the surface storm tracks in CMIP5 models. *Journal of Climate*, **30 (13)**, 4965–4981.

Boyle, J., S. Klein, D. Lucas, H.-Y. Ma, J. Tannahill, and S. Xie, 2015: The parametric sensitivity of CAM5's MJO. *Journal of Geophysical Research: Atmospheres*, **120 (4)**, 1424–1444.

Bretherton, C. S., M. E. Peters, and L. E. Back, 2004: Relationships between water vapor path and precipitation over the tropical oceans. *Journal of climate*, **17 (7)**, 1517–1528.

Brown, R. G., and C. Zhang, 1997: Variability of midtropospheric moisture and its effect on cloud-top height distribution during TOGA COARE. *Journal of the atmospheric sciences*, **54 (23)**, 2760–2774.

Bryan, G. H., and J. M. Fritsch, 2002: A benchmark simulation for moist nonhydrostatic numerical models. *Monthly Weather Review*, **130 (12)**, 2917–2928.

Burleyson, C. D., Z. Feng, S. M. Hagos, J. Fast, L. A. Machado, and S. T. Martin, 2016: Spatial variability of the background diurnal cycle of deep convection around the goamazon2014/5 field campaign sites. *Journal of Applied Meteorology and Climatology*, **55 (7)**, 1579–1598.

Camargo, S. J., M. K. Tippett, A. H. Sobel, G. A. Vecchi, and M. Zhao, 2014: Testing the performance of tropical cyclone genesis indices in future climates using the HiRAM model. *Journal of Climate*, **27 (24)**, 9171–9196.

Chen, C.-C., J. Richter, C. Liu, M. Moncrieff, Q. Tang, W. Lin, S. Xie, and P. Rasch, 2021: Effects of organized convection parameterization on the MJO and precipitation in E3SMv1. Part I: Mesoscale heating. *Journal of Advances in Modeling Earth Systems*, **13 (6)**, e2020MS002 401.

Chen, D., and A. Dai, 2018: Dependence of estimated precipitation frequency and intensity on data resolution. *Climate dynamics*, **50 (9)**, 3625–3647.

Chen, Y., E. E. Ebert, K. J. Walsh, and N. E. Davidson, 2013: Evaluation of TRMM 3B42 precipitation estimates of tropical cyclone rainfall using PACRAIN data. *Journal of Geophysical Research: Atmospheres*, **118 (5)**, 2184–2196.

Chern, J.-D., W.-K. Tao, S. E. Lang, T. Matsui, J.-L. Li, K. I. Mohr, G. M. Skofronick-Jackson, and C. D. Peters-Lidard, 2016: Performance of the goddard multiscale modeling framework with goddard ice microphysical schemes. *Journal of Advances in Modeling Earth Systems*, **8 (1)**, 66–95.

Covey, C., P. J. Gleckler, C. Doutriaux, D. N. Williams, A. Dai, J. Fasullo, K. Trenberth, and A. Berg, 2016: Metrics for the diurnal cycle of precipitation: Toward routine benchmarks for climate models. *Journal of Climate*, **29 (12)**, 4461–4471.

Dai, A., 2006: Precipitation characteristics in eighteen coupled climate models. *Journal of climate*, **19 (18)**, 4605–4630.

De Rooy, W. C., and A. Pier Siebesma, 2010: Analytical expressions for entrainment and detrainment in cumulus convection. *Quarterly Journal of the Royal Meteorological Society*, **136 (650)**, 1216–1227.

Del Genio, A. D., Y. Chen, D. Kim, and M.-S. Yao, 2012: The MJO transition from shallow to deep convection in CloudSat/CALIPSO data and GISS GCM simulations. *Journal of Climate*, **25 (11)**, 3755–3770.

Del Genio, A. D., and J. Wu, 2010: The role of entrainment in the diurnal cycle of continental convection. *Journal of Climate*, **23 (10)**, 2722–2738.

Derbyshire, S., I. Beau, P. Bechtold, J.-Y. Grandpeix, J.-M. Piriou, J.-L. Redelsperger, and P. Soares, 2004: Sensitivity of moist convection to environmental humidity. *Quarterly Journal of the Royal Meteorological Society: A journal of the atmospheric sciences, applied meteorology and physical oceanography*, **130 (604)**, 3055–3079.

Donner, L. J., 1993: A cumulus parameterization including mass fluxes, vertical momentum dynamics, and mesoscale effects. *Journal of Atmospheric Sciences*, **50 (6)**, 889–906.

Donner, L. J., and Coauthors, 2011: The dynamical core, physical parameterizations, and basic simulation characteristics of the atmospheric component AM3 of the GFDL global coupled model CM3. *Journal of Climate*, **24 (13)**, 3484–3519.

Emanuel, K. A., J. David Neelin, and C. S. Bretherton, 1994: On large-scale circulations in convecting atmospheres. *Quarterly Journal of the Royal Meteorological Society*, **120 (519)**, 1111–1143.

Eyring, V., and Coauthors, 2019: Taking climate model evaluation to the next level. *Nature Climate Change*, **9 (2)**, 102–110.

Feng, Z., F. Song, K. Sakaguchi, and L. R. Leung, 2021: Evaluation of mesoscale convective systems in climate simulations: Methodological development and results from MPAS-CAM over the United States. *Journal of Climate*, **34 (7)**, 2611–2633.

Ferrier, B. S., and R. A. Houze, 1989: One-dimensional time-dependent modeling of GATE cumulonimbus convection. *Journal of Atmospheric Sciences*, **46 (3)**, 330–352.

Gaustad, K., and L. Riihimaki, 1996: Atmospheric Radiation Measurement (ARM) Climate Research Facility. Updated hourly. MWR Retrievals (MWRRET1LILJCLOU). 1998-01-01 to 2010-12-31, Tropical Western Pacific (TWP) Central Facility, Manus I., PNG (C1). Atmo-

spheric Radiation Measurement (ARM) Climate Research Facility Data Archive: Oak Ridge, Tennessee, USA. Data set accessed 2016 at http://dx.doi.org/10.5439/1027369.

Gaustad, K., and L. Riihimaki, 1998: Atmospheric Radiation Measurement (ARM) Climate Research Facility. Updated hourly. MWR Retrievals (MWRRET1LILJCLOU). 1999-01-01 to 2008-12-31, Tropical Western Pacific (TWP) Central Facility, Nauru Island (C2). Atmospheric Radiation Measurement (ARM) Climate Research Facility Data Archive: Oak Ridge, Tennessee, USA. Data set accessed 2016 at http://dx.doi.org/10.5439/1027369.

Gent, P. R., and Coauthors, 2011: The community climate system model version 4. *Journal of climate*, **24 (19)**, 4973–4991.

Gonzalez, A. O., and X. Jiang, 2017: Winter mean lower tropospheric moisture over the Maritime Continent as a climate model diagnostic metric for the propagation of the Madden-Julian oscillation. *Geophysical Research Letters*, **44 (5)**, 2588–2596.

Han, J., and C. S. Bretherton, 2019: Tke-based moist eddy-diffusivity mass-flux (edmf) parameterization for vertical turbulent mixing. *Weather and Forecasting*, **34 (4)**, 869–886.

Hannah, W. M., and E. D. Maloney, 2014: The moist static energy budget in NCAR CAM5 hindcasts during DYNAMO. *Journal of Advances in Modeling Earth Systems*, **6 (2)**, 420–440.

Harrop, B. E., P.-L. Ma, P. J. Rasch, R. B. Neale, and C. Hannay, 2018: The role of convective gustiness in reducing seasonal precipitation biases in the Tropical West Pacific. *Journal of Advances in Modeling Earth Systems*, **10 (4)**, 961–970.

Henderson, S. A., E. D. Maloney, and S.-W. Son, 2017: Madden–Julian oscillation Pacific teleconnections: The impact of the basic state and MJO representation in general circulation models. *Journal of Climate*, **30 (12)**, 4567–4587.

Hilburn, K., and F. Wentz, 2008: Intercalibrated passive microwave rain products from the unified microwave ocean retrieval algorithm (UMORA). *Journal of Applied Meteorology and Climatology*, **47 (3)**, 778–794.

Hirota, N., Y. N. Takayabu, M. Watanabe, M. Kimoto, and M. Chikira, 2014: Role of convective entrainment in spatial distributions of and temporal variations in precipitation over tropical oceans. *Journal of Climate*, **27 (23)**, 8707–8723.

Holdridge, D., and J. Kyrouac, 1997: Atmospheric Radiation Measurement (ARM) Climate Research Facility. Uupdated hourly. Surface Meteorological Instrumentation (MET). 1998-01-01 to 2010-12-31, Tropical Western Pacific (TWP) Central Facility, Manus I., PNG (C1). Atmospheric Radiation Measurement (ARM) Climate Research Facility Data Archive: Oak Ridge, Tennessee, USA. Data set accessed 2016 at http://dx.doi.org/10.5439/1025220.

Holdridge, D., and J. Kyrouac, 1998: Atmospheric Radiation Measurement (ARM) Climate Research Facility. Uupdated hourly. Surface Meteorological Instrumentation (MET). 1999-01-01 to 2008-12-31, Tropical Western Pacific (TWP) Central Facility, Nauru Island (C2). Atmospheric Radiation Measurement (ARM) Climate Research Facility Data Archive: Oak Ridge, Tennessee, USA. Data set accessed 2016 at http://dx.doi.org/10.5439/1025220.

Holloway, C. E., and J. D. Neelin, 2007: The convective cold top and quasi equilibrium. *Journal of Atmospheric Sciences*, **64 (5)**, 1467–1487.

Holloway, C. E., and J. D. Neelin, 2009: Moisture vertical structure, column water vapor, and tropical deep convection. *Journal of Atmospheric Sciences*, **66 (6)**, 1665–1683.

Holloway, C. E., and J. D. Neelin, 2010: Temporal relations of column water vapor and tropical precipitation. *Journal of the Atmospheric Sciences*, **67 (4)**, 1091–1105.

Holloway, C. E., A. A. Wing, S. Bony, C. Muller, H. Masunaga, T. S. L'Ecuyer, D. D. Turner, and P. Zuidema, 2017: Observing convective aggregation. *Surveys in Geophysics*, **38 (6)**, 1199–1236.

Houghton, H. G., and H. E. Cramer, 1951: A theory of entrainment in convective currents. *Journal of Atmospheric Sciences*, **8 (2)**, 95–102.

Hourdin, F., and Coauthors, 2013: LMDZ5B: the atmospheric component of the IPSL climate model with revisited parameterizations for clouds and convection. *Climate Dynamics*, **40 (9-10)**, 2193–2222.

Houze, R. A., 2004: Mesoscale convective systems. *Reviews of Geophysics*, **42 (4)**.

Houze, R. A., 2014: *Cloud dynamics*. Academic press.

Houze, R. A., 2018: 100 years of research on mesoscale convective systems. *Meteorological Monographs*, **59**, 17–1.

Hurrell, J. W., and Coauthors, 2013: The Community Earth System Model: a framework for collaborative research. *Bulletin of the American Meteorological Society*, **94 (9)**, 1339–1360.

Hwang, Y.-T., and D. M. Frierson, 2013: Link between the double-Intertropical Convergence Zone problem and cloud biases over the Southern Ocean. *Proceedings of the National Academy of Sciences*, **110 (13)**, 4935–4940.

Janowiak, J., B. Joyce, and P. Xie, 2017: NCEP/CPC L3 Half Hourly 4km Global (60S - 60N) Merged IR V1. Accessed 7-Jan-2020, Edited by Andrey Savtchenko, Greenbelt, MD, Goddard Earth Sciences Data and Information Services Center.

Jansson, F., G. van den Oord, I. Pelupessy, J. H. Grönqvist, A. P. Siebesma, and D. Crommelin, 2019: Regional superparameterization in a global circulation model using large eddy simulations. *Journal of Advances in Modeling Earth Systems*, **11 (9)**, 2958–2979.

Jeevanjee, N., 2017: Vertical velocity in the gray zone. *Journal of Advances in Modeling Earth Systems*, **9 (6)**, 2304–2316.

Jeevanjee, N., and D. M. Romps, 2016: Effective buoyancy at the surface and aloft. *Quarterly Journal of the Royal Meteorological Society*, **142 (695)**, 811–820.

Jensen, M. P., and A. D. Del Genio, 2006: Factors limiting convective cloud-top height at the ARM Nauru Island climate research facility. *Journal of climate*, **19 (10)**, 2105–2117.

Jiang, X., 2017: Key processes for the eastward propagation of the Madden-Julian Oscillation based on multimodel simulations. *Journal of Geophysical Research: Atmospheres*, **122 (2)**, 755–770.

Jiang, X., M. Zhao, E. D. Maloney, and D. E. Waliser, 2016: Convective moisture adjustment time scale as a key factor in regulating model amplitude of the Madden-Julian Oscillation. *Geophysical Research Letters*, **43 (19)**, 10–412.

Jiang, X., and Coauthors, 2015: Vertical structure and physical processes of the Madden-Julian oscillation: Exploring key model physics in climate simulations. *Journal of Geophysical Research: Atmospheres*, **120 (10)**, 4718–4748.

Jung, J.-H., and A. Arakawa, 2008: A three-dimensional anelastic model based on the vorticity equation. *Monthly weather review*, **136 (1)**, 276–294.

Kain, J. S., and J. M. Fritsch, 1990: A one-dimensional entraining/detraining plume model and

its application in convective parameterization. *Journal of Atmospheric Sciences*, **47 (23)**, 2784–2802.

Kanamitsu, M., W. Ebisuzaki, J. Woollen, S.-K. Yang, J. Hnilo, M. Fiorino, and G. Potter, 2002: NCEP/DOE AMIP-II Reanalysis (R-2). *Bulletin of the American Meteorological Society*, **83 (11)**, 1631–1644.

Khairoutdinov, M., and D. Randall, 2006: High-resolution simulation of shallow-to-deep convection transition over land. *Journal of Atmospheric Sciences*, **63 (12)**, 3421–3436.

Khairoutdinov, M. F., and D. A. Randall, 2001: A cloud resolving model as a cloud parameterization in the NCAR Community Climate System Model: Preliminary results. *Geophysical Research Letters*, **28 (18)**, 3617–3620.

Khairoutdinov, M. F., and D. A. Randall, 2003: Cloud resolving modeling of the ARM summer 1997 IOP: Model formulation, results, uncertainties, and sensitivities. *Journal of Atmospheric Sciences*, **60 (4)**, 607–625.

Kim, D., A. H. Sobel, E. D. Maloney, D. M. Frierson, and I.-S. Kang, 2011: A systematic relationship between intraseasonal variability and mean state bias in AGCM simulations. *Journal of Climate*, **24 (21)**, 5506–5520.

Kim, D., and Coauthors, 2014: Process-oriented MJO simulation diagnostic: Moisture sensitivity of simulated convection. *Journal of Climate*, **27 (14)**, 5379–5395.

Kim, D., and Coauthors, 2018: Process-oriented diagnosis of tropical cyclones in high-resolution GCMs. *Journal of Climate*, **31 (5)**, 1685–1702.

Klingaman, N. P., X. Jiang, P. K. Xavier, J. Petch, D. Waliser, and S. J. Woolnough, 2015a: Vertical structure and physical processes of the Madden-Julian oscillation: Synthesis and summary. *Journal of Geophysical Research: Atmospheres*, **120 (10)**, 4671–4689.

Klingaman, N. P., G. M. Martin, and A. Moise, 2017: ASoP (v1.0): A set of methods for analyzing scales of precipitation in general circulation models. *Geoscientific Model Development*, **10 (1)**, 57–83.

Klingaman, N. P., and Coauthors, 2015b: Vertical structure and physical processes of the Madden-

Julian oscillation: Linking hindcast fidelity to simulated diabatic heating and moistening. *Journal of Geophysical Research: Atmospheres*, **120 (10)**, 4690–4717.

Kuang, Z., and C. S. Bretherton, 2006: A mass-flux scheme view of a high-resolution simulation of a transition from shallow to deep cumulus convection. *Journal of the Atmospheric Sciences*, **63 (7)**, 1895–1909.

Kumar, V. V., C. Jakob, A. Protat, C. R. Williams, and P. T. May, 2015: Mass-flux characteristics of tropical cumulus clouds from wind profiler observations at darwin, australia. *Journal of the Atmospheric Sciences*, **72 (5)**, 1837–1855.

Kuo, Y.-H., J. D. Neelin, and C. R. Mechoso, 2017: Tropical convective transition statistics and causality in the water vapor–precipitation relation. *Journal of the Atmospheric Sciences*, **74 (3)**, 915–931.

Kuo, Y.-H., K. A. Schiro, and J. D. Neelin, 2018: Convective transition statistics over tropical oceans for climate model diagnostics: Observational baseline. *Journal of the Atmospheric Sciences*, **75 (5)**, 1553–1570.

Kuo, Y.-H., and Coauthors, 2020: Convective transition statistics over tropical oceans for climate model diagnostics: GCM evaluation. *Journal of the Atmospheric Sciences*, **77 (1)**, 379–403.

Langenbrunner, B., and J. Neelin, 2017: Multiobjective constraints for climate model parameter choices: Pragmatic Pareto fronts in CESM1. *Journal of Advances in Modeling Earth Systems*, **9 (5)**, 2008–2026.

Langenbrunner, B. G., 2015: *Quantifying uncertainty in precipitation climatology, twenty-first century change, and teleconnections in global climate models*. University of California, Los Angeles.

Lecoanet, D., and N. Jeevanjee, 2019: Entrainment in resolved, dry thermals. *Journal of the Atmospheric Sciences*, **76 (12)**, 3785–3801.

LeMone, M. A., and E. J. Zipser, 1980: Cumulonimbus vertical velocity events in gate. part i: Diameter, intensity and mass flux. *Journal of Atmospheric Sciences*, **37 (11)**, 2444–2457.

Li, Y., E. J. Zipser, S. K. Krueger, and M. A. Zulauf, 2008: Cloud-resolving modeling of deep convection during kwajex. part i: Comparison to trmm satellite and ground-based radar observations. *Monthly weather review*, **136 (7)**, 2699–2712.

Lin, J.-L., 2007: The double-ITCZ problem in IPCC AR4 coupled GCMs: Ocean–atmosphere feedback analysis. *Journal of Climate*, **20 (18)**, 4497–4525.

Lin, J. W.-B., and J. D. Neelin, 2003: Toward stochastic deep convective parameterization in general circulation models. *Geophysical research letters*, **30 (4)**.

Lintner, B. R., C. E. Holloway, and J. D. Neelin, 2011: Column water vapor statistics and their relationship to deep convection, vertical and horizontal circulation, and moisture structure at Nauru. *Journal of Climate*, **24 (20)**, 5454–5466.

Lipps, F. B., and R. S. Hemler, 1982: A scale analysis of deep moist convection and some related numerical calculations. *Journal of the Atmospheric Sciences*, **39 (10)**, 2192–2210.

Louf, V., C. Jakob, A. Protat, M. Bergemann, and S. Narsey, 2019: The relationship of cloud number and size with their large-scale environment in deep tropical convection. *Geophysical Research Letters*, **46 (15)**, 9203–9212.

Lucas, C., E. J. Zipser, and M. A. Lemone, 1994: Vertical velocity in oceanic convection off tropical australia. *Journal of Atmospheric sciences*, **51 (21)**, 3183–3193.

Madden, R. A., and P. R. Julian, 1971: Detection of a 40–50 day oscillation in the zonal wind in the tropical Pacific. *Journal of Atmospheric Sciences*, **28 (5)**, 702–708.

Maloney, E. D., Á. F. Adames, and H. X. Bui, 2019a: Madden–Julian oscillation changes under anthropogenic warming. *Nature Climate Change*, **9 (1)**, 26–33.

Maloney, E. D., and Coauthors, 2019b: Process-oriented evaluation of climate and weather forecasting models. *Bulletin of the American Meteorological Society*, **100 (9)**, 1665–1686.

Mapes, B., and R. Neale, 2011: Parameterizing convective organization to escape the entrainment dilemma. *Journal of Advances in Modeling Earth Systems*, **3 (2)**.

Mapes, B., S. Tulich, J. Lin, and P. Zuidema, 2006: The mesoscale convection life cycle: Building block or prototype for large-scale tropical waves? *Dynamics of atmospheres and oceans*, **42 (1-4)**, 3–29.

Marsham, J. H., S. B. Trier, T. M. Weckwerth, and J. W. Wilson, 2011: Observations of elevated convection initiation leading to a surface-based squall line during 13 June IHOP_2002. *Monthly Weather Review*, **139 (1)**, 247–271.

Martinez-Villalobos, C., and J. D. Neelin, 2021: Climate models capture key features of extreme precipitation probabilities across regions. *Environmental Research Letters*, **16 (2)**, 024 017.

Masunaga, H., and Z. J. Luo, 2016: Convective and large-scale mass flux profiles over tropical oceans determined from synergistic analysis of a suite of satellite observations. *Journal of Geophysical Research: Atmospheres*, **121 (13)**, 7958–7974.

Mather, J., T. P. Ackerman, W. Clements, F. Barnes, M. Ivey, L. Hatfield, and R. Reynolds, 1998: An atmospheric radiation and cloud station in the tropical western Pacific. *Bulletin of the American Meteorological Society*, **79 (4)**, 627–642.

Mechoso, C. R., and Coauthors, 1995: The seasonal cycle over the tropical pacific in coupled ocean–atmosphere general circulation models. *Monthly Weather Review*, **123 (9)**, 2825–2838.

Mohr, K. I., and E. J. Zipser, 1996: Mesoscale convective systems defined by their 85-ghz ice scattering signature: Size and intensity comparison over tropical oceans and continents. *Monthly weather review*, **124 (11)**, 2417–2437.

Moncrieff, M. W., 1992: Organized convective systems: Archetypal dynamical models, mass and momentum flux theory, and parametrization. *Quarterly Journal of the Royal Meteorological Society*, **118 (507)**, 819–850.

Moncrieff, M. W., C. Liu, and P. Bogenschutz, 2017: Simulation, modeling, and dynamically based parameterization of organized tropical convection for global climate models. *Journal of the Atmospheric Sciences*, **74 (5)**, 1363–1380.

Morrison, H., 2016: Impacts of updraft size and dimensionality on the perturbation pressure and vertical velocity in cumulus convection. Part II: Comparison of theoretical and numerical solutions and fully dynamical simulations. *Journal of the Atmospheric Sciences*, **73 (4)**, 1455–1480.

Morrison, H., 2017: An analytic description of the structure and evolution of growing deep cumulus updrafts. *Journal of the Atmospheric Sciences*, **74 (3)**, 809–834.

Muller, C. J., L. E. Back, P. A. O'Gorman, and K. A. Emanuel, 2009: A model for the relationship between tropical precipitation and column water vapor. *Geophysical Research Letters*, **36 (16)**.

Neale, R. B., J. H. Richter, and M. Jochum, 2008: The impact of convection on ENSO: From a delayed oscillator to a series of events. *Journal of climate*, **21 (22)**, 5904–5924.

Neale, R. B., and Coauthors, 2010: Description of the NCAR Community Atmosphere Model (CAM 4.0). *NCAR Tech. Note NCAR/TN-485+ STR*, 224pp.

Neale, R. B., and Coauthors, 2012: Description of the NCAR community atmosphere model (CAM 5.0). *NCAR Tech. Note NCAR/TN-486+ STR*, 289pp.

Neelin, J. D., O. Peters, and K. Hales, 2009: The transition to strong convection. *Journal of the Atmospheric Sciences*, **66 (8)**, 2367–2384.

Neelin, J. D., O. Peters, J. W.-B. Lin, K. Hales, and C. E. Holloway, 2008: Rethinking convective quasi-equilibrium: Observational constraints for stochastic convective schemes in climate models. *Philosophical Transactions of the Royal Society A: Mathematical, Physical and Engineering Sciences*, **366 (1875)**, 2579–2602.

Nesbitt, S. W., R. Cifelli, and S. A. Rutledge, 2006: Storm morphology and rainfall characteristics of trmm precipitation features. *Monthly Weather Review*, **134 (10)**, 2702–2721.

O'Gorman, P. A., and T. Schneider, 2009: The physical basis for increases in precipitation extremes in simulations of 21st-century climate change. *Proceedings of the National Academy of Sciences*, **106 (35)**, 14 773–14 777.

Ogura, Y., and N. A. Phillips, 1962: Scale analysis of deep and shallow convection in the atmosphere. *J. atmos. Sci*, **19 (2)**, 173–179.

Oueslati, B., and G. Bellon, 2013: Convective entrainment and large-scale organization of tropical precipitation: Sensitivity of the CNRM-CM5 hierarchy of models. *Journal of Climate*, **26 (9)**, 2931–2946.

Oueslati, B., and G. Bellon, 2015: The double ITCZ bias in CMIP5 models: Interaction between SST, large-scale circulation and precipitation. *Climate dynamics*, **44 (3-4)**, 585–607.

Padullés, R., E. Cardellach, K.-N. Wang, C. O. Ao, F. J. Turk, and M. d. l. Torre-Juárez, 2018: Assessment of global navigation satellite system (GNSS) radio occultation refractivity under heavy precipitation. *Atmospheric Chemistry and Physics*, **18 (16)**, 11 697–11 708.

Pan, H.-l., and W.-S. Wu, 1995: Implementing a mass flux convection parameterization package for the NMC medium-range forecast model. *NMC Office Note 409*, 40pp.

Parker, M. D., 2008: Response of simulated squall lines to low-level cooling. *Journal of the Atmospheric Sciences*, **65 (4)**, 1323–1341.

Parsons, D. B., J.-L. Redelsperger, and K. Yoneyama, 2000: The evolution of the tropical western Pacific atmosphere-ocean system following the arrival of a dry intrusion. *Quarterly Journal of the Royal Meteorological Society*, **126 (563)**, 517–548.

Petch, J., D. Waliser, X. Jiang, P. Xavier, and S. Woolnough, 2011: A global model intercomparison of the physical processes associated with the Madden–Julian oscillation. *GEWEX News*, **21 (3)**, 3–5.

Peters, J., H. Morrison, G. Zhang, and S. Powell, 2021: Improving the physical basis for updraft dynamics in deep convection parameterizations. *Journal of Advances in Modeling Earth Systems*, **13 (2)**, e2020MS002 282.

Peters, O., and J. D. Neelin, 2006: Critical phenomena in atmospheric precipitation. *Nature physics*, **2 (6)**, 393–396.

Plant, R., 2010: A review of the theoretical basis for bulk mass flux convective parameterization. *Atmospheric Chemistry and Physics*, **10 (8)**, 3529–3544.

Plant, R., and G. C. Craig, 2008: A stochastic parameterization for deep convection based on equilibrium statistics. *Journal of the Atmospheric Sciences*, **65 (1)**, 87–105.

Qian, Y., and Coauthors, 2018: Parametric sensitivity and uncertainty quantification in the version 1 of E3SM atmosphere model based on short perturbed parameter ensemble simulations. *Journal of Geophysical Research: Atmospheres*, **123 (23)**, 13–046.

Raymond, D. J., and A. M. Blyth, 1986: A stochastic mixing model for nonprecipitating cumulus clouds. *Journal of Atmospheric Sciences*, **43 (22)**, 2708–2718.

Redelsperger, J., D. Parsons, and F. Guichard, 2002: Recovery processes and factors limiting cloud-top height following the arrival of a dry intrusion observed during TOGA COARE. *Journal of Atmospheric Sciences*, **59 (16)**, 2438–2457.

Richter, J. H., and P. J. Rasch, 2008: Effects of convective momentum transport on the atmospheric

circulation in the Community Atmosphere Model, version 3. *Journal of Climate*, **21 (7)**, 1487–1499.

Ridout, J. A., 2002: Sensitivity of tropical Pacific convection to dry layers at mid-to upper levels: Simulation and parameterization tests. *Journal of the atmospheric sciences*, **59 (23)**, 3362–3381.

Rio, C., F. Hourdin, J.-Y. Grandpeix, and J.-P. Lafore, 2009: Shifting the diurnal cycle of parameterized deep convection over land. *Geophysical Research Letters*, **36 (7)**.

Robe, F. R., and K. A. Emanuel, 1996: Moist convective scaling: Some inferences from three-dimensional cloud ensemble simulations. *Journal of Atmospheric Sciences*, **53 (22)**, 3265–3275.

Romps, D. M., 2010: A direct measure of entrainment. *Journal of the Atmospheric Sciences*, **67 (6)**, 1908–1927.

Romps, D. M., and Z. Kuang, 2010: Do undiluted convective plumes exist in the upper tropical troposphere? *Journal of the Atmospheric Sciences*, **67 (2)**, 468–484.

Rowell, D. P., 2012: Sources of uncertainty in future changes in local precipitation. *Climate dynamics*, **39 (7-8)**, 1929–1950.

Sahany, S., J. D. Neelin, K. Hales, and R. B. Neale, 2012: Temperature–moisture dependence of the deep convective transition as a constraint on entrainment in climate models. *Journal of Atmospheric Sciences*, **69 (4)**, 1340–1358.

Sahany, S., J. D. Neelin, K. Hales, and R. B. Neale, 2014: Deep convective transition characteristics in the Community Climate System Model and changes under global warming. *Journal of Climate*, **27 (24)**, 9214–9232.

Sanderson, B. M., 2011: A multimodel study of parametric uncertainty in predictions of climate response to rising greenhouse gas concentrations. *Journal of Climate*, **24 (5)**, 1362–1377.

Schiro, K., F. Ahmed, S. Giangrande, and J. Neelin, 2018: GoAmazon2014/5 points to deep-inflow approach to mesoscale-organized and unorganized deep convection. *Proc. Natl. Acad. Sci. USA*, **115**, 4577–4582.

Schiro, K. A., J. D. Neelin, D. K. Adams, and B. R. Lintner, 2016: Deep convection and column

water vapor over tropical land versus tropical ocean: A comparison between the Amazon and the tropical western Pacific. *Journal of the Atmospheric Sciences*, **73 (10)**, 4043–4063.

Schiro, K. A., H. Su, Y. Wang, B. Langenbrunner, J. H. Jiang, and J. D. Neelin, 2019: Relationships between tropical ascent and high cloud fraction changes with warming revealed by perturbation physics experiments in CAM5. *Geophysical Research Letters*, **46 (16)**, 10 112–10 121.

Sherwood, S. C., S. Bony, and J.-L. Dufresne, 2014: Spread in model climate sensitivity traced to atmospheric convective mixing. *Nature*, **505 (7481)**, 37–42.

Sherwood, S. C., and R. Wahrlich, 1999: Observed evolution of tropical deep convective events and their environment. *Monthly Weather Review*, **127 (8)**, 1777–1795.

Siebesma, A. P., P. M. Soares, and J. Teixeira, 2007: A combined eddy-diffusivity mass-flux approach for the convective boundary layer. *Journal of the atmospheric sciences*, **64 (4)**, 1230–1248.

Siebesma, A. P., and Coauthors, 2003: A large eddy simulation intercomparison study of shallow cumulus convection. *Journal of the Atmospheric Sciences*, **60 (10)**, 1201–1219.

Slawinska, J., O. Pauluis, A. J. Majda, and W. W. Grabowski, 2015: Multiscale interactions in an idealized walker cell: Simulations with sparse space–time superparameterization. *Monthly weather review*, **143 (2)**, 563–580.

Smith, R., and Coauthors, 2010: The parallel ocean program (POP) reference manual ocean component of the community climate system model (CCSM) and community earth system model (CESM). *LAUR-01853*, **141**, 1–140.

Sobel, A. H., S. E. Yuter, C. S. Bretherton, and G. N. Kiladis, 2004: Large-scale meteorology and deep convection during TRMM KWAJEX. *Monthly Weather Review*, **132 (2)**, 422–444.

Song, X., and G. J. Zhang, 2011: Microphysics parameterization for convective clouds in a global climate model: Description and single-column model tests. *Journal of Geophysical Research: Atmospheres*, **116 (D2)**.

Stechmann, S. N., and J. D. Neelin, 2011: A stochastic model for the transition to strong convection. *Journal of the atmospheric sciences*, **68 (12)**, 2955–2970.

Stechmann, S. N., and J. D. Neelin, 2014: First-passage-time prototypes for precipitation statistics. *Journal of the Atmospheric Sciences*, **71 (9)**, 3269–3291.

Stokes, G. M., and S. E. Schwartz, 1994: The Atmospheric Radiation Measurement (ARM) Program: Programmatic background and design of the cloud and radiation test bed. *Bulletin of the American Meteorological Society*, **75 (7)**, 1201–1222.

Su, H., and Coauthors, 2017: Tightening of tropical ascent and high clouds key to precipitation change in a warmer climate. *Nature communications*, **8 (1)**, 1–9.

Sundqvist, H., 1988: Parameterization of condensation and associated clouds in models for weather prediction and general circulation simulation. *Physically-based modelling and simulation of climate and climatic change*, Springer, 433–461.

Suselj, K., M. J. Kurowski, and J. Teixeira, 2019: On the factors controlling the development of shallow convection in eddy-diffusivity/mass-flux models. *Journal of the Atmospheric Sciences*, **76 (2)**, 433–456.

Suzuki, K., G. Stephens, A. Bodas-Salcedo, M. Wang, J.-C. Golaz, T. Yokohata, and T. Koshiro, 2015: Evaluation of the warm rain formation process in global models with satellite observations. *Journal of the Atmospheric Sciences*, **72 (10)**, 3996–4014.

Tao, W.-K., and M. W. Moncrieff, 2009: Multiscale cloud system modeling. *Reviews of Geophysics*, **47 (4)**.

Tompkins, A. M., 2001: Organization of tropical convection in low vertical wind shears: The role of water vapor. *Journal of the atmospheric sciences*, **58 (6)**, 529–545.

Torri, G., Z. Kuang, and Y. Tian, 2015: Mechanisms for convection triggering by cold pools. *Geophysical Research Letters*, **42 (6)**, 1943–1950.

Trenberth, K. E., J. Fasullo, and L. Smith, 2005: Trends and variability in column-integrated atmospheric water vapor. *Climate dynamics*, **24 (7)**, 741–758.

Trenberth, K. E., and C. J. Guillemot, 1998: Evaluation of the atmospheric moisture and hydrological cycle in the NCEP/NCAR reanalyses. *Climate Dynamics*, **14 (3)**, 213–231.

TRMM, 2011a: TRMM Precipitation Radar rainfall rate and profile L2 1.5 hours V7. Green-

belt, MD, Goddard Earth Sciences Data and Information Services Center. Available at https://disc.gsfc.nasa.gov/datacollection/TRMM_2A25_7.html. Accessed 19-Aug-2016.

TRMM, 2011b: TRMM (TMPA) Rainfall Estimate L3 3 hour 0.25 degree x 0.25 degree V7. Greenbelt, MD, Goddard Earth Sciences Data and Information Services Center. Available at https://disc.gsfc.nasa.gov/datacollection/TRMM_3B42_7.html. Accessed 8-Aug-2016.

Voigt, A., and Coauthors, 2016: The tropical rain belts with an annual cycle and a continent model intercomparison project: TRACMIP. *Journal of Advances in Modeling Earth Systems*, **8 (4)**, 1868–1891.

Waliser, D. E., B. Tian, X. Xie, W. T. Liu, M. J. Schwartz, and E. J. Fetzer, 2009: How well can satellite data characterize the water cycle of the Madden-Julian Oscillation? *Geophysical research letters*, **36 (21)**.

Wang, Y., G. J. Zhang, and Y.-J. He, 2017: Simulation of precipitation extremes using a stochastic convective parameterization in the NCAR CAM5 under different resolutions. *Journal of Geophysical Research: Atmospheres*, **122 (23)**, 12–875.

Wentz, F. J., C. Gentemann, and K. A. Hilburn, 2015: Remote Sensing Systems TRMM TMI Daily Environmental Suite on 0.25 deg grid, Version 7.1. Remote Sensing Systems, Santa Rosa, CA. Available online at https://www.remss.com/missions/tmi. Accessed 8-Jul-2016.

Wing, A. A., K. Emanuel, C. E. Holloway, and C. Muller, 2017: Convective self-aggregation in numerical simulations: A review. *Shallow Clouds, Water Vapor, Circulation, and Climate Sensitivity*, Springer, 1–25.

Wing, A. A., and K. A. Emanuel, 2014: Physical mechanisms controlling self-aggregation of convection in idealized numerical modeling simulations. *Journal of Advances in Modeling Earth Systems*, **6 (1)**, 59–74.

Wing, A. A., and Coauthors, 2020: Clouds and convective self-aggregation in a multimodel ensemble of radiative-convective equilibrium simulations. *Journal of advances in modeling earth systems*, **12 (9)**, e2020MS002 138.

Wu, C.-M., M.-H. Lo, W.-T. Chen, and C.-T. Lu, 2015: The impacts of heterogeneous land surface fluxes on the diurnal cycle precipitation: A framework for improving the gcm representation

of land-atmosphere interactions. *Journal of Geophysical Research: Atmospheres*, **120 (9)**, 3714–3727.

Yang, Q., A. J. Majda, and M. W. Moncrieff, 2019: Upscale impact of mesoscale convective systems and its parameterization in an idealized gcm for an mjo analog above the equator. *Journal of the Atmospheric Sciences*, **76 (3)**, 865–892.

Yano, J.-I., C. Liu, and M. W. Moncrieff, 2012: Self-organized criticality and homeostasis in atmospheric convective organization. *Journal of the Atmospheric Sciences*, **69 (12)**, 3449–3462.

Yano, J.-I., and M. W. Moncrieff, 2016: Numerical archetypal parameterization for mesoscale convective systems. *Journal of the Atmospheric Sciences*, **73 (7)**, 2585–2602.

Yano, J.-I., and R. S. Plant, 2020: Why does arakawa and schubert's convective quasi-equilibrium closure not work? mathematical analysis and implications. *Journal of the Atmospheric Sciences*, **77 (4)**, 1371–1385.

Yau, M. K., and R. R. Rogers, 1996: *A short course in cloud physics*. Elsevier.

Yokohata, T., J. D. Annan, M. Collins, C. S. Jackson, M. Tobis, M. J. Webb, and J. C. Hargreaves, 2012: Reliability of multi-model and structurally different single-model ensembles. *Climate dynamics*, **39 (3)**, 599–616.

Yuval, J., and P. A. O'Gorman, 2020: Stable machine-learning parameterization of subgrid processes for climate modeling at a range of resolutions. *Nature communications*, **11 (1)**, 1–10.

Zhang, G. J., and N. A. McFarlane, 1995: Sensitivity of climate simulations to the parameterization of cumulus convection in the Canadian Climate Centre general circulation model. *Atmosphere-ocean*, **33 (3)**, 407–446.

Zhao, M., I. M. Held, S.-J. Lin, and G. A. Vecchi, 2009: Simulations of global hurricane climatology, interannual variability, and response to global warming using a 50-km resolution GCM. *Journal of Climate*, **22 (24)**, 6653–6678.

Zhao, M., and Coauthors, 2018a: The GFDL global atmosphere and land model AM4.0/LM4.0: 1. Simulation characteristics with prescribed SSTs. *Journal of Advances in Modeling Earth Systems*, **10 (3)**, 691–734.

Zhao, M., and Coauthors, 2018b: The GFDL global atmosphere and land model AM4.0/LM4.0: 2.

Model description, sensitivity studies, and tuning strategies. *Journal of Advances in Modeling Earth Systems*, **10 (3)**, 735–769.

Zhu, H., and H. H. Hendon, 2015: Role of large-scale moisture advection for simulation of the MJO with increased entrainment. *Quarterly Journal of the Royal Meteorological Society*, **141 (691)**, 2127–2136.